



Development of Electrical Impedance Methods for 3D Cell Cultures

Canali, Chiara

Publication date:
2015

Document Version
Publisher's PDF, also known as Version of record

[Link back to DTU Orbit](#)

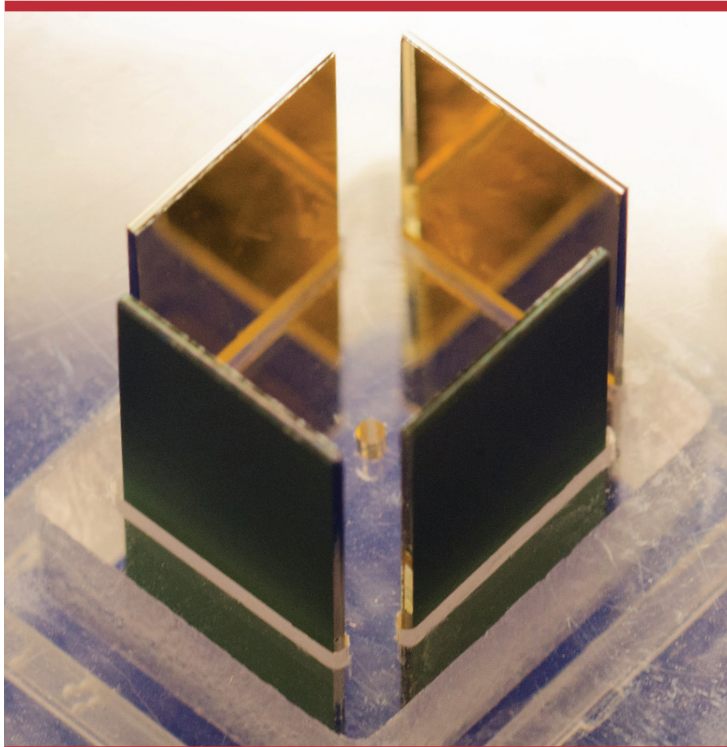
Citation (APA):
Canali, C. (2015). *Development of Electrical Impedance Methods for 3D Cell Cultures*. DTU Nanotech.

General rights

Copyright and moral rights for the publications made accessible in the public portal are retained by the authors and/or other copyright owners and it is a condition of accessing publications that users recognise and abide by the legal requirements associated with these rights.

- Users may download and print one copy of any publication from the public portal for the purpose of private study or research.
- You may not further distribute the material or use it for any profit-making activity or commercial gain
- You may freely distribute the URL identifying the publication in the public portal

If you believe that this document breaches copyright please contact us providing details, and we will remove access to the work immediately and investigate your claim.



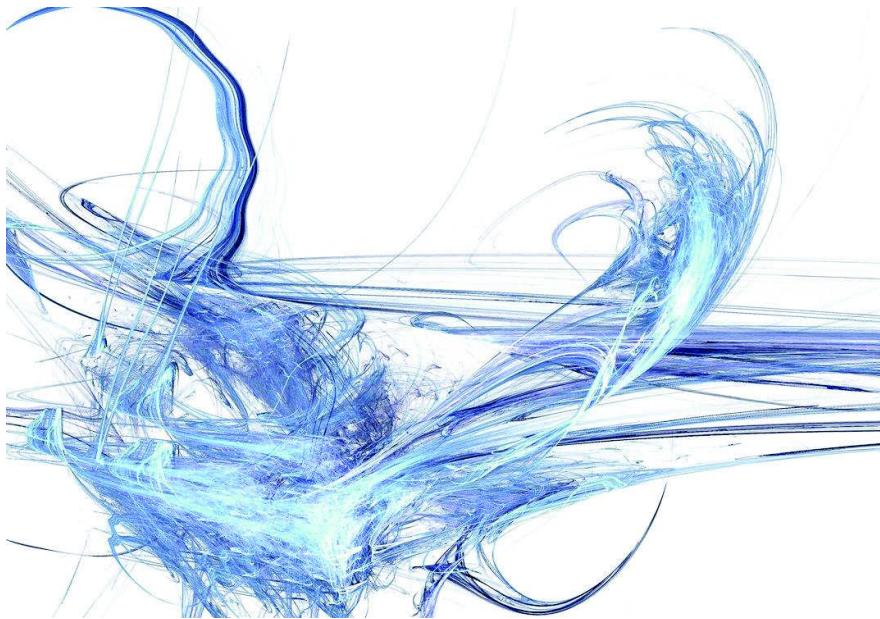
Development of Electrical Impedance Methods for 3D Cell Cultures

Towards Monitoring Tissue
Engineering Processes

Chiara Canali
PhD Thesis August 2015



Development of Electrical Impedance Methods for 3D Cell Cultures Towards Monitoring Tissue Engineering Processes



Chiara Canali

A thesis submitted to the Technical University of Denmark
For the degree of Doctor of Philosophy, 2015

DTU Nanotech
Department of Micro- and Nanotechnology

In the cover: image adapted from “Electric waves”
by ImaginationScape (2012–2015) with permission

A thesis submitted for the degree of Doctor of Philosophy
Department of Micro- and Nanotechnology
Ph.D. program in Electronics, Communication and Space Science
Technical University of Denmark
August 2015

*This thesis is dedicated to my father William:
Each cable soldered during this Ph.D. brought
back happy memories of my childhood spent in
playing science with you*

No. Try not. Do... or do not. There is no try.
Master Yoda

You can do anything if you have enthusiasm.
Henry Ford

Contents

Abstract.....	4
Resumé på Dansk.....	6
Preface.....	8
List of Abbreviations	10
List of Useful Definitions.....	14
List of Publications and Submitted Manuscripts	18
My Contribution to the Papers	20
List of Conference Contributions.....	22
CHAPTER 1 Introduction	26
1.1 Motivation	26
1.2 Organisation of the Thesis	30
1.3 Summary of the Research	30
CHAPTER 2 Tissue Engineering.....	34
2.1 The 3D Environment.....	35
2.2 Bioreactors for tissue engineering.....	41
CHAPTER 3 Electrical Impedance Spectroscopy.....	44
3.1 Theory.....	46
3.2 Impedance Measurement Setups.....	57
3.2.1 Electrode Polarisation	58
3.2.2 Electrode Configurations.....	61
3.2.3 The Reciprocity Theorem and Sensitivity in Impedance Measurements.....	65
3.2.4 Finite Element Analysis.....	67
CHAPTER 4 Electrical Impedance Tomography.....	73

4.1	Electrode Configurations in EIT	77
4.2	Image Reconstruction in EIT	79
4.3	Software Algorithms for Image Reconstruction in EIT.....	82
CHAPTER 5	Conclusions.....	85
5.1	Final Remarks and Future Perspectives	88
	Acknowledgments	91
	References	95
	APPENDIX I Publications and Submitted Manuscripts	111
	APPENDIX II Conference Contributions	129

Abstract

The research carried out in this thesis has been developed within the EU-funded FP7 project 'NanoBio4Trans' (grant no: 304842) aimed at developing, optimising and validating an *in vivo*-like extracorporeal bioartificial liver with integrated sensors. The main focus of the NanoBio4Trans project was to develop a perfusion bioreactor array for 3D cell culture and detection platform, integrating different sensor arrays for monitoring cell populations using a combination of electrical impedance and optical techniques. 3D cell cultures based on human cells may provide a potential bridge for the gap between animal models and human studies and help understanding the basic mechanisms of biological processes and disease. To engineering complex tissues as a liver is a challenge that requires efforts from several research fields comprising cell and molecular biology, material science, chemistry and sensing technology in order to promote progress towards tangible improvements in biomedicine, pharmacology and toxicology.

Most electrical impedance measurements, including electrical impedance spectroscopy and *bioimpedance*, are commonly used to describe material properties that impede the flow of an alternating current and facilitate storage of electrical charge. Impedance-based techniques are a well-established tool for the electrochemical investigation of reaction mechanisms as well as properties of porous electrodes and electrically passive materials. Moreover, their applications cover a wide range of disciplines, spanning from geophysics and material science, to microbiology and non-invasive real-time monitoring of biological systems both *in vivo* and *in vitro*. Physiological impedance measurements on tissue and organs are often used for tissue characterisation and disease diagnosis, reflecting cell dimensions, density and integrity and have been defined as *bioimpedance*.

This thesis presents the development and exploration of impedance-based methods with applications in different stages of tissue engineering processes. These include: (i) accurate determination of conductivity in a 3D environment; (ii) characterisation of the 3D scaffold supporting cell growth in terms of hydrogel polymerisation and degree of porosity; (iii) monitoring of cell loading and spatial distribution of cell aggregates in 3D; (iv) integration of electrodes in perfusion bioreactors for impedance-based real-time monitoring of cell proliferation; and (v) investigation of electrical impedance tomography (EIT) as a potential

method for image reconstruction in miniaturised 3D culture chambers with possible future applications in tissue engineering. Special emphasis was placed on the effect of the electrode configurations and their 3D arrangement in impedance measurements to achieve 3D spatial information. This objective was addressed using *finite element simulations*, electrochemical validation, *phantom* experiments mimicking cell aggregates and cell-based experiments.

Resumé på Dansk

Arbejdet beskrevet i denne afhandling er blevet udført under det EU-støttede FP7 projekt, "NanoBio4Trans" (grant nr. 304842), hvis formål er at udvikle, optimere og validere en *in vivo*-lignende kunstig ekstrakorporal lever med integrerede sensorer. Det primære fokus i Nano4BioTrans projektet var at udvikle et perfusionsbioreaktor array til cellekulturer i 3D, en detektionsplatform samt integration af forskellige sensor-arrays til monitorering af cellepopulationer ved en kombination elektrisk impedans og optiske teknikker. 3D cellekulturer baseret på humane celler kan potentielt bygge bro mellem animalske modeller og humane studier, og hjælpe med at forstå de underliggende mekanismer for biologiske processer og sygdomme. Fremstilling af så komplekse organer som en lever, er en udfordring der kræver en indsats fra forskellige forskningsområder som celle- og molekylær biologi, materiale videnskab, kemi og sensor-teknologi, for at kunne opnå fremskridt inden for biomedicin, farmakologi, og toksikologi.

Elektriske impedans målinger, inklusive elektrisk impedans spektroskopi og bioimpedans, bruges normalt til at analysere materialer som hindrer vekselstrøm og faciliterer en ophobning af elektrisk ladning. Impedans-baserede teknikker er veletablerede værktøjer til elektrokemisk undersøgelse af reaktionsmekanismer samt egenskaber for porøse elektroder og elektrisk passive materialer. Derudover dækker applikationerne over en lang række af discipliner, lige fra geofysik og materialeteknologi, til mikrobiologi og ikke-invasiv realtid monitorering af biologiske systemer, både *in vivo* og *in vitro*. Fysiologiske impedansmålinger på væv og organer kaldes også for bioimpedans, og bruges ofte til vævskarakterisering, diagnosticering af sygdomme, og måling af cellers dimensioner, densitet og integritet.

Denne afhandling præsenterer udviklingen og undersøgelsen af impedans-baserede metoder med applikationer i forskellige trin af vævs-fremstillingsprocesser. Disse inkluderer (i) præcis bestemmelse af konduktivitet i et 3D miljø; (ii) karakterisering af 3D stilladser til support af cellevækst, i form af hydrogel polymerisering og grader af porøsitet; (iii) monitorering af cellemængde og rumlig distribution af celleaggregater i 3D; (iv) integration af impedans sensorer i perfusionsbioreaktorer til realtid monitorering af cellespredning; og (v) undersøgelse af elektrisk impedans tomografi (EIT) som en potentiel metode til billeddannelse i nedskalerede 3D kulturkamre med mulige fremtidige applikationer indenfor

vævsfremstilling. Et særligt fokus har været på effekten af elektrodekonfigurationen og dens 3D placering på impedansmålingernes mulighed for at opnå rumlig information. Dette mål blev adresseret ved hjælp af *finite element simuleringer*, elektrokemisk validering samt *phantom* eksperimenter til imitation af celleaggregater og cellebaserede eksperimenter.

Preface

This thesis is presented as a partial requirement for obtaining a Ph.D. degree from the Technical University of Denmark (DTU). The research was financed by the EU Commission within the framework of the FP7 project 'NanoBio4Trans' (grant no: 304842) and carried out at the Department of Micro- and Nanotechnology (DTU Nanotech) in the period from September 2012 to August 2015. The Ph.D. project was supervised by Professor Jenny Emnéus, leader of the Bioanalytics group, and co-supervised by Associate Professor Arto Heiskanen (Bioanalytics group) and Associate Professor Martin Dufva, leader of the Fluidic Array System and Technology (FAST) group.

Kgs. Lyngby,

31st August, 2015

Chiara Canali



List of Abbreviations

The abbreviations and acronyms used in this thesis are explained in the following.

\emptyset	Diameter
Z	Impedance magnitude (or module) [Ω]
∇	Nabla or Del, is the differential vector operator
2D	Two-dimensional
3D	Three-dimensional
AC	Alternating current
a-EIT	Absolute electrical impedance tomography
B	Magnetic flux density [$V \cdot s/m^2$]
BAL	Bioartificial liver
BM	Basement membrane
BMP	Bone morphogenetic protein
C	Capacitance [F]
CC	Current-carrying, current injecting, stimulating, driving
C_{dl}	Double-layer capacitance [F]
CE	Counter electrode
C_p	Polarisation capacitance [F]
CPE	Constant phase element [$S \cdot s^\alpha$], with α CPE element exponent
D	Displacement field flux [C/m^2]
DC	Direct current
E	Electric flux density [V/m]
ECIS®	Electric cell-substrate impedance sensing
ECM	Extracellular matrix
EIS	Electrical impedance spectroscopy
EIT	Electrical impedance tomography
<i>F</i>	Linear frequency [Hz]
FE	Finite element
f-EIT	Dynamic frequency-varying electrical impedance tomography
H	Magnetic field strength [A/m]
H	Height
HA	Hyaluronic acid
I	Current [A]
IDEs	Interdigitated electrodes

KKT	Kramers–Kronig transforms
MPS	Sodium 3-mercapto-1-propanesulfonate
MSC	Mesenchymal stem cells
PBS	Phosphate buffered saline
PGs	Proteoglycans
Pt	Platinum
PU	Signal pick-up, recording, receiving, registering
Q	Electric charge [C]
q_v	Charge density [C/m ³]
R	Resistance [Ω]
R_{CT}	Charge-transfer resistance [Ω]
RE	Reference electrode
R_p	Polarisation resistance [Ω]
R_s	Solution resistance [Ω]
S	Sensitivity [m ⁻⁴]
S	Sensitivity factor (sensitivity matrix and back-projection algorithm in EIT)
SAM	Self-assembled monolayer
T	Terminal, electrode, lead (e.g. 2T measurements)
t-EIT	Dynamic time-varying electrical impedance tomography
U	Voltage [V]
$U_{(-)}$	Modulation potential (i.e., AC-polarisation potential) [V]
U_0	DC-polarisation potential [V]
VID	Volume impedance density
WE	Working electrode
Y	Admittance [S]
Y_{Im}	Imaginary admittance [S]
Y_p	Polarisation admittance
Y_{Re}	Real admittance [S]
Z	Impedance [Ω]
Z_{Im}	Imaginary impedance [Ω]
Z_p	Polarisation impedance [Ω]
Z_{Re}	Real impedance [Ω]
Z_W	Warburg impedance [S·s ^{1/2}]
ϵ_0	Permittivity of free space (1, by definition)
ϵ_{Im}	Imaginary permittivity
ϵ_r	Relative permittivity
ϵ_{Re}	Real permittivity

ρ	Resistivity [$\Omega\cdot\text{cm}$]
σ	Conductivity [S/m]
ϕ	Phase angle [$^\circ$]
ω	Angular frequency [rad]
J	Imaginary unit, $j^2 = -1$
\mathbf{J}	Current density vector
\mathbf{J}_f	Current density of free charges [A/m ²]

List of Useful Definitions

For convenient reference, a list of definitions giving a short description of concepts that frequently recur in this thesis is reported below. The key words will be reported in *italic* through the thesis.

<i>Bioimpedance</i>	Electrical impedance measurements in biological materials (e.g. tissues, organs, whole organisms).
<i>Counter electrode (CE):</i>	In electrochemistry, an electrode that completes the electric circuit formed with the working electrode (WE) through the electrolyte. It is the site of electron transfer processes which are opposite to the ones taking place at the WE. For instance, for every electron participating in oxidation at the WE, one electron is involved in reduction at the CE.
<i>Current-carrying (CC) electrodes:</i>	(or current injecting, stimulating, driving). Inject the AC input (e.g. current) in the system.
<i>Electrode polarisation impedance (Z_p):</i>	Comprises the interface impedance at the electrode/sample interface (e.g. electrode interface impedance in an electrolyte solution).
<i>Forward problem:</i>	Calculation of the electrical voltage distribution when the signal source (i.e. current) and the resistivity distribution within the sample are known. Maxwell's equations govern the physics of the problem. The forward problem is a <i>well-posed</i> problem.
<i>Finite element (FE) method (or analysis)</i>	Is a numerical method for solving problems in engineering and physics where exact mathematical solutions cannot be obtained. Approximate solutions are obtained in two steps. First, the space of the problem is divided into a collection of geometrical objects (<i>mesh elements</i> , or <i>voxels</i> for 3D geometries), where each object is represented by a set of element equations to the original problem. Afterwards, all sets of element equations are systematically recombined into a global system of equations for the final calculation. The final calculation is the weighted sum of all the element equations.
<i>Ill-posed problem:</i>	Mathematical problem for which a small error in the input data can result in much larger errors in the problem's solution. In other terms, the solution is highly sensitive to variations in

	the input data.
<i>Impedivity:</i>	When studying the response of materials to alternating electric fields, impedivity is a complex quantity analogous to resistivity in direct current experiments. Impedivity is the sum of a real component ('resistivity') and an imaginary component ('reactivity').
<i>Inverse problem:</i>	Calculation of the internal resistivity of the sample based on sequential impedance measurements. The optimal solutions are obtained from the values that minimise the difference between the measured and the predicted (obtained by solving the <i>forward problem</i>) voltages. The inverse problem is an <i>ill-posed problem</i> .
<i>Linear system:</i>	A system whose output is proportional to its input. In impedance measurements, the output and the input may be a sinusoidal voltage and a sinusoidal current, respectively. For any linear system: (i) doubling the input voltage doubles the output current and (ii) the property of the weighted sum of the output signal is superimposed on the weighted sum of the input signal.
<i>Mesh element:</i>	A <i>FE</i> mesh is the discretisation of a 1D, 2D or 3D object in an equivalent system of several elementary geometrical elements of various shapes arranged to approximate the object geometry. The mesh elements can only intersect along a face, an edge or a node and never otherwise.
<i>Naïve cells</i>	Undifferentiated pluripotent stem cells.
<i>Phantom:</i>	A test object, with defined electrical and geometrical properties, which can be used to find the spatial sensitivity (i.e. the smallest detectable volume with respect to the measurement chamber size) of an impedance-based method.
<i>Reference electrode (RE):</i>	In electrochemistry, a non-polarisable electrode with a stable, well defined potential. It is used to adjust the potential at the WE. Examples are: Ag/AgCl electrode, standard hydrogen electrode and saturated calomel electrode.
<i>Signal pick-up (PU) electrodes:</i>	(or recording, receiving, registering). Record the AC output of the system (e.g. voltage) to the injected AC input (e.g. current).
<i>Transfer function:</i>	(or network function). Is a function in time (or frequency) between an output and an input function. Impedance is a transfer function as it is the ratio of the voltage to the current.

<i>Transimpedance:</i>	(or mutual impedance, or transfer impedance). Is the ability of the <i>PU electrodes</i> to sense the injected current between the <i>CC electrodes</i> in 4T measurements.
<i>Voxel:</i>	A sub-volume in a 3D object, which can be a <i>mesh element</i> when performing <i>FE analysis</i> .
<i>Well-posed problem:</i>	Mathematical problem for which: (i) a solution exists, (ii) the solution is unique and (iii) the behaviour of the solution changes together with changes in the initial conditions. This means that a small error in the input data results in small errors in the solution of the problem.
<i>Working electrode (WE):</i>	In electrochemistry, an electrode at which the electrochemical reaction of interest takes place. Its potential is controlled with respect to the RE in a three-electrode system.

List of Publications and Submitted Manuscripts

This thesis is based on the following papers, which will be referred to in the text by their Roman numerals. The papers are appended at the end of the thesis (**Appendix I**).

- Paper I. Impedance-based monitoring for tissue engineering applications**
C. Canali, A. Heiskanen, Ø. G. Martinsen, S. Mohanty, M. Dufva, A. Wolff and J. Emnéus
International Federation for Medical and Biological Engineering (IFMBE) proceeding of the 2nd Latin-American Conference on Bioimpedance (*CLABIO*, September 30 – October 2 2015, Montevideo, Uruguay)
- Paper II. Conductometric analysis in bio-applications: A universal impedance spectroscopy-based approach using modified electrodes**
C. Canali, L. B. Larsen, Ø. G. Martinsen and A. Heiskanen
Sens. Actuators B, 2015, 212, 544–550
- Paper III. Impedance spectroscopic characterisation of porosity in 3D cell culture scaffolds with different channel networks**
C. Canali, S. Mohanty, A. Heiskanen, Ø. G. Martinsen, H. B. Muhammad, M. Dufva, A. Wolff and J. Emnéus
Electroanalysis, 2015, 27, 93–99
- Paper IV. Fabrication of scalable and structured tissue engineering scaffolds using water dissolvable sacrificial 3D printed moulds**
S. Mohanty; L. B. Larsen, J. Trifol Guzman, P. Szabo, H. V. R. Burry, C. Canali, M. Dufva, J. Emnéus and A. Wolff
Mater. Sci. Eng. C, 55, 2015, 569–578

- Paper V. Bioimpedance monitoring of 3D cell culturing – Complementary electrode configurations for enhanced spatial sensitivity**
C. Canali, A. Heiskanen, H. B. Muhammad, P. Høyum, F. Pettersen, M. Hemmingsen, A. Wolff, M. Dufva, Ø. G. Martinsen and J. Emnéus
Biosens. Bioelectron., 2015, 63, 72–79
- Paper VI. An impedance method for spatial sensing of 3D cell constructs – towards applications in tissue engineering**
C. Canali, C. Mazzoni, L. B. Larsen, A. Heiskanen, Ø. G. Martinsen, A. Wolff, M. Dufva and J. Emnéus
Analyst, 2015, 140, 6079–6088
- Paper VII. Perfusion bioreactor array with integrated impedance sensors for tissue engineering applications**
L. B. Larsen[†], C. Canali[†], M. Hemmingsen, K. Kuldeep, S. Mohanty, R. Pimentel, L. H. Jensen, M. Skolimowski, A. Wolff, F. Okkels, A. Heiskanen, M. Dufva and J. Emnéus
Manuscript to be submitted to *Biotechnology and Bioengineering*
- Paper VIII. Electrical impedance tomography for miniaturised 3D systems**
C. Canali[†], K. Aristovich[†], L. Ceccarelli, L. B. Larsen, A. Heiskanen, Ø. G. Martinsen, A. Wolff, M. Dufva and J. Emnéus
Manuscript submitted to *Analyst*

[†] These two authors contributed equally to this work.

My Contribution to the Papers

- Paper I.** I reviewed some of the impedance-based methods that I have developed for future monitoring of the tissue engineering process. I wrote the paper.
- Paper II.** I designed, planned and performed the experiments. I evaluated the results, wrote most of the MatLab script and wrote the paper.
- Paper III.** I designed, planned and performed the experiments. I evaluated the results and wrote the paper.
- Paper IV.** I corrected the manuscript.
- Paper V.** I performed part of the *finite element (FE) models*, cell culturing and impedance measurements. I designed, planned and performed the experiments and evaluated the results. I wrote the paper.
- Paper VI.** I performed the *FE models* and cell-based work. I designed and planned the experiments and evaluated the results. I wrote the paper.
- Paper VII.** I performed the *FE models* for the optimisation of the impedance measurements. I made the scaffolds, seeded the cells and performed the impedance measurements. I participated in the evaluation of the impedance measurements results. I provided sections of the manuscript concerning impedance spectroscopy and corrected the manuscript.
- Paper VIII.** I designed, planned and performed the experiments. I evaluated the results and wrote the manuscript in collaboration with Prof. David Holder's group at the University College London.

List of Conference Contributions

The work described in this thesis was presented (presenting author is underlined) during the conferences listed below (reverse chronological order). The abstracts are appended at the end of the thesis (**Appendix II**).

I. Electrical impedance spectroscopy with optimised electrode configurations for 3D tissue engineering applications

C. Canali, H. B. Muhammad, A. Heiskanen, C. Mazzoni, L. Ceccarelli, Ø. G. Martinsen, A. Wolff, M. Dufva and J. Emnéus

23rd International Symposium on Bioelectrochemistry and Bioenergetics (BES2015)

June 14–18 2015, Malmö, Sweden

(POSTER)

II. On-line monitoring of 2D and 3D cell cultures: electrode configurations for impedance based sensors

C. Canali, C. Caviglia, K. Zór, H. B. Muhammad, A. Heiskanen, Ø. G. Martinsen, T. L. Andresen, A. Wolff, M. Dufva and J. Emnéus

World Congress on Medical Physics & Biomedical Engineering (IUPESM WC2015)

June 7–12 2015, Toronto, Canada

(ORAL)

III. Enhanced multielectrode configurations in miniaturized 3D electrical impedance spectroscopy and tomography – monitoring the overall process of tissue engineering with spatial sensing for future challenges in microfluidics

C. Canali, H. B. Muhammad, A. Heiskanen, C. Mazzoni, L. Ceccarelli, Ø. G. Martinsen, D. Holder, A. Wolff, M. Dufva and J. Emnéus

World Congress on Medical Physics & Biomedical Engineering (IUPESM WC2015)

June 7–12 2015, Toronto, Canada

(ORAL)

IV. Perfusion-based three dimensional (3D) tissue engineering platform with integrated bioimpedance sensing

H. B. Muhammad, C. Canali, A. Heiskanen, M. Hemmingsen, A. Wolff, M. Dufva and J. Emnéus

EMBS Micro and Nanotechnology in Medicine Conference (MNM2014)

December 8–14 2014, Turtle Bay Resort, Oahu, HI, USA

(POSTER)

V. Impedance-based detection for facing new challenges in biotechnology: enhanced 3D sensing, conductometry and electrode functionalization

C. Canali, A. R. Heiskanen, H. B. Muhammad, M. Dufva, A. Wolff and J. Emnéus

Danish Electrochemical Society Annual Meeting (DEF2014)

October 9–10 2014, Copenhagen, Denmark

(ORAL)

VI. An innovative EIS based 3D printed conductometer

C. Canali, A. Heiskanen, H. B. Muhammad, M. Dufva and J. Emnéus

14th International Conference on Electroanalysis (ESEAC2014)

June 11–15 2014, Malmö, Sweden

(POSTER)

VII. Electrochemical impedance spectroscopy is a versatile technique for new challenges in 3D cell culture

C. Canali, H. B. Muhammad, A. Heiskanen, S. Mohanty, M. Dufva, A. Wolff and J. Emnéus

14th International Conference on Electroanalysis (ESEAC2014)

June 11–15 2014, Malmö, Sweden

(POSTER)

VIII. A multiplexed electrical impedance-based device for bioengineering applications

C. Canali, Ø. G. Martinsen, H. B. Muhammad, A. Heiskanen, M. Dufva, A. Wolff and J. Emnéus

25th Anniversary World Congress on Biosensors (BIOSENSORS2015)

May 27–30 2014, Melbourne, Australia

(POSTER)

IX. Development of a lab-on-a-chip system with integrated sensors for 3D tissue engineering applications

H. B. Muhammad, C. Canali, S. Mohanty, M. Hemmingsen, M. Skolimowski, M. Dufva, A. Wolff and J. Emnéus

15th International Conference on Biomedical Engineering (ICBME2013)

December 4–7 2013, Singapore

(ORAL)

X. A bioimpedance-based sensing system for monitoring cellular dynamics in a 3D culture environment

C. Canali, H. B. Muhammad, Ø. G. Martinsen, A. Heiskanen, M. Dufva, A. Wolff and J. Emnéus

15th International Conference on Biomedical Engineering (ICBME2013)

December 4–7 2013, Singapore

(ORAL)

XI. Design and optimisation of a lab-on-a-chip system with integrated sensors for 3D tissue engineering applications

H. B. Muhammad, C. Canali, S. Mohanty, M. Hemmingsen, M. Skolimowski, M. Dufva, A. Wolff and J. Emnéus

39th International Conference on Micro and Nano Engineering (MNE2013)

September 16–19 2013, London, UK

(ORAL)

CHAPTER 1

Introduction

1.1 Motivation

Over the last 30 years, tissue engineering has resulted in important advances in materials science, cell and molecular biology, chemistry and engineering, holding great promise in regenerative medicine, modelling of real biological systems, cell-based assays and drug and toxicity screening [1]. Within the field of tissue engineering, 3D cell cultures have been shown to more accurately mimic the natural cellular environment in terms of tissue-specific architecture, mechanical and biochemical signalling as well as cell-cell interaction [2]. A plethora of biomaterials have been developed as scaffolds for supporting cell growth in 3D, displaying tuneable properties with regards to stiffness, porosity and functionalisation with bioactive molecules. Such structures provide the appropriate mechanotransduction and biochemical cues to guide cell differentiation and assembly into 3D tissues. In fact, while cells grown in monolayer are flat and forced to have an apical-basal polarity, most of the cell types require a third dimension in order to acquire an *in vivo*-like morphology and, hence, their specificity and function [3]. Accordingly, key events in the life cycle of a cell, such as proliferation, migration and apoptosis, are regulated by 'organising principles' that maintain tissue homeostasis. Such principles comprise the extracellular matrix (ECM) composition, cell-cell and cell-ECM interactions [4]. Therefore, the assembly of cells into tissues is an extremely dynamic and highly regulated set of events in time (from seconds to weeks) and space (from 10 μm to 10 cm) [5] which warrants the development of standardised protocols, new cell lines and quantitative *in vitro* analysis methods [6].

Following the behaviour of cells in tissue engineering systems and 3D cell cultures requires rigorous control of the spatial and temporal gradients of physical (e.g. flow rate and shear stress), chemical (e.g. oxygen tension and metabolite concentrations) and biological cues (e.g. extracellular matrix proteins and growth factors) delivered through the environment [7]. An appropriate sensing technology would provide a relevant tool for simultaneous monitoring of the 3D environment and cellular properties during the development of the tissue construct, including production of metabolites, cell proliferation and differentiation, scaffold

remodelling and biodegradation. An on-line monitoring system would allow avoiding traditional destructive endpoint detection methods or fixed time point analyses. However, a major challenge in this regard is to build an experimental setup that facilitates non-invasive and non-destructive monitoring of the 3D environment under sterile conditions and in real-time. Moreover, the sensors should be significantly smaller in size compared to the ones that are commercially available and commonly used in large scale bioprocesses, such as fermentation. Other significant requirements should include: (i) a response independent of the culture medium flow rate, (ii) a lifetime of several weeks, and (iii) a stable response over time [8]. Low cost and disposability or, alternatively, possibility of easy sterilisation, would be further added values.

Among the various sensors conventionally used to monitor bioprocesses, oxygen sensors have been most successfully adapted for tissue engineering conditions. In fact, oxygen concentration directly impacts on the cell response in terms of ECM production, growth [9], and differentiation [10]. Malda et al. built and validated a glass microelectrode system which was adapted from the Clark electrode [11] to penetrate a porous scaffold and engineered cartilage tissue [12]. The sensor was shown to yield reproducible measurements of the oxygen gradients, with high spatial resolution. Acosta et al. produced and tested fluorescent oxygen-sensing microparticles that can be suspended in any transparent tissue engineering scaffold for quantitative and spatial monitoring of the 3D culture using fluorescence microscopy [13,14]. Tian et al. developed a macroporous and flexible nanowire able to self-organise in rectangular biocompatible networks where excitable cells (e.g. neurons, cardiomyocytes, smooth muscle cells) can be grown [15]. While providing structural support, the scaffold could probe the extracellular and intracellular electrical activity using the field-effect transistor technology.

However, while monitoring the composition of the 3D environment is gradually entering the practice of bioreactor-based tissue engineering, monitoring the structure and function of the engineered constructs is still a challenging and rather unexplored field [16]. From the early studies on 2D cultures, a number of label-free techniques have emerged for non-invasive real-time determination of cell-substrate interactions [17]. Among these are electrical quartz crystal microbalance (QCM) [18], refractive index based technologies (e.g. infrared surface plasmon spectroscopy [19]), optical waveguide lightmode spectroscopy (OWLS) [20] and

electrical impedance spectroscopy (EIS) [21]. In 1984, Giæver and Keese pioneered the use of EIS to monitor cell adhesion, spreading and proliferation on a flat surface (electric cell-substrate impedance sensing, ECIS®) [21,22]. Such method relies on the insulating properties of cell membrane, which affect the ionic environment at the electrode/electrolyte interface. Hence, the measurements reflect the electrode *polarisation impedance* (Z_p) modulated by adhering cells. The ECIS® technology paved the way to several impedance-based methods for real-time monitoring of cell adhesion, spreading [23], motility [24] and proliferation, as well as wound healing [25] and cytotoxicity [26–28] in 2D cultures. However, in tissue engineering, cells are grown inside biomaterial scaffolds that provide a third dimension for cell adhesion and proliferation compared to a flat surface. Therefore, in such applications, the electrodes can be interfaced with the scaffold laden with cells in a 3D arrangement. For this purpose, technical solutions can be adapted from physiological impedance measurements, which have been widely described by Grimnes and Martinsen and defined as *bioimpedance*. When developing impedance-based sensors for tissue engineering applications, the miniaturisation and the need for continuous long-term measurements make the electrode stability and position two crucial factors to carefully consider. Moreover, number, spacing and orientation of electrodes need to be evaluated with respect to the geometry of the cell culture chamber, to maximise the measurements sensitivity. The first step towards the application of EIS to monitor cell proliferation in 3D was set by Lei et al. using 2-terminal (2T) measurements and thin agarose layers as scaffolds ($4 \times 2 \times 1$ mm) [29]. 2T measurements were also applied by Tully-Dartez et al. for discrimination between chitosan-based 3D cell culture scaffolds with different random porosity using cylindrical probes penetrating into the material [30]. In general, EIS may offer significant advantages on conventional microscopy techniques that function well for thin, optically transparent cell cultures but would require thorough optimisation for 3D constructs. In fact, cell culture scaffolds may be thick and highly scattering, preventing light from penetrating without significant distortion [31,32]. Different epi-illumination imaging techniques that rely on light collected in the backward direction (fluorescence or backscattered light) may be used. These include confocal microscopy, multiphoton microscopy and optical coherence microscopy and are well suited for observing dynamic changes over time [32]. However, they require well-trained personnel, able to adjust important parameters, such as the optical contrast, the resolution and the light penetration depth avoiding damaging the sample. Moreover, the main conditions for real-time monitoring

are the availability of 3D culture systems having compatible size with such instrumentation and the ability to keep sterile conditions during the analysis. In such a context, impedance-based methods may provide an alternative or synergic approach for non-invasive monitoring of the 3D environment, gathering information on the scaffold supporting cell organisation (e.g. hydrogel polymerisation, degree of crosslinking and porosity), monitoring cell loading, proliferation and possibly metabolism [33], as well as their spatial distribution in 3D.

Inspired by this dynamic and challenging scenario, this Ph.D. thesis has been developed within the EU-funded FP7 project 'NanoBio4Trans' (grant no: 304842) aimed at developing, optimising and validating an *in vivo*-like extracorporeal bioartificial liver (BAL) with integrated sensors. The main focus of the NanoBio4Trans project was to develop a perfusion bioreactor array platform for 3D cell culture and detection, integrating different sensor arrays for monitoring cell populations using a combination of electrical impedance and optical techniques (in collaboration with Luxcel Biosciences, Cork, Ireland). The project addressed key issues in research on human induced pluripotent stem cells (hiPSCs) in collaboration with Takara Bio Europe AB (Göteborg, Sweden) with the ultimate goal of upscaling the optimised 3D growth and differentiation protocols for the growth of a BAL, with dimensions in the order of cm³ to dm³. My Ph.D. project aims at the development and exploration of electrical impedance-based methods with application in different stages of tissue engineering processes. These include: (i) accurate determination of conductivity in a 3D environment; (ii) scaffold characterisation in terms of hydrogel polymerisation and degree of porosity; (iii) monitoring of cell loading and spatial distribution of cell aggregates in 3D; (iv) integration of electrodes in perfusion bioreactors for real-time impedance-based monitoring of cell proliferation; and (v) investigation of electrical impedance tomography (EIT) as a potential method for image reconstruction in miniaturised 3D culture chambers with possible future applications in tissue engineering. My work on EIT is the result of collaboration with electronic engineers and physicists from Prof. David Holder's group at the University College London, who provided expertise and technical skills for image reconstruction. All in all, the obtained results form the basis for the future development of miniaturised 3D EIT systems for monitoring tissue engineering processes, requiring several inputs from different scientific areas spanning from biotechnology to electronic engineering and mathematics.

1.2 Organisation of the Thesis

The aim of this Ph.D. project was not only to develop a 3D cell culture platform with integrated impedance sensors, but moving a step further by applying it as a complementary tool in biomedical engineering to address relevant applications and questions in biology, chemistry and material science. The emphasis has been on electrical impedance-based methods for future application in monitoring the different stages in tissue engineering processes using different electrode configurations.

This thesis is divided into three main chapters, which guide the reader through the field of tissue engineering and provide the essential technical background to understand the impedance-based methods presented in my papers. **Chapter 2** introduces the concept of 'tissue engineering' and discusses the relevance of the 3D environment for cell culturing in relation to gradients of physicochemical stimuli (e.g. matrix stiffness and porosity as well as growth factors and hormones). **Chapter 3** describes the basic theory of EIS, focusing on electrode polarisation, electrode configurations, reciprocity, and *finite element (FE) analysis*. **Chapter 4** aims at giving a simplified view of electrical impedance tomography (EIT). The ambition of the chapter is to provide the reader with a simple overview of the main aspects involved in EIT, which is not the main object of this thesis and goes beyond my main scientific background in pharmaceutical biotechnology and bioanalytical chemistry. **Chapter 5** concludes the thesis presenting some future perspectives and challenges of my work. Appendix I is a collection of the publications and manuscripts that have been produced throughout this 3-year Ph.D. project. **Appendix II** comprises the abstracts summarising the contributions that have been presented at international conferences during my Ph.D.

1.3 Summary of the Research

Paper I provides an overview of some of the impedance-based methods that I have developed to sense different stages of tissue engineering processes. Scaffolds can be characterised in terms of porosity and hydrogel polymerisation. Different electrode configurations can be used for monitoring cell loading, proliferation and spatial location of cell aggregates within large gelatin-based 3D scaffolds.

Paper II shows that EIS, together with an appropriate electrode modification protocol and automated spectral analysis can be applied for quick and reproducible conductivity determinations in physiological solutions and cell culture medium. The medium resistance (and, therefore, the conductivity) can be extracted from the impedance magnitude at the frequency where the phase angle is closest to 0° without need to validate and analyse a specific equivalent circuit. The relevance of this work for future monitoring of tissue engineering process lies in the fact that, cell adhesion, proliferation and metabolism create an heterogeneous and dynamic chemical environment [34]. Variations in the ionic strength of the culture medium determine changes in conductivity, which are subsequently reflected in changes in the measured impedance.

Paper III illustrates how the conductivity of the medium filling the pores of a scaffold can also serve as the basis for porosity determination using Archie's law [35]. Different networks of structured or random channels can be detected along with several degrees of porosity. The use of gold (Au) plate electrodes facilitate interfacing with a scaffold without the necessity of penetrating into the bulk material [30], which gives a significant advantage for measurements when using scaffolds made of brittle or tough elastomeric materials.

Paper IV describes the fabrication technique used for producing the scaffolds with networks of structured channels and several degrees of porosity characterised using EIS in **Paper III**. A water soluble 3D printed negative template was used as a mould for casting polymer elastomers to create the scaffolds, which were also tested for *in vitro* culturing of human hepatoblastoma (HepG2) cells over a 12-day culture period.

In **Paper V**, I use EIS to investigate the dynamics involved in the whole process of 3D cell culturing, starting from polymerisation of a bare gelatin-based 3D scaffold, to encapsulation and proliferation of mesenchymal stem cells (MSCs). Different configurations of Au plate electrodes (two- and three-terminal measurements, 2T and 3T) can be used. By switching between different combinations of electrode couples (sensing modes), it was possible to generate a multiplexing-like approach, which allows for collecting spatially distributed information within the 3D space.

In **Paper VI**, I present the characterisation and validation of multiplexed 4-terminal (4T) impedance measurements as a method for sensing the spatial location of cell aggregates within large gelatin-based 3D scaffolds. 4T impedance measurements are commonly

employed to minimise errors due to electrode interface impedance (e.g. *polarisation impedance, Z_p*), focusing on the mere properties of the sample. The use of needle electrodes allows placement of an increasing number of electrodes in the measurement chamber due to their smaller size compared to the plates used in **Paper V**. With a higher number of electrodes, the number of possible electrode combinations (sensing modes) increases, carrying a higher degree of 3D spatial information.

Needle electrodes can also be integrated in perfusion bioreactors to contact the surface of 3D scaffolds loaded with cells in a non-invasive manner and facilitate impedance-based real-time monitoring of cell proliferation. **Paper VII** presents the development of a perfusion bioreactor array platform, which enables culture of cells seeded in thick porous 3D scaffolds. This was demonstrated by culturing HepG2 cells at different flow rates for 7 days. The bioreactor design allows the placement of two vertical needle electrodes in contact with each scaffold for 2T impedance measurements. The impedance magnitude was shown to correlate with increasing cell densities while allowing discrimination between bare and cell-loaded scaffolds over a 19-day culture period.

Paper VIII shows that the integration of vertical needle electrodes along the perimeter of a miniaturised chamber allows sequential impedance measurements that can be used for image reconstruction of small 3D test objects placed into a physiological solution. For such application, two different approaches are compared in terms of the sequence of electrode couples activated for 4T measurements and the chosen algorithm for image reconstruction. The chosen number of electrodes, and consequently the number of electrode configurations, aims at maximising the quality of image reconstruction while minimising the number of required measurements. This is significant when designing a technique suitable for future tissue engineering applications where time-based monitoring of cellular behaviour in 3D scaffolds is of interest. This work is the result of collaboration with electronic engineers and physicists from Prof. David Holder's group at the University College London, who provided expertise and technical skills for image reconstruction. All in all, the obtained results form the basis for the future development of miniaturised 3D EIT systems for monitoring the process of tissue engineering, requiring several inputs from different scientific areas spanning from biotechnology to electronic engineering and mathematics.

CHAPTER 2

Tissue Engineering

Tissue engineering was first defined by Langer and Vacanti in 1993 as an interdisciplinary field that applies the principles of engineering (materials science and biomedical engineering) and the life sciences (biochemistry, genetics, cell and molecular biology) to the development of biological substitutes which can restore, maintain, or improve tissue functions [36]. Cells, scaffolds and biochemical cues are often referred to as the 'tissue engineering triad', being the key components of engineered tissues [37]. Scaffold matrices, typically made of polymeric biomaterials, provide the structural support for cell adhesion and may deliver growth factors and hormones promoting tissue development [38] (Figure 2.1).

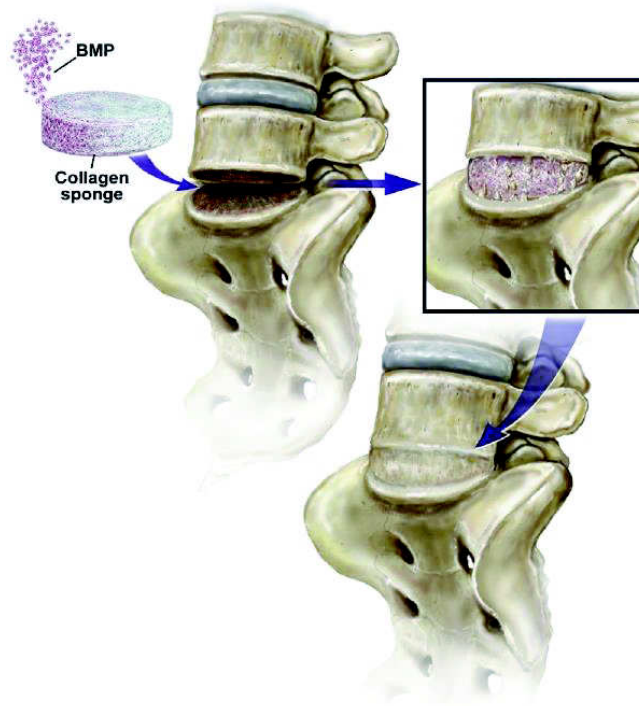


Figure 2.1| Regeneration of bone tissue using a biocompatible and biodegradable collagen scaffold laden with autologous cells from the patient. Chemical factors (e.g. bone morphogenetic protein, BMP) may be loaded in the polymeric matrix to induce stem cell differentiation and maturation. Medtronic (Minneapolis, Minnesota, USA) developed a spine fusion device (Infuse® Bone Graft/LT-Cage® Lumbar Tapered Fusion Device) containing a collagen sponge infused with BMP that is now in clinical use. The image is reprinted from [39] with permission.

Currently, studies for the development of biocompatible materials have been carried out using both natural and synthetic molecules. Computer-assisted design and manufacture techniques are applied to carefully design 3D scaffolds in terms of architecture and pore size, mechanical and physicochemical properties [40]. The scaffold interface with cells should be optimised at a molecular level to mimic the same degree of stiffness of natural tissues [41] and by incorporating growth and differentiation factors, specific receptors and anchorage sites [42]. Furthermore, microfluidic circulations can be implemented in *in vitro* bioreactors to support oxygen and nutrients transport to the inner region of the scaffold, while efficiently removing metabolic waste products from the cells growing in the artificial tissue [40].

2.1 The 3D Environment

Epithelial cells exist *in vivo* as multilayer sheets and can be cultured on flat substrates *in vitro* providing responses to drugs and certain toxins that naturally mimic those of real tissues [43]. However, most cells require cues from a 3D environment in order to form relevant physiological tissues *in vitro* [6,44]. Culturing cells in 3D provides another dimension for external mechanical inputs and cell adhesion, which dramatically affects the extracellular matrix (ECM) production via dynamic remodelling [45] (Figure 2.2). The biochemical composition and the sterical and mechanical properties of the ECM control how the mechanical forces are transmitted to the cells and, hence, cell shape and organisation [3,6]. The ECM comprises various molecules (i.e. water, proteins and polysaccharides) secreted by the cells and providing a milieu of physical cues and binding ligands that connect the cytoskeleton of the cells to the cellular microenvironment [46]. In the ECM, the collagen fibres resist tensional forces exerted by the cells and the proteoglycans (PGs) control hydration. The degree of hydration determines the resistance to compressive forces and hinders proteins (e.g. adhesive glycoproteins such as laminin and tenascin) to move out from the ECM due to their high and fixed charge density [47,48]. In fact, the ECM not only mediates cell adhesion and presents key stimuli to the cells, but it can also bind growth factors and relevant molecules to limit their diffusion [49].

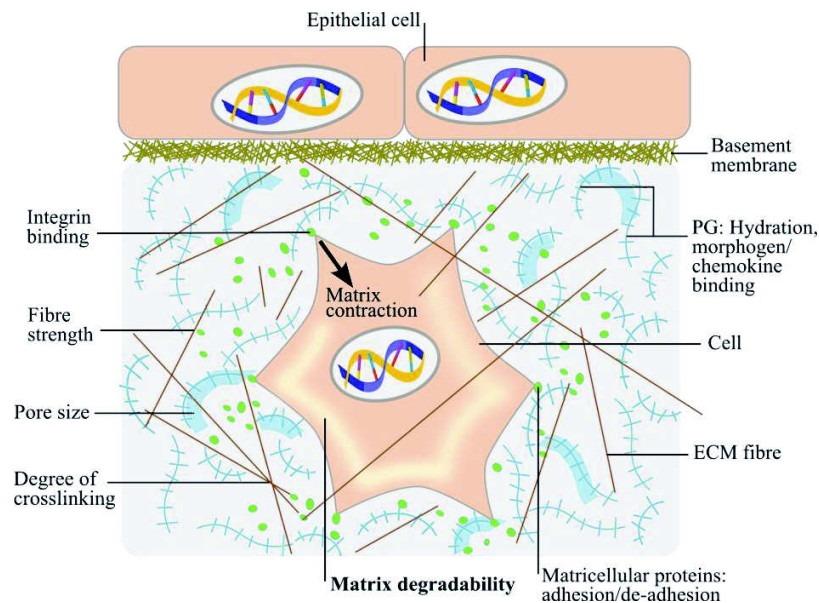


Figure 2.2] Important elements of the 3D environment for engineering cell function. The ECM is composed of several types of macromolecules, where polysaccharide chains of glycosaminoglycans and proteoglycans (PG) form a highly hydrated gelatin-like network in which fibrous proteins (including collagen, elastin, and fibronectin) and growth factors are embedded [50]. The gel allows rapid diffusion of nutrients and bioactive molecules, whereas the fibres provide mechanical strength and organise the matrix. Integrins are the principal receptors on mammalian cell surface mediating cell-cell and cell-ECM adhesion [51,52]. The basement membrane (BM) is a thin layer of ECM that surrounds muscle, fat and Schwann cells anchoring them to the epithelial and endothelial cells on top [53]. The BM contains collagen, PG and laminin acting as a mechanical barrier to prevent malignant cells from invading the deeper tissues. It is also involved in angiogenesis (i.e. the growth of new blood vessels from the existing vessels) [54,55].

A robust control of mechanical stimulation and soluble factors (e.g. hormones and growth factors) should be exerted in order to differentiate cells down the desired lineage and generate a functional tissue [49,56,57]. Functional 3D tissues are created *in vitro* by combining cells with biocompatible polymeric scaffolds that facilitate cell-cell contact, cell-matrix adhesion, proliferation and differentiation [58]. Aside from mechanical cues, the scaffold affects solute diffusion, may bind many effector proteins (e.g. growth factors and enzymes) and release biochemical signals in the cellular environment [59,60], thereby establishing tissue-scale solute concentration gradients, as well as local pericellular gradients [61,62]. Similarly, the ECM actively participates in the establishment, separation and maintenance of differentiated tissues and organs *in vivo* by regulating the abundance of growth factors and receptors, the level of hydration and the pH of the local environment [45]. Moreover, the ECM shows narrow tissue specificity and, when mature, it can undergo dynamic remodelling in response to environmental stimuli (e.g. applied force or injury). This

enables the tissue to maintain homeostasis and respond to physiological stress and disease [63]. Cells exert stresses on the ECM during tissue remodelling, morphogenesis, differentiation and normal physiological functioning. In turn, the ECM regulates the cellular response depending on stiffness [64], porosity and biochemical properties. Accordingly, it mediates integrin-ligand bonds formed by a cell with its surroundings. Integrins are a large family of transmembrane receptors that facilitate cell adhesion to proteins in the extracellular space and also transmit signals that control several biological processes spanning from cell proliferation to survival and migration [65–67]. Deregulation of the integrin-mediated signalling pathways was shown to be involved in cell migration and invasion in tumours [68,69] by influencing the ECM collagen stiffness [70,71]. In general, the stiffer the ECM, the more difficult it is for cells to exert forces and to remodel it, with a significant influence (activation or inhibition) on cell functions (e.g. endothelial organisation [72]).

The greatest degree of morphological and phenotypic similarity to the *in vivo* situation occurs within ECM-like gels, in which cells proliferate and form acini (i.e. sac-like tissue structure in the shape of an acinus) or ducts [73,74]. Natural polymers have been used to make natural hydrogels as scaffolds for tissue engineering due to their biocompatibility, biodegradability and biological functions [75]. Among these are: (i) proteins, such as collagen [76], gelatin [77], fibrin [78], silk [79], Matrigel™ [80], and genetically engineered proteins such as calmodulin (i.e. a calcium-binding protein) [81] and elastin-like polypeptides [82]; (ii) polysaccharides, such as hyaluronic acid (HA) [83], alginate [84], dextran [85] and chitosan [86]; (iii) protein/polysaccharide hybrid polymers, such as collagen/HA [87], laminin/cellulose [88], gelatin/chitosan [89] and fibrin/alginate [90]. Many studies were carried out using collagen gels, showing that cells acquire their specific morphogenesis only when the collagen is released from the scaffold and allows cells to contract. The release of collagen can occur only if the gel matrix is not too stiff (i.e. the collagen concentration is not too high) [74]. Mixing Matrigel™ and collagen I in defined proportions was demonstrated to allow the release of relatively constant chemical signals, with variable stiffness over a range covering values that are measured in normal (soft) and malignant (stiff) breast tissues [64]. Tensional stress (i.e. increased gel stiffness) can elicit a plethora of biochemical responses in the cell, altering how the cell responds to an exogenous cue and inducing morphogenetic changes during development [91], disease and cancer [64,92,93].

The first step towards the production of a synthetic ECM was the adaptation of 2D thin films of ligand-modified polyacrylamide gels for the analysis of cell response to the ECM flexibility in terms of traction/retraction forces during locomotion [94]. By varying the ratio of monomer (acrylamide) to crosslinker (N,N'-Methylene-bis-acrylamide), the elastic modulus of polyacrylamide gels can be tuned from 0.1 to 10 kPa, which is a relevant range to a wide variety of cells [94–96]. Accordingly, Engler et al. showed that *naïve* mesenchymal stem cells (MSCs) can specify lineage and commit to phenotypes with extreme sensitivity to tissue elasticity level [97]. Soft matrices that mimic brain (0.1 – 1 kPa) act as neurogenic, stiffer matrices that mimic muscle (8 – 17 kPa) act as myogenic and rather rigid matrices that mimic collagenous bone (25 – 40 kPa) act as osteogenic (Figure 2.3). During the initial week in culture, the addition of soluble biochemical factors elicits the genetic reprogramming of these lineages. However, after several weeks in culture, the cell commitment to the lineage is specified by the matrix elasticity. Consistently, the commitment of differentiated cell types was shown to be elasticity-insensitive.

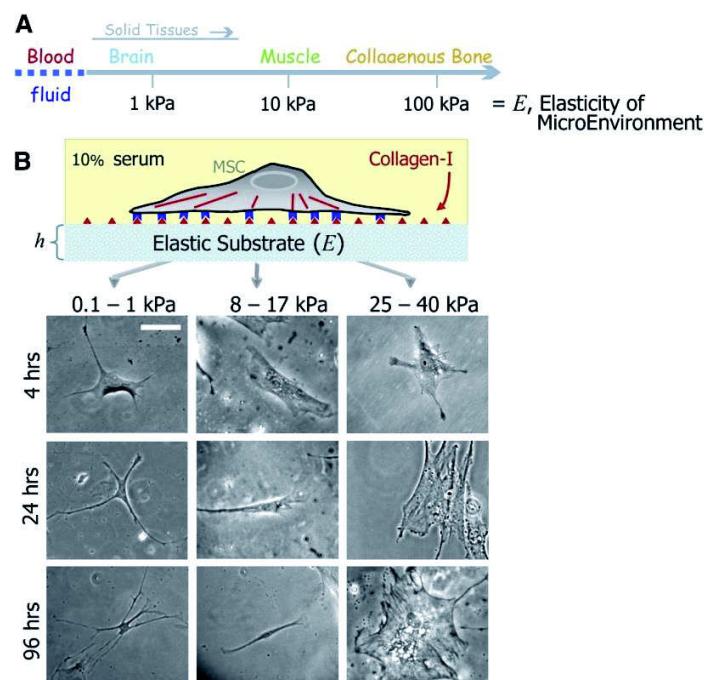


Figure 2.3] Tissue elasticity and differentiation of *naïve* MSCs [97,98]. (A) ECM stiffness is measured by the elastic modulus, E . – (B) 2D gel scaffolds allow for control of (i) E through crosslinking and (ii) cell adhesion by covalent attachment of collagen I and substrate thickness, h . *Naïve* MSCs are initially small and round. Over time, they acquire a branched shape when grown on matrices with $E \sim E_{\text{BRAIN}}$ (0.1 – 1 kPa), a spindle shape for environments with $E \sim E_{\text{MUSCLE}}$ (8 – 17 kPa) and a polygonal shape on stiff collagen matrices (25 – 40 kPa). Scale bar is 20 μm . The image is reprinted from [97] with permission.

However, 2D thin films do not recapitulate the normal mechanical environment of most cell types [99] and can lead to de-differentiation or loss of function [100]. This creates the need of moving towards synthetic 3D ECMs [6]. The realisation of 3D cell culture scaffolds goes beyond the mere control of the cell adhesion sites [101] and the matrix viscoelasticity [102,103] but entails also the control of two crucial factors: (i) the micro- and nanoporosity, which regulates cell adhesion [104], motility [105] and the transport of soluble molecules through the ECM [106]; (ii) the growth-factor binding sites, which regulate the diffusion of soluble molecules (e.g. heparin [107]) and the ECM degradation (e.g. transforming growth factor- β [108], basic fibroblast growth factor [109]).

In **Paper V** I use large gelatin matrices to validate an impedance-based method for gaining spatial sensitivity when monitoring the entire process of 3D cell culturing in a large hydrogel scaffold (from polymerisation of the bare scaffold to encapsulation and proliferation of MSCs). As the work focuses on the development of the sensing method, a simple approach for producing gelatin scaffolds is presented using the microbial enzyme transglutaminase. In **Paper VI** I use similar large gelatin matrices to embed artificial 3D cell constructs and validate an impedance method for spatial sensing of cell aggregates placed in different positions inside the scaffold. In both **Paper V** and **VI**, the culture chambers can maintain scaffolds of maximal size of $19 \times 16 \times 10$ mm in tight contact with the electrodes placed at their periphery. The production of large polymeric scaffolds was one of the technological objectives of the NanoBio4Trans project in order to (i) adapt and upscale optimised growth and differentiation protocols in a 3D environment and (ii) grow an extracorporeal bioartificial liver (BAL) with dimensions in the order of cm^3 to dm^3 .

Embedded cells in a 3D scaffold can exert translational forces to pull and push as well as torque their surrounding [110]. Reilly and Engler reviewed how the scaffold porosity strongly regulates how cells 'feel' their environment (Figure 2.4) [100]. If the pore size is too large, i.e. $> 100 \mu\text{m}$, cells can only spread on a scaffold strut by attaching their basal surface to the material, in a totally similar manner as conventional 2D cultures (Figure 2.4 *top*). In such a case the scaffold is generally stiff to prevent the large pores to collapse. Hence, the cellular environment is mainly dominated by the mechanical properties of the scaffold and, consequently, the cell exerts large forces. On the other hand, when the porosity is small, i.e. $<$

50 μm , the cell can adhere in full 3D and exert smaller forces (Figure 2.4 *bottom*). This latter environment was shown to facilitate stem cell differentiation [100].

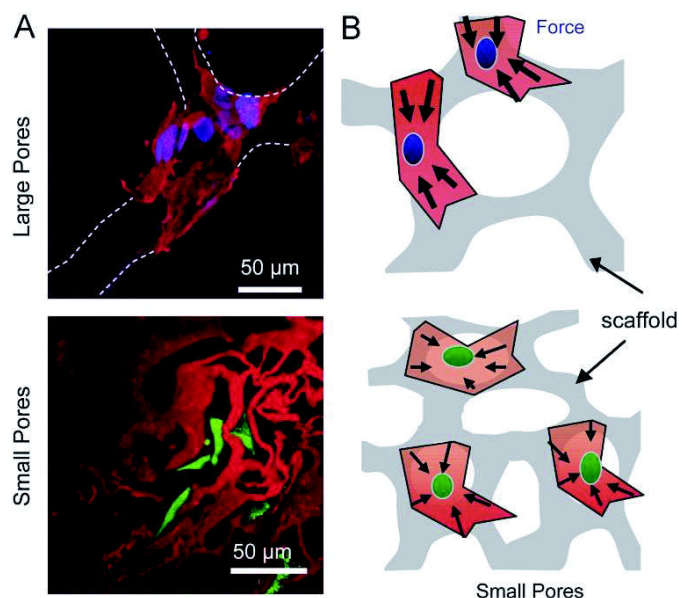


Figure 2.4| The porosity of 3D scaffolds influences cell contractility and differentiation. (A) *Top*: MSCs stained with rhodamine-phalloidin (actin cytoskeleton) and DAPI (nucleus) are flattened on the walls of a 3D scaffold (dotted lines) with large pores (> 100 μm). *Bottom*: Confocal section of osteoblasts (green) embedded within a porous collagen-glycosaminoglycan 3D scaffold (red) with small pores (< 50 μm). – (B) The scaffold porosity strongly influences how the cells ‘feel’ their environment. Scaffolds having extremely large pores, i.e. > 100 μm (*top*), are generally stiff in order to prevent the pores to collapse. In such a case, cells can only spread on one surface of the scaffold, in a similar way as 2D cultures. For most scaffolds made out of stiff polymers, the cellular environment is dominated by the mechanical properties of the scaffold so that the cells exert large forces (big arrows). This does not promote cell differentiation (blue nuclei). However, when the porosity is small, i.e. < 50 μm (*bottom*), cells can adhere to the matrix in full 3D and exert smaller forces (smaller arrows). This increases the level of cell differentiation (green nuclei). The image is reprinted from [100] with permission.

Paper IV describes the fabrication technique used for producing the scaffolds with networks of structured channels and several degrees of porosity which have been characterised using EIS in **Paper III**. A water soluble 3D printed negative template was used as a mould for casting polymer elastomers to create the scaffolds, which were also tested for *in vitro* culturing of human hepatoblastoma (HepG2) cells over a 12-day culture period. Although elastomeric scaffolds are not biodegradable for transplantation, they can be relevant to support the growth of extracorporeal organs [111] and allow the controlled release of molecules influencing cell metabolism [112,113]. Furthermore, the fabrication protocol presented in **Paper IV** allows scalability up to sizes relevant for bioartificial organs, such as extracorporeal BALs, and can also be applied to hydrogels.

In general, it is challenging to decouple the effects of elasticity, porosity and chemistry in a 3D cell culture environment and examine the contribution of each individual cue. However, the chemistry determining the matrix stiffness can also change protein (e.g. collagen) concentration, ligand density and molecule permeability within the microenvironment. Therefore, the scaffold mechanical properties may be coupled with ligand chemistry in order to develop biofunctional materials [114] which influence cell lineage. Accordingly, Battista et al. showed that the formation of embryoid bodies (i.e. 3D aggregates of pluripotent stem cells) is inhibited in collagen gel scaffolds with stiffness of 34 kPa but not when it is decreased to 16 kPa [115]. In the same study they have also demonstrated that the addition of fibronectin to the soft collagen gel induced endothelial differentiation, whereas laminin promoted cardiac muscle cell differentiation [115]. The current trend in scaffold design is direct toward achieving independently tuneable stiffness, adhesive chemistry, suitable porosity and stable permeability [116–118].

2.2 Bioreactors for tissue engineering

Within a 3D culture environment, concentration gradients may exist for any soluble factor that is consumed by cells (i.e. biomolecules and oxygen) or any product of their metabolic activity. Such gradients depend on the competition between the diffusion of nutrients and the dissipation of the products of cell metabolic activity in the bulk medium by both convection and diffusion [34,119]. The average local concentrations of biomolecules affect the local cellular behaviour, so that they can cause cells in the middle of the tissue to behave differently from cells located at the tissue surface. Furthermore, local concentrations can elicit cell gradient-dependent responses, as chemotactic migration [34,120]. Among basic nutrients, oxygen is usually the most readily depleted due to its relatively low solubility in culture medium, while glucose and amino acids gradients are almost negligible [121,122]. Even for a 2D culture, the oxygen concentration at the cell surface under 2 mm of quiescent culture medium is typically only 10 – 50% of the concentration at the air-liquid interface [34]. Therefore, efforts to control oxygen delivery to 3D cultures also include reducing gradients in the culture medium surrounding the tissue while controlling the tissue dimensions [123]. For this purpose, several type of bioreactors that control the culture medium flow through the tissue surface have been realised (Figure 2.5) [8]. Such systems span from membrane-based

reactors (in which cells are cultured outside semipermeable, hollow-fibre membranes, Figure 2.5A) to perfusion reactors (where cells are grown in porous scaffolds and the fluid is pumped around them, Figure 2.5B) and stirred-suspension-culture reactors (in which aggregates of cells are kept in suspension) [124–126]. Early work aimed toward very large scale cultures for extracorporeal organ support (e.g. liver, pancreas, kidneys) [127,128], then intermediate ‘macroscale’ systems were realised for application in drug discovery [129] and finally, microfluidic systems were developed for increasing throughput and improving control of microenvironment conditions in order to achieve organ-like performance [130–133].

The integration of microfluidics with 3D scaffolds allows the dynamic manipulation of the culture conditions at the chemical and biomechanical levels, with precise control of the culture medium flow at the nanoliter scale [134]. This ensures the continuous supply of nutrients and oxygen through the volume of the porous scaffold while removing the metabolic waste and facilitates the establishment of more *in vivo*-like conditions, such as complex chemical gradients. Choi et al. have fabricated a microfluidic system embedding 3D calcium alginate scaffolds seeded with multiple cell types. The microfluidic channels enable efficient convective and diffusive mass transfer of small and large solutes between the cell culture and the surrounding medium and quantitative control of the culture environment [135]. Trietsch et al. have realised a platform for 3D cell culture, co-culture and invasion studies under continuous perfusion in a microtiter-plate format which is compatible with conventional fluorescent assays, as well as confocal microscopy and equipment for high-content screening [136]. Such systems have opened up new perspectives for bridging the gap between *in vitro* and *in vivo* models.

Paper VII presents the development of a perfusion bioreactor array platform with integrated electrodes, which enables culture of cells seeded in thick porous 3D scaffolds. The platform is the result of one technological objective of the NanoBio4Trans project aimed at developing an impedance sensing system into a perfusion-based BAL support platform able to sustain the growth of the BAL, while allowing real-time monitoring of its growth. Initially, the suitability of the platform for cell culture was demonstrated by growing HepG2 cells in the bioreactors under different flow rates for 7 days. Cell density and viability as well as metabolic activity (albumin secretion) were assessed using a combination of imaging and bioanalytical techniques. Additionally, the bioreactor design was modified by integrating two vertical

needle electrodes in contact with each scaffold to facilitate 2T impedance measurements for real-time monitoring of cell proliferation over a 19-day period. The impedance magnitude was shown to correlate with increasing cell densities while allowing discrimination between bare and cell-loaded scaffolds.

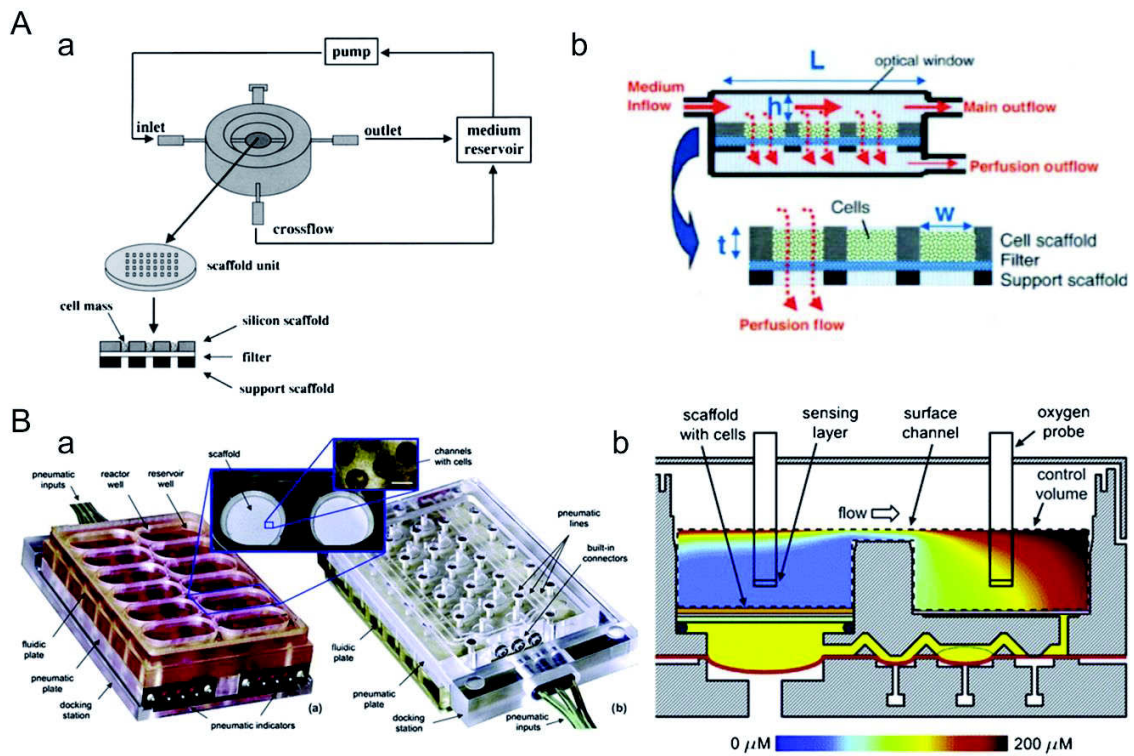


Figure 2.5| Evolution of bioreactors for hepatocyte 3D tissue culture. (A) Example of an early bioreactor: (a) functioning diagram [130] and (b) schematic of scaffold and reactor housing facilitating both cross-flow and through-tissue perfusion [137]. – (B) (a) Later reactors allowed culturing of up to twelve tissue constructs at a time [131] and were supported by a pneumatic platform to control the flow through each tissue construct. (b) Modelled oxygen concentrations for a perfusion bioreactor shown in (a) [131]. The image is reprinted from [126] with permission.

CHAPTER 3

Electrical Impedance Spectroscopy

Electrical impedance measurements, including electrical impedance spectroscopy (EIS) and *bioimpedance*, are commonly used to describe material properties that impede the flow of an alternating current (AC) and facilitate storage of electrical charge. Impedance-based techniques are a well-established tool for the electrochemical investigation of reaction mechanisms [138] as well as properties of porous electrodes [139] and electrically passive materials [30,35,140,141]. Moreover, their applications cover a wide range of disciplines, spanning from geophysics [142,143] and material science [144,145], to microbiology [146,147] and non-invasive real-time monitoring of biological systems both *in vivo* [148–150] and *in vitro* [21,29,151]. Physiological impedance measurements on tissue and organs are often used for tissue characterisation and disease diagnosis, reflecting cell dimensions, density and integrity [148,150,152–155] and have been defined as *bioimpedance* [156]. The concept of *bioimpedance* originated at the beginning of the 20th century, when Rudolf Höber discovered the frequency dependence of blood conductivity and presented proof that blood and muscle cells have a resistive dielectric membrane enclosing a conducting electrolyte solution [157]. In 1921, Maurice Philippon described the behaviour of the impedance magnitude of red blood cells, falling from a high value of $3890 \Omega \cdot \text{cm}^{-3}$ at 1 kHz to only $200 \Omega \cdot \text{cm}^{-3}$ when extrapolated between 3.5 MHz and infinity [158]. Moreover, Philippon defined the frequency dependence of capacitance across a tissue and called it ‘polarisation capacitance’, similarly to that found for a metal electrode/electrolyte interface [159]. In the 1950s, Herman P. Schwan widely described the electrical properties of tissues and cell suspensions [160]. Importantly, he interpreted the frequency dependence of muscle tissue capacitance as a phenomenon of ‘dielectric relaxation’ [161] (Figure 3.1), i.e., a delay in molecular polarisation with respect to a change in the applied electric field to a dielectric medium. As one of the founders of biomedical engineering and main contributor to the field of *bioimpedance*, Schwan studied electrode polarisation in biological materials [162,163] and mastered four-electrode techniques [164] and gigahertz measurements [165].

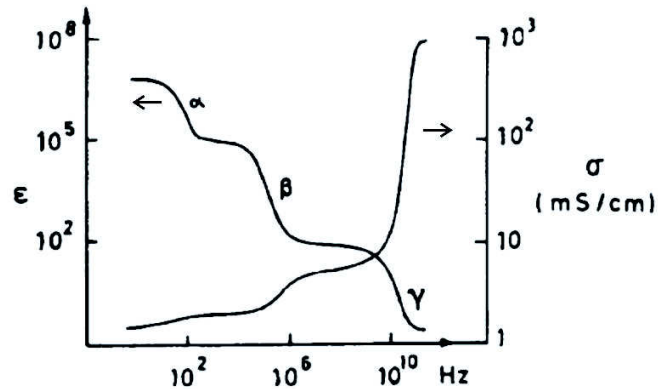


Figure 3.1 Dielectric constant ϵ (decreasing) and conductivity σ (increasing) as function of frequency for a generic soft tissue, such as muscle. Three different regions (i.e. 'dielectric dispersions') were originally found and labelled according to Schwan's terminology: α , β and γ . At low frequency (below 1 Hz and up to 100 kHz), α dispersion is influenced by counterion polarisation effects on the cell membrane. The large β dispersion is centred at ~ 1 MHz and is primarily due to charging of the membrane capacitance. Therefore, β dispersion depends on cell membrane composition and shape. At high frequencies, the dielectric properties of the tissue are dominated by the dielectric properties of water (γ dispersion). Accordingly, γ dispersion is centred at ~ 20 GHz because of the rotational diffusion of water dipoles [166]. The image is reprinted from [160] with permission.

Presently, Sverre Grimnes and Ørjan G. Martinsen are among those who have pioneered investigations in the field of *bioimpedance* applications in medicine, biology and physiology [167–171]. Their research activity was started around 1980 by Grimnes at the clinical engineering department of Oslo University Hospital. After receiving reports from surgeons claiming that they could perceive an 'electrical sensation' of vibration around the eyes when looking into the ocular lens of their microscopes, he started thorough investigations. Grimnes was able to measure an electrical current of a few microamperes flowing between the eyepiece and the skin of the operator, which was far less than the human perception limit of about one milliamperere. This led him to discover a new sensing mechanism that he called 'electrovibration' [172,173] and is due to the electrostatic forces caused in the skin by the electric field in a low conductive (e.g. dry) stratum corneum. Such electric field is produced when moving the skin over the metal surface of a non-grounded device connected to the mains. In the 1990s, Martinsen joined Grimnes research activity and started working on the passive electrical properties of human skin [140,174]. The uppermost layer of dead cells in the epidermis is the stratum corneum and is a very poor conductor of electricity. However, when the skin is moistened with water, the stratum corneum becomes more conductive. Therefore, when the body is perspiring, the filled sweat ducts create several small shunt paths for the current, increasing the skin conductance. Based on this principle Martinsen, Grimnes

and collaborators developed a small instrument for the impedance measurement of sweat activity called Sudologger (BioGauge AS, Oslo). Although similar methods had been used during many years in applications such as lie detection, the Sudologger uses AC instead of direct current (DC) and advanced signal processing. Moreover, measurements of sweat activity can be also a measure of the autonomous nervous system activity in an individual. Accordingly, especially in the palms of the hands and the soles of the feet, sweating is mainly psychologically controlled instead of responding to temperature variations in the body. Sweat activity measurements, together with other *bioimpedance* methods, are currently used in Grimnes and Martinsen group to early identify conditions of severe hypoglycemia in diabetics [175]. Another branch of research within which *bioimpedance* methods were developed by Martinsen, Grimnes and collaborators is the needle positioning system. Impedance measurements and multivariate analysis can be used to know the type of tissue and the exact anatomical location when positioning the needle tip during surgery or when administering analgesia. The clinician can inject small AC currents through a needle when pushing it into the tissue in order to measure the impedance, which reflects the properties of the tissue in close proximity to the needle tip, due to its sharpness [150,155,176]. In 2000, Grimnes and Martinsen published the book 'Bioimpedance and Bioelectricity basics', which has now come out in its third edition [177] illustrating both the theoretical and practical aspects of *bioimpedance*.

3.1 Theory

Bioimpedance, as EIS and more generally impedance, is a *transfer function* (or network function) method where the sample is perturbed with a sinusoidal wave input current and the response voltage is measured at the output. If the measured system is *linear*, the response is sinusoidal having the same frequency as the input. Accordingly, for any *linear system*: (i) doubling the input current doubles the output voltage and (ii) the property of the weighted sum of the output voltage is superimposed with the weighted sum of the input current.

A purely sinusoidal voltage may be expressed as in Eq. 3.1:

$$u = U \sin \omega t \quad (3.1)$$

where ω is the angular frequency, which is 2π times the linear frequency f in Hz. It is convenient to think of this voltage as a rotating vector (or 'phasor'), as shown in Figure 3.2. Its length is the amplitude U and its frequency of rotation is ω . The observed voltage at any time, u , is the component of the phasor projected on some particular axis (normally that at 0°).

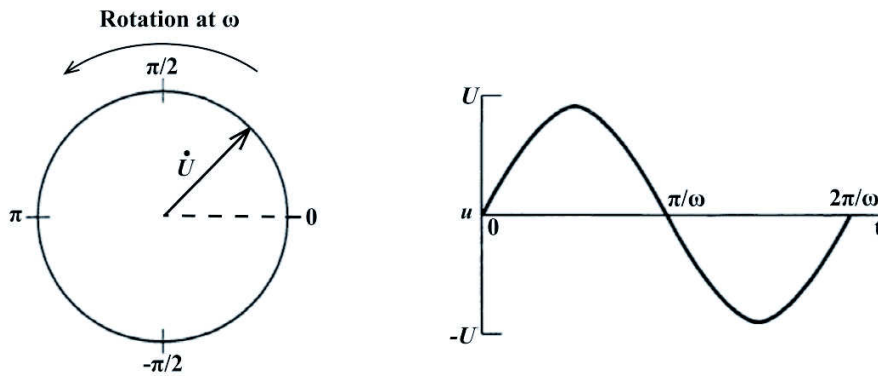


Figure 3.2| Phasor diagram (*left*) for an alternating voltage $u = U \sin \omega t$ (*right*). The image is reprinted from [178] with permission.

In AC techniques as impedance, both current, i , and voltage, u , are represented by separate phasors, \dot{I} and \dot{U} , rotating at the same frequency ω . As shown in Figure 3.3, they are generally not in phase and, hence, their phasors are separated by a phase angle ϕ [178,179]. One of the phasors, generally \dot{U} , is taken as reference and ϕ is measured with respect to it.

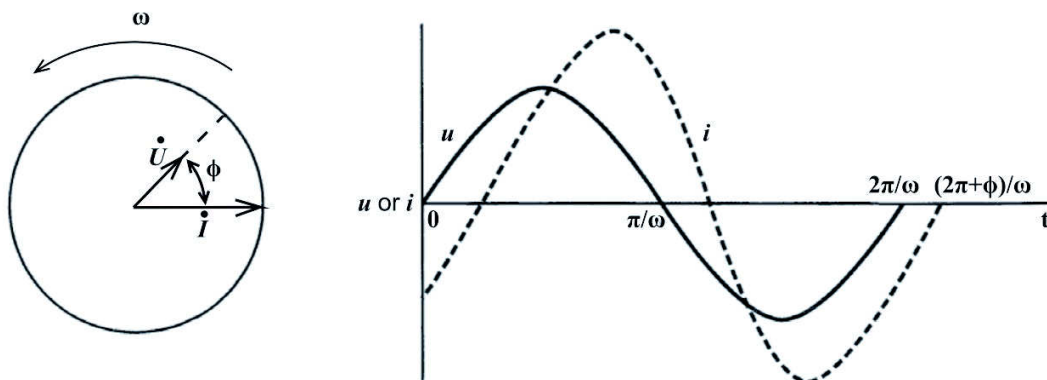


Figure 3.3| Phasor diagram (*left*) showing the relation between alternating current and voltage at frequency ω (*right*). The image is reprinted from [178] with permission.

In the figure, the current lags the voltage and it can be generally expressed as:

$$i = I \sin(\omega t + \phi) \quad (3.2)$$

where ϕ is negative.

For a clearer view, these concepts may be applied to the analysis of some simple circuits. First, we can consider a pure resistor, R , across which a sinusoidal voltage, $u = U \sin \omega t$, is applied. According to Ohm's law the current is:

$$I = \frac{U}{R} \sin \omega t \quad (3.3)$$

or, in phasor notation:

$$\dot{i} = \frac{\dot{U}}{R} \quad (3.4)$$

$$\dot{U} = \dot{i} \cdot R \quad (3.5)$$

The phase angle is zero resulting in the phasor diagram below:

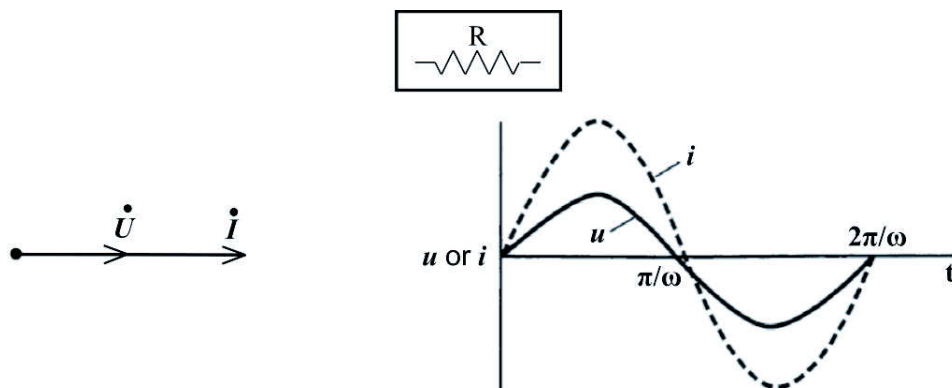


Figure 3.4] Phasor diagram (*left*) showing the relation between the voltage across a resistor and the current through the resistor (*right*). The image is reprinted from [178] with permission.

Now, if considering a pure capacitor, C , the fundamental relation is $q = C \cdot u$ (where q is the electric charge) or $I = C \frac{du}{dt}$, so that:

$$i = \omega C U \cos \omega t \quad (3.6)$$

$$I = \frac{U}{X_C} \sin \left(\omega t + \frac{\pi}{2} \right) \quad (3.7)$$

where X_C is the capacitive reactance, $X_C = \frac{1}{\omega C}$. The phase angle is $\frac{\pi}{2}$, and the current leads the voltage, as shown in the phasor diagram:

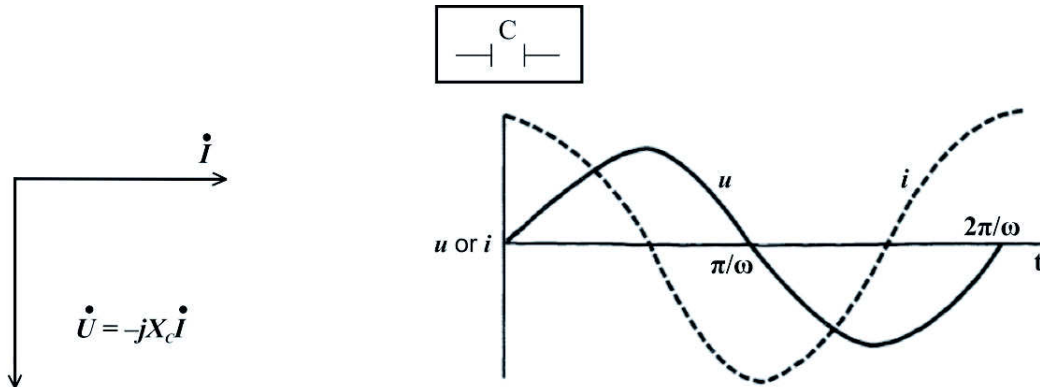


Figure 3.5] Phasor diagram (*left*) showing the relation between the voltage across a capacitor and the current through the capacitor (*right*). The image is reprinted from [178] with permission.

By defining the capacitive reactance, the phasor diagram has now expanded to a plane, so that it is convenient to represent phasors using complex notation. Components along the y-axis are assigned as imaginary and are multiplied by $j = \sqrt{-1}$, while components along the x-axis are real. Although the complex notation allows mathematical handling of the vector components, both components are real in the sense of being measurable by phase angle. In circuit analysis, the current phasor is conventionally plotted along the x-axis as shown in Figure 3.5, even though the current's phase angle is experimentally measured with respect to the voltage. The voltage is:

$$\dot{U} = -jX_C \dot{i} \quad (3.8)$$

By comparing Eqs. 3.5 and 3.8, it can be inferred that X_C must carry dimensions of resistance but, unlike R , its magnitude falls with increasing frequency [178].

Now consider a simple circuit where a capacitor and a resistor are in series and a voltage, \dot{U} , is applied across them. At all times \dot{U} must equal the sum of the individual voltage drops across the resistor and the capacitor; so that:

$$\dot{U} = \dot{U}_R + \dot{U}_C \quad (3.9)$$

$$\dot{U} = \dot{i}(R - jX_C) \quad (3.10)$$

$$\dot{U} = iZ \quad (3.11)$$

This means that the voltage is linked to the current through a vector $Z = R - jX_C$, which is called 'impedance'. The impedance is generally represented as:

$$Z(\omega) = Z_{Re} - jZ_{Im} \quad (3.12)$$

where Z_{Re} and Z_{Im} are the real and imaginary parts of the impedance, respectively. In the simple case of a capacitor and resistor in series, $Z_{Re} = R$ and $Z_{Im} = X_C = \frac{1}{\omega C}$. The magnitude of Z is written $|Z|$ and is given by:

$$|Z|^2 = R^2 + X_C^2 = (Z_{Re})^2 + (Z_{Im})^2 \quad (3.13)$$

And the phase angle ϕ is:

$$\phi = \tan^{-1} \frac{Z_{Im}}{Z_{Re}} = \tan^{-1} \frac{X_C}{R} = \tan^{-1} \frac{1}{\omega RC} \quad (3.14)$$

The impedance is a kind of generalised resistance, and Eq. 3.11 is a generalised version of Ohm's law. It embodies both Eq. 3.5 and Eq. 3.8 as special cases. The phase angle expresses the balance between capacitive and resistive components in the series circuit. For a pure resistance, $\phi = 0$; for a pure capacitance, $\phi = \frac{\pi}{2}$; and for mixtures, intermediate phase angles are observed [178]. The phasor diagram for an RC series network is shown in Figure 3.6.

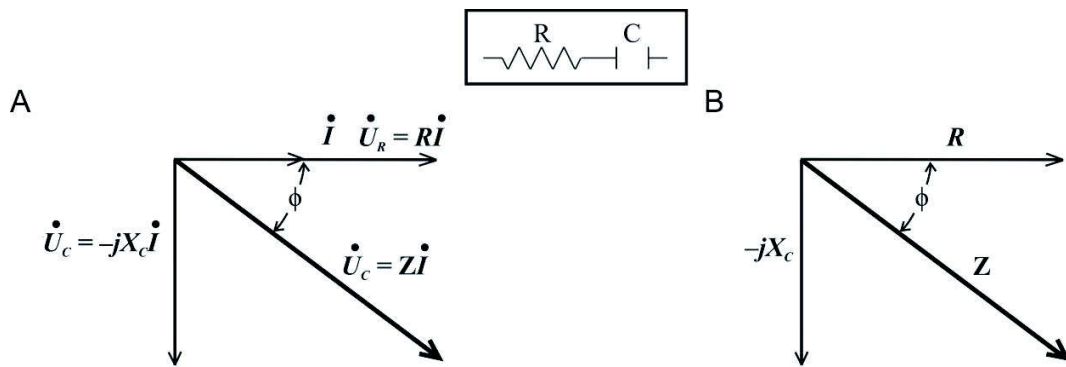


Figure 3.6] (A) Phasor diagram showing the relation between the current and the voltage in the simple case of a capacitor, C, and a resistor, R, in series. The voltage across the whole network is \dot{U} , and \dot{U}_R and \dot{U}_C are its components across the resistance and the capacitance. (B) An impedance vector diagram derived from the phasor diagram in (A). The image is reprinted from [178] with permission.

As impedance is a *transfer function*, Z can be experimentally calculated as the ratio between the phasor \dot{U} , representing the voltage measured across the system, and the phasor \dot{I} , representing the current injected through the system:

$$Z(\omega) = \frac{\dot{U}}{\dot{I}} \quad (3.15)$$

which is equivalent to Eq. (3.12) and holds for all *linear systems*. Although biological systems are not *linear systems*, the amplitude of the sinusoidal perturbation applied to the sample may be sufficiently small within the linearity range of the system to generate a pseudo-linear behaviour. Nonlinear systems would otherwise generate harmonics that modify the signal waveform. Aside from linearity, other conditions for obtaining ‘good’ impedance measurements are stability, causality and finiteness for all frequencies, which will be defined later in this section. When these conditions are valid, the system under study neither changes with time while the impedance spectrum is recorded nor continues to oscillate after the excitation is stopped. Hence, the output response is solely due to the applied perturbation input [180,181].

Experimentally, conventional instrumentation for impedance measurements can operate by injecting the current through the sample or applying a potential. In the first case (galvanostatic mode), the instrument controls the injected current between the *current-carrying (CC) electrodes* and measures the potential response of the system between the *signal pick-up (PU) electrodes* to calculate the impedance. In potentiostatic mode, the applied potential is controlled and the current response of the system is measured. Hence, when working in potentiostatic mode, the instrument calculates the inverse of impedance (or admittance, Y), which is then converted to impedance by a dedicated software. The potentiostatic mode is commonly used in electrochemical applications, where a control of the applied potential allows, e.g., electron-transfer equilibrium studies and assessing the charge/discharge cycle of fuel cells and batteries [182–184]. In *bioimpedance* measurements on living tissues, galvanostatic measurements are typically used in order to tightly control the injected current and provide a non-invasive approach which adheres to medical safety regulations [185–188]. However, when performing impedance measurements on 3D cell cultures and tissue engineering constructs, no experimental protocols have been previously established. Such impedance measurements may be carried out in both potentiostatic and

galvanostatic mode, but the protocol must be optimised to not affect the cell viability and the integrity of the scaffold material.

The Kramers–Kronig transforms (KKT) provide a good set of tools for data validation in impedance measurements. These were independently derived by Kramers and Kronig when working on x-ray optics in 1926 and 1927. If the real part of a linear function of frequency is known over the complete frequency spectrum, it is possible to calculate the imaginary part, and vice versa. In order to comply with the KKT, any data set must show:

- Linearity of the response (previously discussed in this section),
- Stability, i.e. the system neither changes with time nor continue to oscillate after the perturbation is stopped,
- Causality, i.e. the measured response is solely due to the applied perturbation signal,
- Finiteness, i.e. the function has finite values for all frequencies, including $\omega \rightarrow 0$ and $\omega \rightarrow \infty$ [189,190].

The KKT rule states that the imaginary part of the impedance function is completely determined by the form of the real part over the frequency range $0 < \omega < \infty$. With the impedance defined as $Z = R + jX_C$, the KKT are:

$$R(\omega) - R(\infty) = \frac{2}{\pi} \int_0^{\infty} \frac{fX_C(f) - \omega X_C(\omega)}{f^2 - \omega^2} df \quad (3.16)$$

where ω is the angular frequency of transform and f is the linear frequency of integration.

To calculate DC values, ω is set to zero obtaining:

$$R(0) - R(\infty) = \frac{2}{\pi} \int_0^{\infty} \frac{X_C(f)}{f} df = \frac{2}{\pi} \int_{-\infty}^{+\infty} X_C(\ln f) d(\ln f) \quad (3.17)$$

$$X_C(\omega) = -\frac{2\omega}{\pi} \int_0^{\infty} \frac{R(f) - R(\omega)}{f^2 - \omega^2} df \quad (3.18)$$

$$\phi(\omega) = \frac{2\omega}{\pi} \int_0^{\infty} \frac{\ln|Z(f)|}{f^2 - \omega^2} d\ln f \quad (3.19)$$

In order to obtain a complete frequency spectrum, one of the data representations for R (i.e. the real part of the impedance, Z_{Re}), X_C (i.e. the imaginary part of the impedance, X_C), $|Z|$, or ϕ

must be known [191]. Eqs. 3.16 and 3.17 provide imaginary axis-to-real axis transformation, while Eq. 3.18 yields the real axis-to-imaginary axis transform [192–195], as depicted in Figure 3.7. In general terms, if the system behaviour is described by the KKT, falling impedance with increasing frequency shall correspond to negative phase angles [196].

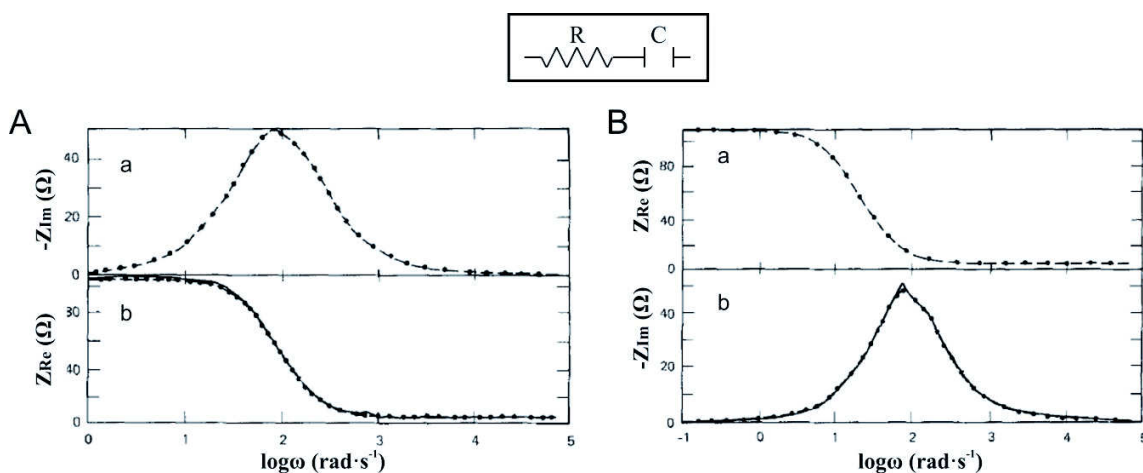


Figure 3.7] (A) Imaginary axis-to-real axis KKT of impedance data for a generic RC circuit: (a) $-Z_{Im}$ vs. $\log_{10}\omega$ and (b) Z_{Re} vs. $\log_{10}\omega$. – (B) Real axis-to-imaginary axis KKT of impedance data for a generic RC circuit: (a) Z_{Re} vs. $\log_{10}\omega$ and (b) $-Z_{Im}$ vs. $\log_{10}\omega$. Dotted line represents experimental data at discrete frequencies and continuous line is the fit to the equivalent circuit using nonlinear least squares (NLLS) regression methods. The image is reprinted from [194] with permission.

Aside from direct integration of the KKT, experimental, graphical and regression methods can be applied to check whether the impedance data meet the KKT [197]. There are two standard graphical representations used in presenting impedance data: complex plane plots and Bode (or Wessel) plots. Complex plane plots can be presented as, for instance, complex impedance plane plots ($-Z_{Im}$ vs. Z_{Re} ; known as Nyquist plot), complex admittance plane plots ($-Y_{Im}$ vs. Y_{Re}) and complex dielectric plane plots ($-\epsilon_{Im}$ vs. ϵ_{Re} ; known as Cole–Cole plot) [198,199]. A Nyquist plot is generally used when faradaic phenomena related to electrochemical redox reactions are involved. The Nyquist plot reports Z_{Re} on the x-axis and the negative of Z_{Im} on the y-axis. Figure 3.8 shows a schematic representation of a Nyquist plot for an electrode in contact with an electrolyte containing equimolar concentration of a redox couple (e.g. ferri-/ferrocyanide, $\text{Fe}(\text{CN})_6^{3-/4-}$). In the Nyquist plot, the semicircle at high frequencies comprises the faradaic processes controlled by electron transfer (i.e. by the reaction kinetics), while the straight line in the low frequency part describes diffusion-controlled processes [200]. Such behaviour can

be fitted to the so-called Randles' equivalent circuit using nonlinear least squares (NLLS) regression methods [201].

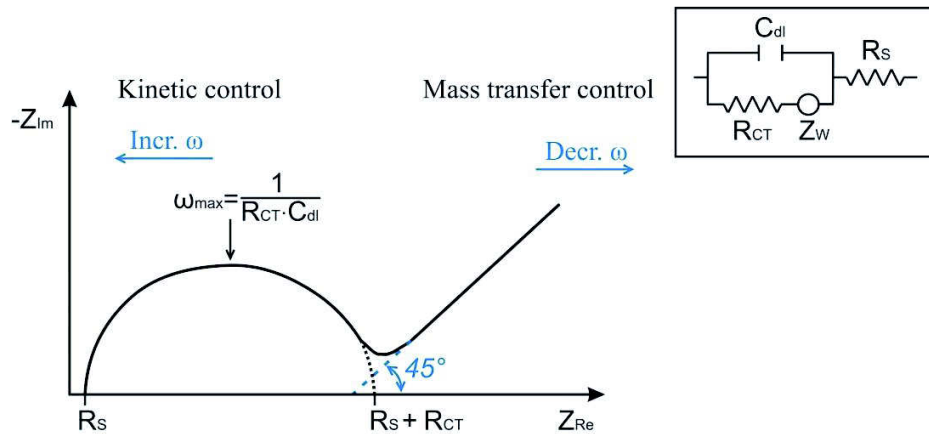


Figure 3.8| A schematic representation of Nyquist plot for an electrode in contact with an electrolyte containing equimolar concentration of a redox couple whose behaviour can be fitted to the Randles' equivalent circuit (insert). R_s is the solution resistance and models the signal loss due to the current spreading through the solution. The interface impedance can be divided into two main components, the faradaic and non-faradaic interface impedance. The faradaic impedance describes the behaviour of electrochemical redox reactions, characterised by charge transfer resistance (R_{CT}) and mass transfer resistance (Warburg impedance, Z_W). The non-faradaic impedance comprises the impedance contribution of the electrical double layer capacitance (C_{dl} , Section 3.2.1). R_{CT} is the resistance to electron transfer between the electrode surface and redox couple in the solution. R_s and R_{CT} can be graphically determined from the Nyquist plot. The line at 45° indicates Z_W .

Physiological solutions, such as phosphate buffered saline (PBS), do not contain electroactive species and, therefore, when performing impedance measurements, only non-faradaic processes take place at the electrode interface. Consequently, such processes do not have any defined R_{CT} and the characteristic semicircle of a Nyquist plot is not seen (Figure 3.9A). The straight line obtained in Figure 3.9A corresponds to a semicircle in the admittance plane (Figure 3.9B) and to a characteristic recessed semicircle in the complex permittivity plane (Cole-Cole plot, Figure 3.9C), where the presence of DC conductivity (as R_s) results in divergence ('tailing') of the recessed semicircle which could be related to e.g., solution resistance [199]. Heiskanen et al. [182] pointed out another possibility that the resistive behaviour could arise from the presence of finite charge transfer processes in complex electrolyte mixtures such as cell culture medium. Surface inhomogeneities of electrodes have been also shown to cause resistive behaviour which leads in tailing of Cole-Cole plot [202].

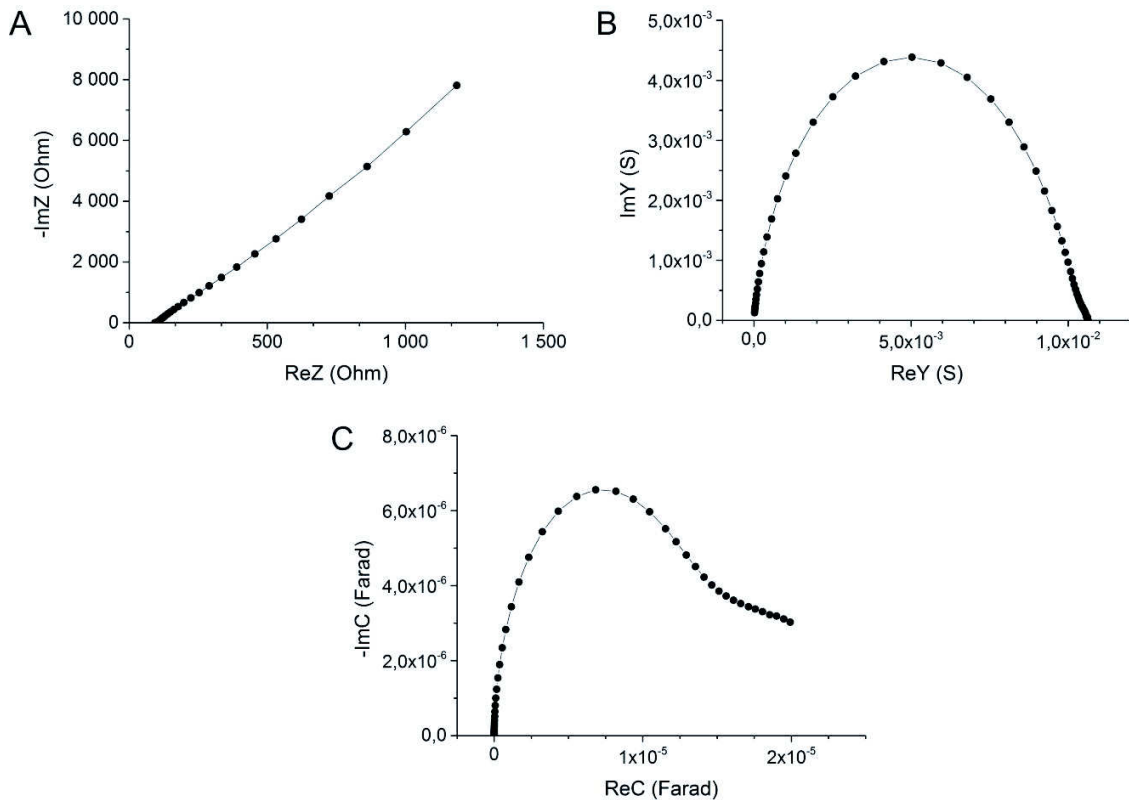


Figure 3.9] Impedance measurements on physiological PBS. Representation in the (A) complex impedance plane (Nyquist plot), (B) complex admittance plane and (C) complex permittivity plane (Cole-Cole plot). Real and imaginary capacitance (ReC and -ImC) are the angular frequency normalised imaginary and real admittance, respectively [182,203].

Bode plots are commonly used to present the resistive and capacitive behaviour of the measured impedance in electrolyte solutions without redox couples (e.g. physiological solutions). Bode diagrams are log-log plots which usually report $|Z|$ and ϕ as function of frequency. For a pure capacitor, ϕ is -90° ; for a pure resistor, ϕ is 0° . For an RC circuit, ϕ is dependent on frequency with values between the limits determined by the pure capacitor and resistor [204]. Figure 3.10 shows an example of Bode plots for physiological PBS using the setup described in **Paper II**. In the Bode plot for $|Z|$, asymptotic values at low and high frequencies provide values for R_s and R_{CT} , respectively [204]. In Figure 3.10 the high-frequency part of the spectrum (200 kHz – 1 MHz) is slightly deviating from the ideal case of series of a resistor and a capacitor. This may be due to parasitics which depend on the setup geometry and the capacitive coupling between the connecting wires, power supply and surrounding environment.

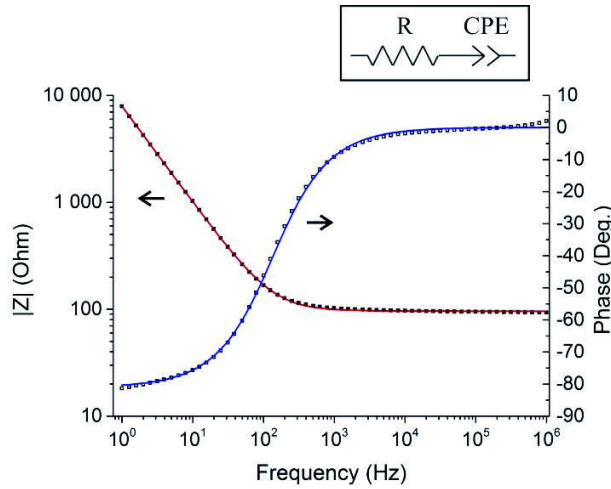


Figure 3.10] Spectral analysis of physiological PBS using the setup described in **Paper II** and an R-CPE circuit for modelling. Black dots and black squares represent real data for $|Z|$ and ϕ , respectively. Fits for $|Z|$ and ϕ are presented as red and blue lines, respectively.

Equivalent circuit models can be used to fit the different physical properties that contribute to the total measured impedance. A model that provides a good representation of the impedance measurements can serve as a basis for curve fitting using NLLS regression methods [205]. The comparison between model and experiment can motivate modifications to the model or to the experimental setup. Using a two-terminal (2T) setup, physiological samples may behave as a resistor and a capacitor in series, depending on the setup geometry. When considering an RC circuit, the current flowing through the circuit elements is the same, but the potential drop is different, so that the respective impedances must be added in series.

$$Z_{total}(\omega) = R + Z_C(\omega) = R + \frac{1}{j\omega C} \quad (3.20)$$

Accordingly, at very low frequencies ($\omega \rightarrow 0$), $Z_C \gg R$ and the total impedance is approximately that of the capacitor ($Z_{total} \sim Z_C$). On the other hand, at very high frequencies ($\omega \rightarrow \infty$), the impedance of the capacitor approaches zero and the total impedance is approximately that of the resistor ($Z_{total} \sim R$). However, a pure RC equivalent circuit model is too simple to mimic the impedance behaviour of complex biomaterials or detect the electrode-surface phenomena at all frequencies. A better representation can be obtained by considering non-ideal frequency-dependent components, as in the case of the constant phase element (CPE, Figure 3.10) [206]. A CPE comprises a capacitor and a resistor and it is often

used to model the electrical double layer at the electrode interface (Section 3.2.1) which is influenced by, e.g., surface roughness and impurities [203], charge accumulation [201], or geometrical constraints [204].

3.2 Impedance Measurement Setups

When considering a system consisting of electrodes and a 3D sample, important electrical characteristics are principally influenced by the geometrical configuration of the electrodes. Parameters such as the electrode geometry and number, spacing and orientation should be carefully considered in order to maximise the sensitivity field distribution and spatial resolution of the impedance measurement. *Finite element (FE) analysis* (Section 3.2.4) may provide a useful tool to simulate impedance measurements using a number of different setups and evaluate their performance. A clear distinction must be made between source electrode systems (or current injecting, *current-carrying*, *CC*, stimulating, driving) and recording electrode systems (or signal *pick-up*, *PU*, receiving, registering). The same electrode couple may serve as both (two-terminal, 2T, configuration), or there may be separate 3- or 4-electrode systems (three- or four-terminal, 3T or 4T, configurations).

This thesis aims at the development of impedance-based methods with application in different stages of tissue engineering processes. Different electrode configurations have been explored. 2T measurements are described for:

- Accurate determination of conductivity in physiological solutions and cell culture medium (**Paper II**);
- Monitoring hydrogel scaffold polymerisation (**Paper V**);
- Porosity determination (**Paper III**) in elastomeric scaffolds (**Paper IV**);
- Real-time monitoring of cell proliferation in perfusion bioreactors (**Paper VII**).

3T measurements are used for monitoring cell loading and proliferation in hydrogel scaffolds (**Paper V**), whereas 4T measurements are applied for:

- Sensing the spatial location of cell aggregates within large hydrogel scaffolds (**Paper VI**);
- The investigation of EIT as a potential method for image reconstruction in miniaturised 3D culture chambers with possible future applications in tissue engineering (**Paper VIII**).

3.2.1 Electrode Polarisation

When applying an electrical perturbation to a biological sample, the ions tend to move towards the electrode/sample interface and this leads to the formation of an electrical double layer. The applied voltage drops rapidly in this layer causing a huge electrical polarisation of the sample [162].

The electrical double layer consists of two layers of charges: (i) the formed surface charge and (ii) the neutralising layer of ions. Such an arrangement forms a plate-capacitor. In the second layer, the ions are not compacted, but other fully hydrated ions can be loosely attached to this layer and form a diffuse layer [207]. Therefore, the total capacitance of the electrical double layer (C_{dl}) comprises two capacitances in series:

$$\frac{1}{C_{dl}} = \frac{1}{C_H} + \frac{1}{C_{GC}} \quad (3.21)$$

where C_H and C_{GC} are the capacitive contributions of the compact Helmholtz layer and diffuse Gouy–Chapman layer, respectively [208]. The thermal motion of hydrated ions affects the integrity of the diffuse layer and the ionic strength of the electrolyte under study. Thermal motion increases the dispersion of ions in the diffuse layer, whereas an increased ionic strength increases the compactness of the double layer. Moreover, as in a capacitor where the capacitance is inversely proportional to the charge distance, the value of C_{GC} increases with increased ionic strength, making its contribution to C_{dl} negligible. Therefore, in dilute solutions or low conductive samples, the diffuse layer (C_{GC}) is the principal contributor to C_{dl} , whereas in concentrated solutions or high conductive samples, the predominant contribution to C_{dl} is from the compact layer (C_H) [208].

Electrode polarisation impedance (Z_p) may be described as the interface impedance between the electrode surface and the sample and can be defined as:

$$Z_p = R_p - j\omega C_p \quad (3.22)$$

where R_p and C_p are the polarisation resistance and the polarisation capacitance, respectively. When a metal electrode is immersed in a sample (saline solution, cellular suspension, or tissue) a DC-polarisation potential (U_0) is found at the electrode-sample interface with no current flow (Figure 3.11A,C). If a small alternating current is injected, $I_{(-)}$, it flows through the interface between the electrode and the sample, modulating the DC-polarisation potential

with an alternating potential, referred to as ‘modulation potential’, $U_{(\sim)}$, which lags the change in current $I_{(\sim)}$, as shown in Figure 3.11B,D [209].

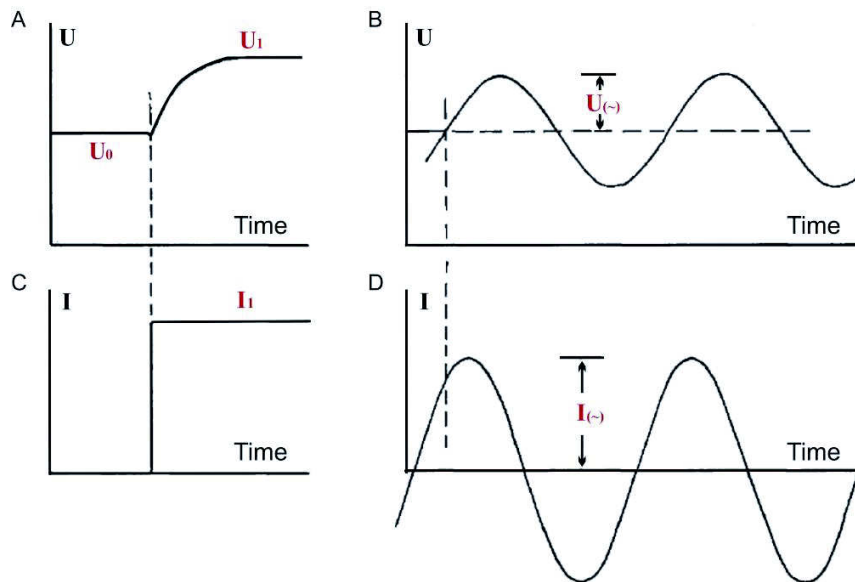


Figure 3.11 | Polarisation potential of a metal electrode in the time (A-C) and frequency domain (B-D). Dashed lines indicate time of alternating current, $I_{(\sim)}$, injection. The image is reprinted from [209] with permission.

In condition of linearity, $U_{(\sim)}$ is smaller in comparison with the DC-polarisation potential U_0 and the alternating current $I_{(\sim)}$ is sufficiently small to make $U_{(\sim)}$ proportional to $I_{(\sim)}$. Thus, the alternating current aspect of electrode polarisation is best characterised by a capacitive impedance Z_p , corresponding to the double layer of charges on the electrode surface. This primarily applies in the linearity range where Z_p is almost independent of the current flow through the electrode/sample interface [209]. Platinum (Pt) electrodes are an optimal choice for alternating current work giving two major advantages. First, their Z_p is lower than that of electrodes made of other materials [210] and, moreover, their surface may be deposited with a fine porous coat of Pt black, which increases the metal surface area and, hence, reduces *electrode* Z_p by up to four orders of magnitude [191,209]. Such an approach is generally referred to as ‘platinisation’ [211].

In 1984, Giæver and Keese [21,22] proposed a method for monitoring 2D cell cultures taking advantage of impedance measurements reflecting the *electrode* Z_p modulated by adhering cells grown on a planar electrode. Such method, called ‘electric cell-substrate impedance sensing’ (ECIS®), was patented and brought into market by Applied BioPhysics, Inc. It is a

label-free real-time impedance-based technique to study complex cell behaviour directed by the cell cytoskeleton (e.g. cell adhesion, migration, proliferation and response to drugs and toxicants). However, when performing impedance measurements on tissues and organs, Z_p is often considered a source of error. Moreover, its effect can depend on sample conductivity and temperature and on the electrode structure, composition and surface roughness. These can be further complicated by electrochemical reactions taking place on the electrode [212]. Z_p is particularly disturbing in the case of highly conducting materials such as most biological samples (e.g. skin, liver, muscle, breast, blood), and at low frequencies, which are often investigated in physiological research. Z_p can also be disturbing when monitoring biologically generated potentials (e.g. electroencephalography, electrocardiography, myography) and high input impedance measuring equipment is commonly used to remove such influence [163]. Traditionally, the definition of Z_p as a source of error in physiological measurements has led to rejection of data especially in the frequency range 10 – 50 kHz [163,213–217]. Kalvøy et al. found that in impedance measurements where one spherical electrode is dominant in a system of two electrodes (i.e. unipolar measurements), the ratio between Z_p and the tissue impedance is inversely proportional to the electrode radius [218,219]. Methods for reducing Z_p contribution to the overall measured impedance include:

- Increasing the impedance of the sample, e.g., by increasing its size (as in the case of tissues) or volume (for cell suspensions) [220];
- Measuring Z_p separately and then subtract it from the measured total impedance [220];
- Substituting the sample with one showing known impedance behaviour to calibrate the measurement system [209,221];
- Use of a 4T configuration [164,209,222].

Although Z_p is commonly considered a source of error in physiological measurements, a number of scientific publications have also opened perspectives in using Z_p to retrieve more information in sample characterisation. Accordingly, Schwan found that Z_p depends on cell concentration in a suspension and on the tissue type [160,163,166,209,220] and Kalvøy et al. showed that Z_p data may be used to improve tissue discrimination [150].

3.2.2 Electrode Configurations

When performing impedance measurements, two electrodes (an electrode ‘pair’ or ‘couple’) are needed to close the electric circuit to allow the AC current flow (*CC electrodes*) and two *PU electrodes* facilitate potential measurements. The *CC electrodes*, the sample and the electrolytes all contribute to the measured impedance and behave as physically in series, so that their contributions must be added. Two-, three- and four-terminal (T) configurations may be used and they are illustrated in Figure 3.12.

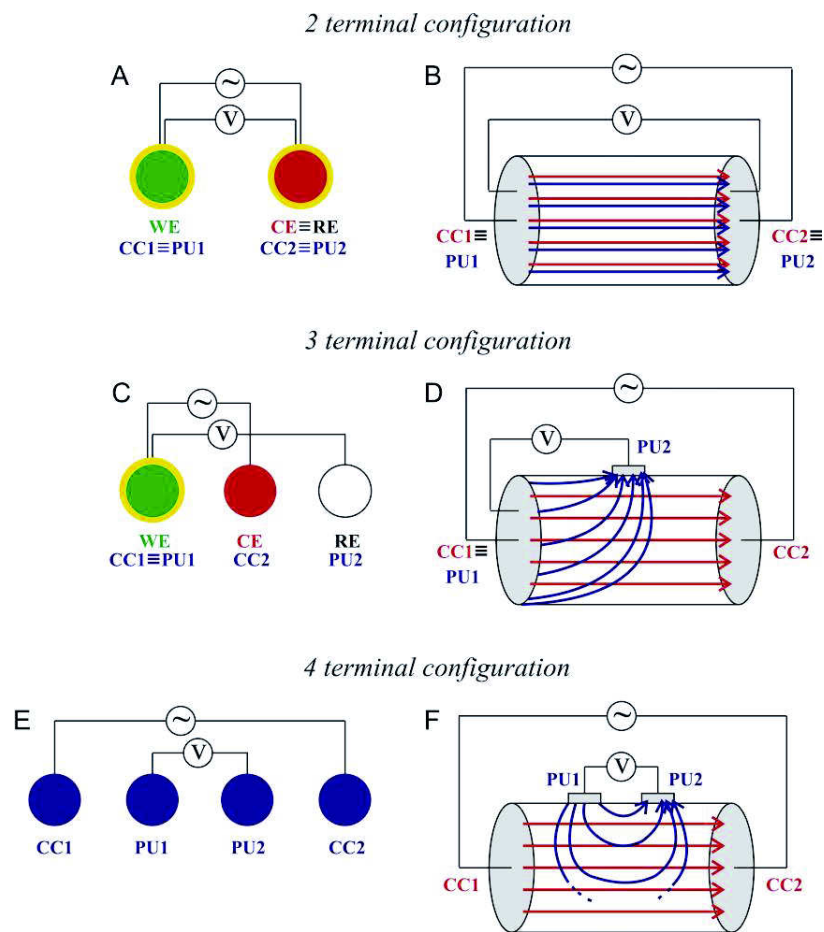


Figure 3.12 Schematics of (A) 2T, (C) 3T (E) and 4T configurations in a generic cylindrical conductor (**Paper I**). Vectors for the CC and PU electric fields are reported in red and blue, respectively, in B, D and F. In electrochemical analysis *WE* (green) is the *working electrode*, *CE* (red) is the *counter electrode*, *RE* (white) is the *reference electrode*. In *bioimpedance* measurements *CC1* and *CC2* form the *current-carrying couple*; *PU1* and *PU2* form the *voltage pick-up couple*. Z_p at the electrode surface is reported in yellow, if present (A and C). For the representation of the sensitivity fields (B, D, F), red and blue arrows refer to the direction of CC and PU electric fields, respectively.

In the 2T configuration (Figure 3.12A,B), the same electrode pair serves as both *CC* and *PU couple* and the measured impedance typically includes Z_p at both electrode surfaces (Figure 3.12A), which adds in series to the impedance of the sample [170]. Both *CC electrodes* are within the sensitivity zone for the measurement (Figure 3.12B) and, therefore, the measured impedance is affected by their Z_p . The sensitivity field is always positive [223]. In general, 2T measurements provide the simplest approach for conductivity analysis (**Paper II**) and when integrating impedance monitoring of cell cultures in perfusion-based bioreactors (**Paper VII**). In the 3T configuration (Figure 3.12C,D), one electrode is common between the *CC* and *PU couple* (i.e. the *working electrode*, *WE*, Figure 3.12C). In other words, the *WE* is the only *CC electrode* that is within the sensitivity zone for the measurement (Figure 3.12D) and hence, the measured impedance is affected by its Z_p (which also reflects the sample volume in its close proximity, Figure 3.12D), as is discussed in **Paper V**. In **Paper V**, I use different 2T and 3T configurations and Au plate electrodes to investigate the dynamics involved in the whole process of 3D cell culturing from polymerisation of a bare gelatin-based scaffold to encapsulation and proliferation of mesenchymal stem cells (MSCs). By switching between different combinations of electrode couples (sensing modes), it is possible to generate a multiplexing-like approach, which allows for collecting spatially distributed information within the 3D space. The influence of Z_p in 2T and 3T measurements was demonstrated by performing EIS analysis in physiological PBS containing an equimolar concentration of the ferri-/ferrocyanide ($\text{Fe}(\text{CN})_6^{3-/4-}$) redox couple. Figure 3.13A shows the effect of one 550 Ω resistor added in series to the *WE* in a 2T or 3T configuration. Since in a 2T configuration the measured impedance includes Z_p at both electrode surfaces, the Nyquist plot is shifted by 550 Ω when the resistor is added to either the *WE* and the *CE* (Figure 3.13Aa). Using a 3T configuration, Z_p affects only the *WE* and, accordingly, the Nyquist plot is shifted by 550 Ω only when the resistor is added to the *WE* (Figure 3.13Ab). Figure 3.13B shows the effect of *CE* modification with a negatively charged self-assembled monolayer (SAM) of sodium 3-mercaptopropyl-1-propanesulfonate (MPS). As the potential is applied between the *WE* and the *CE*, when the *CE* is functionalised with thiols, it repels negative ions from the $\text{Fe}(\text{CN})_6^{3-/4-}$ couple. After MPS modification of the *CE*, there is a significant increase of R_{CT} using the 2T configuration (Figure, 3.13Ba). On the other hand, if the *CE* is modified with MPS in a 3T configuration (Figure, 3.13Bb), the Nyquist plots before and after functionalisation are superimposable as the measurement is carried out between the *WE* and the *RE*.

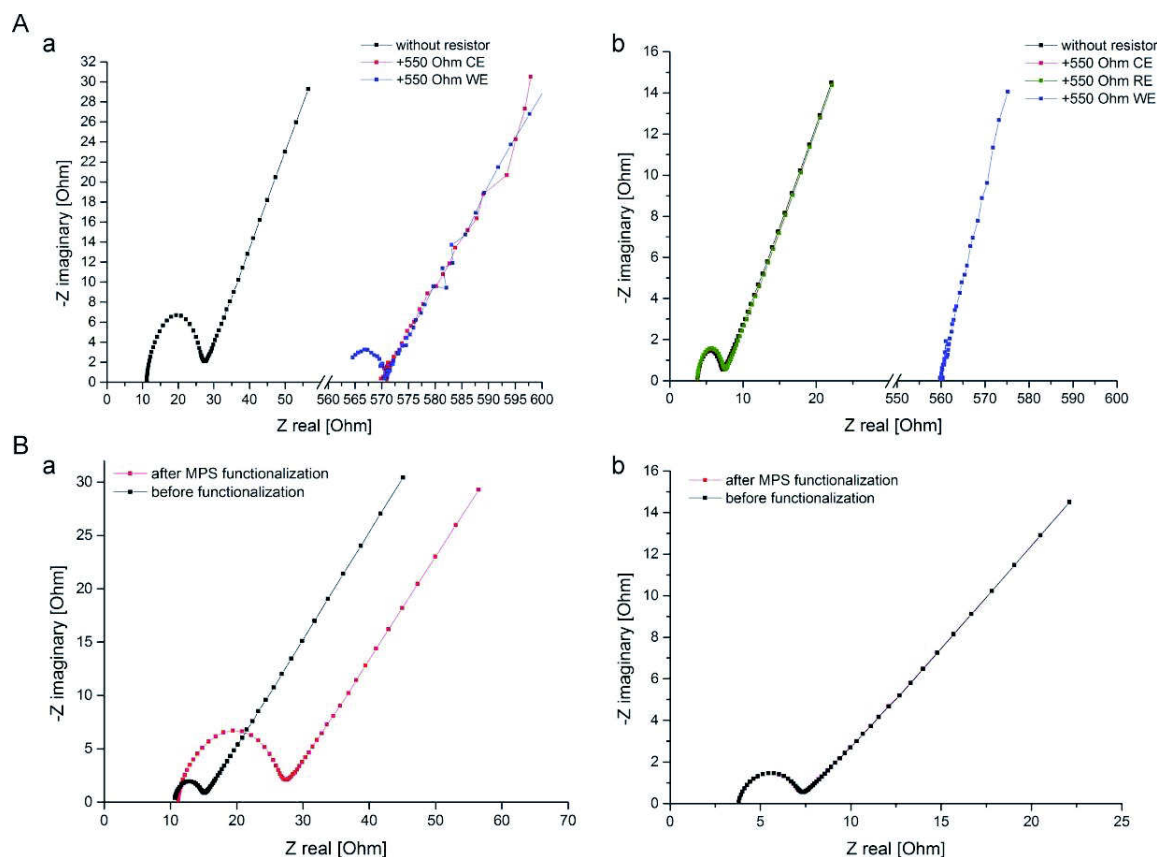


Figure 3.13 Influence of Z_p on 2T and 3T measurements (**Paper V**). (A) Effect of one 550 Ω resistor added in series to the WE in a (a) 2T or (b) 3T configuration. – (B) Effect of the CE modification with a negatively charged SAM of MPS in a (a) 2T or (b) 3T configuration.

In the 4T configuration (Figure 3.12E, F), two separate couples of *CC* and *PU electrodes* are used. This configuration theoretically eliminates all Z_p contributions; hence it is typically used for samples having low impedance (i.e. less than few $k\Omega$, which would otherwise be obscured by Z_p) [224] and for physiological measurements, where a specific focus on mere properties of the biological sample is needed. In 4T measurements the *CC couple* is placed outside the sensitivity zone for the measurement (Figure 3.12F) and, hence, the measured impedance is not affected by Z_{pCC} . The *PU electrodes* measure the potential which results from the injected current. The impedance given by the ratio between the measured potential and injected current is a *transimpedance*, i.e. the ability of the *PU electrodes* to sense the injected current, which is dependent on both the *impedivity* of the sample (i.e. the property of ‘actual’ impedance) and the measurement setup geometry. *Transimpedance* applications to biological samples are commonly referred to as *bioimpedance*. On virtue of ideal voltage amplifiers for

impedance analysis, *PU electrodes* are not current carrying (Figure 3.14) so that Z_{pPU} does not contribute to the measured impedance (Figure 3.12E). Modern voltage amplifiers (Figure 3.14) have input impedance (Z_{amp}) in the $G\Omega$ range, meaning that they allow measuring impedance values up to the $M\Omega$ level without the sensitivity field being influenced by Z_{pCC} . This further explains why, in 4T configuration, the sensing is not influenced by Z_{pCC} even when the *CC* and *PU electrodes* are close to each other [191,222,225].

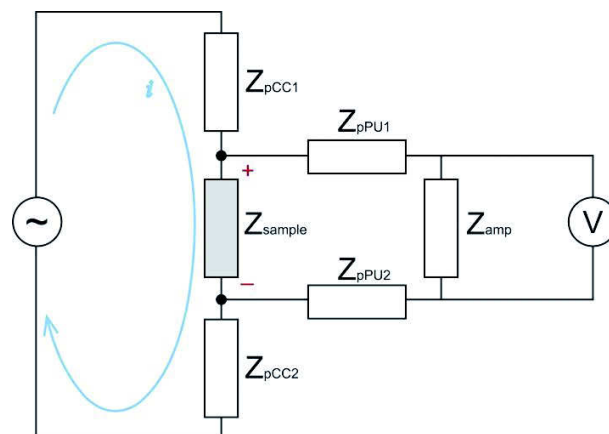


Figure 3.14 | Schematics of a 4T measurement. The sensing is focused on the sample as the *CC couple* is placed outside the sensitivity zone for the measurement and the *PU couple* is not current-carrying. This means that the measured impedance is approximately the impedance of the sample (Z_{sample}). Z_{pCC} and Z_{pPU} are the *polarisation impedance* of the *CC* and *PU electrodes*, respectively. Z_{amp} is the input impedance of the voltage amplifier.

In **Paper VI**, I show multiplexed 4T impedance measurements for sensing the spatial location of cell aggregates within large gelatin-based 3D scaffolds using different couples of *CC* and *PU electrodes*. The use of needle electrodes facilitates the placement in the small measurement chamber and allows increasing the electrode number, due to their smaller size compared to plates. Increasing the number of electrodes increases the number of possible electrode combinations (sensing modes) with a higher degree of 3D spatial information. In light of this concept, in **Paper VIII** I apply 4T impedance measurements for EIT image reconstruction (Chapter 4) of small 3D test objects placed in a miniaturised chamber with integrated vertical electrodes. The chosen number of electrodes and consequently number of electrode configurations aims at maximising the quality of image reconstruction while minimising the number of required measurements. This is significant when designing a technique suitable for tissue engineering applications where time-based monitoring of cellular behaviour in 3D scaffolds is of interest.

3.2.3 The Reciprocity Theorem and Sensitivity in Impedance Measurements

The reciprocity theorem is a general principle, which holds for all *linear systems* and was first described by Hermann von Helmholtz over 150 years ago. In the early days of impedance analysis it was erroneously understood that the measured impedance only reflects the *impedivity* of the sample. However, in general terms, the reciprocity theorem states that the ratio between an alternating potential and current (i.e. the *transimpedance*) is unchanged if one interchanges the sites where the current is injected and the potential is measured [226]. As *transimpedance* depends on both *impedivity* of the sample and the measurement setup geometry, it can be used for calculating the sample properties as conductivity (σ), resistivity (ρ) and relative permittivity (ϵ_r) only for homogeneous and uniform materials [225]. This implies that for a biological sample of complex composition:

- The measurement sensitivity must be affected with some amount by all the small sub-volumes (i.e. *voxels*) in the sample (each of them displaying its own resistivity);
- The *voxels* of the sample do not all equally contribute to the total measured impedance;
- The sample should behave similarly close to both the electrode couples;
- The *voxels* between the electrode couples and close to the electrode couples contribute more than the *voxels* far away from the couples [225].

As defined from Ohm's law, the resistivity ρ is the proportionality constant between the voltage, U , and the current density vectors, \mathbf{J} . For an isotropic sample, where the *impedivity* is uniform in all the orientations, \mathbf{J} is the product of the conductivity of the sample and the electric field. The *transimpedance*, Z , can be written as the following volume integration (dv):

$$Z = \iiint \rho \frac{\mathbf{J}_{CC} \cdot \mathbf{J}_{PU}}{I_{CC} \cdot I_{PU}} dv \quad (3.23)$$

This means that the total measured impedance is the sum of all the local resistivity values of each *voxels* in the sample [223].

The measurement sensitivity (S) is the scalar value [m^{-4}] representing the projection of the CC current density vectors on the PU current density vectors [227,228] (e.g. Figure 3.15). S is affected to some extent by all the *voxels* in the sample but it is independent on ρ , as explained above.

$$S = \frac{\mathbf{J}_{CC} \cdot \mathbf{J}_{PU}}{I_{CC} \cdot I_{PU}} \quad (3.24)$$

S is a positive (or negative) value if measured impedance increases (or decreases) when the *impedivity* of that region increases. This may be clearly seen by drawing the current density vectors \mathbf{J}_{CC} and \mathbf{J}_{PU} between the *CC* and *PU* electrode couples [226]. If they are:

- In the same direction, $S > 0$ (as the angle between the two vectors is acute);
- Superimposed, $S = S_{max}$ (as the angle between the two vectors is 0 and this is the case for 2T measurements);
- In the opposite direction, $S < 0$ (as the angle between the two vectors is obtuse);
- Perpendicular, $S = 0$.

In 2T measurements, CC and PU current densities are identical, therefore:

$$Z = \iiint \rho |\mathbf{J}|^2 du \quad (3.25)$$

and:

$$S = |\mathbf{J}|^2 \quad (3.26)$$

If the sample is homogeneous, ρ can be placed outside the integration sign in Eq. 3.23 and hence the contribution of the impedance each *voxel* to the total impedance is simply a function of $|\mathbf{J}|^2$. In general, the variation of S in the space is referred to as ‘sensitivity field’.

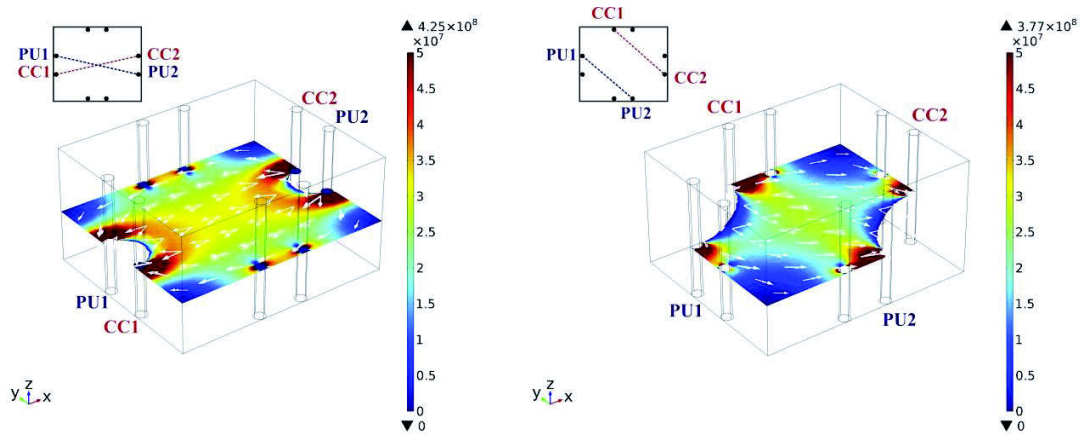


Figure 3.15] FE simulations of S [m^{-4}] distribution (slice view) for two different 4T combinations of vertical needle electrode couples (geometry is presented in **Paper VI**). White arrows are the current density vectors between the *CC* and *PU* electrode couples. White areas in the horizontal cross-sections are associated with negative sensitivity. – Inserts at the top left of each FE model show top-view schematics of the 4T sensing modes. Red and blue dashed lines represent the directions of CC and PU electric fields, respectively.

3.2.4 Finite Element Analysis

It may be challenging to realise impedance measurement setups of experimental relevance. The measurement setup should be able to detect a specific property or phenomenon with sensitivity. This issue is mainly centred on tailoring parameters such as the electrodes number, spacing and orientation in order to maximise S . One way to tackle this matter may be to build and test a number of different setups and then choose the one showing the best S to the impedance analysis. However, this would obviously be time- and resource-consuming. A valid alternative is the use of *FE analysis* to simulate impedance measurements and evaluate how much S is affected by the resistivity of each *voxel* in the sample. Such an approach entails the solution of a '*forward problem*', i.e. the calculation of the electrical voltage distribution when the signal source and the resistivity distribution within the sample are known [229]. The *forward problem* is a mathematical problem for which (i) a solution exists, (ii) the solution is unique and (iii) the solution behaviour changes together with changes in the initial conditions. This means that small errors in the input data result in small errors in the solution of the problem (i.e. the *forward problem* is a *well-posed problem*).

FE models for solving the *forward problem* are generally idealised to static DC systems without polarisation phenomena and frequency dependence. Therefore, in such a case, the potential difference between two points in the sample (Φ_{12}) is equal to the voltage difference found between two electrodes connected to those two points, $\Phi_{12} = V_{12}$ [223,230]. Any problem concerning the distribution of current or electric field in a homogeneous or composite material can be solved using the four Maxwell's equations (Table 3.1) if the excitation and the electrical properties of the materials are known. Therefore, Maxwell's equations can describe the behaviour of any system during impedance measurements [176,191]. When solving differential equations, as Maxwell's equations, there are generally two different types of problems to be solved:

- Initial value problems, when the unknown function is given at a specific point (e.g. at a time, and the values at future times need to be calculated);
- Boundary value problems, when the unknown function is given at the boundary of a material, and the inner values are to be computed.

Table 3.1 Maxwell's equations. \mathbf{E} = electric flux density; q = charge [C]; q_v = charge density [C/m^3]; ϵ_0 = permittivity of free space; \mathbf{B} = magnetic flux density [$V \cdot s/m^2$]; \mathbf{H} = magnetic field strength [A/m], \mathbf{J}_r = current density of free charges [A/m^2], \mathbf{D} = displacement field flux [C/m^2]. The table is reprinted from [206] with permission.

Eq.	Differential form	Explanation by integral
3.27	$\nabla \cdot \mathbf{E} = \frac{q_v}{\epsilon_0}$	Gauss law: Flux of \mathbf{E} through a closed surface = net enclosed charge/ ϵ_0
3.28	$\nabla \times \mathbf{E} = \frac{-\partial \mathbf{B}}{-\partial t}$	Faraday's law of induction: Line integral of \mathbf{E} around a loop = - rate of change of flux of \mathbf{B} through the loop
3.29	$\nabla \cdot \mathbf{B} = 0$	Gauss law for magnetism: Flux of \mathbf{B} through a closed surface = 0
3.30	$\nabla \times \mathbf{H} = \mathbf{J}_r + \frac{\partial \mathbf{D}}{\partial t}$	Ampère's law: Line integral of \mathbf{H} around a loop = current density of free charges through the loop + rate of change of flux of \mathbf{D} through the loop

Boundary value problems are the common situation in *bioimpedance* [231,232], EIS [176] and EIT applications [233–235], where the current (or voltage, or conductivity, etc.) distribution in a sample is to be computed from a given excitation applied through the electrode surfaces. The typical approach to tackle boundary value problems involves two consecutive steps:

1. Divide the space of the problem into a collection of sub-spaces (*mesh elements* or *voxels* for 3D geometries), where each sub-space is represented by a set of element equations related to the original problem;
2. Systematically recombine all sets of element equations into a global system of equations for the final calculation. The final calculation is the weighted sum of all the element equations.

This means that a set of differential equations is used in each *mesh element* to compute the weight equation for solving the boundary problem. Each calculation introduces a small error to the final calculation but, in the ideal case, the error diminishes as the number of *mesh elements* is increased. High quality *meshes* can be crucial for the accuracy of the obtained solution and several factors need to be taken into account, such as the quality and the number of elements in the *mesh*. The quality of the *mesh* should be optimised prior to computing the approximate solution. This can reduce the time taken to compute the solution and increase the solution accuracy [236]. *Mesh* optimisation entails the minimisation of errors until the

asymptotic convergence of the equation results [237–239]. However, in the case of *ill-posed problems* the situation may be far more complicated. *Ill-posed problems* are usually tackled for image reconstruction in EIT (Chapter 4) and are problems where a small error in the initial data can result in much larger errors in the final calculation [240]. This means that, in such a case, there is no guarantee that the sum of an increasing number of *mesh elements* introduce a small error to the final calculation in the *FE analysis*.

In order to reduce the time for computation while obtaining an accurate representation of the impedance measurement, it is important to define the real system in the simplest possible way when building the *FE model*. Hence, a 3D system may be reduced by symmetry, or a purely DC- resistive model may be used to simulate *transimpedance*. In order to calculate the local contribution of each *mesh element* to the measured *transimpedance*, it is possible to weight S for the resistivity contribution of all the elements. When applying such an approach to a 3D sample, we obtain the so-called ‘volume impedance density’ (VID) [223]. VID is the integration of S over the entire sample volume and, accordingly, it corresponds to the expression that defines the *transimpedance*, Z (Eq. 3.23).

Figure 3.15 shows some examples of *FE analysis* in impedance measurements that I performed during my Ph.D. project. Figure 3.15Ab shows S distribution for planar interdigitated electrodes (IDEs, Figure 3.15Aa) and Figure 3.15Bc is the simplified 2D *FE model* of the potential distribution in a 3D porous scaffold soaked in physiological PBS (Figure 3.15Bb) using 2T measurements and the setup shown in Figure 3.15Ba (**Paper III**). Figure 3.15Cb,c shows S distribution for 2T impedance measurements performed in the perfusion bioreactor in Figure 3.15Ca containing the porous scaffold shown in Figure 3.15Bb (**Paper IV**). The model accounts for the influence of the cell culture medium flow through the scaffold on the S of the impedance measurements.

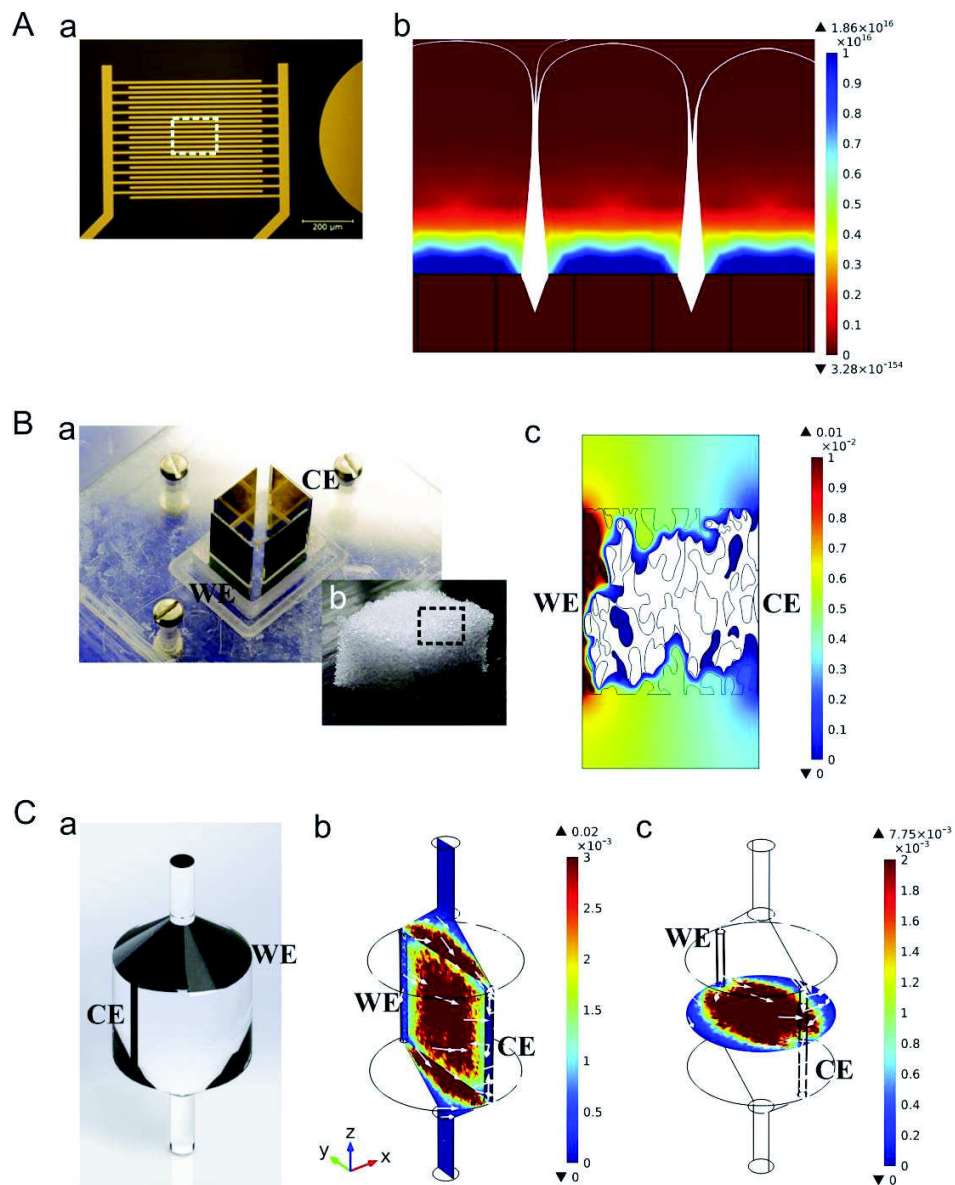


Figure 3.15 Examples of *FE analysis* applied to impedance measurements. (A) (a) Image of a 2D setup with IDEs (top view) and (b) simulation of S (m^{-4} , zoom in on the side view). Streamlines for the current density through the cell culture medium on top of the electrodes are reported in white. – (B) (a) Photograph of the electrode setup used for 2T measurements of (b) a porous 3D scaffold soaked in physiological PBS. (c) Simplified 2D simulation (top view) of the electric potential distribution during the measurements (**Paper III**). – (C) (a) CAD rendering of a perfusion bioreactor with integrated vertical needles for 2T impedance measurements housing a porous 3D scaffold (**Paper VII**). Simulation of S (m^{-4}) in the (b) xz plane and (c) xy plane. The model accounts for the influence of the cell culture medium flow through the scaffold ($3.3 \mu\text{L}/\text{min}$, bottom to top) on the impedance measurements.

CHAPTER 4

Electrical Impedance Tomography

Electrical impedance Tomography (EIT) is an imaging technique based on multiple impedance measurements between several electrode couples to map the electrical properties (e.g. conductivity, σ , or permittivity, ϵ) of a sample. Its first use goes back to 1930s when Conrad and Marcel Schlumberger showed that electrical measurements taken in boreholes could help identifying the geological formations in their proximity. They also found that, by varying the electrodes spacing, the measured resistivity is indicative of different depths within the ground [241–244]. Regardless of the approach used, EIT is currently applied in different fields, spanning from geological studies [241] (Figure 4.1A) and industrial applications [245,246] to medical research and diagnosis [247] (Figure 4.1B).

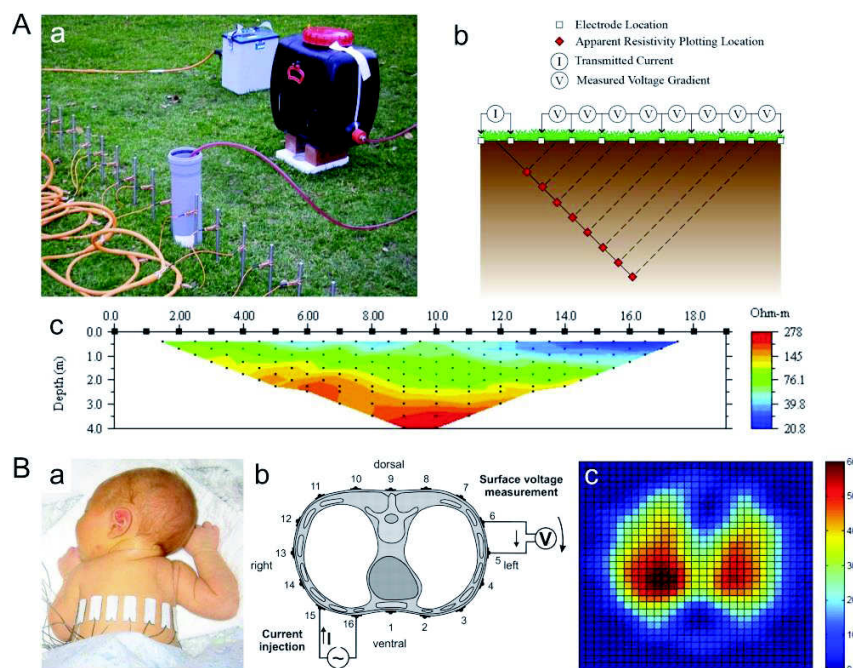


Figure 4.1 Examples of EIT applications. (A) Geophysical studies (www.epa.gov): (a, b) example of setup and (c) map of the resistivity distribution in the ground. – (B) Non-invasive monitoring of lung ventilation in infants: (a, b) setup [248,249] and (c) image reconstruction [250]. High ventilated regions are shown in red, low ventilated regions are in blue.

The application of EIT as a medical imaging technique is usually attributed to Ross P. Henderson and John G. Webster [251], although the first medical EIT system was realised by

David C. Barber and Brian H. Brown in 1984 [252]. Together, Barber and Brown published the first electrical impedance tomogram showing the cross section of a human forearm in 1983 [253]. Since then, incredible progress has been made in developing new EIT methods, configurations and measurement devices as well as in defining optimised signal processing algorithms. Presently, Jari Kaipio, Erkki Somersalo and Marko Vauhkonen are focusing their research in the field of *inverse problems*, with emphasis on computational and statistical aspects of image reconstruction in EIT [254,255]. In the same field of applied mathematics, Bill Lionheart and Andy Adler are actively working on the design of more effective reconstruction algorithms for EIT applications [256,257]. Furthermore, Adler's research also focuses on optimisation of electrode configurations [258,259] and application of EIT for monitoring lung [260] and heart [261] functions. In the field of EIT imaging of brain activity, Richard Bayford and David Holder [262] have demonstrated the capability of this technique to provide a new portable imaging solution which could transform the management of pathologies as acute stroke [263] and intractable epilepsy [264]. Recently, Holder and collaborators showed that EIT can provide images of fast electrical activity in the brain with a resolution of milliseconds [265]. This method may open new perspectives in understanding how the information is processed in the brain. Aside from such experimental applications, two commercial dynamic EIT devices for monitoring lung function in intensive care patients have been introduced on the market in 2001 (PulmoVista® 500, Dräger, Lübeck, Germany) and 2010 (Enlight®, Timpel, São Paulo, Brazil). Up to date, about twenty different designs of EIT setups have been constructed since 1983, which may employ (i) current injection through adjacent [266,267], opposite [268] or offset-opposite [269,270] pairs of electrodes; (ii) 2D or 3D imaging [271–273]; and (iii) measurements based on 2- or 4T electrode configurations [274,275].

In the most conventional EIT approach, low-amplitude alternating current (AC) is injected at single or few frequencies through different electrode pairs and voltages are consecutively recorded by all remaining pairs on the sample surface using the 4T method introduced by Schwan in 1963 [164]. This allows impedance measurements with minimised influence of *electrode polarisation* (Z_p) [276]. For most physiological measurements, an AC current at above 10 kHz is used as there is less risk of exciting nerves without affecting electrode stability. When the current is injected across a conductive and heterogeneous biological sample such as a tissue or organ, it flows in 3D mainly between the electrodes. The current

invests all the parts of the sample with different extents depending on the different conductivities of the parts. Several impedance measurements are made between electrode pairs placed on the sample's boundary (Figure 4.1Aa and Ba; Figure 4.3), each measurement representing the impedance of the sample weighted according to the current flow distribution [277]. Both impedance and changes in impedance (with time or frequency) can be imaged. In the first case, 'absolute' (or 'static') images are obtained by mapping the absolute conductivity distribution of the sample based on one single set of measurements [278]. Because of this, absolute EIT (a-EIT) is extremely prone to errors, which may derive from uncertainty of electrode position and errors in the computational models, including boundary geometry. On the other hand, when mapping dynamic changes in impedance, the change in resistivity can be measured at two different time points ('time-difference EIT', t-EIT) [279], or at two or more different frequencies ('frequency-difference EIT', f-EIT) [280]. It is important to notice that the impedance of biological tissues changes slowly with frequency, so that most f-EIT applications require a comparison across a frequency range of 6 – 7 orders of magnitude, where large impedance changes are expected. However, a confounding factor is that the background impedance also changes significantly with frequency, leading to small differential impedance changes [281].

The main advantages of EIT are non-invasiveness, low cost and good temporal resolution [277,282]. Such features have promoted the successful application of EIT in medicine for screening a number of disease conditions such as breast cancer [283,284] and stroke [285,286] as well as monitoring brain function [287,288], lung ventilation [289,290] and gastric emptying [291,292]. However, for two main reasons, EIT has not been routinely used in everyday clinical practice, yet [293]. First, EIT displays relatively poor spatial resolution (approximately 15% of electrode diameter compared to 1 mm in computed tomography and magnetic resonance imaging), which is further decreased in the regions that are more distant from the electrode array [269]. Secondly, in EIT the *inverse problem* is *ill-posed* (i.e. small errors in measurements may cause larger artefacts in the reconstructed image), making the method sensitive to noise [294,295]. Artefacts may be reduced to produce smoother images by (i) using algorithms for image regularisation [296]; (ii) adjusting the amplitude of the injected current and optimising the electrode (iii) number and (iv) configuration (and, hence, the current patterns for the impedance measurements) to achieve the best sensitivity distribution for the impedance measurements in a reasonable time of analysis [297,298].

Increasing the electrode number enables to improve the image quality as it improves the *ill-posed* condition in image reconstruction (Figure 4.2). Additionally, several examples of electrode configurations have been investigated [268,269] and two examples are described in Section 4.1.

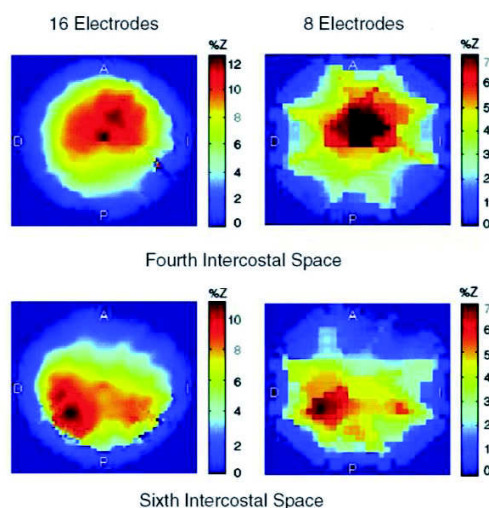


Figure 4.2] Example of study concerning the minimum number of electrodes and their position on the human thorax required to reconstruct an EIT image that allows the estimation of single lung function [299]. Comparison of images reconstructed with 16 (*left*) and 8 (*right*) electrodes placed at the fourth (*top*) and sixth (*bottom*) intercostal spaces. De Lema et al. showed that the 8-electrode image was of poor quality with regard to thoracic morphology, but there were no statistically significant differences in single lung function information between results calculated with 16 or 8 electrodes. Concerning the determination of the optimal intercostal space for EIT analysis, the reconstructed images at the fourth intercostal space showed more artefacts than those at the sixth intercostal space, making monitoring of single lung function at the fourth intercostal space difficult or impossible. The image is reprinted from [299] with permission.

Although the first medical applications of EIT started already thirty years ago on human organs of tens of centimetres in diameter [253], only a few *in vitro* applications have so far been developed for monitoring cell cultures. Linderholm et al. [300] mapped the migration of cells in culture during epithelial stratification using an array (5 μm x 4 mm) of 16 linear electrodes. The cultured cells were adherent on the electrodes, modulating the interface impedance. Rahman et al. [301] used EIS to map *in vitro* cellular morphology in 2D cultures using a circular microelectrode array with 8 peripheral electrodes and a central counter electrode. Sun et al. [302] imaged a multi-nuclear single cellular mould, *Physarum polycephalum*, grown on a 2D chip consisting of 16 equally spaced electrodes placed at the periphery of a 6 mm culture chamber (Figure 4.3A). Meir and Rubinsky [303] presented a preliminary mathematical model for EIT imaging of a single electroporated cell using

simulated data. Recently, Lee et al. [304,305] optimised new electrode configurations and a customised algorithm based on the back-projection approach that can be potentially used for monitoring 3D tissue cultures. These were tested using a 3D agar scaffold with test objects placed in a cuboidal measurement chamber ($2.4 \times 4.8 \times 2.4 \text{ cm}^3$, Figure 4.3B). Additionally, performed numerical simulations showed the possibility for further miniaturisation of the setup.

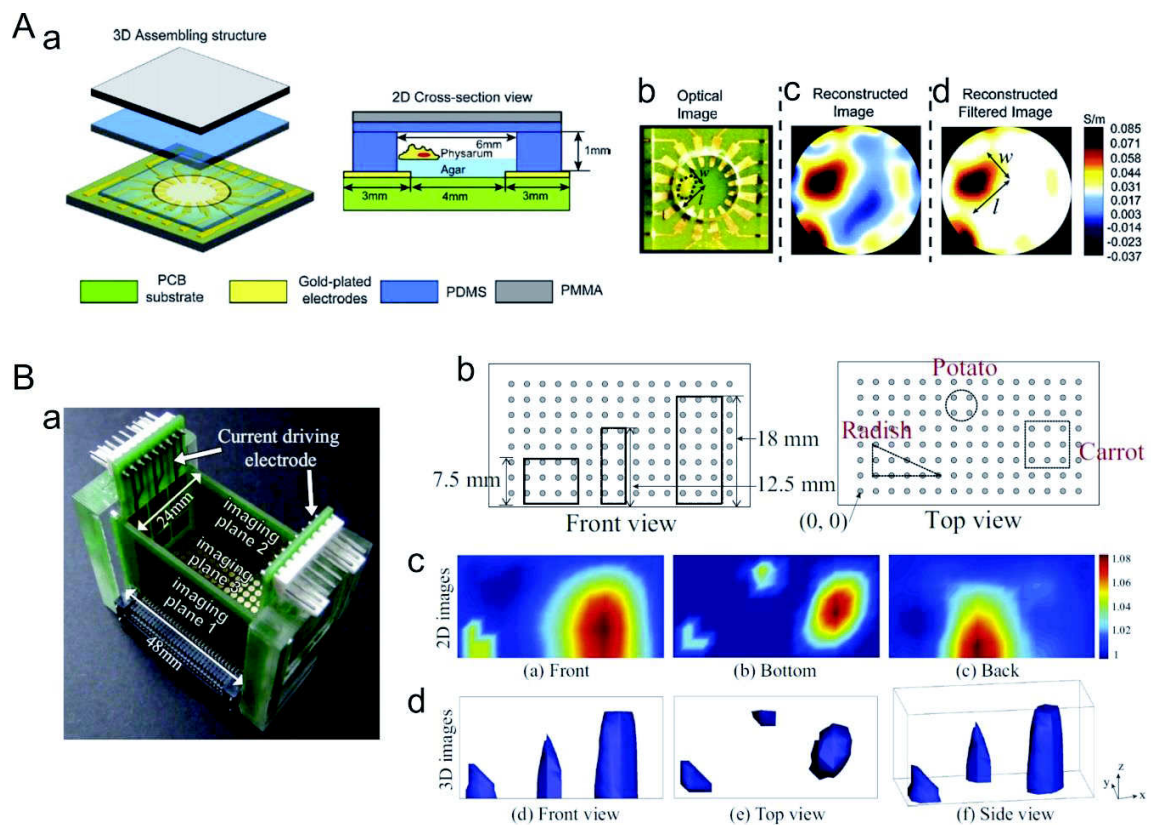


Figure 4.3| (A) (a) Structure and cross-section of the EIT chip used to image a 2D culture of *Physarum polycephalum* by Sun et al. [266]. (b) Picture of *P. polycephalum* grown on agar gel on the EIT chip, (c) corresponding reconstructed image and (d) filtered image where the ‘ghost images’ are removed by filtering the low conductivity regions. The *P. polycephalum* cell is more conductive than the agar gel, exhibiting a brighter red region in the reconstructed image. The image is reprinted from [266] with permission. – (B) (a) Sample container designed for potential 3D tissue culture monitoring by Lee et al. [304]. (b) The system was tested using a 3D agar scaffold with biological objects (pieces of radish, potato and carrot). Images were reconstructed in (c) 2D and (d) 3D. The image is reprinted from [304] with permission.

4.1 Electrode Configurations in EIT

In the common practice, impedance measurements in EIT are performed using several combinations of 4T configurations to remove the influence of Z_p . The electrode number and

the current patterns are generally optimised to achieve the highest sensitivity field distribution within the sample in a reasonable time of analysis. Each current injection pattern in EIT has its own current distribution profile within the sample and, therefore, different current patterns show different sensitivity and spatial resolution. Image reconstruction studies with *phantoms* of known electric properties are crucial to validate a developed EIT system and compare different current injection methods [229,248,288,306,307]. In order to provide a theoretical background to the reader for better understanding of the work presented in **Paper VIII**, this thesis provides a specific focus on the ‘adjacent’ and the ‘opposite’ methods.

The ‘adjacent method’ (or ‘neighbouring method’) [308], is the simplest current driven pattern, where the current is injected through adjacent pairs of electrodes and the voltage is sequentially measured from all the other adjacent electrode pairs without including any of the *CC electrodes* [309]. Therefore, the measured voltage is maximum between adjacent electrode pairs, while the voltage is only ~ 2.5% of that value with opposite electrode pairs [310]. This implies lower distinguishability of the objects placed in the centre of the measurement chamber with better focus on the peripheral regions of the chamber [311]. Figure 4.4 shows the adjacent method for a cylindrical sample with an outer ring of 16 equally spaced electrodes [270].

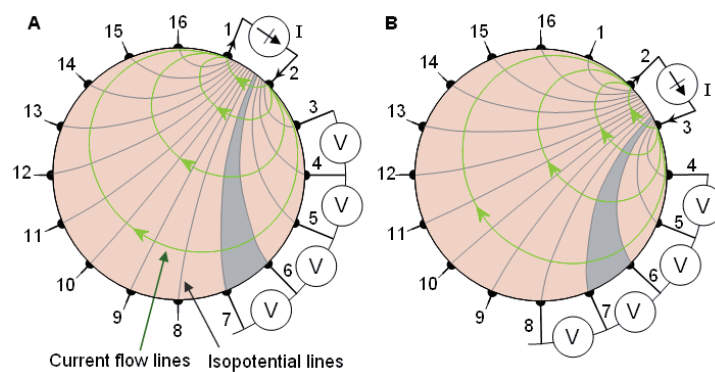


Figure 4.4| Adjacent method for a cylindrical sample with 16 equally spaced electrodes. (A) The current is first injected between electrodes 1–2. The current density is highest between these electrodes, rapidly decreasing as a function of distance. The voltage is sequentially measured between 3–4, 4–5, ..., 15–16 for a total of 13 independent measurements. Each measurement represents the impedance between the equipotential lines intersecting the *current carrying (CC)* and *pick-up (PU)* electrodes. – (B) The next set of 13 voltage measurements is obtained by injecting the current between electrodes 2–3. At the end, $16 \times 13 = 208$ voltage measurements are obtained. However, the measurements in which the *CC* and *PU* couples are swapped lead to identical impedance values due to reciprocity (Section 3.2.3). Therefore, only 104 measurements are independent. The image is reprinted from [270] with permission.

In the ‘opposite method’ (or ‘polar method’) [268,269,312], the current is injected through two diametrically opposite electrodes (16 and 8 in Figure 4.5). The adjacent electrode to the current-injecting electrode (electrode 1 in Figure 4.5) is used as the voltage reference for all the sequential voltage measurements. The voltage is measured from all the other electrodes except from the *CC couple*. The electrode arrangement used in the polar configuration provides a more uniform current distribution and better central (but not peripheral) sensitivity compared to the adjacent configuration [252].

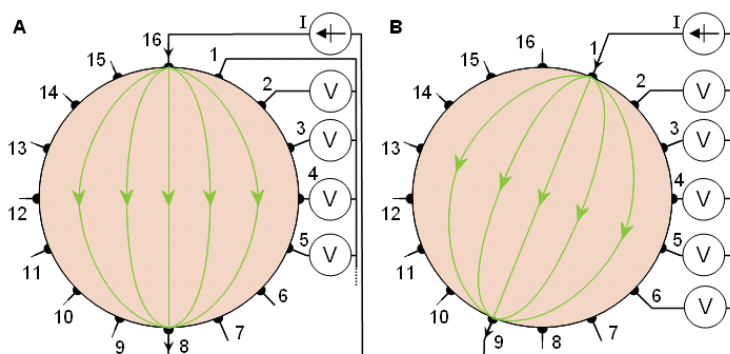


Figure 4.5] Opposite method for a cylindrical sample with 16 equally spaced electrodes. (A) The current is first injected through the electrodes 16–8. The voltage is sequentially measured between 1–2, 1–3, 1–4, 1–5, 1–6, 1–7, 1–9, ..., 1–15 for a total of 13 independent measurements. – (B) The next set of 13 voltage measurements is obtained by injecting the current through the electrodes 1–9. At the end, 104 independent measurements are obtained. The image is reprinted from [270] with permission.

4.2 Image Reconstruction in EIT

All methods for image reconstruction in EIT are based on the ‘sensitivity matrix’ approach [313,314], which uses a matrix (or table) relating the resistivity of each *voxel* in the sample to the recorded voltages [315] and requires setting up a computational *mesh* suitable for the solution. The *finite element (FE) method* is commonly used to solve the current flow equations in each *voxel*, so that the expected voltages can be calculated for each electrode combination [316]. Although the injected current flows through the entire sample, it flows more in certain sub-volumes than in others, depending on their conductivity. Therefore, each *voxel* in the sample contributes to the measured voltage at a specified *PU pair* with a different weight, depending on:

- Resistance inside the *voxel*,
- Amount of current reaching the *voxel*,

- Distance between the *voxel* and the *PU electrodes*.

Therefore, each *PU couple* is more sensitive to a certain sub-volume in the sample and the contribution from *voxels* located far away from the CC-PU couple may be negligible [317]. The total voltage at the *PU pair* is the sum of the contributions of all *voxels* weighted by the factor s , specific of each *voxel*. The s factor indicates how much effect a specified *voxel* has over the total voltage and it is used to generate the sensitivity matrix. The calculation of the voltage distribution (i.e. the predicted voltages) when the injected current and the resistivity distribution within the sample are known is the solution of the '*forward problem*' (Section 3.2.4, Figure 4.6) [229]. In its simplest form, the sensitivity matrix approach assumes that there is a linear relationship between the resistance of each *voxel* and its effect on the measured voltage, which is almost true for small changes in impedance (i.e. below $\sim 20\%$). However, this limit is usually exceeded in any physiological sample but this may be overcome by using more accurate nonlinear approaches (which are not the objective of this thesis). In general, accurate images can be produced, typically with a spatial resolution of $\sim 10\%$ of the sample's diameter [317].

Once the sensitivity matrix has been generated, the effect of the resistivity of each *voxel* on the total voltage can be obtained by mathematically inverting the matrix. This requires the solution of the '*inverse problem*', i.e. the calculation of the internal resistance of the sample, based on voltage measurements using a specified injected current (which is known) [229]. As the sensitivity matrix has been generated, the effect of each *voxel* on the total voltage is known. Therefore the s factor relating the resistance of each *voxel* to the measured voltage for each electrode combination is known as well. The solution of the *inverse problem* is achieved by mathematically inverting the sensitivity matrix, to obtain all the resistivities [317]. The optimal solution is given by the values that minimise the difference between the measured and predicted voltages (Figure 4.7), the latter of which has been obtained by solving the *forward problem*.

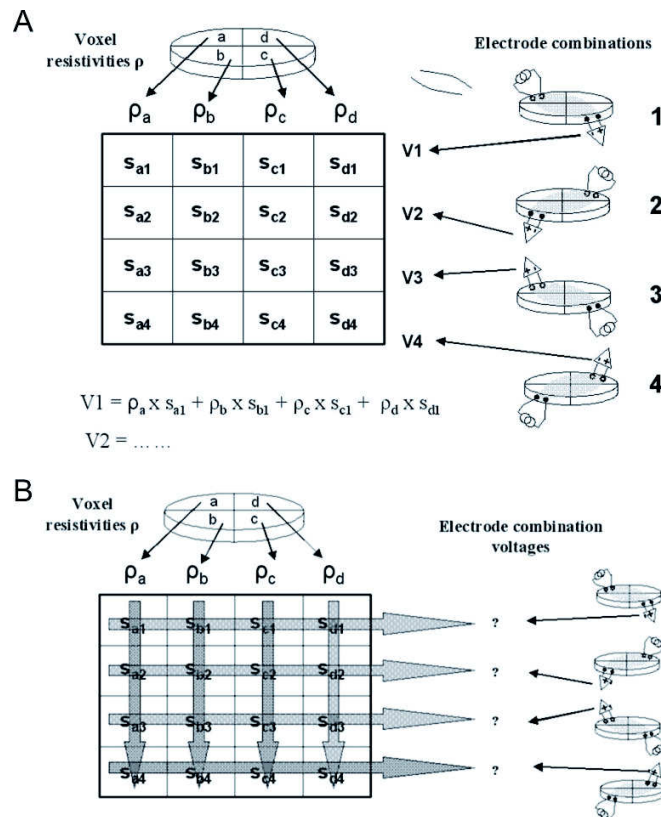


Figure 4.6] Solution of the *forward problem* in EIT. The sample is a disc where measurements are performed using only four electrode combinations, resulting in just four *voxels*. (A) Concept of ‘sensitivity matrix’: each column represents the resistivity of one *voxel* in the sample; each row represents the measured voltage for one combination of *CC* and *PU electrodes*. The injected current flows through the entire sample, but each *PU couple* is more sensitive to a certain sub-volume, shown in grey. The resulting voltage is the sum of the resistivities of all *voxels* weighted by the factor *s*, specific of each *voxel*. *s* indicates how much effect a specified *voxel* has over the total voltage and it is used to generate the sensitivity matrix. – (B) In a computer simulation, if the resistivities of all *voxels* are known, then the expected voltages for each combination of *CC* and *PU electrodes* may be calculated using *s*. The image is reprinted from [317] with permission.

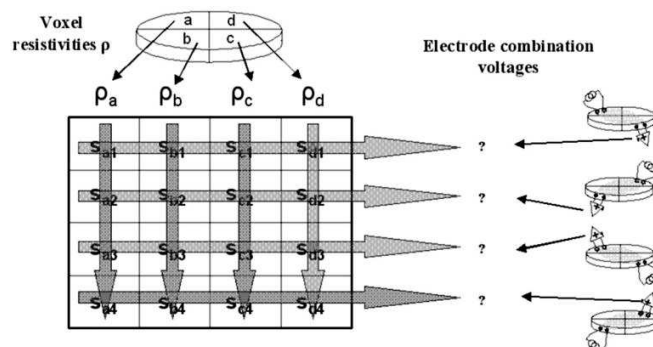


Figure 4.7] Solution of the *inverse problem* in EIT. The sample is a disc where measurements are performed using only four electrode combinations, resulting in just four *voxels*. The aim is to calculate the resistivities of all *voxels* once the voltages are known from the measurements. This can be achieved by mathematically inverting the sensitivity matrix presented in Figure 4.6. The image is reprinted from [317] with permission.

Theoretically, the solution of the *inverse problem* could give an absolutely accurate result. The accuracy of the result strictly depends on the accuracy of the input data, which is often, however, affected by experimental errors. In fact, the experimentally recorded voltages may be affected by noise. Moreover, the number of *voxels* associated with unknown conductivities chosen in the *forward problem* may not correspond to the real number of sub-volumes with varying conductivity within the sample. In addition to this, very little current passes through many of the *voxels*, making the factor s for those voxels (and the corresponding values in the matrix) approach zero. Division by such very small numbers causes instabilities in the mathematical solution, resulting in poor resolution of the reconstructed image or inability to reconstruct any image. For these reasons, the *inverse problem* is an *ill-posed problem*.

4.3 Software Algorithms for Image Reconstruction in EIT

In EIT, the *FE method* is generally used for solving the *well-posed* forward calculations [316], while the solution of the *ill-posed inverse problem* typically requires a nonlinear solver (i.e. a software algorithm that calculates the solution of a system of nonlinear equations) and need regularisation in order to obtain a unique and stable solution [318,319]. Most of the commercially available *FE* programs, as Comsol Multiphysics, are commonly used for solving the *forward problem* in *bioimpedance* measurements [230] (**Paper V** and **VI**), although they might also be applied for solving the *inverse problem* in EIT. However, *FE* programs are generally unsuitable for image reconstruction of physiological samples, which have complex and heterogeneous composition. The main reason is that their conventional approach of calculating the sensitivity matrix is not optimised *ad hoc*, and the electrode modelling is not accurate [320,321]. Only few applications in *phantom* experiments have been carried out using the Comsol Multiphysics suite [294,322–324] and the back-projection algorithm [253,325], which has been widely used as mathematical approach to build the sensitivity matrix in EIT applications due to its computational simplicity. The back-projection algorithm allows weighting the resistivity (ρ) of each *voxel* in the sample by the specific factor s (Section 4.2), accounting for (i) the current path between any CC-PU electrode pair and (ii) the difference between the *voxels* size. The current path can be mathematically related to the impedance measurement sensitivity distribution and found by solving the *forward problem* for a homogeneous medium [325].

More powerful suites of programs are often used in EIT. Among these latter, EIDORS finds a wide range of application fields [266,326,327] due to the open source architecture, which allows easier modification and customisation [320,328]. EIDORS is the acronym for ‘electrical impedance and diffuse optical tomography reconstruction software’ and its first version was released in 2000 by Vauhkonen et al. [255]. It implements a MatLab package for (i) 2D and 3D *mesh* generation, (ii) solving the *forward problem*, (iii) image reconstruction and display. The commercial programs RES2DINV and RES3DINV (GeoTomo LLC, Houston, USA) are widely used for 2D and 3D EIT surveys on geological regions of moderate complexity in geophysics [329]. Linderholm et al. [330] extended the application field of RES2DINV to impedance imaging of cell migration and epithelial stratification. Finally, several custom made algorithms [265,305,331,332] and methods [171] have been developed so far and there is still a continuous effort to improve the quality of their performance [333].

In **Paper VIII**, I explored the potential of electrical impedance tomography (EIT) for imaging miniaturised 3D samples, aiming at future applications in tissue engineering and 3D cell culturing. My work on EIT is the result of collaboration with electronic engineers and physicists from Prof. David Holder’s group at the University College London, who provided expertise and technical skills for image reconstruction. The analysis is performed in a miniaturised measurement chamber ($\varnothing = 10$ mm, $h = 10$ mm) where eight Au plated needle electrodes are vertically integrated along the perimeter and two alternative methods are presented. First, a computationally simple method based on the adjacent configuration and back-projection algorithm was evaluated. Comsol Multiphysics (AC/DC module) was used for solving both the *forward* and the *inverse problem* in t-EIT. Subsequently, a more elaborate method was verified. Such method uses the “polar-offset” configuration (a variant of the polar configuration [268], having an additional electrode at the centre of the chamber) and a customised reconstruction algorithm by Aristovich et al. [265] that was previously validated for EIT imaging of neural activity. The customised reconstruction algorithm gives the possibility of performing both t-EIT and f-EIT. All the *FE simulations* and impedance measurements on test objects leading to image reconstruction utilised an electrolyte having an ionic strength close to physiological solutions. The chosen number of electrodes and consequently number of electrode configurations aims at maximising the quality of image reconstruction while minimising the number of required measurements. This is significant when designing a technique suitable for tissue engineering applications where time-based

monitoring of cellular behaviour in 3D scaffolds is of interest. The results outline the potentials of the two different EIT approaches in miniaturised 3D systems suitable for tissue engineering applications. The adjacent configuration and back-projection algorithm, which shows applicability for t-EIT imaging of conductive test objects, can provide a simple approach for faster screening of cell behaviour in conductive scaffolds for, e.g., cardiac [334] and neural tissue engineering [335]. The “polar-offset” configuration and the customised algorithm, sensitive to non-conductive objects, can provide means to monitor tissue engineering processes in more conventional polymeric scaffolds loaded with cells. Considering the heterogeneity of such cell loaded scaffolds, f-EIT may provide better images due to differential frequency-dependence between the scaffold material and cells. However, as f-EIT can only be approximated to a linear mathematical problem for impedance contrasts less than 20%, which is usually exceeded in any physiological sample, the f-EIT approach will be further tested and optimised for monitoring tissue engineering processes. On the other hand, for imaging the process of scaffold biodegradation, analogous to the behaviour of, e.g., starch-leaking potato *phantoms*, t-EIT may be a more suitable solution. Figure 4.8 shows the result of the t-EIT method based on the adjacent configuration and back-projection algorithm using Comsol Multiphysics, which I personally developed.

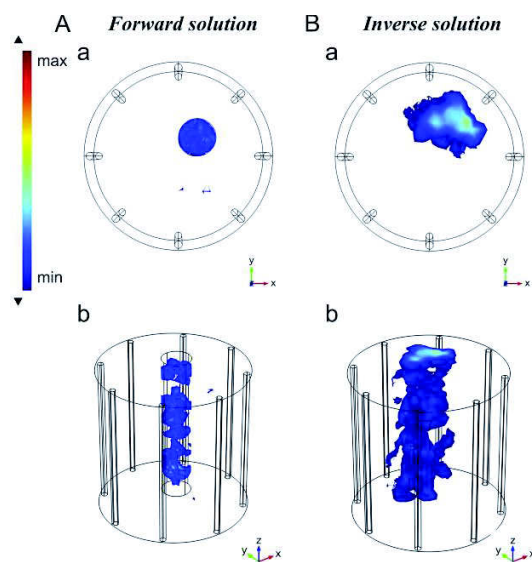


Figure 4.8| t-EIT using the adjacent configuration and the back-projection algorithm (Comsol Multiphysics) for a cylindrical stainless steel object (\varnothing 2 mm and h 10 mm) in a miniaturised measurement chamber (\varnothing and h 10 mm; eight Au plated electrodes with \varnothing 0.4 mm and h 10 mm along the periphery) filled with electrolyte of $\sigma = 1.3$ S/m (**Paper VIII**). (A) Computation of the *forward problem* and (B) solution of the *inverse problem*; (a) top view and (b) isometric view. The colour scale gives a qualitative representation of the test object impedance.

CHAPTER 5

Conclusions

The major aim of my Ph.D. project was to develop and explore the potential of impedance-based methods for non-invasive real-time monitoring of different stages involved in tissue engineering processes. The main challenge was to build non-invasive sensing methods for future application in simultaneous monitoring of the 3D environment and cellular properties during the development of tissue constructs, including scaffold properties, cell aggregates spatial distribution and cell proliferation. Impedance may offer significant advantages on conventional microscopy techniques that function well for thin, optically transparent cell cultures but would require thorough optimisation for 3D constructs. Cell culture scaffolds may be thick and highly scattering, preventing light from penetrating without significant distortion. Moreover, imaging techniques as confocal and multiphoton microscopy require well-trained personnel, able to adjust important parameters, such as the optical contrast, the resolution and the light penetration depth avoiding damaging the sample. Finally, the main conditions for real-time monitoring are the availability of 3D culture systems having compatible size with such instrumentation and the ability to keep sterile conditions during the analysis. In such a context, impedance-based methods may provide an alternative or synergic approach for non-invasive monitoring of the 3D environment.

My work demonstrated that impedance measurements can form the basis for: (i) accurate determination of conductivity in a 3D environment; (ii) scaffold characterisation in terms of hydrogel polymerisation and degree of porosity; (iii) monitoring of cell loading and spatial distribution of cell aggregates in 3D; (iv) integration of electrodes in perfusion bioreactors for real-time impedance-based monitoring of cell proliferation; and (v) investigation of electrical impedance tomography (EIT) as a potential method for image reconstruction in miniaturised 3D culture chambers with possible future applications in tissue engineering. Special emphasis was placed on the effect of the electrode configurations and their 3D arrangement in impedance measurements to achieve 3D spatial information. This objective was addressed using *finite element (FE)* simulations, electrochemical validation, *phantom* experiments mimicking cell aggregates and cell-based experiments.

The key element, which is common to all the methods that I have presented in this thesis, is the conductivity of the 3D environment, which is reflected in impedance measurements. The conductivity of a physiological solution or cell culture medium is modified when a porous structure as a scaffold is introduced. When cells are seeded on such a structure, they may or may not form a uniform population inside the scaffold volume and proliferate over time. Due to their membrane, they behave as insulating particles that decrease the overall conductivity of the 3D environment, thus increasing the measured impedance. Different sub-volumes of the environment are associated with different impedance values, depending on the scaffold properties and the cell concentration in those zones. Moreover, cell proliferation, death and metabolism further contribute to change the medium conductivity over time.

I established and verified a universal protocol for quick conductivity determinations using electrical impedance spectroscopy (EIS), electrode modification and automated spectral analysis. It allows running reproducible conductivity determinations in physiological solutions, cell culture medium and protein-containing solutions. The approach relies on simple spectral analysis to determine the frequency at which the phase angle is closest to 0° . The impedance magnitude at that frequency corresponds to the solution resistance (R_s), which can be used to calculate the conductivity. This protocol eliminates the need for evaluating a specific equivalent circuit using nonlinear regression which is generally required in EIS-based conductivity determinations. Unlike commercial instruments, typically operating at a few predetermined frequencies, which, depending on the solution composition, may not yield an accurate estimation of R_s , my universal protocol, based on analysis of complete spectra, has the advantage that R_s , and consequently the corresponding conductivity, can be determined with certainty independent of the solution composition. The validity of the protocol was extended to bio-applications by applying an optimised electrode modification method using a protein-repellent coating of poly(ethylene glycol) methyl ether thiol. This allowed precise and reproducible conductivity determinations without influence of electrode fouling in protein-containing solutions, such as cell culture medium.

I also demonstrated that EIS measurements, used to calculate the conductivity of the medium filling the pores of cell culture scaffolds, can serve as the basis for porosity determination using Archie's law. Different networks of structured or random channels with several degrees of porosity were produced using water soluble 3D printed negative templates serving as a

mould for casting polymer elastomers to create the scaffolds, which were also tested for *in vitro* culturing of human hepatoblastoma (HepG2) cells over a 12-day culture period. The use of gold plate electrodes for the EIS analysis facilitate interfacing with a scaffold without the necessity of penetrating into the bulk material, which gives a significant advantage for measurements when using scaffolds made of brittle or tough elastomeric materials. Moreover the non-invasiveness of the method shows compatibility with setups where cell culturing is to be performed.

Furthermore, I showed the use of different 2-, 3-, and 4T configurations of plate or needle electrodes to achieve spatial sensing in the tissue engineering process. Such configurations were simulated and optimised using the *FE method* and further tested with electrochemistry, impedance measurements, or *phantom* experiments mimicking cell aggregates. I used 2T- and 3T configurations to monitor the polymerisation of a bare gelatin-based 3D scaffold, sense the encapsulation and proliferation of mesenchymal stem cells over a period of three days. By switching between the different combinations of electrode couples (sensing modes), it was possible to generate a multiplexing-like approach, which allowed collecting spatially distributed information within the 3D space. This achievement set the challenge of performing EIT imaging in miniaturised measurement chambers suitable for future applications in 3D cell culturing. Such an objective was achieved in collaboration with electronic engineers and physicists from Prof. David Holder's group at the University College London, who provided expertise and technical skills for image reconstruction. For such application, two different approaches were validated in terms of the sequence of electrode couples activated for 4T measurements and the algorithm used for image reconstruction. The chosen number of electrodes and the consequent number of electrode configurations aimed at maximising the quality of image reconstruction while minimising the number of required measurements. This is significant when designing a technique suitable for future tissue engineering applications where time-based monitoring of cellular behaviour in 3D scaffolds is of interest.

Finally, I showed the possibility to integrate impedance sensing in bioreactors allowing non-invasive real-time monitoring of cell proliferation in porous 3D scaffolds in perfusion culture. The platform is the result of one technological objective of the NanoBio4Trans project aimed at developing an impedance sensing system into a perfusion-based bioartificial liver (BAL)

support platform able to sustain the growth of the BAL, while allowing real-time monitoring of its growth. To demonstrate the suitability of the platform for cell culture, HepG2 cells were grown in the system at different flow rates and cell proliferation and viability as well as metabolic activity (albumin secretion) were analysed using a combination of imaging and bioanalytical techniques. Additionally, the bioreactor design was modified to allow the placement of two vertical needle electrodes in contact with each porous 3D scaffold in order to facilitate 2T impedance measurements for real-time monitoring of cell proliferation.

5.1 Final Remarks and Future Perspectives

The work that I presented in this thesis shows the development of impedance-based methods with application in different stages of tissue engineering processes. I showed that impedance-based methods may be powerful tools providing advantages on conventional microscopy techniques which otherwise would require extensive optimisation for thick 3D tissue engineering constructs in terms of (i) technical parameters to be adopted during the analysis; (ii) 3D culture systems having compatible size with such instrumentation and (iii) the ability to keep sterile conditions during the analysis. Impedance-based methods allow non-invasive monitoring of the 3D environment, gathering information on the scaffold supporting cell organisation (e.g. hydrogel polymerisation and porosity), cell loading and proliferation, as well as spatial distribution of cell aggregates in 3D.

The universal protocol that I developed for conductivity determinations using EIS could be further tested for monitoring variations in cell culture medium conductivity while culturing cells in a 3D environment over time. A thorough evaluation of several culture conditions may allow sensing the production of specific metabolites, cell death and the effect of drugs or toxicants. Moreover, when optimising EIS-based analysis in a setup where cells are cultured in serum-containing media, it is necessary to investigate also the influence of protein adsorption on the scaffold material. In this regard, the EIS-based method for porosity determinations that I presented can be further optimised by performing experiments with alternative techniques allowing the precise determination of the empirical parameters (e.g. geometrical constraint of channel architecture and their degree of medium saturation) needed for solving Archie's equation. The method could be also validated for a wide range of scaffold materials and

geometries, opening perspectives for future studies on more complex combined architectures of structured and random pores.

Systematic experiments aiming at on-line monitoring of 3D cell cultures need to be performed using also the methods that I established for multiplexed 2-, 3- and 4T impedance spatial sensing. The culmination of the scientific research that I carried out would be the complete characterisation of the growing 3D tissue, starting from the bare scaffold to cell adhesion, proliferation and possibly differentiation in the same measurement setup during the same experiment. A further accomplishment of my work would address the implementation of multiplexed impedance measurements in perfusion bioreactors. In this case, a major challenge is the electrode optimisation in terms of manufacture and deposition inside the bioreactor to provide sufficient sensitivity for the impedance measurements. Moreover, easy access to the electrodes for electrical connections is needed in order to perform the measurements directly inside the incubator and keep the cells at a constant physiological condition.

In parallel, additional work could be performed using the platform which has been developed as part of this thesis integrating 2T impedance sensing in perfusion bioreactors. In accordance with one of the objectives of the NanoBio4Trans project, such a system should be tested for the full growth of an extracorporeal BAL perfused with human blood plasma. Furthermore, it could serve as tool to support and monitor the growth of other bioartificial organs like kidneys, heart and intestine or a combination of them in a 'body-on-a-platform' system. This would be significant in order to establish more *in vivo*-like drug screening conditions in pharmaceutical industry.

Finally, my work on EIT is just a first step towards establishing more standardised protocols for performing EIT analysis on miniaturised systems suitable for tissue engineering applications. The obtained results have brought up many research perspectives for which several technical issues need to be solved and refined. In this regards, the further development of such EIT methods warrants the collaboration among scientists from different technological areas spanning from biotechnology to physics and electronic engineering. Additional thorough work is required for testing more combinations of electrode configurations and customised reconstruction algorithms. Furthermore, the presented measurement chamber could be implemented with deep-brain stimulation electrodes, which

carry an insulated shaft and a small conductive tip. Several rings of such electrodes placed at different heights along the vertical axis of the chamber would produce a number of cross-sectional images that together cover the entire volume of the 3D sample. This would provide a useful tool for cell culture scaffold characterisation and monitoring *in vitro* tissue cultures over time.

Altogether, this thesis describes an attempt of bringing impedance technologies to a 'new level' bridging more conventional electrochemical applications with physiological measurements, proving the potential and suitability of impedance methods for future monitoring of tissue engineering processes.

Acknowledgments

This Ph.D. thesis is the culmination of a life-long interest in science which has been a work of love and passion. Many people have made this possible over the years and probably I won't be able to mention all of them.

Firstly I would like to thank my supervisor *Prof. Jenny Emnéus*, who first believed in me. Thank you for giving me the chance of building my *own* route in research and starting new collaborations, being open to explore the potential of my scientific ideas.

I am especially grateful to *Prof. Ørjan Grøttem Martinsen*, who has been (and still is) a source of great inspiration. You are a precious example of committed researcher who truly enjoys science: it's always a pleasure to attend your explanations about physics and discuss about science with you. You have always kept my motivation alive with positivity and inspired to give my best.

My heartfelt thanks go to *Assoc. Prof. Arto Heiskanen*. I'll keep very good memories of our pleasant (and sometimes hilarious too) scientific discussions, crazy overnight milling sessions and inspiring brainstorming together. I have made treasure of all of this, even though an entire life won't be enough to reach your amazing wisdom in science.

I also thank *Assoc. Prof. Martin Dufva* for being a concrete scientist and a marvellous person, along with his impressive talent as graphic illustrator; and *Assoc. Prof. Anders Wolff* for his valuable suggestions when preparing scientific posters.

A sincere acknowledgement is for all my colleagues at DTU Nanotech, who created a pleasant atmosphere where I enjoyed working: *Ada* (you rock sista!! Thanks for your tips, tea breaks and friendship), *Vida* (you are a peach! ...and a lovely friend and an outstanding electrochemist!), *Fozia* (the sweetest ever!), *Yuwadee* (an inspiration of hard work), *Haseena*, *Mette* (a truly rocket biologist!) and *Agnieszka* (thanks for your esteem and support).

Special thanks go to all the researchers from the Department of Physics at the University of Oslo and the Department of Clinical and Biomedical Engineering at Oslo University Hospital: *Per*, *Fred-Johan*, *Håvard*, *Christian*, *Tormod*, *Humayra*, *Runar*, *Bernt*, *Lars Andreas*. You made my stay in Oslo so warm and very welcoming and shared with me good tips and hard-core expertise.

I would also like to thank *Prof. David Holder, Dr. Kirill Aristovich and Dr. Thomas Dowrick* from the University College London, who critically provided invaluable advices when I faced the intricate world of impedance tomography for the first time.

My Master students *Lorenzo and Chiara* need to be mentioned here too. I'm really proud of what you accomplished making science together. It has been a pleasure to work with you and see you tackling challenges, learning and growing in science and I hope I have been a good mentor for you guys. I'm also proud of saying that I've learnt so much from you. This is what science should be: an open discussion and not a univocal and sterile transfer of knowledge.

Many friends based all over the world must be remembered, although I'll be able to mention just few of them here. *Ale*, thanks for constantly being my wingwoman, laughing till we bellyache and always here to pick up the pieces when I fall apart. You are a cornerstone in my life, no matter the distance, and you'll always have a special place in my heart. *Mikki, Letty, Vale, Matte and Poldo, Chiara P. and Kira, Chiara Z., Carly, Gabro, Parid* (thanks for always being there for me), *Lorenzo, Filo and all the friends from Pesaro*: you're the best ever! Thanks for making my visits in Italy always fun and lively, as time never passed: you're always in my heart. Simply love you guys! *Claudia*: you have made Denmark a warm place to live. You are a wonderful person and friend, as well as a scientist of integrity (and, mostly, the best buddy for travelling!). *Kinga*: I have always appreciated your honesty and depth, in science as well as in life. I learnt many great deals from you, thanks. *Adi and Ricca*: you always make me feel in the right place guys! I had memorable moments of fun, trips and sparkling soirées with you. You are exceptional friends and lovely people and will always have a special corner of my heart. *Simo*: great photographer, fashion victim, personal shopper, amazing dancing buddy, TEM fairy. Thanks for your sweetness and hugs, for every moment of fun together and illegally pushing chewing gum! *Rodrigo*: you are the 'real' engineer. I have learnt many things from you in this field and had very good times together. You're a sinusoid oscillating between nagging and laughing: once one sets the proper filter for the nagging part, then it's impossible not to love you. My heartfelt thanks also to many other friends: *Kuldeep* (thanks 'boss', Nanotech wouldn't be the same without you!), *Alessandro* (I love our fun chats about science and life, you are awesome!), *Pavel, Suhith, Solène, Kamrul, Christopher, Alberto, Alex, Giovanni, Sune, Marco M.* (thanks for your friendship, advices in life and science and affection), *Marco T.* (you are a lovely person, a very good and supportive friend and brilliant scientist, thanks!), *Raj,*

José, François, Paolino, Letizia, Silvia, Andrea, Daniele (thanks for our Sunday tea breaks together and pleasant chats!), *Umberto, Lidia, Esben, Mikkel, Peter, Nis, Kasper, Anders* and everyone who simply spent just a second of his day smiling to me when passing in the corridor at work. A warm acknowledgment goes also to the technicians and the administrative staff here at DTU Nanotech: *Jannik, Lene, Lotte, Ina, Ole, Louise, Jette, Dorte, Nanna, Jasper, Mette and Majken* and to the cleanroom technicians at DTU Danchip: *Majken and Conny*.

And finally, the last and most important space of this chapter is for my beloved family. A lovely acknowledgement goes to *my grandmother Norma*: you have always provided me with the right motivation for setting new challenges throughout my whole life and the strength to tackle them with all my zeal and energies. You taught me to fight for cultural freedom and look at my objectives with ambition. This is invaluable. Thanks to *my parents*, for their love, support and patience. A special thank you is to my *mom Doris*: I know how much it has been difficult for you to accept my freaking need of independence and being out of a traditional, quiet lifestyle and you cannot imagine how much I appreciate your lovely way of trying to 'fit' it. Once, Jim Henson said: "If you can't beat them, join them". A special thank you goes *my grandfather Paolo*: your dedication to hard work has always been source of inspiration for me; your love and comprehension have been of great support in every moment of my life. Thank you heartily to my uncle *Pascal*: you have always been a marvellous and lovely supporter. Your enthusiasm and positivity will surely guide me to succeed in science and in life.

References

- [1] P. Zorlutuna, The expanding world of tissue engineering: The building blocks and new applications of tissue engineered constructs, *IEEE Rev. Biomed. Eng.* 6 (2013) 47–62. doi:10.1016/j.biotechadv.2011.08.021.Secreted.
- [2] K.M. Yamada, E. Cukierman, Modeling tissue morphogenesis and cancer in 3D, *Cell*. 130 (2007) 601–610. doi:10.1016/j.cell.2007.08.006.
- [3] B.M. Baker, C.S. Chen, Deconstructing the third dimension: how 3D culture microenvironments alter cellular cues, *J. Cell Sci.* 125 (2012) 3015–3024. doi:10.1242/jcs.079509.
- [4] M.J. Bissell, D.C. Radisky, A. Rizki, V.M. Weaver, O.W. Petersen, The organizing principle: Microenvironmental influences in the normal and malignant breast, *Differentiation*. 70 (2002) 537–546. doi:10.1046/j.1432-0436.2002.700907.x.
- [5] L.G. Griffith, G. Naughton, Tissue engineering-current challenges and expanding opportunities, *Science* (80-.). 295 (2002) 1009–1014. doi:10.1126/science.1069210.
- [6] F. Pampaloni, E.G. Reynaud, E.H.K. Stelzer, The third dimension bridges the gap between cell culture and live tissue, *Nat. Rev. Mol. Cell Biol.* 8 (2007) 839–845.
- [7] J.J. Crowe, S.C. Grant, T.M. Logan, T. Ma, A magnetic resonance-compatible perfusion bioreactor system for three-dimensional human mesenchymal stem cell construct development, *Chem. Eng. Sci.* 66 (2011) 4138–4147. doi:10.1016/j.ces.2011.05.046.
- [8] D. Wendt, S. a. Riboldi, M. Cioffi, I. Martin, Potential and bottlenecks of bioreactors in 3D cell culture and tissue manufacturing, *Adv. Mater.* 21 (2009) 3352–3367. doi:10.1002/adma.200802748.
- [9] S.W.O. Driscoll, J.S. Fitzsimmons, C.N. Commisso, Role of oxygen tension during cartilage formation by periosteum, *J. Orthopaedic Res.* 15 (1997) 682–687.
- [10] S.D. Westfall, S. Sachdev, P. Das, L.B. Hearne, M. Hannink, R.M. Roberts, et al., Identification of oxygen-sensitive transcriptional programs in human embryonic stem cells, *Stem Cells Dev.* 17 (2008) 869–881. doi:10.1089/scd.2007.0240.
- [11] L.C. Clarck Jr., Monitor and control of blood and tissue oxygen tensions, *Trans. Am. Soc. Artif. Intern. Organs.* 2 (1956) 41–47.
- [12] J. Malda, J. Rouwkema, D.E. Martens, E.P. Le Comte, F.K. Kooy, J. Tramper, et al., Oxygen gradients in tissue-engineered PEGT/PBT cartilaginous constructs: measurement and modeling, *Biotechnol. Bioeng.* 86 (2004) 9–18. doi:10.1002/bit.20038.
- [13] M. a. Acosta, J.B. Leach, Fluorescent microparticles for sensing cell microenvironment oxygen levels within 3D scaffolds, *IFMBE Proc.* 32 IFMBE (2010) 332–335. doi:10.1007/978-3-642-14998-6_85.
- [14] L. Wang, M. a. Acosta, J.B. Leach, R.L. Carrier, Spatially monitoring oxygen level in 3D microfabricated cell culture systems using optical oxygen sensing beads., *Lab Chip.* 13 (2013) 1586–92. doi:10.1039/c3lc41366g.
- [15] B. Tian, J. Liu, T. Dvir, L. Jin, J.H. Tsui, Q. Qing, et al., Macroporous nanowire nanoelectronic scaffolds for synthetic tissues, *Nat. Mater.* 11 (2012) 987–994. doi:10.1038/nmat3403.
- [16] J.J. Pancrazio, F. Wang, C. a. Kelley, Enabling tools for tissue engineering, *Biosens. Bioelectron.* 22 (2007) 2803–2811. doi:10.1016/j.bios.2006.12.023.
- [17] T.S. Hug, Biophysical methods for monitoring cell-substrate interactions in drug discovery, *Assay Drug Dev. Technol.* 1 (2003) 479–488. doi:10.1089/154065803322163795.
- [18] J. Wegener, A. Janshoff, C. Steinem, The quartz crystal microbalance as a novel means to study cell-substrate interactions in situ, *Cell Biochem. Biophys.* 34 (2001) 121–151. doi:10.1385/CBB:34:1:121.
- [19] V. Yashunsky, V. Lirtsman, M. Golosovsky, D. Davidov, B. Aroeti, Real-time monitoring of epithelial cell-cell and cell-substrate interactions by infrared surface plasmon spectroscopy, *Biophys. J.* 99 (2010) 4028–4036. doi:10.1016/j.bpj.2010.10.017.
- [20] T.S. Hug, J.E. Prenosil, M. Morbidelli, Optical waveguide lightmode spectroscopy as a new method to study adhesion of anchorage-dependent cells as an indicator of metabolic state, *Biosens. Bioelectron.* 16 (2001) 865–874.

- [21] I. Giaever, C.R. Keese, Monitoring fibroblast behavior in tissue culture with an applied electric field, *Proc. Natl. Acad. Sci. U. S. A.* 81 (1984) 3761–3764. <http://www.pubmedcentral.nih.gov/articlerender.fcgi?artid=345299&tool=pmcentrez&rendertype=abstract>.
- [22] I. Giaever, C.R. Keese, A morphological biosensor for mammalian cells, *Nature*. 366 (1993) 591–592.
- [23] J. Wegener, C.R. Keese, I. Giaever, Electric cell-substrate impedance sensing (ECIS) as a noninvasive means to monitor the kinetics of cell spreading to artificial surfaces, *Exp. Cell Res.* 259 (2000) 158–66. doi:10.1006/excr.2000.4919.
- [24] I. Giaever, C.R. Keese, Micromotion of mammalian cells measured electrically, *Proc. Natl. Acad. Sci. U. S. A.* 88 (1991) 7896–7900. doi:10.1073/pnas.88.17.7896.
- [25] C.R. Keese, J. Wegener, S.R. Walker, I. Giaever, Electrical wound-healing assay for cells in vitro, *Proc. Natl. Acad. Sci. U. S. A.* 101 (2004) 1554–1559. doi:10.1073/pnas.0307588100.
- [26] R. Meissner, B. Eker, H. Kasi, A. Bertsch, P. Renaud, Distinguishing drug-induced minor morphological changes from major cellular damage via label-free impedimetric toxicity screening, *Lab Chip*. 11 (2011) 2352–2361. doi:10.1039/c1lc20212j.
- [27] R. Meissner, P. Joris, B. Eker, A. Bertsch, P. Renaud, A microfluidic-based frequency-multiplexing impedance sensor (FMIS), *Lab Chip*. 12 (2012) 2712–2718. doi:10.1039/c2lc40236j.
- [28] C. Caviglia, K. Zór, L. Montini, V. Tilli, S. Canepa, F. Melander, et al., Impedimetric toxicity assay in microfluidics using free and liposome-encapsulated anticancer drugs, *Anal. Chem.* 87 (2015) 2204–2212. doi:10.1021/ac503621d.
- [29] K.F. Lei, M.-H. Wu, C.-W. Hsu, Y.-D. Chen, Real-time and non-invasive impedimetric monitoring of cell proliferation and chemosensitivity in a perfusion 3D cell culture microfluidic chip, *Biosens. Bioelectron.* 51 (2014) 16–21. doi:10.1016/j.bios.2013.07.031.
- [30] S. Tully-Dartez, H.E. Cardenas, P.-F.S. Sit, Pore characteristics of chitosan scaffolds studied by electrochemical impedance spectroscopy, *Tissue Eng. - Part C Methods*. 16 (2010) 339–45. doi:10.1089/ten.TEC.2009.0132.
- [31] L.E. Smith, R. Smallwood, S. Macneil, A comparison of imaging methodologies for 3D tissue engineering, *Microsc. Res. Tech.* 73 (2010) 1123–33. doi:10.1002/jemt.20859.
- [32] B.W. Graf, S.A. Boppart, Imaging and analysis of three dimensional cell culture models, *Methods Mol. Biol.* 591 (2010) 211–227.
- [33] M.R. Lornejad-Schäfer, W. Hilber, C. Schäfer, Construction of an impedance monitoring system for cell seeding and drug screening in a 3D cell culture model, *J. Biosens. Bioelectron.* 5 (2014). doi:10.4172/2155-6210.1000151.
- [34] L.G. Griffith, M.A. Swartz, Capturing complex 3D tissue physiology in vitro, *Nat. Rev. Mol. Cell Biol.* 7 (2006) 211–224. doi:10.1038/nrm1858.
- [35] G.E. Archie, The electrical resistivity log as an aid in determining some reservoir characteristics, *Pet. Technol.* (1942) 54–62. doi:10.2118/942054-G.
- [36] R. Langer, J.P. Vacanti, Tissue engineering, *Science* (80-.). 260 (1993) 920–926.
- [37] B.P. Chan, K.W. Leong, Scaffolding in tissue engineering: general approaches and tissue-specific considerations, *Eur. Spine J.* 17 (2008) S467–S479. doi:10.1007/s00586-008-0745-3.
- [38] D. Howard, L.D. Buttery, K.M. Shakesheff, S.J. Roberts, Tissue engineering: strategies, stem cells and scaffolds, *J. Anat.* 213 (2008) 66–72. doi:10.1111/j.1469-7580.2008.00878.x.
- [39] A.J. Russell, T. Bertram, Moving into the clinic, in: R. Lanza, R. Langer, J.P. Vacanti (Eds.), *Princ. Tissue Eng.*, Fourth Ed., Academic Press, San Diego, CA, USA, 2013: pp. 57–81.
- [40] M. Lee, B.M. Wu, J.C.Y. Dunn, Effect of scaffold architecture and pore size on smooth muscle cell growth, *J. Biomed. Mater. Res. - Part A.* 87 (2008) 1010–1016. doi:10.1002/jbm.a.31816.
- [41] D. Dado, S. Levenberg, Cell-scaffold mechanical interplay within engineered tissue, *Semin. Cell Dev. Biol.* 20 (2009) 656–664. doi:10.1016/j.semcdb.2009.02.001.
- [42] M. Tallawi, E. Rosellini, N. Barbani, M.G. Cascone, R. Rai, G. Saint-pierre, et al., Strategies for the chemical and biological functionalization of scaffolds for cardiac tissue engineering: a review, *J. R. Soc. Interface.* 12 (2015). doi:10.1098/rsif.2015.0254.

- [43] F.M. Watt, Selective migration of terminally differentiating cells from the basal layer of cultured human epidermis, *J. Cell Biol.* 98 (1984) 16–21. doi:10.1083/jcb.98.1.16.
- [44] C.D. Roskelley, P.Y. Desprez, M.J. Bissell, Extracellular matrix-dependent tissue-specific gene expression in mammary epithelial cells requires both physical and biochemical signal transduction, *Proc. Natl. Acad. Sci. U. S. A.* 91 (1994) 12378–12382. doi:10.1073/pnas.91.26.12378.
- [45] J.K. Mouw, G. Ou, V.M. Weaver, Extracellular matrix assembly: a multiscale deconstruction, *Nat. Rev. Mol. Cell Biol.* 15 (2014) 771–785. doi:10.1038/nrm3902.
- [46] M.W. Tibbitt, K.S. Anseth, Hydrogels as extracellular matrix mimics for 3D cell culture, *Biotechnol. Bioeng.* 103 (2009) 655–63. doi:10.1002/bit.22361.
- [47] F.T. Bosman, I. Stamenkovic, Functional structure and composition of the extracellular matrix, *J. Pathol.* 200 (2003) 423–428. doi:10.1002/path.1437.
- [48] J. a Hubbell, Matrix effects, in: R. Lanza, R. Langer, J.P. Vacanti (Eds.), *Princ. Tissue Eng.*, Fourth Ed., Academic Press, San Diego, CA, USA, 2013: pp. 407–421. doi:10.1016/B978-0-12-398358-9.00021-5.
- [49] D.E. Discher, D.J. Mooney, P.W. Zandstra, Growth factors, matrices, and forces combine and control stem cells, *Science* (80-.). 324 (2009) 1673–1677. doi:10.1126/science.1171643.
- [50] R.O. Hynes, The extracellular matrix: not just pretty fibrils, *Science* (80-.). 326 (2009) 1216–1219. doi:10.1126/science.1176009.Extracellular.
- [51] D. Ingber, Integrins as mechanochemical transducers, *Curr. Opin. Cell Biol.* 3 (1991) 841–848.
- [52] R.O. Hynes, Integrins: Bidirectional, allosteric signaling machines, *Cell.* 110 (2002) 673–687. doi:10.1016/S0092-8674(02)00971-6.
- [53] P.D. Yurchenco, Basement membranes: Cell scaffoldings and signaling platforms, *Cold Spring Harb. Perspect. Biol.* 3 (2011) 1–27. doi:10.1101/cshperspect.a004911.
- [54] C. Frantz, K.M. Stewart, V.M. Weaver, The extracellular matrix at a glance, *J. Cell Sci.* 123 (2010) 4195–4200. doi:10.1242/jcs.023820.
- [55] W. Halfter, J. Candiello, H. Hu, P. Zhang, E. Schreiber, M. Balasubramani, Protein composition and biomechanical properties of in vivo-derived basement membranes, *Cell Adhes. Migr.* 7 (2013) 64–71. doi:10.4161/cam.22479.
- [56] M.J. Bissell, A. Rizki, I.S. Mian, Tissue architecture: the ultimate regulator of breast epithelial function, *Curr. Opin. Cell Biol.* 15 (2003) 753–762. doi:10.1016/j.ceb.2003.10.016.
- [57] S. Ding, P.G. Schultz, A role for chemistry in stem cell biology, *Nat. Biotechnol.* 22 (2004) 833–840. doi:10.1038/nbt987.
- [58] J.P. Vacanti, M. a Morse, W.M. Saltzman, a J. Domb, A. Perez-Atayde, R. Langer, Selective cell transplantation using bioabsorbable artificial polymers as matrices, *J. Pediatr. Surg.* 23 (1988) 3–9. doi:10.1016/S0022-3468(88)80529-3.
- [59] K. Chatterjee, M.F. Young, C.G. Simon Jr., Fabricating gradient hydrogel scaffolds for 3D cell culture, *Comb. Chem. High Throughput Screen.* 14 (2011) 227–236.
- [60] S. Sant, M.J. Hancock, J.P. Donnelly, D. Iyer, A. Khademhosseini, Biomimetic gradient hydrogels for tissue engineering, *Can. J. Chem. Eng. Technol.* 88 (2011) 899–911. doi:10.1002/cjce.20411.BIOMIMETIC.
- [61] M. Ehrbar, V.G. Djonov, C. Schnell, S. a. Tschanz, G. Martiny-Baron, U. Schenk, et al., Cell-demanded liberation of VEGF121 from fibrin implants induces local and controlled blood vessel growth, *Circ. Res.* 94 (2004) 1124–1132. doi:10.1161/01.RES.0000126411.29641.08.
- [62] A.S. Gobin, J.L. West, Effects of epidermal growth factor on fibroblast migration through biomimetic hydrogels, *Biotechnol. Prog.* 19 (2003) 1781–1785. doi:10.1021/bp0341390.
- [63] P. Lu, K. Takai, V.M. Weaver, Z. Werb, Extracellular matrix degradation and remodeling in development and disease, *Cold Spring Harb. Perspect. Biol.* 3 (2011) 1–24. doi:10.1101/cshperspect.a005058.
- [64] M.J. Paszek, V.M. Weaver, The tension mounts: mechanics meets morphogenesis and malignancy, *J. Mammary Gland Biol. Neoplasia.* 9 (2004) 325–342. doi:10.1007/s10911-004-1404-x.
- [65] D. Chodniewicz, R.L. Klemke, Regulation of integrin-mediated cellular responses through assembly of a CAS/Crk scaffold, *Biochim. Biophys. Acta - Mol. Cell Res.* 1692 (2004) 63–76. doi:10.1016/j.bbamcr.2004.03.006.

- [66] S.H. Kim, J. Turnbull, S. Guimond, Extracellular matrix and cell signalling: The dynamic cooperation of integrin, proteoglycan and growth factor receptor, *J. Endocrinol.* 209 (2011) 139–151. doi:10.1530/JOE-10-0377.
- [67] N. De Franceschi, H. Hamidi, J. Alanko, P. Sahgal, J. Ivaska, Integrin traffic - the update, *J. Cell Sci.* 128 (2015) 839–852. doi:10.1242/jcs.161653.
- [68] J.S. Desgrosellier, D. a Cheresh, Integrins in cancer: biological implications and therapeutic opportunities, *Nat. Rev. Cancer.* 10 (2010) 9–22. doi:10.1038/nrc2965.
- [69] A. Jeney, Extracellular matrix as target for antitumor therapy, *Onco. Targets. Ther.* 8 (2015) 1387–1398.
- [70] V. Seewaldt, ECM stiffness paves the way for tumor cells, *Nat. Med.* 20 (2014) 332–333. doi:10.1111/j.1463-1326.2010.01310.x.
- [71] K.R. Levental, H. Yu, L. Kass, J.N. Lakins, J.T. Emler, S.F.T. Fong, et al., Matrix crosslinking forces tumor progression by enhancing integrin signaling, *Cell.* 139 (2009) 891–906. doi:10.1016/j.cell.2009.10.027.
- [72] A.L. Sieminski, R.P. Hebbel, K.J. Gooch, The relative magnitudes of endothelial force generation and matrix stiffness modulate capillary morphogenesis in vitro, *Exp. Cell Res.* 297 (2004) 574–584. doi:10.1016/j.yexcr.2004.03.035.
- [73] J. Debnath, J.S. Brugge, Modelling glandular epithelial cancers in three-dimensional cultures, *Nat. Rev. Cancer.* 5 (2005) 675–688. doi:10.1038/nrc1695.
- [74] M. a Wozniak, P.J. Keely, Use of three-dimensional collagen gels to study mechanotransduction in T47D breast epithelial cells, *Biol. Proced. Online.* 7 (2005) 144–161. doi:10.1251/bpo112.
- [75] J. Zhu, R.E. Marchant, Design properties of hydrogel tissue-engineering scaffolds, *Expert Rev. Med. Devices.* 8 (2011) 607–626. doi:10.1586/erd.11.27.
- [76] J. Glowacki, S. Mizuno, Collagen scaffolds for tissue engineering, *Biopolymers.* 89 (2008) 338–344. doi:10.1002/bip.20871.
- [77] E. Kaemmerer, F.P.W. Melchels, B.M. Holzapfel, T. Meckel, D.W. Huttmacher, D. Loessner, Gelatine methacrylamide-based hydrogels: an alternative three-dimensional cancer cell culture system, *Acta Biomater.* 10 (2014) 2551–2562. doi:10.1016/j.actbio.2014.02.035.
- [78] P. De la Puente, D. Ludeña, Cell culture in autologous fibrin scaffolds for applications in tissue engineering, *Exp. Cell Res.* 322 (2014) 1–11. doi:10.1016/j.yexcr.2013.12.017.
- [79] Y. Wang, D.J. Blasioli, H.-J. Kim, H.S. Kim, D.L. Kaplan, Cartilage tissue engineering with silk scaffolds and human articular chondrocytes, *Biomaterials.* 27 (2006) 4434–4442. doi:10.1016/j.biomaterials.2006.03.050.
- [80] C.S. Hughes, L.M. Postovit, G. a Lajoie, Matrigel: a complex protein mixture required for optimal growth of cell culture, *Proteomics.* 10 (2010) 1886–1890. doi:10.1002/pmic.200900758.
- [81] D. Sengupta, S.C. Heilshorn, Protein-engineered biomaterials: highly tunable tissue engineering scaffolds, *Tissue Eng. - Part B Rev.* 16 (2010) 285–293. doi:10.1089/ten.teb.2009.0591.
- [82] S.R. MacEwan, A. Chilkoti, Elastin-like polypeptides: biomedical applications of tunable biopolymers, *Biopolymers.* 94 (2010) 60–77. doi:10.1002/bip.21327.
- [83] J.B. Leach, K. a Bivens, C.W. Patrick, C.E. Schmidt, Photocrosslinked hyaluronic acid hydrogels: natural, biodegradable tissue engineering scaffolds, *Biotechnol. Bioeng.* 82 (2003) 578–589. doi:10.1002/bit.10605.
- [84] C.K. Kuo, P.X. Ma, Ionically crosslinked alginate hydrogels as scaffolds for tissue engineering: Part 1. Structure, gelation rate and mechanical properties, *Biomaterials.* 22 (2001) 511–521. doi:10.1016/S0142-9612(00)00201-5.
- [85] B.K. Denizli, H.K. Can, Z.M.O. Rzaev, A. Guner, Preparation conditions and swelling equilibria of dextran hydrogels prepared by some crosslinking agents, *Polymer (Guildf).* 45 (2004) 6431–6435. doi:10.1016/j.polymer.2004.07.067.
- [86] I.-Y. Kim, S.-J. Seo, H.-S. Moon, M.-K. Yoo, I.-Y. Park, B.-C. Kim, et al., Chitosan and its derivatives for tissue engineering applications, *Biotechnol. Adv.* 26 (2008) 1–21. doi:10.1016/j.biotechadv.2007.07.009.
- [87] N. Davidenko, J.J. Campbell, E.S. Thian, C.J. Watson, R.E. Cameron, Collagen-hyaluronic acid scaffolds for adipose tissue engineering, *Acta Biomater.* 6 (2010) 3957–3968. doi:10.1016/j.actbio.2010.05.005.

- [88] S.E. Stabenfeldt, A.J. García, M.C. LaPlaca, Thermoreversible laminin-functionalized hydrogel for neural tissue engineering, *J. Biomed. Mater. Res. - Part A*. 81 (2007) 771–780. doi:10.1002/jbm.a.
- [89] S. Sakai, I. Hashimoto, K. Kawakami, Synthesis of an agarose-gelatin conjugate for use as a tissue engineering scaffold, *J. Biosci. Bioeng.* 103 (2007) 22–26. doi:10.1263/jbb.103.22.
- [90] Y. Huang, S. Onyeri, M. Siewe, A. Moshfeghian, S. V Madihally, In vitro characterization of chitosan-gelatin scaffolds for tissue engineering, *Biomaterials*. 26 (2005) 7616–7627. doi:10.1016/j.biomaterials.2005.05.036.
- [91] T. Rozario, D.W. DeSimone, The extracellular matrix in development and morphogenesis: a dynamic view, *Dev. Biol.* 341 (2010) 126–140. doi:10.1016/j.ydbio.2009.10.026.
- [92] T.R. Cox, J.T. Erler, Remodeling and homeostasis of the extracellular matrix: implications for fibrotic diseases and cancer, *Dis. Model. Mech.* 4 (2011) 165–178. doi:10.1242/dmm.004077.
- [93] C. Bonnans, J. Chou, Z. Werb, Remodelling the extracellular matrix in development and disease, *Nat. Rev. Mol. Cell Biol.* 15 (2014) 786–801. doi:10.1038/nrm3904.
- [94] Y.L. Wang, R.J. Pelham, Preparation of a flexible, porous polyacrylamide substrate for mechanical studies of cultured cells, *Methods Enzymol.* 298 (1998) 489–496. doi:10.1016/S0076-6879(98)98041-7.
- [95] E.J. Semler, P. a. Lancin, A. Dasgupta, P. V. Moghe, Engineering hepatocellular morphogenesis and function via ligand-presenting hydrogels with graded mechanical compliance, *Biotechnol. Bioeng.* 89 (2005) 296–307. doi:10.1002/bit.20328.
- [96] C. a Reinhart-King, M. Dembo, D. a Hammer, The dynamics and mechanics of endothelial cell spreading, *Biophys. J.* 89 (2005) 676–689. doi:10.1529/biophysj.104.054320.
- [97] A.J. Engler, S. Sen, H.L. Sweeney, D.E. Discher, Matrix elasticity directs stem cell lineage specification, *Cell*. 126 (2006) 677–689. doi:10.1016/j.cell.2006.06.044.
- [98] A.J. Engler, H.L. Sweeney, D.E. Discher, J.E. Schwarzbauer, Extracellular matrix elasticity directs stem cell differentiation, *J. Musculoskelet. Neuronal Interact.* 7 (2007) 335.
- [99] A.J. Engler, L. Richert, J.Y. Wong, C. Picart, D.E. Discher, Surface probe measurements of the elasticity of sectioned tissue, thin gels and polyelectrolyte multilayer films: Correlations between substrate stiffness and cell adhesion, *Surf. Sci.* 570 (2004) 142–154. doi:10.1016/j.susc.2004.06.179.
- [100] G.C. Reilly, A.J. Engler, Intrinsic extracellular matrix properties regulate stem cell differentiation, *J. Biomech.* 43 (2010) 55–62. doi:10.1016/j.jbiomech.2009.09.009.
- [101] M.D. Pierschbacher, E. Ruoslahti, Cell attachment activity of fibronectin can be duplicated by small synthetic fragments of the molecule, *Nature*. 309 (1984) 30–33.
- [102] L.Q. Wan, J. Jiang, D.E. Miller, X.E. Guo, V.C. Mow, H.H. Lu, Matrix deposition modulates the viscoelastic shear properties of hydrogel-based cartilage grafts, *Tissue Eng. - Part A*. 17 (2011) 1111–1122. doi:10.1089/ten.tea.2010.0379.
- [103] C. Li, L. Wang, Z. Yang, G. Kim, H. Chen, Z. Ge, A viscoelastic chitosan-modified three-dimensional porous poly(L-Lactide-co-ε-caprolactone) scaffold for cartilage tissue engineering, *J. Biomater. Sci. Polym. Ed.* 23 (2012) 405–424. doi:10.1163/092050610X551970.
- [104] F.J. O'Brien, B. a. Harley, I. V. Yannas, L.J. Gibson, The effect of pore size on cell adhesion in collagen-GAG scaffolds, *Biomaterials*. 26 (2005) 433–441. doi:10.1016/j.biomaterials.2004.02.052.
- [105] B.A.C. Harley, H.-D. Kim, M.H. Zaman, I. V. Yannas, D.A. Lauffenburger, L.J. Gibson, Microarchitecture of three-dimensional scaffolds influences cell migration behavior via junction interactions, *Biophys. J.* 95 (2008) 4013–4024. doi:10.1529/biophysj.107.122598.
- [106] A.G. Mitsak, J.M. Kempainen, M.T. Harris, S.J. Hollister, Effect of polycaprolactone scaffold permeability on bone regeneration in vivo, *Tissue Eng. Part A*. 17 (2011) 1831–1839. doi:10.1089/ten.TEA.2010.0560.
- [107] R. Flaumenhaft, D. Moscatelli, D.B. Rifkin, Heparin and heparan sulfate increase the radius of diffusion and action of basic fibroblast growth factor, *J. Cell Biol.* 111 (1990) 1651–1659. doi:10.1083/jcb.111.4.1651.
- [108] W.H. Baricos, S.L. Cortez, M. Deboisblanc, S. Xin, Transforming growth factor-β is a potent inhibitor of extracellular matrix degradation by cultured human mesangial cells, *J. Am. Soc. Nephrol.* 10 (1999) 790–795.
- [109] H. Im, X. Li, P. Muddasani, K. Gun-Hee, F. Davis, J. Rangan, et al., Basic fibroblast growth factor accelerates matrix degradation via a neuro-endocrine pathway in human adult articular chondrocytes, *Cell*. 125 (2010) 452–463. doi:10.1002/jcp.21317.Basic.

- [110] Y. Chen, S.J. Dodd, M. a Tangrea, M.R. Emmert-Buck, A.P. Koretsky, Measuring collective cell movement and extracellular matrix interactions using magnetic resonance imaging, *Sci. Rep.* 3 (2013) 1879. doi:10.1038/srep01879.
- [111] S. Bosi, R. Rauti, J. Laishram, A. Turco, D. Lonardoni, T. Nieuw, et al., From 2D to 3D: novel nanostructured scaffolds to investigate signalling in reconstructed neuronal networks, *Sci. Rep.* 5 (2015) 9562. doi:10.1038/srep09562.
- [112] H.J. Kim, H. Matsuda, H. Zhou, I. Honma, Ultrasound-triggered smart drug release from a poly(dimethylsiloxane) - mesoporous silica composite, *Adv. Mater.* 18 (2006) 3083-3088. doi:10.1002/adma.200600387.
- [113] Y. Fu, W.J. Kao, Drug release kinetics and transport mechanisms of non-degradable and degradable polymeric delivery systems, *Expert Opin. Drug Deliv.* 7 (2010) 429-444. doi:10.1517/17425241003602259.
- [114] D.N. Woolfson, Z.N. Mahmoud, More than just bare scaffolds: towards multi-component and decorated fibrous biomaterials, *Chem. Soc. Rev.* 39 (2010) 3464-3479. doi:10.1039/c0cs00032a.
- [115] S. Battista, D. Guarnieri, C. Borselli, S. Zeppetelli, A. Borzacchiello, L. Mayol, et al., The effect of matrix composition of 3D constructs on embryonic stem cell differentiation, *Biomaterials.* 26 (2005) 6194-6207. doi:10.1016/j.biomaterials.2005.04.003.
- [116] I. Wheelodon, A. Farhadi, A.G. Bick, E. Jabbari, A. Khademhosseini, Nanoscale tissue engineering: spatial control over cell-materials interactions, *Nanotechnology.* 22 (2011) 212001. doi:10.1088/0957-4484/22/21/212001.
- [117] P. Worthington, D.J. Pochan, S. a. Langhans, Peptide hydrogels - Versatile matrices for 3D cell culture in cancer medicine, *Front. Oncol.* 5 (2015) 1-10. doi:10.3389/fonc.2015.00092.
- [118] S. Dolly, S. Deepti, Z. Sunmi, H. Sung Soo, Nano-biomimetics for nano/micro tissue regeneration, *J. Biomed. Nanotechnol.* 10 (2014) 3141-3161.
- [119] H. Yu, I. Meyvantsson, I. a Shkel, D.J. Beebe, Diffusion dependent cell behavior in microenvironments, *Lab Chip.* 5 (2005) 1089-1095. doi:10.1039/b504403k.
- [120] T.M. Keenan, A. Folch, Biomolecular gradients in cell culture systems, *Lab Chip.* 8 (2008) 34-57. doi:10.1039/b711887b.
- [121] K. Kellner, G. Liebsch, I. Klimant, O.S. Wolfbeis, T. Blunk, M.B. Schulz, et al., Determination of oxygen gradients in engineered tissue using a fluorescent sensor, *Biotechnol. Bioeng.* 80 (2002) 73-83. doi:10.1002/bit.10352.
- [122] R. Glicklis, J.C. Merchuk, S. Cohen, Modeling mass transfer in hepatocyte spheroids via cell viability, spheroid size, and hepatocellular functions, *Biotechnol. Bioeng.* 86 (2004) 672-680. doi:10.1002/bit.20086.
- [123] E. Volkmer, S. Otto, H. Polzer, M. Saller, D. Trappendreher, D. Zagar, et al., Overcoming hypoxia in 3D culture systems for tissue engineering of bone in vitro using an automated, oxygen-triggered feedback loop, *J. Mater. Sci. Mater. Med.* 23 (2012) 2793-2801. doi:10.1007/s10856-012-4725-0.
- [124] C. Yates, C.R. Shepard, G. Papworth, A. Dash, D. Beer Stolz, S. Tannenbaum, et al., Novel three-dimensional organotypic liver bioreactor to directly visualize early events in metastatic progression, *Adv. Cancer Res.* 97 (2007) 225-246. doi:10.1016/S0065-230X(06)97010-9.
- [125] G. Ceccarelli, N. Bloise, M. Vercellino, R. Battaglia, L. Morgante, M.G.C. De Angelis, et al., In vitro osteogenesis of human stem cells by using a three-dimensional perfusion bioreactor culture system: a review, *Recent Pat. Drug Deliv. Formul.* 7 (2013) 29-38. doi:10.2174/187221113804805801.
- [126] M.R. Ebrahimkhani, J. a S. Neiman, M.S.B. Raredon, D.J. Hughes, L.G. Griffith, Bioreactor technologies to support liver function in vitro, *Adv. Drug Deliv. Rev.* 69-70 (2014) 132-157. doi:10.1016/j.addr.2014.02.011.
- [127] G. Pless, I. Steffen, K. Zeilinger, I.M. Sauer, E. Katenz, D.C. Kehr, et al., Evaluation of primary human liver cells in bioreactor cultures for extracorporeal liver support on the basis of urea production, *Artif. Organs.* 30 (2006) 686-694. doi:10.1111/j.1525-1594.2006.00285.x.
- [128] Y. Martin, P. Vermette, Bioreactors for tissue mass culture: design, characterization, and recent advances, *Biomaterials.* 26 (2005) 7481-503. doi:10.1016/j.biomaterials.2005.05.057.
- [129] J.P. Miranda, A. Rodrigues, R.M. Tostões, S. Leite, H. Zimmerman, M.J.T. Carrondo, et al., Extending hepatocyte functionality for drug-testing applications using high-viscosity alginate-encapsulated three-

- dimensional cultures in bioreactors, *Tissue Eng. Part C Methods*. 16 (2010) 1223–1232. doi:10.1089/ten.tec.2009.0784.
- [130] M.J. Powers, D.M. Janigian, K.E. Wack, C.S. Baker, D. Beer Stolz, L.G. Griffith, Functional behavior of primary rat liver cells in a three-dimensional perfused microarray bioreactor, *Tissue Eng*. 8 (2002) 499–513. doi:10.1089/107632702760184745.
- [131] K. Domansky, W. Inman, J. Serdy, A. Dash, M.H.M. Lim, L.G. Griffith, Perfused multiwell plate for 3D liver tissue engineering, *Lab Chip*. 10 (2010) 51–58. doi:10.1016/j.biotechadv.2011.08.021.Secreted.
- [132] Y.-C. Toh, T.C. Lim, D. Tai, G. Xiao, D. van Noort, H. Yu, A microfluidic 3D hepatocyte chip for drug toxicity testing, *Lab Chip*. 9 (2009) 2026–2035. doi:10.1039/b900912d.
- [133] D. Huh, G. a Hamilton, D.E. Ingber, From 3D cell culture to organs-on-chips, *Trends Cell Biol*. 21 (2011) 745–54. doi:10.1016/j.tcb.2011.09.005.
- [134] M. Mehling, S. Tay, Microfluidic cell culture, *Curr. Opin. Biotechnol*. 25 (2014) 95–102.
- [135] N.W. Choi, M. Cabodi, B. Held, J.P. Gleghorn, L.J. Bonassar, A.D. Stroock, Microfluidic scaffolds for tissue engineering, *Nat. Mater*. 6 (2007) 908–915. doi:10.1038/nmat2022.
- [136] S.J. Trietsch, G.D. Israëls, J. Joore, T. Hankemeier, P. Vulto, Microfluidic titer plate for stratified 3D cell culture, *Lab Chip*. 13 (2013) 3548–3554. doi:10.1039/c3lc50210d.
- [137] M.J. Powers, K. Domansky, M.R. Kaazempur-Mofrad, A. Kalezi, A. Capitano, A. Upadhyaya, et al., A microfabricated array bioreactor for perfused 3D liver culture, *Biotechnol. Bioeng*. 78 (2002) 257–69. <http://www.ncbi.nlm.nih.gov/pubmed/11920442> (accessed February 12, 2014).
- [138] H. Schichlein, A.C. Müller, M. Voigts, A. Krügel, E. Ivers-tiffe, Deconvolution of electrochemical impedance spectra for the identification of electrode reaction mechanisms in solid oxide fuel cells, *J. Appl. Electrochem*. 32 (2002) 875–882. doi:10.1023/A:1020599525160.
- [139] R.W. de Boer, A. van Oosterom, Electrical properties of platinum electrodes: impedance measurements and time-domain analysis, *Med. Biol. Eng. Comput*. 16 (1978) 1–10.
- [140] Ø.G. Martinsen, S. Grimnes, J. Karlsen, Electrical methods for skin moisture assessment, *Ski. Pharmacol*. 8 (1995) 237–245.
- [141] J.J. Santana, J.E. González, J. Morales, S. González, R.M. Souto, Evaluation of ecological organic paint coatings via electrochemical impedance spectroscopy, *Int. J. Electrochem. Sci*. 7 (2012) 6489–6500.
- [142] S. Kahraman, M. Alber, Electrical impedance spectroscopy measurements to estimate the uniaxial compressive strength of a fault breccia, *Bull. Mater. Sci*. 37 (2014) 1543–1550.
- [143] P. Glover, What is the cementation exponent? A new interpretation, *Lead. Edge*. 28 (2004) 82–85.
- [144] A. Lisińska-Czekaj, D. Czekaj, AC impedance studies on ferroelectromagnetic ceramics, *IOP Conf. Ser. Mater. Sci. Eng*. 18 (2011) 092045. doi:10.1088/1757-899X/18/9/092045.
- [145] T.S.S. Kumar, Characterization of biomaterials, Elsevier, 2013. doi:10.1016/B978-0-12-415800-9.00002-4.
- [146] P. Silley, S. Forsythe, Impedance microbiology - a rapid change for microbiologist, *J. Appl. Bacteriol*. 80 (1996) 233–243.
- [147] X. Dominguez-Benetton, S. Sevda, K. Vanbroekhoven, D. Pant, The accurate use of impedance analysis for the study of microbial electrochemical systems, *Chem. Soc. Rev*. 41 (2012) 7228–7246. doi:10.1039/c2cs35026b.
- [148] H.-G. Jahnke, A. Heimann, R. Azendorf, K. Mpoukouvalas, O. Kempfski, A. a Robitzki, et al., Impedance spectroscopy-an outstanding method for label-free and real-time discrimination between brain and tumor tissue in vivo, *Biosens. Bioelectron*. 46 (2013) 8–14. doi:10.1016/j.bios.2013.02.013.
- [149] Y. Lee, O. Kwon, C.S. Shin, S.M. Lee, Use of bioelectrical impedance analysis for the assessment of nutritional status in critically III patients, *Clin. Nutr. Res*. 4 (2015) 32–40.
- [150] H. Kalvøy, L. Frich, S. Grimnes, O.G. Martinsen, P.K. Hol, A. Stubhaug, Impedance-based tissue discrimination for needle guidance, *Physiol. Meas*. 30 (2009) 129–140. doi:10.1088/0967-3334/30/2/002.
- [151] P. Daza, A. Olmo, D. Cañete, A. Yúfera, Monitoring living cell assays with bio-impedance sensors, *Sensors Actuators B Chem*. 176 (2013) 605–610. doi:10.1016/j.snb.2012.09.083.
- [152] S. Laufer, A. Ivorra, V.E. Reuter, B. Rubinsky, S.B. Solomon, Electrical impedance characterization of normal and cancerous human hepatic tissue., *Physiol. Meas*. 31 (2010) 995–1009. doi:10.1088/0967-3334/31/7/009.

- [153] D. Parramon, I. Erill, A. Guimerà, A. Ivorra, A. Muñoz, A. Sola, et al., In vivo detection of liver steatosis in rats based on impedance spectroscopy, *Physiol. Meas.* 28 (2007) 813–828. doi:10.1088/0967-3334/28/8/005.
- [154] A. Ivorra, M. Genescà, A. Sola, L. Palacios, R. Villa, G. Hotter, et al., Bioimpedance dispersion width as a parameter to monitor living tissues, *Physiol. Meas.* 26 (2005) S165–S173. doi:10.1088/0967-3334/26/2/016.
- [155] H. Kalvøy, Ø.G. Martinsen, S. Grimnes, Determination of tissue type surrounding a needle tip by electrical bioimpedance, 30th Annu. Int. Conf. IEEE Eng. Med. Biol. Soc. (2008) 2285–2286. doi:10.1109/IEMBS.2008.4649653.
- [156] D. Holder, Brief introduction to bioimpedance, in: *Electr. Impedance Tomogr., First Ed.*, Institute of Physics Publishing, London, UK, 2005: pp. 411–422.
- [157] R. Höber, Eine methode, die elektrische Leitfähigkeit im innern von zellen zu messen, *Pflüger's Arch. Für Die Gesamte Physiol. Des Menschen Und Der Tiere.* 133 (1910) 237–253.
- [158] R. Pethig, I. Schmueser, Marking 100 years since Rudolf Höber's discovery of the insulating envelope surrounding cells and of the beta-dispersion exhibited by tissue, *J. Electr. Bioimpedance.* 3 (2012) 74–79. doi:10.5617/jeb.401.
- [159] Ø.G. Martinsen, G. Sverre, History of bioimpedance and bioelectricity, in: Ø.G. Martinsen, S. Grimnes (Eds.), *Bioimpedance Bioelectr. Basics, Second Ed.*, Academic Press, Oxford, UK, 2008: pp. 313–319.
- [160] H.P. Schwan, Electrical properties of tissues and cell suspensions: mechanisms and models, *Adv. Biol. Med. Phys.* 5 (1957) 147–209. doi:10.1109/IEMBS.1994.412155.
- [161] Ø.G. Martinsen, S. Grimnes, H.P. Schwan, Interface phenomena and dielectric properties of biological tissue, *Encycl. Surf. Colloid Sci.* 20 (2002) 2643–2652.
- [162] H.P. Schwan, Electrode polarization impedance and measurements in biological materials, *Ann. N. Y. Acad. Sci.* 148 (1968) 191–209.
- [163] H.P. Schwan, Linear and nonlinear electrode polarization and biological materials, *Ann. Biomed. Eng.* 20 (1992) 269–288. doi:10.1007/BF02368531.
- [164] H.P. Schwan, C.D. Ferris, Four electrode nulltechniques for biological impedance work, in: D.A. Robinson (Ed.), 16th Annu. Conf. Eng. Med. Biol., Baltimore, Maryland, 1963: pp. 84–85.
- [165] H.P. Schwan, Biological effects of non-ionizing radiations: cellular properties and interactions, *Ann. Biomed. Eng.* 16 (1988) 245–263. doi:10.1007/BF02368002.
- [166] K.R. Foster, Herman P. Schwan: a scientist and pioneer in biomedical engineering, *Annu. Rev. Biomed. Eng.* 4 (2002) 1–27. doi:10.1146/annurev.bioeng.4.092001.093625.
- [167] Ø.G. Martinsen, S. Grimnes, O. Svein, Dielectric properties of some keratinised tissues. Part 1: stratum corneum and nail in situ, *Med. Biol. Eng. Comput.* 35 (1997) 172–176.
- [168] Ø.G. Martinsen, S. Grimnes, E.S. Kongshaug, Dielectric properties of some keratinised tissues. Part 2: human hair, *Med. Biol. Eng. Comput.* 35 (1997) 177–180. doi:10.1007/BF02530034.
- [169] C. Tronstad, G.E. Gjein, S. Grimnes, Ø.G. Martinsen, A.-L. Krogstad, E. Fosse, Electrical measurement of sweat activity, *Physiol. Meas.* 29 (2008) S407–S415. doi:10.1088/0967-3334/29/6/S34.
- [170] H. Kalvøy, G.K. Johnsen, Ø.G. Martinsen, S. Grimnes, New method for separation of electrode polarization impedance from measured tissue impedance, *Open Biomed. Eng. J.* 5 (2011) 8–13. doi:10.2174/1874120701105010008.
- [171] Ø.G. Martinsen, H. Kalvøy, S. Grimnes, B. Nordbotten, P.K. Hol, E. Fosse, et al., Invasive electrical impedance tomography for blood vessel detection, *Open Biomed. Eng. J.* 4 (2010) 135–137. doi:10.2174/1874120701004010135.
- [172] S. Grimnes, Electro-vibration, cutaneous sensation of microampere current, *Acta Physiol. Scand.* 118 (1983) 19–25.
- [173] Ø.G. Martinsen, Bioimpedance, *Pan Eur. Networks Sci. Technol.* (2014) 150–151.
- [174] Ø.G. Martinsen, G. Sverre, J. Karlsen, An instrument for the evaluation of skin hydration by electrical admittance measurements, *Innov. Technol. Biol. Med.* 14 (1993) 1993.
- [175] C. Tronstad, O. Elvebakk, J.O. Høgetveit, T.G. Jenssen, M.R. Bjørgaas, Ø.G. Martinsen, et al., Monitoring of sweat activity for detection of severe hypoglycemia - a pilot study, in: *IEEE Eng. Med. Biol. Soc.*, 2013.
- [176] P. Høyum, H. Kalvøy, Ø.G. Martinsen, S. Grimnes, A finite element model of needle electrode spatial sensitivity, *Physiol. Meas.* 31 (2010) 1369–1379. doi:10.1088/0967-3334/31/10/006.

- [177] S. Grimnes, Ø.G. Martinsen, *Bioimpedance and bioelectricity basics*, Third Ed., Academic Press, Oxford, UK, 2015.
- [178] A.J. Bard, L.R. Faulkner, *Techniques based on concepts of impedance*, in: *Electrochem. Methods Fundam. Appl.*, 2nd editio, John Wiley & Sons, Inc., New York, NY, USA, 2001: pp. 384–434.
- [179] V.F. Lvovich, Graphical representation of impedance spectroscopy data, in: V.F. Lvovich (Ed.), *Impedance Spectrosc. Appl. to Electrochem. Dielectr. Phenom.*, First Ed., John Wiley & Sons, Inc., Hoboken, New Jersey, 2012: pp. 23–35.
- [180] M.E. Orazem, B. Tribollet, The Kramers- Kronig relations, in: M.E. Orazem, B. Tribollet (Eds.), *Electrochem. Impedance Spectrosc.*, First Ed., Hoboken, NJ, USA, 2008.
- [181] P.T. Wojcik, P. Agarwal, M.E. Orazem, A method for maintaining a constant potential variation during galvanostatic regulation of electrochemical impedance measurements, *Electrochim. Acta.* 41 (1996) 977–983.
- [182] A.R. Heiskanen, C.F. Spe, N. Kostesha, T. Ruzgas, J. Emne, Monitoring of *Saccharomyces cerevisiae* cell proliferation on thiol-modified planar gold microelectrodes using impedance spectroscopy, *Langmuir.* 24 (2008) 9066–9073.
- [183] J.Y. Song, H.H. Lee, Y.Y. Wang, C.C. Wan, Two- and three-electrode impedance spectroscopy of lithium-ion batteries, *J. Power Sources.* 111 (2002) 255–267. doi:10.1016/S0378-7753(02)00310-5.
- [184] F. Sundfors, J. Bobacka, a Ivaska, a Lewenstam, Kinetics of electron transfer between Fe(CN)₆^{3-/4-} and poly(3,4-ethylenedioxythiophene) studied by electrochemical impedance spectroscopy, *Electrochim. Acta.* 47 (2002) 2245–2251. doi:10.1016/S0013-4686(02)00063-4.
- [185] P. Kassanos, L. Constantinou, I.F. Triantis, A. Demosthenous, An integrated analog readout for multi-frequency bioimpedance measurements, *IEEE Sens. J.* 14 (2014) 2792–2800. doi:10.1109/JSEN.2014.2315963.
- [186] P. Aberg, I. Nicander, J. Hansson, P. Geladi, U. Holmgren, S. Ollmar, Skin cancer identification using multifrequency electrical impedance - A potential screening tool, *IEEE Trans. Biomed. Eng.* 51 (2004) 2097–2102. doi:10.1109/TBME.2004.836523.
- [187] L. Fabrizi, A. McEwan, T. Oh, E.J. Woo, D.S. Holder, A comparison of two EIT systems suitable for imaging impedance changes in epilepsy, *Physiol. Meas.* 30 (2009) S103–S120. doi:10.1088/0967-3334/30/6/S07.
- [188] U.G. Kyle, I. Bosaeus, A.D. De Lorenzo, P. Deurenberg, M. Elia, J. Manuel Gómez, et al., Bioelectrical impedance analysis-part II: utilization in clinical practice, *Clin. Nutr.* 23 (2004) 1430–1453. doi:10.1016/j.clnu.2004.09.012.
- [189] H. Fujiwara, *Kramers–Kronig relations*, in: *Spectrosc. Ellipsom. Princ. Appl.*, 1st ed., John Wiley & Sons, Inc., West Sussex, England, 2007: pp. 357–360.
- [190] B. Boukamp, *Electrochemical impedance spectroscopy in solid state ionics: recent advances*, *Solid State Ionics.* 169 (2004) 65–73. doi:10.1016/j.ssi.2003.07.002.
- [191] Ø.G. Martinsen, S. Grimnes, *Instrumentation and measurement*, in: G. Martinsen, Ørjan Grøttem Sverre (Ed.), *Bioimpedance Bioelectr. Basics*, Second Ed., Academic Press, Oxford, UK, 2008: pp. 153–193.
- [192] D.D. Macdonald, Reflections on the history of electrochemical impedance spectroscopy, *Electrochim. Acta.* 51 (2006) 1376–1388. doi:10.1016/j.electacta.2005.02.107.
- [193] D.D. Macdonald, Application of Kramers-Kronig transforms in the analysis of electrochemical systems, *J. Electrochem. Soc.* 132 (1985) 2316–2319. doi:10.1149/1.2113570.
- [194] M. Urquidi-Macdonald, S. Real, D.D. Macdonald, Application of Kramers-Kronig transforms in the analysis of electrochemical impedance data II. Transformations in the complex plane, *J. Electrochem. Soc.* 133 (1986) 2018–2024. doi:10.1149/1.2113570.
- [195] M. Urquidi-Macdonald, S. Real, D.D. Macdonald, Applications of Kramers—Kronig transforms in the analysis of electrochemical impedance data—III. Stability and linearity, *Electrochim. Acta.* 35 (1990) 1559–1566.
- [196] S. Grimnes, Ø.G. Martinsen, G.K. Johnsen, Mutual localization of electrode pairs in a 4-electrode measuring system, *J. Phys. Conf. Ser.* 224 (2010) 012074. doi:10.1088/1742-6596/224/1/012074.
- [197] D.P.B.T.B. Strik, A. ter Heijne, H.V.M. Hamelers, M. Saakes, C.J.N. Buisman, Feasibility study on electrochemical impedance spectroscopy for microbial fuel cells: measurement modes and data validation, *ECS Trans.* 13 (2008) 27–41.

- [198] J.R. Macdonald, Analysis of impedance and admittance data for solids and liquids, *J. Electrochem. Soc.* 124 (1977) 1022. doi:10.1149/1.2133473.
- [199] Y.-Z. Wei, S. Sridhar, A new graphical representation for dielectric data, *J. Chem. Phys.* 99 (1993) 3119–3124. doi:10.1063/1.465165.
- [200] F. Lisdat, D. Schäfer, The use of electrochemical impedance spectroscopy for biosensing, *Anal. Bioanal. Chem.* 391 (2008) 1555–1567. doi:10.1007/s00216-008-1970-7.
- [201] F. Mansfeld, H. Shih, H. Greene, C.H.R. Tsai, Analysis of EIS data for common corrosion processes, in: J.R. Scully, D.C. Silverman (Eds.), *Electrochem. Impedance Anal. Interpret.*, 1st Ed., ASTM International, Philadelphia, PA; USA, 1993: pp. 37–53.
- [202] T. Ragheb, L.A. Geddes, Electrical properties of metallic electrodes, *Med. Biol. Eng. Comput.* 28 (1990) 182–186. doi:10.1007/BF02441775.
- [203] S. Yoon, J.H. Jang, B.H. Ka, S.M. Oh, Complex capacitance analysis on rate capability of electric-double layer capacitor (EDLC) electrodes of different thickness, *Electrochim. Acta.* 50 (2005) 2255–2262. doi:10.1016/j.electacta.2004.10.009.
- [204] X. Dominguez-Benetton, S. Sevda, K. Vanbroekhoven, D. Pant, The accurate use of impedance analysis for the study of microbial electrochemical systems, *Chem. Soc. Rev.* 41 (2012) 7228–46. doi:10.1039/c2cs35026b.
- [205] M.E. Orazem, B. Tribollet, An integrated approach to impedance spectroscopy, in: M.E. Orazem, B. Tribollet (Eds.), *Electrochem. Impedance Spectrosc.*, First Ed., John Wiley & Sons, Inc., Hoboken, New Jersey, 2008: pp. 449–459.
- [206] Ø.G. Martinsen, S. Grimnes, Data and models, in: Ø.G. Martinsen, S. Grimnes (Eds.), *Bioimpedance Bioelectr. Basics*, Second Ed., Academic Press, Oxford, UK, 2008: pp. 195–239.
- [207] A.J. Bard, J. de Paula, Double-layer structure and adsorption, in: A.J. Bard, J. de Paula (Eds.), *Electrochem. Methods Fundam. Appl.*, Eight Ed., John Wiley & Sons, Inc., New York, NY, USA, 2001: pp. 552–597.
- [208] E. Gileadi, E. Kirowa-Eisner, P. Penciner, *Interfacial electrochemistry. An experimental approach*, First Ed., Addison-Wesley Publishing Company, Inc, Massachusetts, MA, USA, 1975.
- [209] H.P. Schwan, Alternating current electrode polarization, *Biophysik.* 3 (1966) 181–201.
- [210] P. Mirtaheri, S. Grimnes, Ø.G. Martinsen, Electrode polarization impedance in weak NaCl aqueous solutions, *IEEE Trans. Biomed. Eng.* 52 (2005) 2093–2099. doi:10.1109/TBME.2005.857639.
- [211] A.M. Feltham, M. Spiro, Platinized platinum electrodes, *Chem. Rev.* 71 (1971) 177–193. doi:10.1021/cr60270a002.
- [212] P. Ben Ishai, M.S. Talary, A. Caduff, E. Levy, Y. Feldman, Electrode polarization in dielectric measurements: a review, *Meas. Sci. Technol.* 24 (2013) 102001. doi:10.1088/0957-0233/24/10/102001.
- [213] H. Cao, S. Tungjikusolmun, Y. Bin Choy, J.Z. Tsai, V.R. Vorperian, J.G. Webster, Using electrical impedance to predict catheter-endocardial contact during RF cardiac ablation, *IEEE Trans. Biomed. Eng.* 49 (2002) 247–253. doi:10.1109/10.983459.
- [214] C. Gabriel, S. Gabriel, E. Corthout, The dielectric properties of biological tissues .1. Literature survey, *Phys. Med. Biol.* 41 (1996) 2231–2249. doi:10.1088/0031-9155/41/11/001.
- [215] S. Gabriel, R.W. Lau, C. Gabriel, The dielectric properties of biological tissues: II. Measurements in the frequency range 10 Hz to 20 GHz., *Phys. Med. Biol.* 41 (1996) 2251–2269. doi:10.1088/0031-9155/41/11/002.
- [216] S. Gabriel, R.W. Lau, C. Gabriel, The dielectric properties of biological tissues: III. Parametric models for the dielectric spectrum of tissues., *Phys. Med. Biol.* 41 (1996) 2271–2293. doi:10.1088/0031-9155/41/11/003.
- [217] Y. Kinouchi, T. Iritani, T. Morimoto, S. Ohyama, Fast in vivo measurements of local tissue impedances using needle electrodes, *Med. Biol. Eng. Comput.* (1997) 486–492. <http://www.ncbi.nlm.nih.gov/pubmed/9374052>.
- [218] Ø.G. Martinsen, S. Grimnes, Geometrical analysis, in: G. Martinsen, Ørjan Grøttem Sverre (Ed.), *Bioimpedance Bioelectr. Basics*, 2nd ed., Academic Press, 2008: pp. 127–152.
- [219] H. Kalvøy, L. Frich, S. Grimnes, O.G. Martinsen, P.K. Hol, A. Stubhaug, Impedance-based tissue discrimination for needle guidance., *Physiol. Meas.* 30 (2009) 129–140. doi:10.1088/0967-3334/30/2/002.

- [220] H.P. Schwan, Electrode polarization impedance and measurements in biological materials, *Ann. N. Y. Acad. Sci.* 148 (1968) 191–209. <http://onlinelibrary.wiley.com/doi/10.1111/j.1749-6632.1968.tb20349.x/abstract>.
- [221] C. Davey, H. Davey, D. Kell, On the dielectric properties of cell suspensions at high volume fractions, *J. Electroanal. Chem.* 343 (1992) 319–340. doi:10.1016/0302-4598(92)80023-A.
- [222] S. Grimnes, Ø.G. Martinsen, Sources of error in tetrapolar impedance measurements on biomaterials and other ionic conductors, *J. Phys. D. Appl. Phys.* 40 (2007) 9–14. doi:10.1088/0022-3727/40/1/S02.
- [223] Ø.G. Martinsen, S. Grimnes, Geometrical analysis, in: Ø.G. Martinsen, S. Grimnes (Eds.), *Bioimpedance Bioelectr. Basics*, 2nd Ed., Academic Press, Oxford, UK, 2008: pp. 127–152.
- [224] C.F. Coombs, *Electronic instrument handbook - Basics of electronic instrumentation*, Third Ed., McGraw-Hill, New York, NY, USA, 2000.
- [225] S. Grimnes, Ø.G. Martinsen, *Bioimpedance*, *Encycl. Biomed. Eng.* (2006) 1–9.
- [226] J. Malmivuo, Principle of reciprocity solves the most important problems in bioimpedance and in general in bioelectromagnetism, in: *J. Phys. Conf. Ser.*, 2010. doi:10.1088/1742-6596/224/1/012001.
- [227] P. Bertemes-Filho, B.H. Brown, R.H. Smallwood, A.J. Wilson, Tetrapolar probe measurements: can the sensitivity distribution be improved?, in: *XI Int. Conf. Electr. Bio-Impedance*, Oslo, 2001: pp. 561–564. doi:10.1017/CBO9781107415324.004.
- [228] B.H. Brown, A.J. Wilson, P. Bertemes-Filho, Bipolar and tetrapolar transfer impedance measurements from volume conductor, *Electron. Lett.* 36 (2000) 5–6.
- [229] S. Oh, T. Tang, A.S. Tucker, R.J. Sadleir, Normalization of a spatially variant image reconstruction problem in electrical impedance tomography using system blurring properties, *Physiol. Meas.* 30 (2009) 275–289. doi:10.1016/j.biotechadv.2011.08.021.Secreted.
- [230] F.-J. Pettersen, J.O. Høgetveit, From 3D tissue data to impedance using Simpleware ScanFE+IP and COMSOL Multiphysics – a tutorial, *J. Electr. Bioimpedance*. 2 (2011) 13–32. doi:10.5617/jeb.173.
- [231] K. Hollaus, R. Stollberger, B. Wagner, C. Gerstenberger, C. Magele, H. Hutten, Simulations of the bioimpedance of the human thigh by the finite element method in 3D, in: *48 Int. Wissenschaftliches Kolloquium*, Illmenau, 2003: pp. 8–9.
- [232] H. Scharfetter, P. Brunner, M. Mayer, B. Brandstätter, H. Hinghofer-Szalkay, Fat and hydration monitoring by abdominal bioimpedance analysis: Data interpretation by hierarchical electrical modeling, *IEEE Trans. Biomed. Eng.* 52 (2005) 975–982. doi:10.1109/TBME.2005.846733.
- [233] M. Pidcock, S. Ciulli, S. Ispas, Some boundary problems in electrical impedance tomography, *Physiol. Meas.* 17 Suppl 4 (1996) A91–A96.
- [234] M. Stasiak, J. Sikora, S.F. Filipowicz, 3D electrical impedance tomography forward problem solution approximated by boundary element method, in: *Comput. Probl. Electr. Eng.*, 2004: pp. 123–126.
- [235] A. Nissinen, V. Kolehmainen, J.P. Kaipio, Reconstruction of domain boundary and conductivity in electrical impedance tomography using the approximation error approach, *Int. J. Uncertain. Quantif.* 1 (2011) 203–222. doi:10.1615/Int.J.UncertaintyQuantification.v1.i3.20.
- [236] T. Munson, *Optimizing the quality of mesh elements*, Argonne, IL, USA, 2005.
- [237] J.-F. Remacle, P. Dular, F. Henrotte, a. Genon, W. Legros, Error estimation and mesh optimisation using error in constitutive relation for electromagnetic field computation, *IEEE Trans. Magn.* 31 (1995) 3587–3589. doi:10.1109/20.489578.
- [238] U. Hetmaniuk, P. Knupp, A mesh optimization algorithm to decrease the maximum error in finite element computations, in: *Proc. 17th Int. Meshing Roundtable*, 2008: pp. 533–550.
- [239] C.C. Pain, a. P. Umpheby, C.R.E. de Oliveira, a. J.H. Goddard, Tetrahedral mesh optimisation and adaptivity for steady-state and transient finite element calculations, *Comput. Methods Appl. Mech. Eng.* 190 (2001) 3771–3796. doi:10.1016/S0045-7825(00)00294-2.
- [240] F. Cakoni, D. Colton, eds., *Ill-posed problems*, in: *Qual. Methods Inverse Scatt. Theory*, 1st ed., Springer, Heidelberg, Germany, 2006: pp. 27–43.
- [241] S. Stefanescu, C. Schlumberger, M. Schlumberger, Sur la distribution électrique potentielle autour d'une prise de terre ponctuelle dans un terrain à couches horizontales, homogènes et isotropes, *J. Phys. Le Radium*. 1 (1930) 132–140. doi:10.1051/jphysrad:0193000104013200.
- [242] F.F. Segesman, Well-logging method, *Geophysics*. 45 (1980) 1667–1684.

- [243] a. Samouëlian, I. Cousin, a. Tabbagh, a. Bruand, G. Richard, Electrical resistivity survey in soil science: A review, *Soil Tillage Res.* 83 (2005) 173–193. doi:10.1016/j.still.2004.10.004.
- [244] C. Schlumberger, M. Schlumberger, E.G. Leonardon, Electrical coring: A method of determining bottom-hole data by electrical measurements, *Trans. AIME.* 110 (1934) 237–272.
- [245] T. York, Status of electrical tomography in industrial applications, *J. Electron. Imaging.* 10 (2001) 608. doi:10.1117/1.1377308.
- [246] C.G. Xie, N. Reinecke, M.S. Beck, D. Mewes, R. a. Williams, Electrical tomography technique for process engineering applications, *Chem. Eng. J.* 56 (1995) 127–133.
- [247] R. Bayford, A. Tizzard, Bioimpedance imaging: an overview of potential clinical applications, *Analyst.* 137 (2012) 4635. doi:10.1039/c2an35874c.
- [248] M. Abbasi, A.-R. Naghsh-Nilchi, Precise two-dimensional D-bar reconstructions of human chest and phantom tank via sinc-convolution algorithm, *Biomed. Eng. Online.* 11 (2012) 1–22. doi:10.1186/1475-925X-11-34.
- [249] M. Bodenstein, M. David, K. Markstaller, Principles of electrical impedance tomography and its clinical application, *Crit. Care Med.* 37 (2009) 713–724. doi:10.1097/CCM.0b013e3181958d2f.
- [250] Z. Zhao, D. Steinmann, I. Frerichs, J. Guttmann, K. Möller, PEEP titration guided by ventilation homogeneity: a feasibility study using electrical impedance tomography, *Crit. Care.* 14 (2010) R8. doi:10.1186/cc8860.
- [251] R.P. Henderson, J.G. Webster, An impedance camera for spatially specific measurements of the thorax, *IEEE Trans. Biomed. Eng.* 25 (1978) 250–254. doi:10.1109/TBME.1978.326329.
- [252] D.C. Barber, B.H. Brown, Applied potential tomography, *J. Phys. Sci. Instruments.* 17 (1984) 723–733. doi:10.1088/0022-3735/17/9/002.
- [253] C.C. Barber, B.H. Brown, I.L. Freeston, Imaging spatial distributions of resistivity using applied potential tomography, *Electron. Lett.* 19 (1983) 933. doi:10.1049/el:19830637.
- [254] J. Kaipio, E. Somersalo, *Statistical and computational inverse problems*, First Ed., Sprin, New York, NY, USA, 2005.
- [255] M. Vauhkonen, W.R. Lionheart, L.M. Heikkinen, P.J. Vauhkonen, J.P. Kaipio, A MATLAB package for the EIDORS project to reconstruct two-dimensional EIT images, *Physiol. Meas.* 22 (2001) 107–111. doi:10.1088/0967-3334/22/1/314.
- [256] W. Lionheart, N. Polydorides, A. Borsic, The reconstruction problem, in: D.S. Holder (Ed.), *Electr. Impedance Tomogr.*, First Ed., Institute of Physics Publishing, London, UK, 2005. doi:10.1201/9781420034462.pt1.
- [257] a Borsic, a Adler, A primal–dual interior-point framework for using the L1 or L2 norm on the data and regularization terms of inverse problems, *Inverse Probl.* 28 (2012) 095011. doi:10.1088/0266-5611/28/9/095011.
- [258] B.M. Graham, A. Adler, Electrode placement configurations for 3D EIT, *Physiol. Meas.* 28 (2007) S29–S44. doi:10.1088/0967-3334/28/7/S03.
- [259] A. Boyle, A. Adler, The impact of electrode area, contact impedance and boundary shape on EIT images, *Physiol. Meas.* 32 (2011) 745–54. doi:10.1088/0967-3334/32/7/S02.
- [260] A. Biguri, B. Grychtol, A. Adler, M. Soleimani, Tracking boundary movement and exterior shape modelling in lung EIT imaging, *Physiol. Meas.* 36 (2015) 1119–1135. doi:10.1088/0967-3334/36/6/1119.
- [261] M. Proença, F. Braun, M. Rapin, J. Solà, A. Adler, B. Grychtol, et al., Influence of heart motion on cardiac output estimation by means of electrical impedance tomography: a case study, *Physiol. Meas.* 36 (2015) 1075–1091. doi:10.1088/0967-3334/36/6/1075.
- [262] T. Tidswell, A. Gibson, R.H. Bayford, D.S. Holder, Three-dimensional electrical impedance tomography of human brain activity, *Neuroimage.* 13 (2001) 283–294. doi:10.1006/nimg.2000.0698.
- [263] A. McEwan, A. Romsauerova, R. Yerworth, L. Horesh, R. Bayford, D. Holder, Design and calibration of a compact multi-frequency EIT system for acute stroke imaging, *Physiol. Meas.* 27 (2006) S199–S210. doi:10.1088/0967-3334/27/5/S17.
- [264] K. Boone, a M. Lewis, D.S. Holder, Imaging of cortical spreading depression by EIT: implications for localization of epileptic foci, *Physiol. Meas.* 15 (1994) A189–A198. doi:10.1088/0967-3334/15/2A/024.

- [265] K.Y. Aristovich, G.S. dos Santos, B.C. Packham, D.S. Holder, A method for reconstructing tomographic images of evoked neural activity with electrical impedance tomography using intracranial planar arrays, *Physiol. Meas.* 35 (2014) 1095–109. doi:10.1088/0967-3334/35/6/1095.
- [266] T. Sun, S. Tsuda, K.-P. Zauner, H. Morgan, On-chip electrical impedance tomography for imaging biological cells, *Biosens. Bioelectron.* 25 (2010) 1109–1115. doi:10.1016/j.bios.2009.09.036.
- [267] K. Wu, J. Yang, X. Dong, F. Fu, F. Tao, S. Liu, et al., Comparative study of reconstruction algorithms for electrical impedance tomography, *IEEE Trans. Biomed. Eng.* (2012) 2296–2299.
- [268] A. Adler, J.H. Arnold, R. Bayford, A. Borsic, B. Brown, P. Dixon, et al., GREIT: a unified approach to 2D linear EIT reconstruction of lung images, *Physiol. Meas.* 30 (2009) S35–S55. doi:10.1088/0967-3334/30/6/S03.
- [269] P. Kauppinen, J. Hyttinen, J. Malmivuo, Sensitivity distribution simulations of impedance tomography electrode combinations, *Int. J. Bioelectromagn.* 7 (2006) 344–347.
- [270] J. Malmivuo, R. Plonsey, *Impedance Tomography*, in: *Bioelectromagn. - Princ. Appl. Bioelectric Biomagn. Fields*, 1st ed., Oxford University Press, New York, NY, USA, 1995: pp. 1012–1022.
- [271] D. Stephenson, J. Davidson, W.R.B. Lionheart, B.D. Grieve, T. a York, Comparison of 3D image reconstruction techniques using real electrical impedance measurement data, in: *4th World Congr. Ind. Process Tomogr.*, Aizu, Japan, 2005: pp. 1–8. <http://eprints.ma.man.ac.uk/1221>.
- [272] S. Dmitry, A 2D and 3D electrical impedance tomography imaging using experimental data, in: *11th Conf. Telecommun. Comput. Sci., Lviv-Slavske, Ukraine, n.d.*: p. 61070.
- [273] R. Duraiswami, K. Sarkar, G.L. Chahine, Efficient 2D and 3D electrical impedance tomography using dual reciprocity boundary element techniques, *Eng. Anal. Bound. Elem.* 22 (1998) 13–31. doi:10.1016/S0955-7997(98)00028-9.
- [274] K.G. Boone, D.S. Holder, Current approaches to analogue instrumentation design in electrical impedance tomography, *Physiol. Meas.* 17 (1996) 229–247. doi:10.1088/0967-3334/17/4/001.
- [275] J. Chen, L. Xu, S. Member, Z. Cao, H. Zhou, Four-terminal imaging using a two-terminal electrical impedance tomography system, *IEEE Trans. Instrum. Meas.* 63 (2014) 432–440.
- [276] B.H. Brown, Electrical impedance tomography (EIT): a review, *J. Med. Eng. Technol.* 27 (2003) 97–108. doi:10.1080/0309190021000059687.
- [277] D. Holder, *Electrical impedance tomography of brain function*, in: I. of P. Publishing (Ed.), *Electr. Impedance Tomogr.*, 1st ed., Bristol, 2005: pp. 127–166. doi:10.3389/conf.fnins.2010.05.00003.
- [278] P.J. Vauhkonen, M. Vauhkonen, T. Savolainen, J.P. Kaipio, *Static Three Dimensional Electrical Impedance Tomography*, Dep. Appl. Physics, Univ. Kuopio. (1992) 0–3.
- [279] K.Y. Kim, S.I. Kang, M.C. Kim, S. Kim, Y.J. Lee, M. Vauhkonen, Dynamic electrical impedance tomography with known internal structures, *Inverse Probl. Eng.* 11 (2003) 1–19. doi:10.1080/1068276021000014705.
- [280] J.K. Seo, B. Harrach, E.J. Woo, Recent progress on frequency difference electrical impedance tomography, *ESAIM Proc.* 26 (2009) 150–161. doi:10.1051/proc/2009011.
- [281] a McEwan, G. Cusick, D.S. Holder, A review of errors in multi-frequency EIT instrumentation, *Physiol. Meas.* 28 (2007) S197–S215. doi:10.1088/0967-3334/28/7/S15.
- [282] D. Holder, *Introduction to biomedical electrical impedance tomography*, in: *Electr. Impedance Tomogr.*, 1st ed., Institute of Physics Publishing, Bristol, 2005: pp. 423–449.
- [283] M.S. Campisi, C. Barbre, A. Chola, G. Cunningham, J. Viventi, Breast cancer detection using high-density flexible electrode arrays and electrical impedance tomography, *IEEE Eng. Med. Biol. Soc.* (2014) 1131–1134.
- [284] R.J. Halter, A. Hartov, S.P. Poplack, W.A. Wells, K.M. Rosenkranz, R.J. Barth, et al., Real-Time electrical impedance variations in women with and without breast cancer, *IEEE Trans. Med. Imaging.* 34 (2015) 38–48.
- [285] M. Mhajna, S. Abboud, Assessment of cardiac stroke volume in patients with implanted cardiac pacemaker using parametric electrical impedance tomography: a theoretical 2D study, *Int. J. Numer. Method. Biomed. Eng.* 28 (2012) 72–86. doi:10.1002/cnm.
- [286] B. Packham, H. Koo, a Romsauerova, S. Ahn, a McEwan, S.C. Jun, et al., Comparison of frequency difference reconstruction algorithms for the detection of acute stroke using EIT in a realistic head-shaped tank, *Physiol. Meas.* 33 (2012) 767–786. doi:10.1088/0967-3334/33/5/767.
- [287] D.S. Holder, *Electrical impedance tomography (EIT) of brain function*, *Brain Topogr.* 5 (1992) 87–93.

- [288] A.P. Bagshaw, A.D. Liston, R.H. Bayford, A. Tizzard, A.P. Gibson, a. T. Tidswell, et al., Electrical impedance tomography of human brain function using reconstruction algorithms based on the finite element method, *Neuroimage*. 20 (2003) 752–764. doi:10.1016/S1053-8119(03)00301-X.
- [289] B. Amm, T. Kao, X. Wang, G. Boverman, J. Sabatini, J. Ashe, et al., Real-time 3D electrical impedance imaging for ventilation monitoring of the lung: pilot study, *IEEE Eng. Med. Biol. Soc.* (2014) 6064–6067.
- [290] H. Reinius, J.B. Borges, F. Fredén, L. Jideus, E.D.L.B. Camargo, M.B.P. Amato, et al., Real-time ventilation and perfusion distributions by electrical impedance tomography during one-lung ventilation with capnothorax, *Acta Anaesthesiol. Scand.* 59 (2015) 354–368. doi:10.1111/aas.12455.
- [291] F. Podczeck, C.L. Mitchell, J.M. Newton, D. Evans, M.B. Short, The gastric emptying of food as measured by gamma-scintigraphy and electrical impedance tomography (EIT) and its influence on the gastric emptying of tablets of different dimensions, *J. Pharm. Pharmacol.* 59 (2007) 1527–1536. doi:10.1211/jpp.59.11.0010.
- [292] C.T. Soulsby, M. Khela, E. Yazaki, D.F. Evans, E. Hennessy, J. Powell-Tuck, Measurements of gastric emptying during continuous nasogastric infusion of liquid feed: Electric impedance tomography versus gamma scintigraphy, *Clin. Nutr.* 25 (2006) 671–680. doi:10.1016/j.clnu.2005.11.015.
- [293] R.H. Bayford, Bioimpedance tomography (electrical impedance tomography), *Annu. Rev. Biomed. Eng.* 8 (2006) 63–91. doi:10.1146/annurev.bioeng.8.061505.095716.
- [294] S. Oh, R. Sadleir, Compensating spatial variability of quantity index (QI) in 2D electrical impedance tomography (EIT), in: *COMSOL Conf. 2007*, Boston, MA; USA, 2007.
- [295] S. Oh, T. Tang, R. Sadleir, Quantitative analysis of shape change in electrical impedance tomography (EIT), in: H. Scharfetter, R. Merwa (Eds.), *13th Int. Conf. Electr. Bioimpedance 8th Conf. Electr. Impedance Tomogr.*, Graz, Austria, 2007: pp. 424–427. <http://www.springerlink.com/index/t7385370372p7785.pdf>.
- [296] J.L.L. Queiroz, Influence of regularization in image reconstruction in electrical impedance tomography, *J. Phys. Conf. Ser.* 407 (2012) 012006. doi:10.1088/1742-6596/407/1/012006.
- [297] N. Polydorides, H. McCann, Electrode configurations for improved spatial resolution in electrical impedance tomography, *Meas. Sci. Technol.* 13 (2002) 1862–1870. doi:10.1088/0957-0233/13/12/309.
- [298] J. Liu, H. Xiong, L. Lin, G. Li, Evaluation of measurement and stimulation patterns in open electrical impedance tomography with scanning electrode, *Med. Biol. Eng. Comput.* 53 (2015) 589–597. doi:10.1007/s11517-015-1274-y.
- [299] B. de Lema, P. Casan, P. Riu, Electrical impedance tomography: standardizing the procedure in pneumology, *Arch. Bronconeumol.* 42 (2006) 299–301. doi:10.1016/S1579-2129(06)60146-8.
- [300] P. Linderholm, T. Braschler, J. Vannod, Y. Barranton, M. Brouard, P. Renaud, Two-dimensional impedance imaging of cell migration and epithelial stratification, *Lab Chip*. 6 (2006) 1155–1162. doi:10.1039/b603856e.
- [301] a R. a Rahman, J. Register, G. Vuppala, S. Bhansali, Cell culture monitoring by impedance mapping using a multi-electrode scanning impedance spectroscopy system (CellMap), *Physiol. Meas.* 29 (2008) S227–39. doi:10.1088/0967-3334/29/6/S20.
- [302] T. Sun, S. Tsuda, K.-P. Zauner, H. Morgan, On-chip electrical impedance tomography for imaging biological cells, *Biosens. Bioelectron.* 25 (2010) 1109–1115. doi:10.1016/j.bios.2009.09.036.
- [303] A. Meir, B. Rubinsky, Electrical impedance tomographic imaging of a single cell electroporation, *Biomed. Microdevices*. 16 (2014) 427–37. doi:10.1007/s10544-014-9845-5.
- [304] E.J. Lee, H. Wi, A.L. Mcewan, A. Farooq, H. Sohal, E.J. Woo, et al., Design of a microscopic electrical impedance tomography system for 3D continuous non-destructive monitoring of tissue culture, *Biomed. Eng. Online*. 13 (2014) 1–15.
- [305] E. Lee, J.K. Seo, E.J. Woo, T. Zhang, Mathematical framework for a new microscopic electrical impedance tomography system, *Inverse Probl.* 27 (2011) 055008. doi:10.1088/0266-5611/27/5/055008.
- [306] T. Dai, C. Gómez-Laberge, A. Adler, Reconstruction of conductivity changes and electrode movements based on EIT temporal sequences, *Physiol. Meas.* 29 (2008) S77–S88. doi:10.1088/0967-3334/29/6/S07.
- [307] P. Kauppinen, J. Hyttinen, J. Malmivuo, Sensitivity distribution visualizations of impedance tomography measurement strategies, *Int. J. Bioelectromagn.* 8 (2006) 1–9.
- [308] B.H. Brown, a D. Seagar, The Sheffield data collection system, *Clin. Phys. Physiol. Meas. Physiol. Meas.* 8 Suppl A (1987) 91–97. doi:10.1088/0143-0815/8/4A/012.

- [309] R. Harikumar, R. Prabu, S. Raghavan, Electrical Impedance Tomography (EIT) and its medical applications: a review, *Int. J. Soft Comput. Eng.* 3 (2013) 193–198.
- [310] A. Adler, P.O. Gaggero, Y. Maimaitijiang, Adjacent stimulation and measurement patterns considered harmful, *Physiol. Meas.* 32 (2011) 731–744. doi:10.1088/0967-3334/32/7/S01.
- [311] M. Tang, W. Wang, J. Wheeler, M. McCormick, X. Dong, The number of electrodes and basis functions in EIT image reconstruction, *Physiol. Meas.* 23 (2002) 129–140. doi:10.1088/0967-3334/23/1/312.
- [312] P. Hua, J. Webster, W. Tompkins, Effect of the measurement method on noise handling and image quality of EIT imaging, in: *IEEE Eng. Med. Biol. Soc.*, 1987: pp. 1429–1430.
- [313] L. Zhang, Image reconstruction algorithm for electrical impedance tomography using updated sensitivity matrix, in: *2011 Int. Conf. Soft Comput. Pattern Recognit.*, Ieee, Dalian, China, 2011: pp. 248–252. doi:10.1109/SoCPaR.2011.6089115.
- [314] J.P. Morucci, M. Granie, M. Lei, M. Chabert, W.W. Dai, Direct sensitivity matrix approach for fast 3-D reconstruction in electrical impedance imaging, in: *16th Annu. Int. Conf. IEEE Eng. Med. Biol. Soc.*, 1994: pp. 4–5. doi:10.1109/IEMBS.1994.411915.
- [315] J.P. Morucci, P.M. Marsili, M. Granié, Y. Shi, M. Lei, W.W. Dai, A direct sensitivity matrix approach for fast reconstruction in electrical impedance tomography, *Physiol. Meas.* 15 (1994) A107–A114. doi:10.1088/0967-3334/15/2A/015.
- [316] Y.-B. He, H.-X. Wang, D. Sankowski, Analysis of electrical impedance tomography sensitive field based on multi-terminal network, *Automatika.* 12 (2008) 903–909.
- [317] D. Holder, Introduction to biomedical electrical impedance tomography, in: *Electr. Impedance Tomogr.*, First Ed., Institute of Physics Publishing, London, UK, 2005: pp. 423–449.
- [318] M. Cheney, D. Isaacson, J.C. Newell, Electrical impedance tomography, *SIAM Rev.* 41 (2008) 85–101. doi:10.1007/s00101-007-1273-y.
- [319] J. Nasehi Tehrani, a. McEwan, C. Jin, a. van Schaik, L1 regularization method in electrical impedance tomography by using the L1-curve (Pareto frontier curve), *Appl. Math. Model.* 36 (2012) 1095–1105. doi:10.1016/j.apm.2011.07.055.
- [320] N. Polydorides, W.R.B. Lionheart, A Matlab toolkit for three-dimensional electrical impedance tomography: a contribution to the Electrical Impedance and Diffuse Optical Reconstruction Software project, *Meas. Sci. Technol.* 13 (2002) 1871–1883. doi:10.1088/0957-0233/13/12/310.
- [321] A. Adler, A. Borsic, N. Polydorides, W.R.B. Lionheart, Simple FEMs aren't as good as we thought: experiences developing EIDORS v3.3, in: *9th EIT Conf.* 2008, Dartmouth College, New Hampshire, UK, 2008: pp. 1–4. doi:10.1111/j.1567-1364.2010.00649.x.
- [322] K.J. Alme, S. Mylvaganam, Analyzing 3D and conductivity effects in electrical tomography systems using COMSOL multiphysics EM module, in: *Proc. 2006 Nord. COMSOL Conf.*, 2006. <http://www.comsol.fr/papers/1678/download/Alme.pdf>.
- [323] A. Just, C. Rücker, G. Hahn, G. Hellige, Sensitivity of two different reconstruction algorithms to body shape and electrode position errors in absolute EIT, in: *8th Conf. Electr. Impedance Tomogr.*, Vienna, 2007: pp. 404–407.
- [324] S. Oh, R. Sadleir, Sensitivity distribution field of electrical impedance tomography, in: *COMSOL Conf.* 2005, Boston, MA, USA, 2005.
- [325] N.G. Gençer, M. Kuzuoğlu, Y.Z. İder, Sensitivity matrix analysis of the back-projection algorithm in electrical impedance tomography, in: *Eng. Med. Biol. Soc. 1992 14th Annu. Int. Conf. IEEE*, 1992: pp. 1682–1683.
- [326] J.L. Davidson, C.J.D. Pomfrett, H. McCann, Predicted EIT current densities in the brain using a 3D anatomically realistic model of the head, in: *8th Conf. Electr. Impedance Tomogr.*, Vienna, 2007: pp. 376 – 379.
- [327] L.J. North, A.I. Best, Anomalous electrical resistivity anisotropy in clean reservoir sandstones, *Geophys. Prospect.* 62 (2014) 1315–1326. doi:10.1111/1365-2478.12183.
- [328] A. Adler, W.R.B. Lionheart, Uses and abuses of EIDORS: an extensible software base for EIT, *Physiol. Meas.* 27 (2006) S25–S42. doi:10.1088/0967-3334/27/5/S03.
- [329] W. Zhang, J. Zhang, G. Li, Main menu full waveform tomography with consideration for large topography variations, in: *SEG Tech. Progr. Expand. Abstr.* 2011, Society of Exploration Geophysicists, San Antonio, 2011: pp. 2539–2542.

- [330] P. Linderholm, T. Braschler, J. Vannod, Y. Barranton, M. Brouard, P. Renaud, Two-dimensional impedance imaging of cell migration and epithelial stratification, *Lab Chip*. 6 (2006) 1155–62. doi:10.1039/b603856e.
- [331] M. Jehl, A. Dedner, T. Betcke, K. Aristovich, R. Kloforn, D. Holder, A fast parallel solver for the forward problem in electrical impedance tomography, *IEEE Trans. Biomed. Eng.* 9294 (2014) 1–13. doi:10.1109/TBME.2014.2342280.
- [332] T.J. Yorkey, J.G. Webster, A comparison of impedance tomographic reconstruction algorithms, *Clin. Phys. Physiol. Meas.* 8 (1987) 55–62.
- [333] Z. Zhou, G.S. dos Santos, T. Dowrick, J. Avery, Z. Sun, H. Xu, et al., Comparison of total variation algorithms for electrical impedance tomography, *Physiol. Meas.* 36 (2015) 1193–1209. doi:10.1088/0967-3334/36/6/1193.
- [334] A.M. Martins, G. Eng, S.G. Caridade, J.F. Mano, R.L. Reis, G. Vunjak-Novakovic, Electrically conductive chitosan/carbon scaffolds for cardiac tissue engineering, *Biomacromolecules*. 15 (2014) 635–643. doi:10.1021/bm401679q.
- [335] H. Baniyadi, A. Ramazani S.A., S. Mashayekhan, Fabrication and characterization of conductive chitosan/gelatin-based scaffolds for nerve tissue engineering, *Int. J. Biol. Macromol.* 74 (2015) 360–366. doi:10.1016/j.ijbiomac.2014.12.014.
- [336] J. Rouwkema, S. Gibbs, M.P. Lutolf, I. Martin, G. Vunjak-Novakovic, J. Malda, In vitro platforms for tissue engineering: implications for basic research and clinical translation., *J. Tissue Eng. Regen. Med.* 5 (2011) e164–7. doi:10.1002/term.414.
- [337] K.F. Lei, M.-H. Wu, P.-Y. Liao, Y.-M. Chen, T.-M. Pan, Development of a micro-scale perfusion 3D cell culture biochip with an incorporated electrical impedance measurement scheme for the quantification of cell number in a 3D cell culture construct, *Microfluid. Nanofluidics*. 12 (2011) 117–125. doi:10.1007/s10404-011-0854-x.
- [338] C. Canali, A. Heiskanen, H.B. Muhammad, P. Høyum, F.J. Pettersen, M. Hemmingsen, et al., Bioimpedance monitoring of 3D cell culturing-Complementary electrode configurations for enhanced spatial sensitivity, *Biosens. Bioelectron.* (2015). doi:10.1016/j.bios.2014.07.020.

APPENDIX I

Publications and Submitted Manuscripts

Paper I

Impedance-based monitoring for tissue engineering applications

C. Canali, A. Heiskanen, Ø. G. Martinsen, S. Mohanty, M. Dufva, A. Wolff
and J. Emnéus

International Federation for Medical and Biological Engineering
(IFMBE) proceeding of in the 2nd Latin-American Conference on
Bioimpedance (*CLABIO*, September 30 – October 2 2015, Montevideo,
Uruguay)

Impedance-based monitoring for tissue engineering applications

C. Canali¹, A. Heiskanen¹, Ø.G. Martinsen^{2,3}, S. Mohanty¹, M. Dufva¹, A. Wolff¹ and J. Emnéus¹

¹ Department of Micro- and Nanotechnology, Technical University of Denmark, Kgs. Lyngby, Denmark

² Department of Physics, University of Oslo, Oslo, Norway

³ Department of Biomedical and Clinical Engineering, Oslo University Hospital, Oslo, Norway

Abstract— Impedance is a promising technique for sensing the overall process of tissue engineering. Different electrode configurations can be used to characterize the scaffold that supports cell organization in terms of hydrogel polymerization and degree of porosity, monitoring cell loading, cell proliferation as well as the spatial distribution of cell aggregates in 3D. We have previously shown that impedance measurements allow accurate determination of conductivity in physiological solutions independent of validation and analysis of a specific equivalent circuit. Similarly to a physiological solution, cell culture medium conductivity, and hence the measured impedance, can respond to proliferating or dying cells populating the scaffold. Impedance may therefore be a key parameter for monitoring the biochemical dynamics that modulate 3D mammalian cell cultures over time. Furthermore, the conductivity of the medium filling the pores of the scaffold can serve as the basis for porosity determination using Archie's law. Different networks of structured or random channels and degree of porosity can be detected. In addition, by combining a number of two-, three- and four-terminal (2T, 3T, 4T) configurations, it is possible to obtain complementary information on spatial distribution of cells in a 3D scaffold. 2T- and 3T configurations also reflect the impedance at the interface between an electrode and cell-loaded scaffold (polarization impedance, Z_p), which may convey a further degree of information about the biochemical phenomena taking place in that sub-volume.

Keywords—Impedance, Electrode configurations, Scaffold porosity, Cell aggregate distribution in 3D cultures, Tissue engineering

I. INTRODUCTION

Tissue engineering was first defined by Langer and Vacanti in 1993 as an interdisciplinary field that applies the principles of engineering (materials science and biomedical engineering) and life sciences (biochemistry, genetics, cell and molecular biology) to the development of biological substitutes which can reestablish, maintain, or enhance tissue functions [1]. Biological tissues can be fabricated in vitro by combining biomimetic 3D matrices ("scaffolds") of appropriate stiffness [2] and chemical composition, cells, and biologically active molecules (e.g. growth factors and hormones) [3]. Such 3D environments have been shown to

better reflect the essential cellular functions and increase the predictive power of cell-based drug and toxicity screening [4]. However, a major technological challenge in tissue engineering is the non-invasive on-line monitoring of the 3D organizational complexity, comprising scaffold characterization, cell loading and proliferation. From the early studies on 2D cultures, a number of label-free techniques have emerged, capable of determining the cell-substrate interactions in a non-invasive and real-time manner. These include electrical impedance spectroscopy (EIS), quartz crystal microbalance, refractive index based techniques [5] and microscopic imaging [6]. The latter approach needs to be optimized for tissue engineering applications, especially when using large 3D scaffolds that do not allow deep light penetration. Additionally, the scaffold should be optically transparent and composed of materials with low autofluorescence [4, 7].

In 1984, Giæver and Keese proposed the use of EIS to monitor cell adhesion, spreading and proliferation on a flat surface by relying on the insulating properties of cell membrane, which affect the electrode/electrolyte interface (polarization impedance, Z_p) [8]. Such measurements opened up new perspectives for monitoring of, e.g., cell motility [9], wound-healing [10] and cytotoxicity [11]. However, tissue engineering and 3D culturing systems warrant further advances in impedance-based sensing to gather insights into scaffold architecture and porosity, spatial distribution of cells and chemical changes related to cell proliferation and cell-scaffold interactions. For such purposes, technical solutions can be adapted from physiological impedance measurements, which have been widely described by Grimnes and Martinsen and defined as bioimpedance [12]. In this context, miniaturization and the need for continuous long-term measurements make electrode position and stability, respectively, crucial factors influencing the measurements. Moreover, electrode number, spacing and orientation should be thoroughly optimized with respect to the geometry of the cell culture chamber to maximize the sensitivity field distribution [13, 14].

This paper gives an overview of different impedance-based methods that we have developed and could find application in the overall process of tissue engineering (Fig. 1), from scaffold characterization (e.g. hydrogel

polymerization and porosity) to cell loading, proliferation and 3D spatial distribution using different electrode configurations.

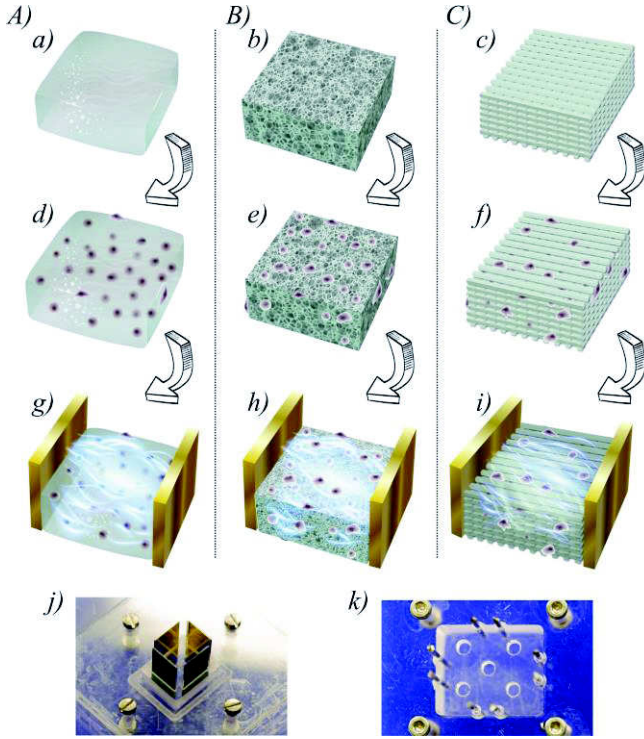


Fig. 1 Cell culture scaffolds can be characterized in terms of degree of polymerization (A), porosity (random pores, B, and structured pores, C), before (a-c) and after (d-f) cell loading using impedance (g-i) with different electrode configurations and setups (j, k) [13, 14].

II. MONITORING TISSUE ENGINEERING PROCESSES

In tissue engineering applications and 3D cell cultures, the scaffold properties (e.g. stiffness, chemical composition, porosity) and the supplied biochemical cues exert a major effect on cell physiology. Cell adhesion, proliferation and metabolism create an extremely heterogeneous and dynamic chemical environment [2, 3]. Variation in ionic strength leads to changes in conductivity, which is reflected by changes in the measured impedance. We have previously demonstrated a simplified approach for obtaining solution resistance (and, therefore, conductivity) by extracting the impedance magnitude at the frequency where the phase angle is closest to 0° without the need of validating and analyzing a specific equivalent circuit [15]. Additionally, changes in conductivity reflect hydrogel scaffold polymerization (e.g. gelatin, collagen), where mobile ions and readily reactive groups progressively lose their mobility

depending on the degree of cross-linking (Fig. 1A) [13]. Moreover, we have shown that conductivity of the interstitial medium can be related to the scaffold's pore geometry by Archie's law (Fig. 1B,C) [16]. We optimized measurements using two gold plate electrodes interfaced with a scaffold (Fig. 1j) eliminating the necessity of penetrating the material, which provides a significant advantage of non-invasivity. Archie's empirical correlation basically corrects the bulk conductivity by a geometric factor, which depends on the cross-sectional area (A), length (l) as well as degree and type of porosity of the scaffold (Fig. 2). Furthermore, when impedance measurements are performed in protein-rich solutions, e.g., cell culture medium, the electrodes may require a protein-repellent functionalization in order to avoid biomolecule physisorption and allow reproducible measurements over time [15].

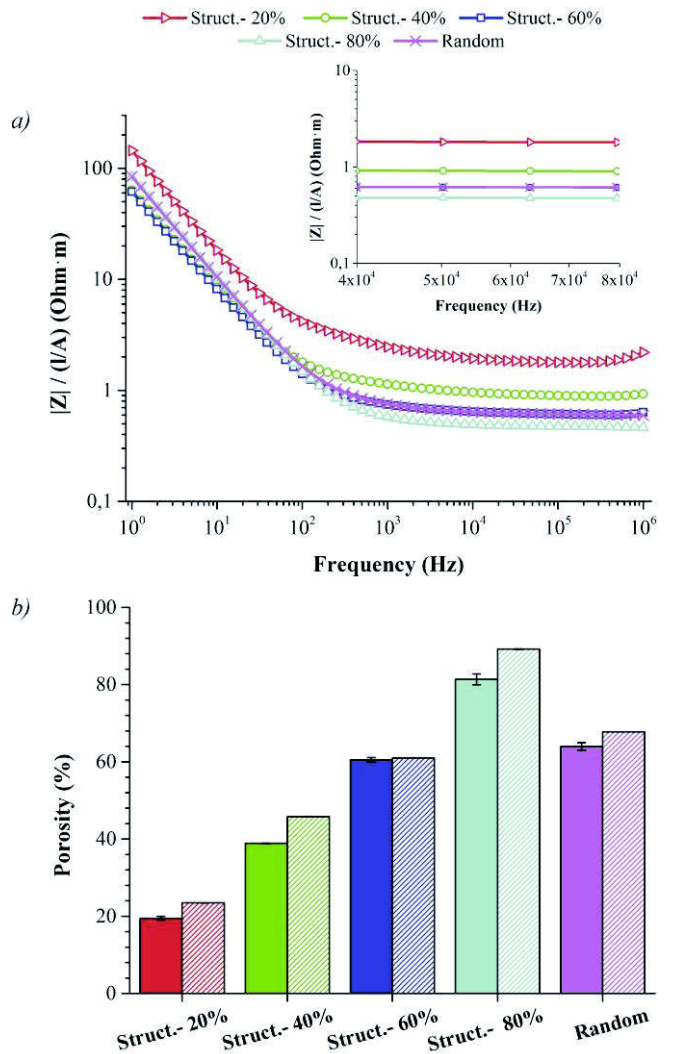


Fig. 2 (a) Normalization of the impedance data for porosity determination of 3D cell culture scaffolds displaying random or structured pores of decreasing size (i.e. 20 – 80 % of polymer composing the matrix). $|Z|$ (Ohm) of the scaffold soaked in physiological buffer was divided by the geometric factor l/A (m^{-1}) characteristic of each scaffold. (b) Comparison of a more conventional weight-based method (■) and impedance measurements (▨). Data are reported as mean \pm standard deviation ($n = 3$). [16]

A significant aspect in impedance monitoring of 3D cell cultures is that cells are not directly adhering on the electrode surface, but they are on a polymeric scaffold in contact with the electrodes via a conductive medium. Spatially distributed information on cell aggregates in the 3D environment can be collected using different combinations of electrode couples and configurations to maximize the sensitivity in the entire sample volume. The finite element method (FEM) is a valuable tool for tailoring parameters, such as electrode number, geometry, orientation and spacing, as well as predicting the distribution of the sensitivity field when using a specific electrode configuration [13]. Different 2-, 3-, and 4T configurations (Fig. 3) may be used in the same experimental setup to focus on specific sub-volumes inside the cell culture chamber that together cover the entire sample volume.

In the 2T configuration (Fig. 3a, b), the same electrode pair serves both as current-carrying (CC) and voltage pick-up (PU) electrodes and the measured bioimpedance typically includes the Z_p at both electrode surfaces, also reflecting the sample volume in close proximity to the electrodes. 2T measurements provide the simplest approach for conductivity analysis, especially when integrating bioimpedance monitoring in perfusion-based systems. In 3T configuration (Fig. 3c, d), one electrode is common for the CC and PU couple (working electrode, WE, in Fig. 3c). This is the only electrode inside the sensitivity zone of the measurement, and hence, the measured impedance is affected by its Z_p . We have previously presented the complementarity of 2T and 3T configurations in obtaining information on spatial distribution of cells in large gelatin scaffolds using plate electrodes [13].

In the 4T configuration (Fig. 3e, f), two separate CC and PU electrode couples are used. The CC couple is placed outside the measurement sensitivity zone, while the PU electrodes measure the so called “transimpedance”. Such a concept is generally referred to as “bioimpedance” in physiological measurements. On virtue of modern voltage amplifiers, the PU electrodes are ideally non-current carrying, eliminating all Z_p contributions to the measurements. Hence, only the properties of the sample are detected. Sequential 4T measurements represent the best method to collect a large matrix of bioimpedance data from several electrode couples to map the impedivity of a sample,

which also comprises changes in conductivity. By applying optimized algorithms, large data matrices provide possibility for constructing an image of the studied object, which is referred to as electrical impedance tomography (EIT, [17]). When using 4T measurements in tissue engineering applications, needle electrodes have a suitable geometry to achieve a high degree of 3D spatial information. We have evaluated the ability of 4T configuration using different CC and PU couple arrangements to sense the location of gelatin-embedded 3D cell aggregates [14].

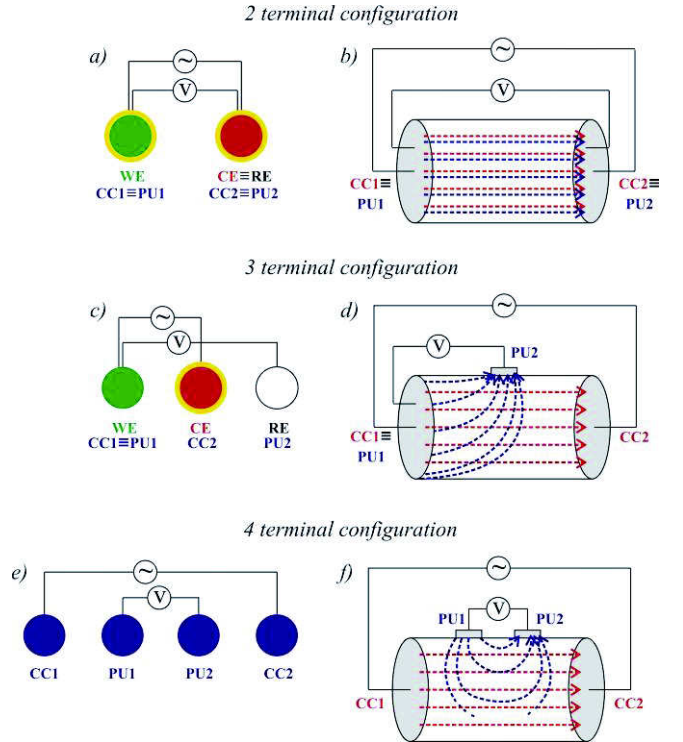


Fig. 3 Schematic of 2T (a), 3T (c) and 4T (e) configurations and their respective sensitivity fields (b, d, f) for a generic conductor. In electrochemical analysis WE (green) is the working electrode, CE (red) is the counter electrode, RE (white) is the reference electrode. In bioimpedance measurements CC1 and CC2 form the current-carrying couple; PU1 and PU2 form the voltage pick-up couple. When present, Z_p at the electrode/sample interface is reported in yellow (a and c). The sensitivity field (b, d, f) depends on the angle between the CC and PU equipotential lines (red and blue arrows, respectively) [18].

III. CONCLUSIONS

Bioimpedance-based methods can be applied in miniaturized 3D systems for future non-invasive monitoring of tissue engineering processes using different electrode geometries and configurations. The scaffold, supporting cell

organization, can be characterized in terms of hydrogel polymerization and degree of porosity, as well as cell loading and proliferation. Information on spatial distribution of cell aggregates in a 3D scaffold can be obtained using the 4T configuration with multiple needle electrodes that map the impedivity distribution in the entire sample volume. Such a method paves the way towards image reconstruction of 3D cell cultures as an application of electrical impedance tomography in tissue engineering.

ACKNOWLEDGMENT

This study and the Ph.D. fellowship of C. Canali were financially supported by the EU-funded project NanoBio4Trans (grant no. 304842).

CONFLICT OF INTEREST

The authors declare that they have no conflict of interest.

REFERENCES

- Langer, R., & Vacanti, J. P. (1993). Tissue engineering. *Science*, 260(5110), 920–926.
- Engler, A. J., Sen, S., Sweeney, H. L., & Discher, D. E. (2006). Matrix elasticity directs stem cell lineage specification. *Cell*, 126(4), 677–689.
- Griffith, L. G., & Swartz, M. A. (2006). Capturing complex 3D tissue physiology in vitro. *Nature reviews. Molecular cell biology*, 7, 211–224.
- Pampaloni, F., Reynaud, E. G., & Stelzer, E. H. K. (2007). The third dimension bridges the gap between cell culture and live tissue. *Nature Reviews Molecular Cell Biology*, 8, 839–845.
- Hug, T. S. (2003). Biophysical methods for monitoring cell-substrate interactions in drug discovery. *Assay and drug development technologies*, 1(3), 479–488.
- Graf, B. W., & Boppart, S. A. (2010). Imaging and analysis of three dimensional cell culture models. *Methods in molecular biology*, 591, 211–227.
- Smith, L. E., Smallwood, R., & Macneil, S. (2010). A comparison of imaging methodologies for 3D tissue engineering. *Microscopy research and technique*, 73(12), 1123–33.
- Giæver, I., & Keese, C. R. (1984). Monitoring fibroblast behavior in tissue culture with an applied electric field. *Proceedings of the National Academy of Sciences of the United States of America*, 81(12), 3761–3764.
- Giæver, I., & Keese, C. R. (1991). Micromotion of mammalian cells measured electrically. *Proceedings of the National Academy of Sciences of the United States of America*, 88, 7896–7900.
- Keese, C. R., Wegener, J., Walker, S. R., & Giæver, I. (2004). Electrical wound-healing assay for cells in vitro. *Proceedings of the National Academy of Sciences of the United States of America*, 101(6), 1554–1559. doi:10.1073/pnas.0307588100
- Caviglia, C., Zór, K., Montini, L., Tilli, V., Canepa, S., Melander, F., ... Emnéus, J. (2015). Impedimetric toxicity assay in microfluidics using free and liposome-encapsulated anticancer drugs. *Analytical Chemistry*, 87, 2204–2212.
- Martinsen, Ø. G., & Grimnes, S. (2014). *Bioimpedance and bioelectricity basics*. (Ø. G. Martinsen & G. Sverre, Eds.) (3rd ed.). London, UK: Academic Press.
- Canali, C., Heiskanen, A., Muhammad, H. B., Høyum, P., Pettersen, F.-J., Hemmingsen, M., ... Emnéus, J. (2015). Bioimpedance monitoring of 3D cell culturing – Complementary electrode configurations for enhanced spatial sensitivity. *Biosensors & bioelectronics*, 63, 72–79.
- Canali, C., Mazzoni, C., Larsen, L. B., Heiskanen, A., Martinsen, Ø. G., Wolff, A., ... Emnéus, J. (2015). An impedance method for spatial sensing of 3D cell constructs – towards applications in tissue engineering. *The Analyst* (in press). doi:10.1039/c5an00987a
- Canali, C., Larsen, L. B., Martinsen, Ø. G., & Heiskanen, A. (2015). Conductometric analysis in bio-applications: a universal impedance spectroscopy-based approach using modified electrodes. *Sensors & Actuators: B. Chemical*, 212, 544–550.
- Canali, C., Mohanty, S., Heiskanen, A., Muhammad, H. B., Martinsen, Ø. G., Dufva, M., ... Emnéus, J. (2015). Impedance spectroscopic characterisation of porosity in 3D cell culture scaffolds with different channel networks. *Electroanalysis*, 27, 193–199.
- Holder, D. (2005). Brief introduction to bioimpedance. In *Electrical impedance tomography* (1st ed., pp. 411–422). Bristol, UK: Institute of Physics Publishing.
- Malmivuo, J. (2010). Principle of reciprocity solves the most important problems in bioimpedance and in general in bioelectromagnetism. In *Journal of Physics: Conference Series*, 224(1), 012001

Author: Chiara Canali
 Institute: Technical University of Denmark
 Street: Produktionstorvet Building 423
 City: Kgs. Lyngby 2800
 Country: Denmark
 Email: chca@nanotech.dtu.dk

Paper II

Conductometric analysis in bio-applications: A universal impedance spectroscopy-based approach using modified electrodes

C. Canali, L. B. Larsen, Ø. G. Martinsen and A. Heiskanen

Sens. Actuators B, 2015, 212, 544–550



Contents lists available at ScienceDirect

Sensors and Actuators B: Chemical

journal homepage: www.elsevier.com/locate/snb

Conductometric analysis in bio-applications: A universal impedance spectroscopy-based approach using modified electrodes

Chiara Canali^a, Layla Bashir Larsen^a, Ørjan Grøttem Martinsen^{b,c}, Arto Heiskanen^{a,*}^a Department of Micro- and Nanotechnology, Technical University of Denmark, Produktionstorvet 423, 2800 Kgs Lyngby, Denmark^b Department of Physics, University of Oslo, Sem Sælands vei 24, Fysikkbygningen, 0371 Oslo, Norway^c Department of Biomedical and Clinical Engineering, Oslo University Hospital, 0372 Oslo, Norway

ARTICLE INFO

Article history:

Received 19 December 2014

Received in revised form 5 February 2015

Accepted 7 February 2015

Available online 16 February 2015

Keywords:

Electrochemical impedance spectroscopy
 Universal protocol for impedance-based conductivity determination
 Customised Matlab-based algorithm for automated spectral analysis
 Protein-repellent electrode modification
 Conductivity measurements in cell culture medium

ABSTRACT

We present a universal protocol for quick and reproducible conductivity determinations in bio-applications using electrochemical impedance spectroscopy (EIS), electrode modification and automated spectral analysis. Two-terminal EIS measurements may be acquired using any standard impedance analyser adjusting the applied sinusoidal potential and frequency range for spectral analysis. An implemented Matlab algorithm displays the acquired spectra, automatically identifies the frequency at which the phase angle (φ) is closest to 0° and determines the impedance magnitude, i.e. the solution resistance (R_S). The corresponding conductivity value is immediately calculated as the ratio of the conductivity cell constant (κ), determined based on calibration, and R_S . This protocol eliminates the need for evaluating a specific equivalent circuit followed by non-linear regression based curve fitting that is generally required in EIS-based conductivity determinations. The protocol is applicable to conductivity determinations using different conductivity cell configurations in any electrolyte solution regardless of its composition, i.e. in solutions with or without electroactive species that give rise to faradaic interface impedance. Conducted measurements showed high reproducibility in good agreement with a commercial conductometer in a wide range of ionic strengths up to five times that of physiological PBS. Since measurements in cell culture medium with bare gold electrodes indicated the need for recalibration to counteract the effect of biomolecule physisorption, the validity of the protocol was further extended using a protein-repellent coating of poly(ethylene glycol) methyl ether thiol self-assembled monolayer. This effectively eliminated electrode fouling, facilitating high reproducibility in repeated conductivity determinations in the presence of proteins.

© 2015 Elsevier B.V. All rights reserved.

1. Introduction

Measurement of solution conductivity is a classical analytical technique that finds application in a wide variety of chemical and biochemical studies, e.g., evaluation of solvent purity, determination of relative ionic strength in solutions, assessment of critical micelle concentration, monitoring of enzymatic reactions and calculation of basic thermodynamic quantities [1], as well as biosensing [2,3]. Although bio-applications most frequently involve measurements in the physiological conductivity range [4,5], low conductivity solutions have been used for, e.g., impedance-based affinity biosensing [6,7], while high conductivity solutions are used as supporting electrolytes in

voltammetric analysis, where concentrations may range up to 3 M [8,9].

Solution conductivity can be explained in terms of ionic mobility, which is directly proportional to temperature with an immediate effect of typically 1–3% per $^\circ\text{C}$ with respect to tabulated values at 25°C . It is also influenced by shifts in pH; acidic or basic solutions increase conductivity since hydrated protons and hydroxyl ions are the most mobile cations and anions, respectively. Variation of conductivity over time may also convey a high degree of information about the chemical dynamics of biological processes. A culture medium containing proliferating or dying cells is an extremely heterogeneous chemical environment, the composition of which is continuously changing depending on cellular metabolism [10]. Conductivity of culture media was correlated to microbial concentration and fermentation activity already in 1898 [11], paving the way to impedance microbiology [12], which gained increased significance in the 1970s

* Corresponding author. Tel.: +45 45 25 68 39; fax: +45 45 88 77 62.
 E-mail address: arto.heiskanen@nanotech.dtu.dk (A. Heiskanen).

with the emergence of frequency response analysers. However, although electrical impedance spectroscopy (EIS) potentially provides extensive information about electron transfer mechanisms, mass transfer phenomena and biochemical activity, the design of an optimised analytical strategy may be highly demanding [13]. Simplified approaches have been devised based on conductivity measurements. Parsons and Sturges developed and tested a simple and relatively quick approach to correlate culture medium conductivity to the total amount of ammonia and amino nitrogen produced by putrefactive anaerobic bacteria [14,15]. Allison et al. extended this technique to metabolic studies on aerobes producing ammonia and lactic acid [10]. Similarly, cell culture medium conductivity may be a key parameter for analysing the complex dynamics that modulate mammalian cell cultures over time [16]. This is particularly relevant for biomedical research which is currently undergoing a shift of paradigm toward 3D cell cultures, needing new non-invasive on-line monitoring technologies [17,18]. Furthermore, EIS has already been shown to be a valuable tool for defining the porosity of 3D cell culture scaffolds by yielding the conductivity of the bulk electrolyte filling the pores [19,20].

The simplest approach for conductivity determination is to apply an alternating electric field between two electrodes and measure the impedance magnitude as an estimation of the solution resistance (R_S), which can be used to calculate conductivity. Alternating current at frequencies above 1 kHz should be used instead of direct current that may lead to electrolysis and electrode polarization [21]. Commercial conductometers are standalone devices which typically operate maximally at few predetermined frequencies. During calibration using a conductivity standard solution, an internal algorithm selects the frequency value depending on the conductivity range to give an accurate estimation of R_S . However, the algorithm may vary between manufacturers and depending on the instrument quality, increasing the possibility of systematic errors in the analysis. Moreover, although commercially available conductivity sensors are manufactured from robust metals, e.g., platinum, stainless steel and titanium, that provide high mechanical stability, they are not designed for measurements in biological solutions. Biomolecule adsorption on the electrode surface increases the measured impedance, hence, yielding a lower apparent conductivity value.

EIS-based conductivity measurements, relying on analysis of complete spectra using equivalent circuits, have been proposed in order to eliminate the need of choosing a specific frequency that may result in measurement inaccuracy [22]. To our best knowledge, such approach has been used especially for lab-on-a-chip devices in impedance microbiological applications [23–25]. Generally, such analysis depends on the electrolyte composition and hence, whether the measured impedance is contributed to by faradaic and/or non-faradaic processes. Additionally, the structure/geometry of a conductivity cell imposes requirements on the used equivalent circuit [22], especially when microfabricated devices having interdigitated electrodes (IDEs) are used [26]. Hence, this approach complicates conductivity determinations, requiring a different equivalent circuit depending on the composition of the used electrolyte solution [13,27] or structure of the conductivity cell [22,26].

To avoid the limitations described above, we hereby present a universal protocol that relies on acquisition and automated analysis of complete impedance spectra as the basis for quick conductivity determinations, as well as electrode modification applicable for measurements in biomolecule containing electrolytes. Conventional two-terminal EIS measurements can be used with the flexibility of choosing both the sinusoidal potential of excitation and frequency range for analysis. A Matlab-based algorithm displays Bode plots for impedance magnitude ($|Z|$) and phase angle

(φ) while it automatically identifies the most suitable frequency for determining R_S , i.e. $|Z|$ at the frequency where φ is closest to 0° . This approach provides two major advantages: the calculated solution conductivity value is (1) based on an accurately determined R_S unlike in the case of an algorithm relying on a few predetermined frequencies, and (2) independent of validation and analysis of a specific equivalent circuit. A commercial conductometer was used for validation and a good agreement between the two methods was found for ionic strength (I) values up to five times that of physiological PBS. Our universal protocol facilitated stable, precise and accurate measurements using inexpensive electrodes and a standard impedance analyser. Moreover, the validity was further extended to conductivity measurements in biomolecule containing electrolytes (i.e. cell culture medium). The influence of protein physisorption on conductivity determination was eliminated using a protein-repellent self-assembled monolayer (SAM) modification of poly(ethylene glycol)-terminated alkanethiol. High precision and reproducibility was achieved in repeated measurements in cell culture medium without the requirement for recalibration during measurements or labour-intensive electrode cleaning after measurements.

2. Materials and methods

2.1. Chemicals and solutions

Potassium hydroxide (semiconductor grade), hydrogen peroxide (30% solution in water), cell culture tested PBS (physiological and $10\times$ concentrate), Roswell Park Memorial Institute medium 1640 (RPMI), fetal bovine serum (FBS), penicillin/streptomycin (P/S), and poly(ethylene glycol) methyl ether thiol (mPEG, average M_n 800) were purchased from Sigma–Aldrich Corporation (St. Louis, MO, USA). Electrochemical measurements were performed on serial dilutions of PBS in the range of 0–1.5 M NaCl (chemical composition of the $10\times$ concentrate given by the supplier: 0.03 M $\text{Na}(\text{PO}_4)_3$, 1.5 M NaCl, 0.0105 M KH_2PO_4). Ultrapure deionized water ($18.2\text{ M}\Omega\text{ cm}$) from Milli-Q system (Millipore Corporation, Billerica, MA, USA) was used for diluting PBS samples and rinsing electrodes. Standard solutions of known conductivity (8.4×10^{-3} , 1.4×10^{-2} , 1.3, 11.2 S/m) were purchased from Hanna Instruments (Kungsbacka, Sweden).

2.2. Measurement protocol

Prior to the first EIS measurement, gold plate electrodes, fabricated by e-beam evaporation on oxidized silicon wafers as previously described [18,20], were cleaned by a 10-min treatment with a mixture of 25% (v/v) H_2O_2 and 50 mM KOH followed by a potential sweep from -200 mV to -1200 mV in 50 mM KOH [27]. Electrodes were mounted on a 3D printed conductivity cell as described in Supplementary Information S1 and shown in Fig. S-1. Impedance spectra were acquired using a Reference 600 potentiostat (Gamry Instruments, Warminster, PA, USA). An alternating potential (rms) of 10 mV was applied in the frequency range between 10 Hz and 1 MHz. The geometrically determined cell constant (κ) was verified by acquiring and analysing three EIS spectra in triplicate samples of each conductivity standard solution. This allowed calculation of the experimental value for κ , which is defined as the product of the solution conductivity and solution resistance (R_S). The results are presented as average \pm standard error of mean (s.e.m.), $n=9$. EIS data processing for automated generation of Bode plots and conductivity determination were implemented as a Matlab (version R2012b) script (detailed description in Supplementary Information S2). *For-loops* allowed presentation of spectra acquired in different solutions in the same Bode plot ($|Z|$ or φ). To calculate the

conductivity, R_s was determined based on the $|Z|$ value in a frequency range where φ is closest to 0° . This was computed using the $\min(X,Y)$ function. Three EIS spectra were acquired in triplicate samples of different PBS dilutions. The relationship between calculated conductivity and I (approximated by NaCl concentration) was determined and validated against the performance of a commercial conductometer (CDM 92, Radiometer Analytical, Copenhagen). The results are presented as average \pm s.e.m., $n=9$. All the measurements were conducted at room temperature in solutions exposed to atmospheric CO_2 .

2.3. Electrode modification for bio-applications

Three EIS spectra were acquired in triplicate samples of cell culture medium. Before and after measurements in cell culture medium, three samples of physiological PBS was analysed to evaluate the influence of medium serum proteins on the electrode performance. The results are presented as average \pm s.e.m., $n=9$. Then, three sets of electrodes were used for measurements after modification with 10 mM mPEG in water for 16 h. The results are presented as average \pm s.e.m., $n=27$. Impedance measurements were performed as described in Section 2.2. CO_2 level in cell culture medium samples was equilibrated in an incubator (5% $\text{CO}_2/95\%$ air) for 30 min prior to measurements. Between measurements in different samples, electrodes were rinsed using Milli-Q water.

3. Results and discussion

3.1. Analysis of PBS dilutions

As first validation of our universal protocol, EIS spectra were acquired in samples of different PBS dilutions (range of 0–1.5 M NaCl) and analysed using the custom-made Matlab algorithm (Supplementary Information S2) that presents data as Bode plots (Fig. 1a, b) and determines R_s in a frequency range where φ is approximately 0° (Fig. 1b). The corresponding conductivity was calculated as the ratio between the conductivity cell constant (κ) and R_s . The calculations were based on the experimentally determined κ , $1.77 \pm 0.02 \text{ cm}^{-1}$ (average \pm s.e.m., $n=9$), obtained by calibration in standard solutions with known conductivity. The geometric definition of κ is the ratio between the distance of the electrodes and the area exposed to the solution. Based on these factors, κ was calculated to be 1.85 cm^{-1} (Fig. S1b), indicating a good agreement between the experimental and geometric value.

The relationship between the determined conductivity and the ionic strength (I) of the PBS dilutions showed very high reproducibility, the overall relative standard error (RSE%) for all the dilutions being only 0.5%. The value also comprises measurements in solutions with very low conductivity, which are more prone to be affected by artifacts due to parasitic conduction paths [28,29]. This means that in solutions with higher conductivity, such as those around physiological I , the obtained variation in measurements was even lower than the above mentioned overall RSE%. Corresponding measurements using the commercial conductometer resulted in an overall RSE% of 3.0%, which is clearly higher than the value obtained with our universal protocol. Further comparison between the methods is shown in Fig. 2. The linear correlation between the determined conductivity and calculated I of the PBS dilutions shown in Fig. 2a indicates that the coefficient of determination (R^2) for our universal protocol was slightly higher (0.998) than the one obtained for the commercial instrument ($R^2=0.991$). The general observation based on Fig. 2a is that both approaches show good agreement in conductivity determination for solutions reaching five times the I value of physiological PBS ($I=8.12 \times 10^{-1} \text{ M}$).

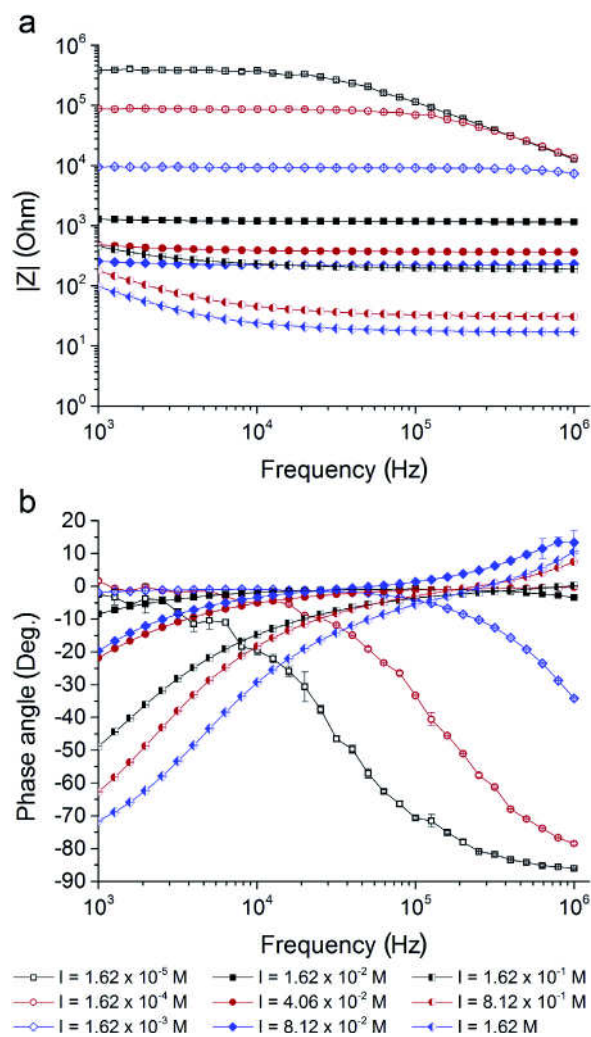


Fig. 1. Averaged EIS spectra (\pm s.e.m., $n=9$) for PBS dilutions ranging from very low to high conductivity: Bode plots for (a) impedance magnitude ($|Z|$) and (b) phase angle (φ).

However, for highly concentrated electrolytes (10 times the I of physiological PBS), the commercial conductometer deviated significantly from the value obtained using our universal protocol, which retained linearity throughout the used I range. Performed regression analysis (Fig. 2b) indicated a very good agreement ($R^2=0.999$) until I five times that of physiological PBS. These results showed that the established universal protocol provides stable, accurate and reproducible measurements in a wide conductivity range.

The impedance spectra acquired in the PBS dilutions were also used to define four frequency ranges applicable for quicker determination of conductivity with single frequency analysis: (1) 1–4 kHz for very low conductivity solutions ($I \leq 1.62 \times 10^{-3} \text{ M}$); (2) 20–50 kHz for low conductivity solutions ($1.62 \times 10^{-3} < I \leq 8.12 \times 10^{-2} \text{ M}$); (3) 200–250 kHz for solutions close to the physiological I ($8.12 \times 10^{-2} < I \leq 1.62 \times 10^{-1} \text{ M}$); (4) 300–400 kHz for solutions above the physiological I ($I > 1.62 \times 10^{-1} \text{ M}$).

In the above described conductivity determinations based on EIS measurements, the applied sinusoidal potential was $10 \text{ mV}_{\text{rms}}$ and the used electrodes had large area with a deposited thin gold film. When using an impedance analyser, the amplitude of the sinusoidal potential may be freely chosen as long as it ensures linearity of the current–voltage response. However, despite the chosen potential amplitude, the measured impedance, and hence

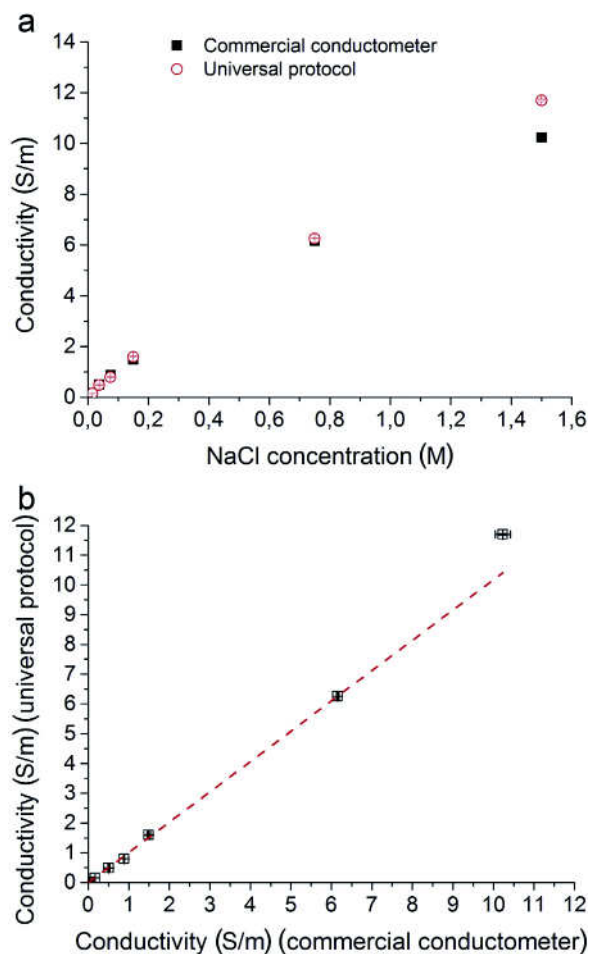


Fig. 2. Comparison of the universal conductivity determination protocol with a commercial conductometer: (a) trend of data point distribution relating increasing NaCl concentration (M) in PBS dilutions to the corresponding conductivity (S/m) and (b) regression analysis. The error bars represent s.e.m. ($n = 9$).

the determined conductivity, is the same provided that the setup does not have a high intrinsic impedance, which could decrease measurement accuracy at low applied potential amplitudes. The validity of our proposed universal protocol was additionally evaluated using other potential amplitudes (25 and 50 mV_{rms}) aside from 10 mV_{rms}. The results are shown in Supplementary Information S3. For EIS measurements using IDEs, different equivalent circuits have been proposed in literature; however, a common feature is the presence of a parallel geometric capacitance [26]. The consequence is that in a frequency range below 1 MHz the absolute value of φ may significantly deviate from 0°. Supplementary Information S4 shows conductivity determinations using IDEs applied in two configurations. The results demonstrate that our universal protocol provides possibility for reliable conductivity determinations in miniaturised devices where the conductivity cell significantly influences the characteristic equivalent circuit, making it different from one that is valid for parallel plate electrodes.

3.2. Electrode modification for bio-applications

To further evaluate the validity of the presented universal protocol for conductivity measurements in biomolecule-containing electrolytes, we determined the conductivity of cell culture medium containing serum proteins. Physisorption of biomolecules on bare gold surfaces is well-known. To easily see the effect of electrode fouling, we determined the conductivity of physiological

PBS before and after measurements in cell culture medium. The performed conductivity measurements clearly indicated that the used electrode surfaces were fouled by physisorbed biomolecules, requiring intensive electrode cleaning and recalibration after each measurement. Therefore, we optimised a protein-repellent electrode modification using self-assembled monolayer (SAM) of a poly(ethylene glycol)-terminated alkanethiol. This approach eliminated the need for labour-intensive electrode cleaning and recalibration that are crucial when using a commercial instrument.

3.2.1. Effect of biological solutions on bare gold electrodes

The impedance spectra presented in Fig. 3a indicate that the spectral behaviour is in accordance with the one previously shown

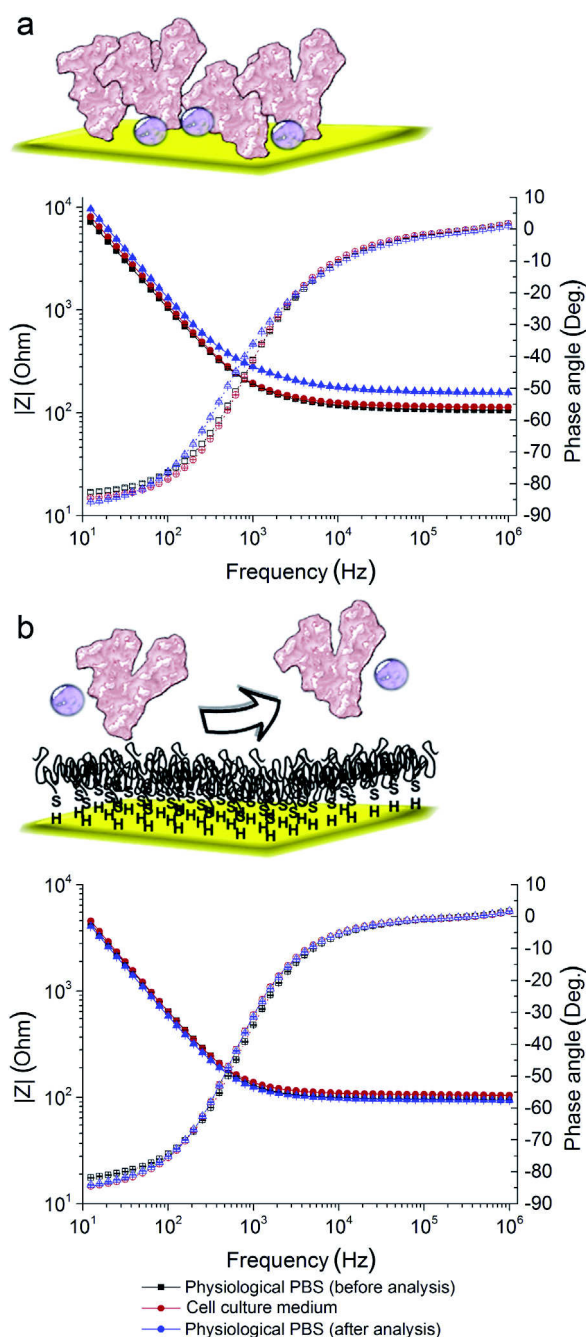


Fig. 3. Averaged EIS spectra (\pm s.e.m.) for physiological PBS and cell culture medium using (a) bare gold electrodes ($n = 9$) and (b) mPEG-modified gold electrodes ($n = 27$). Measurements in PBS were performed before and after analysis of cell culture medium.

Table 1
Influence of biomolecule-containing electrolytes on conductivity measurements: conductivity [S/m] values for physiological PBS and cell culture medium determined using bare and mPEG-modified gold electrodes.

Type of electrolyte	Conductivity [S/m]
Bare gold electrodes ^a	
PBS before measurements in cell culture medium	1.66 ± 0.01
PBS after measurements in cell culture medium	1.12 ± 0.01
PBS after measurements in cell culture medium and recalibration	1.49 ± 0.01
Cell culture medium (RPMI)	1.55 ± 0.01
mPEG-modified gold electrodes ^b	
PBS before measurements in cell culture medium	1.596 ± 0.007
PBS after measurements in cell culture medium	1.603 ± 0.007
Cell culture medium (RPMI)	1.44 ± 0.01

^a Conductivity values are reported as average ± s.e.m., $n=9$.

^b Conductivity values are reported as average ± s.e.m., $n=27$. Three sets of electrodes were evaluated.

for PBS dilutions (Fig. 1). The decrease in conductivity corresponds to a slight upward shift in the Bode plots for $|Z|$ at frequencies above 200 Hz and a clear separation above 5 kHz. Values of conductivity were calculated in the frequency range proposed for performing measurements on solutions with I close to the physiological range, further confirming that the protocol is fully suitable for single frequency analysis. Table 1 summarises the determined conductivity values for PBS and cell culture medium. The obtained results clearly show that measurements in cell culture medium influenced the behaviour of bare gold electrodes. The conductivity value determined for PBS before measurements in medium agreed well with previously shown results [30], whereas after electrode exposure to biomolecules the determined conductivity was clearly lower. Moreover, despite the small distribution of the determined conductivity values (s.e.m.) for cell culture medium, the individual measurements showed a clear trend in terms of decreasing conductivity, which indicates that even during a series of measurements in a biological solution the individual measurement results may be influenced by electrode fouling. When performing conductivity measurements using a commercial conductometer, which has fixed electrodes, calibration using conductivity standard solutions may alleviate the effect of exposure to biomolecule-containing electrolytes. To evaluate this possibility, we recalibrated our conductivity cell after measurements in cell culture medium and repeated conductivity determination of physiological PBS. The obtained result (Table 1) indicates that, despite recalibration, the determined conductivity was still lower than obtained in the original measurements prior to any exposure to cell culture medium. Extensive cleaning might improve electrode behaviour in subsequent measurements; however, it would easily deteriorate the performance of microfabricated thin-film electrodes, shortening their lifetime. This encourages the use of modified electrodes with a stable protein-repellent SAM so that they can be applied to a series of measurements without the influence of electrode fouling.

3.2.2. Effect of biological solutions on mPEG-modified gold electrodes

Analogously to chemical electrode modifications, which behave as capacitors in series with the double layer capacitance [27], adsorbed biomolecules also change the capacitive behaviour of the electrode–electrolyte interface. Results described in Section 3.2.1 clearly indicate that $|Z|$ increases as a consequence of measurements in biomolecule-containing electrolytes when using bare gold electrodes. To eliminate this effect and be able to conduct EIS measurements without the need for extensive electrode cleaning and/or recalibration after each measurement, we evaluated the possibility of using electrodes modified with a protein-repellent coating. Polyethylene glycol (PEG) is a nontoxic

and non-immunogenic polymer which is able to decrease attractive forces between solid surfaces and proteins. Harder et al. showed how this ability is related to PEG molecular conformation and becomes most effective when PEG chain length allows the formation of dense and predominantly helical films of PEG [31]. They speculated that the helical conformation may correlate with the degree of solvation and, consequently, with the stability of the interfacial layer of water, which may repel proteins reaching the electrode surface by diffusion. Hence, PEG-terminated alkanethiol SAMs on gold surfaces have been successfully used to facilitate selective cell patterning and reduce surface fouling [32].

To readily modify gold surfaces and increase the biocompatibility, we used water soluble mPEG-terminated alkanethiol. Initial tests followed by EIS characterisation indicated that a modification time of at least 16 h yielded a robust well-behaved functionalization (data not shown). Three sets of electrodes were calibrated after mPEG modification and κ was calculated to be $(1.52 \pm 0.01) \text{ cm}^{-1}$ (average ± s.e.m., $n=9$). Based on the geometric factors, κ resulted 1.85 cm^{-1} . The larger difference between the calculated and the geometrically determined κ is due to the fact that although κ is generally referred to as the ratio between electrode distance and area, calibration takes into account the condition of the electrode–electrolyte interface, which is different for chemically modified electrodes in comparison with non-modified ones. Fig. 3b shows a set of averaged impedance spectra for PBS and cell culture medium acquired using three sets of modified electrodes (three repetitive spectra acquired for each electrode set in three electrolyte samples). Each spectrum is reported as average ± s.e.m. ($n=27$). In the frequency range 200–250 kHz, where φ is approximately 0° , the spectra acquired in PBS before and after measurements in cell culture medium completely overlap, which means that the mPEG modification was able to protect the electrode surface from the influence of physisorbed biomolecules. The spectra acquired in PBS indicate that the measurements in cell culture medium only had a slight influence on the capacitive behaviour of the electrodes as seen in the shift of φ at frequencies below 100 Hz. The conductivity values for PBS are shown in Table 1 and agree well with values reported in literature [30]. Moreover, the values shown in Table 1 also indicate that, on virtue of the electrode modification, the conducted measurements are highly reproducible between sets of electrodes.

4. Conclusions

We established and verified a universal protocol for quick conductivity determinations using electrochemical impedance spectroscopy (EIS) and electrode modification for bio-applications with high reproducibility. The approach relies on simple spectral analysis to determine the frequency at which the phase angle (φ) is closest to 0° . The impedance magnitude ($|Z|$) at that frequency corresponds to the solution resistance (R_S), which can be used to calculate the conductivity. Unlike commercial instruments, typically operating at a few predetermined frequencies, which, depending on the solution composition, may not yield an accurate estimation of R_S , our universal protocol, based on analysis of complete spectra, has the advantage that R_S , and consequently the corresponding conductivity, can be determined with certainty independent of the solution composition. A Matlab-based algorithm was implemented to display impedance spectra as Bode plots and automatically identify the suitable frequency for determining R_S and calculating solution conductivity. The universal protocol gave results in good agreement with a commercial conductometer in a wide range of electrolyte solutions for ionic strength up to five times that of physiological PBS. The validity of the protocol was extended to bio-applications by applying an optimised electrode modification method using a protein-repellent coating

of poly(ethylene glycol) methyl ether thiol. This allowed precise and reproducible conductivity determinations without influence of electrode fouling, which clearly affected measurements with non-modified electrodes. Our universal protocol combined with protein-repellent electrode modification provides a fast and simple way of performing programmed conductivity monitoring using any impedance analyser, opening possibilities for diverse application areas, ranging from biosensing to cell-based assays and microbiological studies. Moreover, the entire protocol for data treatment and electrode modification may be particularly beneficial for the development of stable, precise and accurate miniaturised devices.

Acknowledgements

This work and the Ph.D. fellowship of C.C. were supported by the EU-funded project NanoBio4Trans (“A new nanotechnology-based paradigm for engineering vascularised liver tissue for transplantation”, grant no: 304842). Additionally, A.H. acknowledges Lundbeck Foundation (grant no. R69-A6408) for financial support.

Appendix A. Supplementary data

Supplementary material related to this article can be found, in the online version, at <http://dx.doi.org/10.1016/j.snb.2015.02.029>.

References

- [1] L. Coury, Conductance measurements part 1: theory, *Curr. Sep.* 18 (1999) 91–96.
- [2] N. Jaffrezic-Renault, S.V. Dzadevych, Conductometric microbiosensors for environmental monitoring, *Sensors* 8 (2008) 2569–2588, <http://dx.doi.org/10.3390/s8042569>.
- [3] M.M. Barsan, M.E. Ghica, C.M.A. Brett, Electrochemical biosensors, in: D.P. Nikolelis, T. Varzakas, A. Erdem, G.-P. Nikoleli (Eds.), *Portable Biosensing Food Toxicants Environ. Pollut.*, Taylor & Francis Group, Boca Raton, 2014, pp. 33–70.
- [4] G. Pucihar, T. Kotnik, M. Kandušer, D. Miklavčič, The influence of medium conductivity on electroporation and survival of cells in vitro, *Bioelectrochemistry* 54 (2001) 107–115, [http://dx.doi.org/10.1016/S1567-5394\(01\)00117-7](http://dx.doi.org/10.1016/S1567-5394(01)00117-7).
- [5] M. Pavlin, M. Kanduser, M. Rebersek, G. Pucihar, F.X. Hart, R. Magjarevic, et al., Effect of cell electroporation on the conductivity of a cell suspension, *Biophys. J.* 88 (2005) 4378–4390, <http://dx.doi.org/10.1529/biophysj.104.048975>.
- [6] J. Ramón-Azcón, E. Valera, A. Rodríguez, A. Barranco, B. Alfaro, F. Sanchez-Baeza, et al., An impedimetric immunosensor based on interdigitated microelectrodes (IDμE) for the determination of atrazine residues in food samples, *Biosens. Bioelectron.* 23 (2008) 1367–1373, <http://dx.doi.org/10.1016/j.bios.2007.12.010>.
- [7] G.L. Damhorst, C.E. Smith, E.M. Salm, M.M. Sobieraj, H. Ni, H. Kong, et al., A liposome-based ion release impedance sensor for biological detection, *Biomed. Microdev.* 15 (2013) 895–905, <http://dx.doi.org/10.1007/s10544-013-9778-4>.
- [8] E.J.F. Dickinson, J.G. Limon-petersen, N.V. Rees, R.G. Compton, Quantitatively diffusional? A theoretical and experimental investigation, *J. Phys. Chem. C* 113 (2009) 11157–11171.
- [9] Q. Li, C. Batchelor-McAuley, N.S. Lawrence, R.S. Hartshorne, C.J.V. Jones, R.G. Compton, A flow system for hydrogen peroxide production at reticulated vitreous carbon via electroreduction of oxygen, *J. Solid State Electrochem.* 18 (2013) 1215–1221, <http://dx.doi.org/10.1007/s10008-013-2250-9>.
- [10] J.B. Allison, J.A. Anderson, W.H. Cole, The method of electrical conductivity in studies on bacterial metabolism, *J. Bacteriol.* 36 (1938) 571–586.
- [11] G.N. Stewart, The changes produced by the growth of bacteria in the molecular concentration and electrical conductivity of culture media, *J. Exp. Med.* 4 (1898) 235–243.
- [12] P. Silley, S. Forsythe, Impedance microbiology—a rapid change for microbiologist, *J. Appl. Bacteriol.* 80 (1996) 233–243.
- [13] X. Dominguez-Benetton, S. Seveda, K. Vanbroekhoven, D. Pant, The accurate use of impedance analysis for the study of microbial electrochemical systems, *Chem. Soc. Rev.* 41 (2012) 7228–7246, <http://dx.doi.org/10.1039/c2cs35026b>.
- [14] L.B. Parsons, W.S. Sturges, The possibilities of the conductivity method as applied to studies of bacterial metabolism, *J. Bacteriol.* 11 (1926) 177–188.
- [15] L.B. Parsons, W.S. Sturges, Conductivity as applied to studies of bacterial metabolism II. Parallelism between ammonia and conductivity in nutrient gelatin cultures of putrefactive anaerobes, *J. Bacteriol.* 12 (1926) 267–272.
- [16] E. Petiot, A. El-Wajjali, G. Esteban, C. Gény, H. Pinton, A. Marc, Real-time monitoring of adherent Vero cell density and apoptosis in bioreactor processes, *Cytotechnology* 64 (2012) 429–441, <http://dx.doi.org/10.1007/s10616-011-9421-2>.
- [17] K.F. Lei, M.-H. Wu, C.-W. Hsu, Y.-D. Chen, Real-time and non-invasive impedimetric monitoring of cell proliferation and chemosensitivity in a perfusion 3D cell culture microfluidic chip, *Biosens. Bioelectron.* 51 (2014) 16–21, <http://dx.doi.org/10.1016/j.bios.2013.07.031>.
- [18] C. Canali, A. Heiskanen, H.B. Muhammad, P. Høyum, F.-J. Pettersen, M. Hemmingsen, et al., Bioimpedance monitoring of 3D cell culturing—complementary electrode configurations for enhanced spatial sensitivity, *Biosens. Bioelectron.* 63 (2015) 72–79, <http://dx.doi.org/10.1016/j.bios.2014.07.020>.
- [19] S. Tully-Dartez, H.E. Cardenas, P.-F.S. Sit, Pore characteristics of chitosan scaffolds studied by electrochemical impedance spectroscopy, *Tissue Eng. Part C. Methods* 16 (2010) 339–345, <http://dx.doi.org/10.1089/ten.TEC.2009.0132>.
- [20] C. Canali, S. Mohanty, A. Heiskanen, H.B. Muhammad, Ø.G. Martinsen, M. Dufva, et al., Impedance spectroscopic characterisation of porosity in 3D cell culture scaffolds with different channel networks, *Electroanalysis* 27 (2015) 193–199, <http://dx.doi.org/10.1002/elan.201400413>.
- [21] P.W. Atkins, *Physical Chemistry*, 8th ed., Oxford University Press, Oxford, 2006, http://dx.doi.org/10.1007/SpringerReference_77053.
- [22] J.P. Diard, P. Landaud, B. Le Gorrec, C. Montella, Automatic measurement of the conductivity of an electrolyte solution by FFT electrochemical impedance spectroscopy, *J. Appl. Electrochem.* 22 (1992) 1180–1184, <http://dx.doi.org/10.1007/BF01297421>.
- [23] B. Timmer, W. Sparreboom, W. Olthuis, P. Bergveld, A. van den Berg, Optimization of an electrolyte conductivity detector for measuring low ion concentrations, *Lab Chip* 2 (2002) 121–124, <http://dx.doi.org/10.1039/b201225a>.
- [24] R. Gómez-Sjöberg, D.T. Morissette, R. Bashir, S. Member, Impedance microbiology-on-a-chip: microfluidic bioprocessor for rapid detection of bacterial metabolism, *J. Microelectromech. Syst.* 14 (2005) 829–838.
- [25] K. Lei, Review on impedance detection of cellular responses in micro/nano environment, *Micromachines* 5 (2014) 1–12, <http://dx.doi.org/10.3390/mi5010001>.
- [26] N.F. Sheppard, R.C. Tucker, C. Wu, Electrical conductivity measurements using microfabricated interdigitated electrodes, *Anal. Chem.* 65 (1993) 1199–1202.
- [27] A.R. Heiskanen, C.F. Spigel, N. Koshesha, T. Ruzgas, J. Emnéus, Monitoring of *Saccharomyces cerevisiae* cell proliferation on thiol-modified planar gold microelectrodes using impedance spectroscopy, *Langmuir* 24 (2008) 9066–9073.
- [28] S. Chechirlian, M. Keddad, H. Takenouti, Specific aspects of impedance measurements in low conductivity media, in: J. Scully, D. Silverman, M. Kendig (Eds.), *Electrochem. Impedance Anal. Interpret.*, ASTM International, Philadelphia, 1993, pp. 23–36.
- [29] K.C. Stewart, D.G. Kolman, S.R. Taylor, The effect of parasitic conduction pathways on EIS measurements in low conductivity media, in: J. Scully, D. Silverman, M. Kendig (Eds.), *Electrochem. Impedance Anal. Interpret.*, ASTM International, Philadelphia, 1993, pp. 73–93.
- [30] A.M. Johnson, D.R. Sadoway, M.J. Cima, R. Langer, Design and testing of an impedance-based sensor for monitoring drug delivery, *J. Electrochem. Soc.* 152 (2005) H6–H11, <http://dx.doi.org/10.1149/1.1824045>.
- [31] P. Harder, M. Grunze, R. Dahint, G.M. Whitesides, P.E. Laibinis, Molecular conformation in oligo (ethylene glycol)-terminated self-assembled monolayers on gold and silver surfaces determines their ability to resist protein adsorption, *J. Phys. Chem. B* 5647 (1998) 426–436.
- [32] S. Lan, M. Veiseh, M. Zhang, Surface modification of silicon and gold-patterned silicon surfaces for improved biocompatibility and cell patterning selectivity, *Biosens. Bioelectron.* 20 (2005) 1697–1708, <http://dx.doi.org/10.1016/j.bios.2004.06.025>.

Biographies

Chiara Canali received the M.Sc. degree in pharmaceutical biotechnology (summa cum laude) from University of Bologna in Italy in 2011. From 2009 to 2012 her research projects were focusing on bioanalytical chemistry and bioluminescence imaging working at University of Bologna, Leiden University Medical Center and Institut Polytechnique de Grenoble. She is currently a Ph.D. student at the Technical University of Denmark (Department of Micro- and Nanotechnology). Her project is focused on the design of bioimpedance-based sensing for applications in tissue engineering.

Layla Bashir Larsen is postdoc at the Technical University of Denmark (Department of Micro- and Nanotechnology). She is a biomedical engineer with a Ph.D. degree in Micro and Nano-engineering (University of Birmingham, UK) and prior clinical experience (within the National Health Service, UK) in the field of rehabilitation engineering. Her research focuses on the applications of engineering in medicine and includes development of sensors, microfluidic devices and tissue engineering support systems.

Ørjan Grøttem Martinsen is professor at the University of Oslo (Department of Physics) since 2002 and head of the Bioimpedance group. He also has a part time position as researcher at the Department of Clinical and Biomedical Engineering at Oslo University Hospital. He became electrical engineer in 1983 and Dr. Scient. in 1995 defending a thesis on the electrical properties of human skin. His research mainly focuses on the passive electrical properties of biological materials and applications of bioimpedance technology in medicine, biology and physiology. His particular expertise is within bioimpedance basic theory, instrumentation, electrode systems and modeling. He is co-editor in chief of *Journal of Electrical Bioimpedance (JEB)* and President of the International Society for Electrical Bioimpedance (ISEBI).

Arto Heiskanen is associate professor at the Technical University of Denmark (Department of Micro- and Nanotechnology) focusing on the development of microfluidic systems with electrochemical detection for cell-based applications. He received the B.Sc. degree in biochemistry from Åbo Akademi University, Turku, Finland, in 1987, the B.Sc. degree in chemistry from the University of the Philippines,

Diliman, Quezon City, in 2001, and both the M.Sc. degree in 2004 and the Ph.D. degree in 2009 from Lund University, Lund, Sweden. He has coauthored over 50 peer-reviewed publications on electrode fabrication and modification as well as development of microfluidic platforms for applications in electrochemical monitoring of cellular functions.

Supplementary Information:

Conductometric analysis in bio-applications: a universal impedance spectroscopy-based approach using modified electrodes

Chiara Canali¹, Haseena Bashir Muhammad¹, Ørjan Grøttem Martinsen^{2,3}, Arto Heiskanen^{1*}

¹ Department of Micro- and Nanotechnology, Technical University of Denmark, Produktionstorvet 423, 2800 Kgs. Lyngby, Denmark

² Department of Physics, University of Oslo, Sem Sælands vei 24, 0371 Oslo, Norway

³ Department of Biomedical and Clinical Engineering, Oslo University Hospital, 0372 Oslo, Norway

Content:

- S1 Fabrication of conductivity cell**
- S2 Automated Matlab script for data analysis**
- S3 Effect of sinusoidal potential amplitude on conductivity determinations**
- S4 Conductivity determinations using interdigitated microelectrodes (μ IDEs)**

S1. Fabrication of conductance cell

We fabricated a 3D printed conductivity cell allowing mounting of two disposable gold plate electrodes to couple electrochemical impedance spectroscopy (EIS) to conductivity determination using an impedance analyser. 3D printing was performed using a Makerbot Replicator 2X (Slottsmöllan, Sweden) and acrylonitrile butadiene styrene (ABS). The printing time for the whole plastic shell of the device was 90 minutes with the resolution of 250 μm . The whole device carries a 10 cm long cylindrical handle for routing electric wires (Fig. S-1a) and epoxy resin was used for sealing all joints. The electrodes (Fig. S-1b) were fabricated by thermally evaporating a 200 nm thick layer of gold on silicon dioxide substrates (wet-oxidized silicon wafers) having a 20-nm titanium adhesion layer. Card edge IDC connectors (female) were used to attach the electrodes (Fig. S-1b) at the opposite short sides of the conductivity cell. Contacts between the IDC connectors and electrical wires for the connection to an impedance analyser were prepared using H20E silver epoxy adhesive from Epoxy Technology, Inc., Billerica, MA, USA.

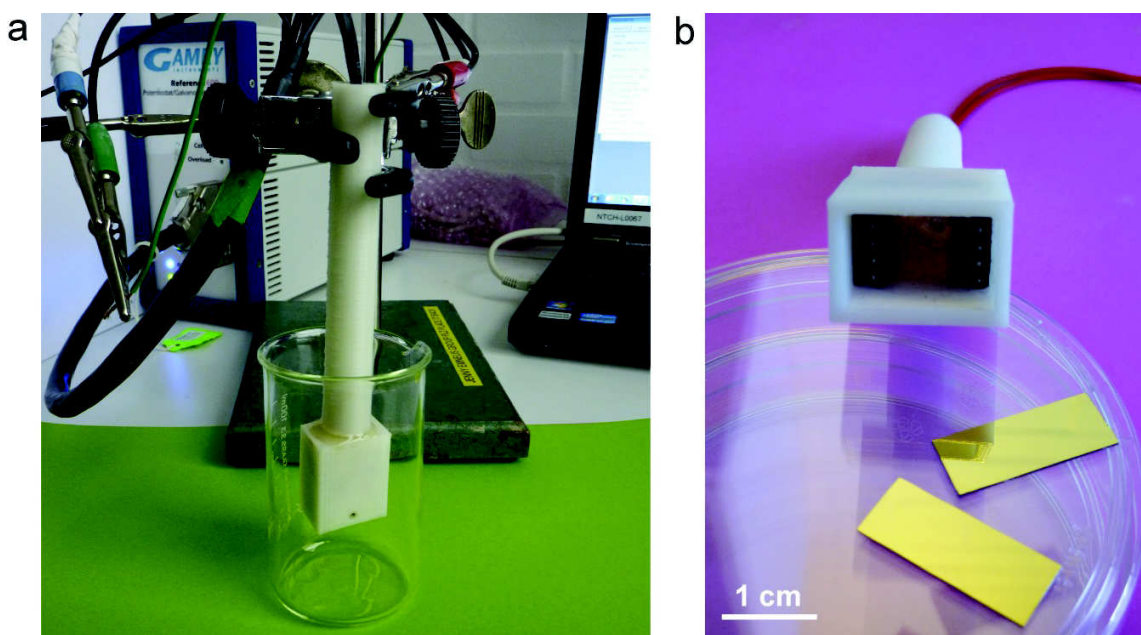


Figure S-1. (a) Photo of the 3D printed conductivity cell connected to an impedance analyser for EIS measurements. (b) A zoom-in photo of the conductivity cell with IDC connectors at the opposite short sides for mounting of the disposable gold electrodes.

S2. Automated Matlab script for data analysis

EIS spectra were acquired using a Reference 600 potentiostat (Gamry Instruments, Warminster, PA, USA).

Raw data files saved from Gamry Framework software (version 6.11) show .DTA extension, only containing tab-separated raw text that can be opened in any text editor or spreadsheet program. EIS data processing for automated generation of Bode plots and conductivity determination were implemented as a Matlab (version R2012b) script, which is shown below.

```
clear all;
clc;
close all;

% Convert the comma to dot for decimal places
file = memmapfile('01.dta', 'writable', true );
comma = uint8(',');
point = uint8('.');
file.Data( transpose( file.Data==comma ) ) = point;

file = importdata ('01.dta','\t', 98)
data = file.data
Zm = data(:,8)
Zr = data(:,5)
Zp = data(:,9)
fr = data(:,4)

% Bode plots for spectra
title_size = 12;
label_size = 10;

figure, %Bode plot for modulus
loglog(fr, Zm, 'LineWidth', 2, 'Color', 'r');
xlabel('Frequency [Hz]', 'fontsize', label_size, 'fontweight', 'b') % x-axis label
ylabel('|Z| [ohm]', 'fontsize', label_size, 'fontweight', 'b') % y-axis label
title('Bode plot for |Z|', 'fontsize', title_size, 'fontweight', 'b') %title

figure, %Bode plot for phase
semilogx(fr, Zp, 'LineWidth', 2);
xlabel('Frequency [Hz]', 'fontsize', label_size, 'fontweight', 'b') % x-axis label
ylabel('Phase [deg]', 'fontsize', label_size, 'fontweight', 'b') % y-axis label
title('Bode plot for phase', 'fontsize', title_size, 'fontweight', 'b') %title

[~, idx] = min(abs(Zp-0)); %finds the closest phase value to 0
zp1= Zp(idx);
zr1= Zr(idx); %takes the real component of Z for that phase value

C = 1.77/zr1*1e2 %C is the conductivity in S/m (1.77 is the cell constant)
```

S3 Effect of sinusoidal potential amplitude on conductivity determinations

To evaluate the effect of sinusoidal potential amplitude on conductivity determinations using our universal method, impedance spectra were recorded by applying sinusoidal potentials 10, 25 and 50 mV_{RMS} for both 1.3 S/m standard solution (used for calibration) and commercial physiological PBS (to calculate σ). Three sets of electrodes were tested in triplicate for the three different applied potential amplitudes, so that data are presented as average \pm s.e.m., $n = 9$. The measurements were conducted at room temperature in solutions exposed to atmospheric CO₂.

For all three cases, κ was calculated by performing EIS measurements on 1.3 S/m standard solution in order to calculate R_s , as described in the manuscript, and the same value was obtained. Well superimposed impedance spectra were obtained using all three potential amplitudes tested and both standard solution and commercial physiological PBS (Fig. S-3). The same conductivity value of 1.61 ± 0.02 S/m was calculated for physiological PBS at 250 kHz.

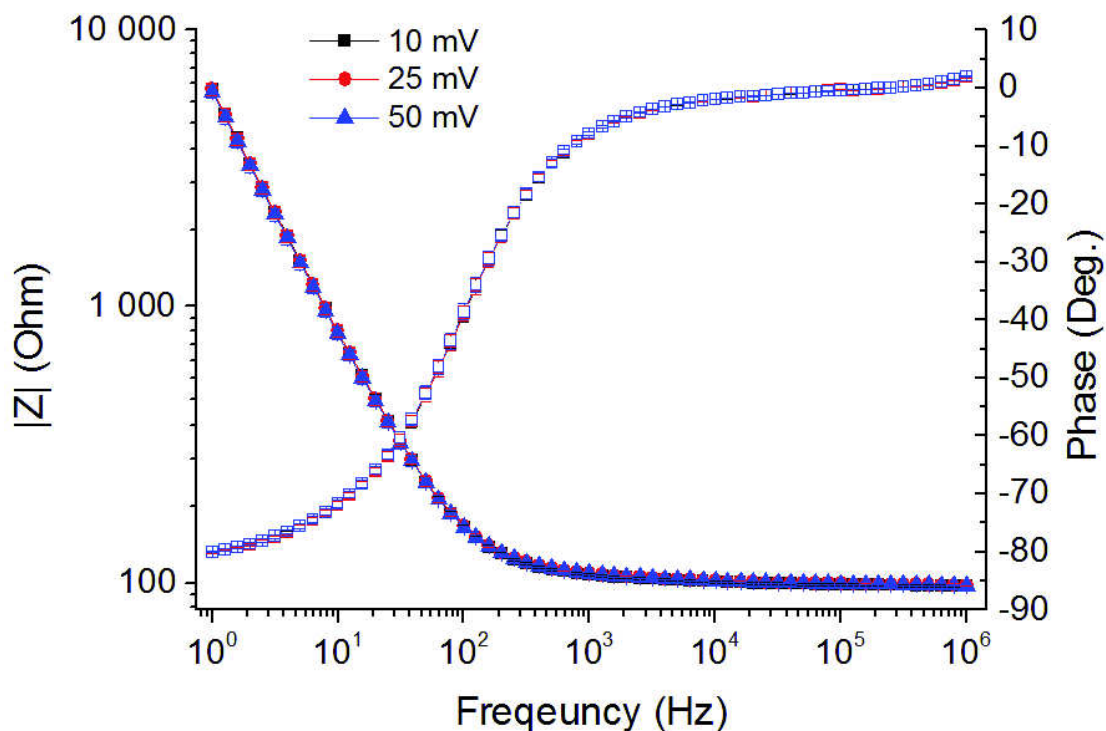


Figure S-3. Effect of different sinusoidal potential amplitudes on EIS analysis in physiological PBS. Data are presented as average \pm s.e.m., $n = 9$.

S4 Conductivity determinations using interdigitated microelectrodes (μ IDEs)

Conductivity determinations were carried out using microchips having twelve measurement sites, each comprising a gold μ IDE (twelve 500 μm long digits having 10 μm width and spacing) and a disc electrode (700 μm in diameter) which is located 900 μm (centre-to-centre) from the μ IDE (Fig. S-4a). The microchips were fabricated using a standard lift-off process on a Si/SiO₂ substrate as previously described elsewhere (M. Dimaki et al. *Sensors*, 2014, *14*, 9505–9521; K. Zór et al. *RSC Adv.*, 2014, *4*, 63761–63771). Two alternative sensing configurations were experimentally compared by recording impedance spectra for both 1.3 S/m standard solution (used for calibration) and commercial physiological PBS (to calculate σ):

- Configuration 1 (Fig. S-4a), for which measurements were performed between the two sides of each μ IDE;
- Configuration 2 (Fig. S-4a), for which measurements were performed between one μ IDE (both sides were connected and used as a working electrode) and the closest disc electrode.

The measurements were conducted at room temperature in solutions exposed to atmospheric CO₂. For both cases, κ was calculated by performing EIS measurements on 1.3 S/m standard solution using four different μ IDEs in order to calculate R_s , as described in the manuscript. Impedance spectra for commercial physiological PBS were recorded with the calibrated μ IDEs. Data are reported as average \pm S.D. (n=4). Conductivity value was calculated at the frequency closest to 0° obtaining 1.58 ± 0.05 S/m using Configuration 1 and 1.58 ± 0.06 S/m using Configuration 2. The batch of PBS used for this measurements was different from the one used for conductivity measurements with plates electrodes.

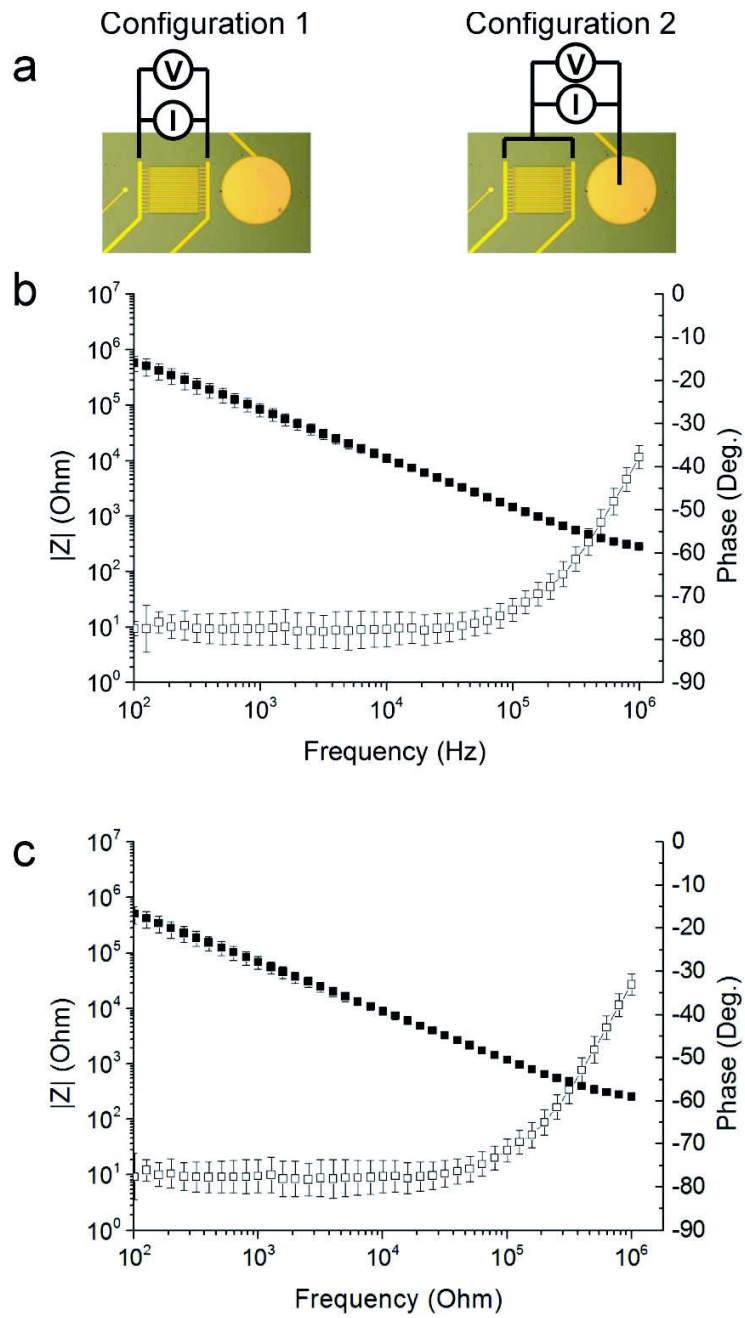


Figure S-4. (a) Two μ IDE configurations used for acquiring EIS spectra in commercial physiological PBS. Bode plots (average \pm SD, $n = 4$) for $|Z|$ (solid symbols) and ϕ (open symbols) for Configuration 1 (b) and Configuration 2 (c).

Paper III

Impedance spectroscopic characterisation of porosity in 3D cell culture scaffolds with different channel networks

C. Canali, S. Mohanty, A. Heiskanen, Ø. G. Martinsen, H. B. Muhammad, M. Dufva, A Wolff and J. Emnéus

Electroanalysis, 2015, 27, 93–99

Impedance Spectroscopic Characterisation of Porosity in 3D Cell Culture Scaffolds with Different Channel Networks

Chiara Canali,^[a] Soumyaranjan Mohanty,^[a] Arto Heiskanen,^[a] Haseena Bashir Muhammad,^[a] Ørjan Grøttem Martinsen,^[b, c] Martin Dufva,^[a] Anders Wolff,^[a] and Jenny Emnéus*^[a]

Abstract: We present the application of electrochemical impedance spectroscopy (EIS) as a method for discriminating between different polydimethylsiloxane (PDMS) scaffolds for three-dimensional (3D) cell cultures. The validity of EIS characterisation for scaffolds having different degree of porosity (networks of structured or random channels) is discussed in relation to Archie's law. Guide-

lines for EIS analysis are presented and demonstrated to provide porosity information in physiological buffer that agrees well with a more conventional weight-based approach. We also propose frequency ranges that may serve as means of single-frequency measurements for fast scaffold characterization combined with in vitro monitoring of 3D cell cultures.

Keywords: Impedance spectroscopy · 3D cell culture scaffold · Porosity · Channel networks · 3D printing

1 Introduction

Over the last two decades, three-dimensional (3D) cell culture systems have gained increasing interest in different fields spanning from biomedical sciences to pharmaceutical research [1]. The 3D format is believed to enable the formation and maintenance of a more in vivo like cellular environment able to supply cells with oxygen, nutrients, and soluble factor gradients (e.g. growth factors and hormones) leading to a more biologically relevant behaviour of cell functionality [2]. Careful considerations need to be taken in the design of 3D scaffolds for supporting cell organisation, proliferation and differentiation [3]. Based on the specific application, they can be fabricated from a variety of biocompatible materials (e.g. biopolymers, synthetic polymers, ceramic, metals). Among these, polydimethylsiloxane (PDMS) is a cheap transparent material with low autofluorescence and can be molded with a resolution down to a few micrometers [4]. It has already been demonstrated to be a suitable cell culture scaffold [5] after chemical and/or physical functionalisation [6] forming a hydrophilic surface, which can be further coated with specific extracellular matrix proteins, such as collagen and laminin.


Different scaffold parameters, such as pore size, geometry, orientation and interconnectivity, as well as channel branching can be tuned in order to influence the diffusion of nutrients and cell organisation within the 3D environment [7]. This can be achieved with traditional fabrication technologies (e.g. solvent-casting/particle leaching, gas foaming, fibre bonding, phase separation, and emulsion freeze drying [8]). Recently, 3D printing has also emerged as a promising technique to precisely control the scaffold architecture [9].

A wide range of methods are currently available for characterising scaffold porosity, spanning from scanning electron microscopy (SEM) to gas adsorption and mercury intrusion porosimetry (MIP). All of them strictly depend on the sample exposure to vacuum conditions [10]. SEM allows characterisation of both the degree of scaffold porosity and pore size, although it requires sectioning and gold sputtering of the sample in order to provide relevant information. Furthermore, sputter coating has the potential disadvantage of causing heat damage to the sample. Gas adsorption may be applied to measure the scaffold surface area and probe its entire surface including irregularities and pore interiors. Prior to the measurements, the sample is pretreated at an elevated temperature in vacuum to remove any contaminants, which increases the risk of its degradation. MIP is a widely used approach to measure pore distribution and connectivity, tortuosity and compressibility in biomaterials. It allows the detection of pore size ranging from 2 up to more than 50 nm in diameter by monitoring the pro-

[a] C. Canali, S. Mohanty, A. Heiskanen, H. B. Muhammad, M. Dufva, A. Wolff, J. Emnéus
Department of Micro- and Nanotechnology, Technical University of Denmark,
2800 Kgs Lyngby, Denmark
*e-mail: jenny.emneus@nanotech.dtu.dk

[b] Ø. G. Martinsen
Department of Physics, University of Oslo,
Oslo, Norway

[c] Ø. G. Martinsen
Department of Biomedical and Clinical Engineering,
Oslo University Hospital,
Oslo, Norway

 Supporting Information for this article is available on the WWW under <http://dx.doi.org/10.1002/elan.201400413>.

gressive intrusion of mercury into a dried structure. However, the strict condition of applied pressure may damage the scaffold [10].

Electrochemical impedance spectroscopy (EIS) is a nondestructive and fast technique, which can be applied at room temperature and atmospheric pressure. It has been applied for the evaluation of pore geometry in random chitosan scaffolds prepared by freeze drying [11]. However, this approach was not validated for different networks of structured or random channels, and a detailed analysis of the performed measurements was not included. EIS has also been shown to be suitable for real-time monitoring of large 3D cell cultures with spatial sensitivity [12]. Hence, EIS has potential for simultaneous structural characterisation of 3D scaffolds and evaluation of cellular behaviour (growth, response to cellular effectors, etc.). This can be possible even in perfusion-based 3D cell culture systems and bioreactors, which are relevant in biomedical engineering.

In this study, we focus on further development of EIS-based characterisation of 3D scaffold porosity to achieve a more universal approach suitable for future biomedical applications. This comprises complete analysis of acquired spectra to find a range of frequencies that provides a high sensitivity for characterisation of scaffolds with i) several networks of structured or random channels, and ii) different degrees of porosity. In our work, PDMS scaffolds were fabricated using a molding process which exploits water soluble negative templates carrying random (from sugar cube) or structured (3D printed) channels. The obtained data for scaffold porosity were validated against a more conventional weight-based method which takes into account the apparent volume (based on external geometric dimensions) of the scaffold and the PDMS density [13].

2 Theory

Archie's law is an empirical correlation usually employed to estimate the amount of hydrocarbons in reservoir rocks [14]. Accordingly, it links the electrical resistivity of the rock to its porosity, to the resistivity of the water that saturates its pores, and to the fractional saturation of the pore space with water. Hence, Archie's law indirectly establishes a relationship between the pore geometry of a rock and the conductivity of the interstitial space due to the presence of hydrocarbons and aqueous environment.

Tully-Dartez et al. [11] applied Archie's law for discrimination between chitosan-based 3D cell culture scaffolds with different random porosity. Here, we further develop the method, making it more universal by applying gold plate electrodes in a measurement setup instead of the more conventional cylindrical probes (already used for geophysical measurements and by Tully-Dartez et al.). Plate electrodes facilitate interfacing with a scaffold without the necessity of penetrating into the bulk material, which gives a significant advantage for measurements when using scaffolds made of brittle or tough elastomeric

materials. Phosphate buffered saline (PBS) was used as bulk electrolyte to saturate the scaffold pores.

According to Archie's law:

$$\sigma_{\text{eff}} = C\sigma_0\varphi_0^m \quad (1)$$

where C is the coefficient of saturation with the electrolyte (ranging from 0.1 to 1), σ_0 is the conductivity of the bulk electrolyte filling the pores, φ_0 is the porosity, and m is the *cementation factor* originally related to the degree of compactness of the rock matrix. Since the scaffold is completely soaked in the electrolyte, C was set equal to 1, assuming complete saturation of the pores. m depends on the grain type, size and shape, the dimension and profile of pores and pore cavities, as well as the size and number of dead-end pores. In general, m increases as the degree of connections of the pore network decreases, and can be between slightly less than one for fractured rocks and around 5 for highly compacted ones [15]. m is difficult to estimate based on physical observations and takes different values depending on the type of rock formation and the calculation method. Experiments have shown that m values are commonly between 1.3 and 3.0; however, it is often assumed to be constant and equal to 2, as in the case of clean sandstone [16]. In only two ideal cases, an analytical solution of the Archie's law has been possible, corresponding to $m=1$ and $m=1.5$. The first case represents a 3D matrix penetrated by an array of straight channels [17], while the second refers to a network of perfect spherical pores [18,19].

Since Archie's law relates the bulk electrical conductivity to the porosity of a rock, it indirectly embeds the concept of electrical conductance, which is based on resistance measurements of the interstitial electrolyte. Conductivity of an electrolyte is determined using a two-electrode setup as the product of a specific cell constant and the inverse of solution resistance. The cell constant is the ratio between the distance separating the electrodes and the area exposed to the electrolyte. Solution resistance can be extracted from impedance magnitude ($|Z|$) at the frequency where the phase angle is equal to 0° . In our work, preliminary EIS estimations of PBS conductivity were conducted and a value of 1.35 S/m was adopted. Archie's law basically corrects the bulk electrical conductivity by a geometric factor, which in our study is specific for each characterised scaffold between the two electrodes. Thereby, the scaffold's effective conductivity can be calculated as:

$$\sigma_{\text{eff}} = \frac{l}{R_b A} \quad (2)$$

where R_b is the bulk solution resistance, A and l are the cross-sectional area and the length of the scaffold, respectively. R_b is the impedance value at the frequency for which the phase angle is equal to 0° . In the presence of a scaffold, the value of R_b is higher than the solution resistance of a pure electrolyte filling the electrochemical

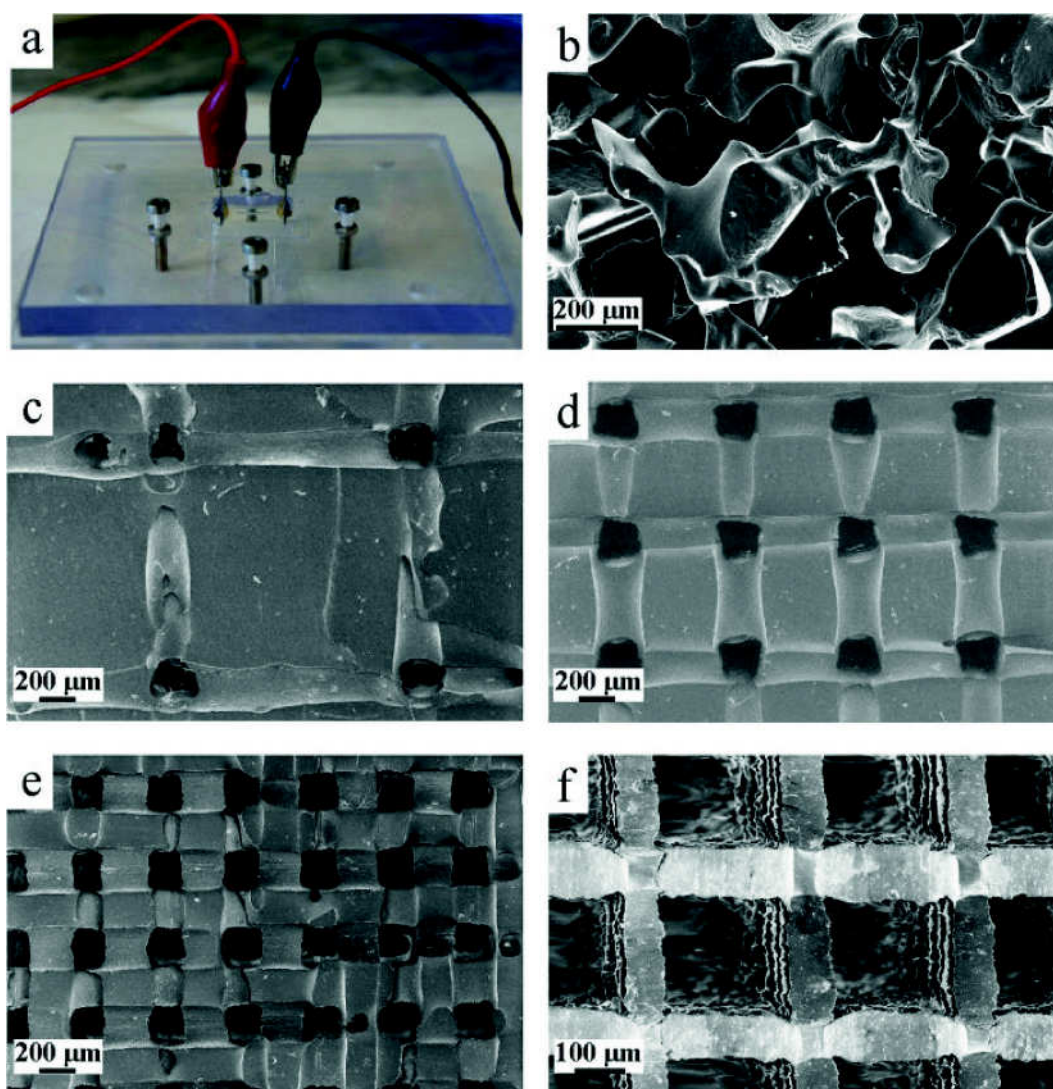


Fig. 1. (a) Photo of the measurement setup. (b–f) SEM images of the PDMS scaffolds: random pore networks (b); structured channels with 20 (c), 40 (d), 60 (e) and 80% (f) infill.

cell, which according to Equation 2 results in a decreased σ_{eff} .

Analogously to what has been previously proposed for sandstone, Tully-Dartez et al. adopted $m=2$ for porosity determination in random chitosan scaffolds. In our work using PDMS-based random scaffolds, the same value of m was used. However, for structured PDMS scaffolds, which are characterised by arrays of straight channels, we chose $m=1$ in accordance with the general considerations presented for geophysical studies [17].

3 Experimental

3.1 Measurement Setup, Scaffold Fabrication and Preparation for Measurements

The measurement setup (Figure 1a) comprising a rectangular chamber was micromilled of polycarbonate and the gold plate electrodes were fabricated by thermally evapo-

rating a 200-nm gold layer onto a wet-oxidized (650-nm oxide layer) silicon wafer coated with a 20-nm titanium adhesion layer [12]. The PDMS scaffolds were fabricated in order to tightly fit them between the electrodes (width 10 mm) placed at the ends of the chamber, resulting in an inter-electrode distance of 14 mm. The height of the chamber was 10 mm.

Random PDMS scaffolds (Figure 1b, Supporting Information Figure S1B) were fabricated with the sugar-templating process proposed by Choi et al. [20] using commercially available sugar cubes. PDMS (Sylgard 184) was purchased from Dow Corning Inc., Midland, MI, USA. Structured scaffolds with arrays of parallel and perpendicular straight channels were fabricated through a molding process where negative templates were 3D printed (Makerbot Replicator 2X, Slottsmöllan, Sweden) using a water soluble filament (polyvinyl alcohol, PVA). Different degrees of infill (i.e. the amount of deposited material during 3D printing) spanning from 20 up to 80% were

used. After PDMS casting, the filaments were dissolved in water under ultrasonication for at least 2 h (dependent on scaffold compactness). In this way, the volumes originally filled with the water soluble polymer became straight channels within the scaffold structure, i.e. the higher the infill %, the higher the achieved scaffold porosity (Fig. 1c–f). Prior to analysis, scaffolds were rendered hydrophilic by combining oxygen plasma treatment (2 minutes for each side; power of 50 W and pressure of 35 Pa) and autoclaving.

In preparation for EIS analysis, scaffolds were manually cut to match as closely as possible the width of the plate electrodes. The length was always strictly kept as the inter-electrode distance. The height of the cut scaffolds varied between 8 and 9 mm.

3.2 EIS Analysis

Prior to any measurements, the gold electrodes were cleaned by a 10-min treatment using a mixture of H₂O₂ (25% v/v) and KOH (50 mM) followed by a potential sweep from –200 mV to –1200 mV in 50 mM KOH [21]. The scaffolds were completely soaked in PBS (Sigma D8662) by applying vacuum and transferred into the measurement setup which was then filled with PBS to have the scaffold fully immersed. The level of PBS was adjusted according to the height of each scaffold.

A sinusoidal potential of 10 mV (rms) with respect to the open circuit potential was applied in the frequency range between 1 Hz and 1 MHz using a Reference 600 potentiostat/galvanostat/ZRA (Gamry Instruments, Warminster, PA, USA). Three scaffolds of each type were used for the measurements and the results are reported as mean ± standard deviation ($n=3$).

The geometric factors described above (inter-electrode distance, l ; electrode width; scaffold height) determine the basis for conductivity measurements using EIS. The bulk conductivity of the electrolyte (PBS) was determined based on calibration with a standard solution having a known conductivity (1.29 S/m, Hanna Instruments, cat. 663–5047). Measurements were conducted using three PBS samples.

3.3 Validation

The scaffolds were imaged using SEM (Supra 40 VP, Zeiss SMT AG, Oberkochen, Germany) as shown in Figure 1b–f. Scaffold porosity was determined using the weight-based method described by Cho et al. [13] by applying the following equation:

$$\text{Porosity} = \frac{V_0 - (m/\rho)}{V_0} \times 100 (\%) \quad (3)$$

where V_0 is the apparent volume of the scaffold calculated using its outer dimension; m is the mass of the scaffold and ρ is the PDMS density (0.965 g/mL). The analysis

was performed on three different samples of each scaffold type and the results are reported as mean ± standard deviation ($n=3$).

4 Results and Discussion

A complete spectral analysis of the experimental data was performed to understand how EIS measurements reflect the structural features of different type of scaffolds in physiological PBS (Figure 2a). The measurements were also compared with EIS behavior of PBS as control. Bode plots for phase angle allow easy visual estimation of the frequency range where the phase angle is close to 0° to obtain the solution resistance. Furthermore, the frequency ranges should exclude the influence of possible parasitics usually appearing above 500 kHz. A very high reproducibility was achieved as shown by the low standard deviation among the measurements. A common frequency range for structural characterisation was inferred from the spectra and reported in Table 1. For fast evaluation of scaffold porosity, the proposed frequency range provides the possibility to conduct single-frequency EIS measurements instead of acquiring and analyzing complete spectra. The frequency ranges presented here are valid for the used PDMS-based scaffolds and may vary depending on the scaffold material and the overall 3D architecture.

Since EIS measurements were performed using an electrolyte which does not contain any redox couple, they merely involve non-faradaic processes associated with the double layer capacitance of the electrodes and the ionic current, the bulk behavior of which is affected by the presence of the scaffolds. Hence, in this case, the acquired spectra are influenced by ionic strength, type of ions and temperature, as well as the material properties and porosity/channel geometry of the different scaffolds.

The scaffolds under investigation are composed of PDMS, which is a non-conducting polymer. Due to this, when a scaffold is placed in the high-conductivity electrolyte, the measured $|Z|$ is expected to increase with decreasing volume of the electrolyte filling the pores. In order to obtain an accurate estimation of σ_{eff} (Equation 2) in the presence of the different scaffolds, their cross-sectional area needs to be taken into account during analysis of EIS data. Therefore, $|Z|$ values over the entire frequency range can be divided by the specific geometric factor l/A of each scaffold, which may have slight variation due to manual cutting. This normalisation approach is reported in Figure 2b and allows an easy discrimination between the different scaffolds based on their specific geometric constraints.

Table 1 and Figure 3 show values of porosity determined for random and structured scaffolds (20–80% infill) using both EIS- and weight-based techniques. The obtained porosity values using the two approaches are comparable. The weight-based method shows a higher standard deviation, which may be due to errors in the weighing, whereas EIS measurements provide a higher

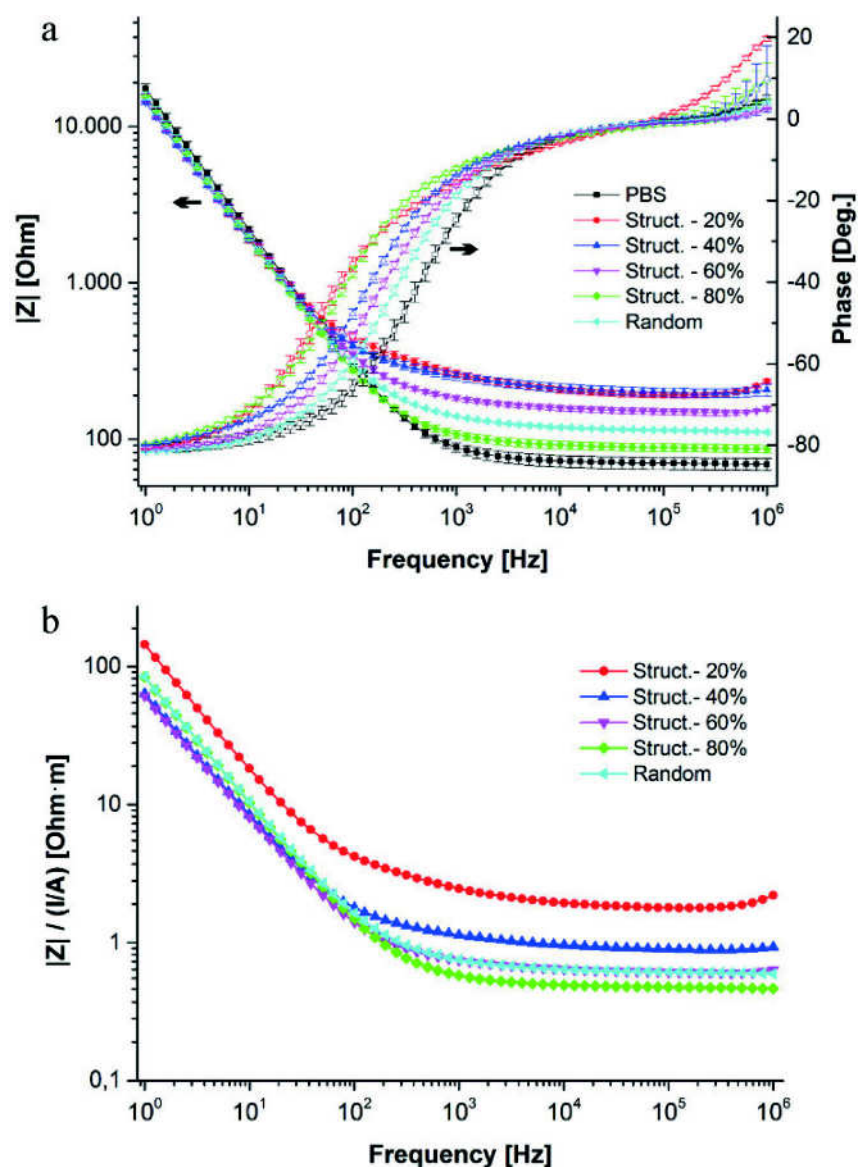


Fig. 2. (a) EIS analysis of the scaffolds soaked in PBS between 1 and 10^6 Hz. Data are reported as mean \pm standard deviation ($n=3$). (b) Normalisation of the impedance data: $|Z|$ (Ohm) of the scaffold soaked in PBS was divided by the geometric factor l/A (m^{-1}) characteristic of each scaffold.

Table 1. Porosity values (%) for random and structured scaffolds (20–80% infill) determined using the weight-based method [13] and EIS measurements in PBS. Values are reported as mean \pm standard deviation ($n=3$) with suitable frequency ranges for EIS analysis.

Scaffold type	Porosity (%): weight-based method	Porosity (%): EIS [a]	Frequency range (kHz) for EIS analysis
Random	64 ± 1	67.75 ± 0.01	50–70
Structured 20%	19.5 ± 0.5	23.47 ± 0.01	50–70
40%	38.89 ± 0.07	45.80 ± 0.04	50–70
60%	60.5 ± 0.5	60.99 ± 0.03	50–70
80%	81 ± 1	89.17 ± 0.05	50–70

[a] In porosity calculation involving Equation 1 and 2, the following parameters were used: $m=1$ for structured scaffolds and $m=2$ for random scaffolds; $C=1$ for all scaffolds and $\sigma_0=1.35 S/m$.

precision for the obtained porosity values reflected by the small standard deviations. Nevertheless, the porosity values determined using the more conventional weight-based technique were considered as guidelines for validation of the EIS-based technique.

On the other hand, when comparing the porosity values determined using the two techniques, it can be clearly seen that the EIS-based technique gives porosity which is larger than the one obtained using the weight-based technique, with exception of the structured scaffold

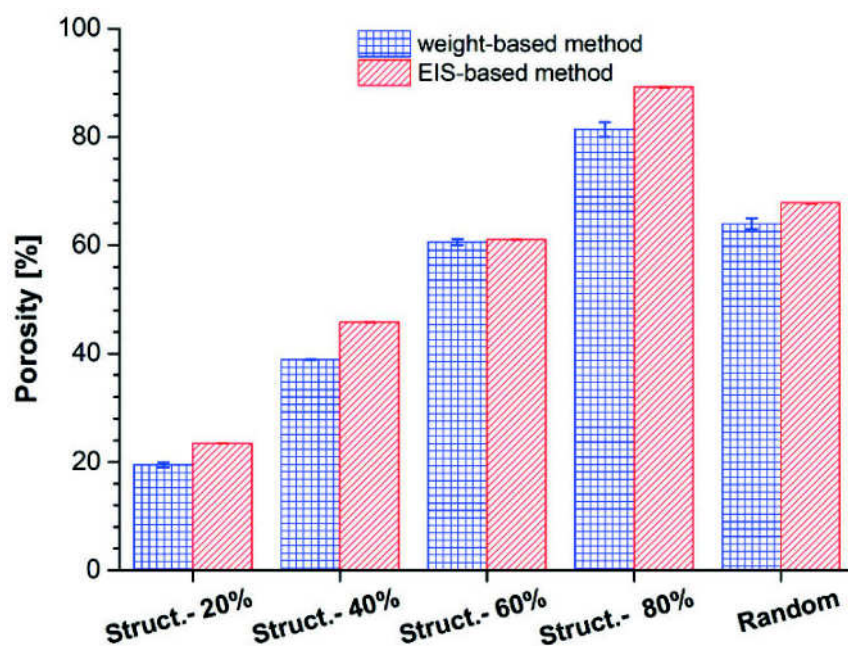


Fig. 3. Evaluation of porosity for random and structured scaffolds using the weight-based method [13] and EIS measurements in PBS. Data are reported as mean \pm standard deviation ($n=3$).

having 60% infill. The deviation between the porosity values obtained using the two techniques entails that the results of the EIS-based approach contain a certain degree of systematic errors. The sources of systematic error may comprise imprecision in cutting the scaffolds and placement in the measurement chamber. These factors can significantly influence the EIS-based results, which are strongly dependent on the degree of contact between the scaffolds and plate electrodes. In case there are voids between the electrodes and scaffolds, the result can be leakage current, i.e. the electric fields can bypass the scaffolds through the surrounding electrolyte. A similar phenomenon was pointed out by Tully-Dartez et al. in measurements using cylindrical electrodes embedded inside the scaffolds. They used sealing with wax as an approach to eliminate the effect of leakage current. In our approach targeting to a more universal technique using plate electrodes at the ends of the scaffolds, introduction of a sealing material would impede the future possibility for combined cell culture investigations.

EIS measurements using the random scaffolds comprise additional complication in comparison with the structured scaffolds due to the fact that the surfaces in contact with the electrodes are corrugated due to the structural features. This results in additional leakage current around the scaffolds due to the larger electrode area which is in direct contact with the surrounding electrolyte. To explore in more detail the effect of the electric field bypassing the scaffold, finite element (FE) simulations of the measurement setup containing two electrodes and the random PDMS scaffold were carried out for studying the electric potential (Supporting Information Fig. S1 B a) and

the current density distribution (Supporting Information Figure S1 B b,c) across the random PDMS scaffold.

The obtained average porosity for random scaffolds agrees fairly well with the weight-based technique. Moreover, the random scaffolds show a porosity which is roughly comparable to the structured scaffold with 60% infill. This means that for a random scaffold, which has curved and dead-end paths able to impede ionic current more strongly than the straight channels of a structured scaffold, the determined porosity entails the presence of larger random void volumes. However, both the EIS- and weight-based technique are affected by the degree of wettability of the scaffold material. In our experiments, the scaffolds were treated using oxygen plasma to allow complete electrolyte penetration. Due to the complex structure of such scaffolds, the plasma treatment may not completely influence the PDMS surface in all dead-end pores, which may decrease the achieved wettability. Therefore, the porosities determined using the two techniques may comprise a certain degree of systematic error since the underlying assumption is complete pore saturation with the electrolyte ($C=1$ in Equation 1). For further development of the EIS-based technique, evaluation of different random scaffolds with varying pore dimensions, geometries and fabrication materials need to be explored, which may lead to a deeper understanding of the degree of electrolyte saturation, i.e. the range of valid C values.

As for geophysical investigations, the valid m values for random porous tissue engineering scaffolds may vary depending on the pore architecture. When using the porosity obtained in weight-based determinations as reference, recalculations of the actual m value for the random scaf-

folds is around 1.75. This means that in further development of the EIS-based technique, analogously to what was mentioned above in connection with electrolyte saturation (C value), investigations are needed to achieve more rigorous understanding of a valid range of m values for different type of random scaffolds. Additionally, other experimental techniques, such as 3D imaging, can be applied for complete empirical validation of m values.

The good agreement between the determined porosities using the two techniques demonstrates that the EIS approach constitutes a significant fast and non-invasive alternative for porosity evaluation. This could be achieved in the same setup where cell-based measurements are to be performed for biomedical applications. The technique can be further validated for a wide range of scaffold materials and geometries, opening perspectives for future studies on more complex combined architectures of structured and random geometries [22,23]. However, to optimise EIS-based porosity determination in a setup where cells are cultured in serum-containing medium, it is necessary to further investigate the influence of protein adsorption on the scaffold material and electrodes, which based on our preliminary experiments has an effect on the impedance measurements.

5 Conclusions

Previous studies have shown the possibility of applying EIS measurements to determine the porosity of tissue engineering scaffolds using cylindrical electrodes that penetrate into the material. Here, we demonstrated a more universal EIS-based approach using plate electrodes interfaced to ends of the scaffold. Our results prove the potential of EIS measurements in characterising 3D cell culture scaffolds with different networks of structured or random channels, and several degrees of porosity in a setup where cell culturing is to be performed. To further optimise the EIS-based technique, additional experimental work combined with alternative techniques is required in order to take into consideration the geometrical constraint of channel architecture and their degree of electrolyte saturation (i.e. suitable range of m and C values, respectively).

Acknowledgements

This work and the Ph.D. fellowship of C. Canali were supported by the EU-funded project *NanoBio4Trans* ("A new nanotechnology-based paradigm for engineering vascularised liver tissue for transplantation", Grant No: 304842).

References

- [1] R. Edmondson, J. J. Broglie, A. F. Adcock, L. Yang, *Assay Drug Dev. Technol.* **2014**, *12*, 207–218.
- [2] M. Matsusaki, C. P. Case, M. Akashi, *Adv. Drug Deliv. Rev.* **2014**, DOI: 10.1016/j.addr.2014.01.003.
- [3] E. Carletti, A. Motta, C. Migliaresi, *Meth. Mol. Biol.* **2011**, *695*, 17–39.
- [4] A. Mata, A. J. Fleischman, S. Roy, *Biomed. Microdev.* **2005**, *7*, 281–293.
- [5] A. Díaz Lantada, H. Alarcón Iniesta, B. Pareja Sánchez, J. P. García-Ruiz, *Adv. Mater. Sci. Eng.* **2014**, DOI: 10.1155/2014/612976.
- [6] D. Bodas, C. Khan-Malek, *Microelectron. Eng.* **2006**, *83*, 1277–1279.
- [7] T. S. Karande, J. L. Ong, C. M. Agrawal, *Ann. Biomed. Eng.* **2004**, *32*, 1728–1743.
- [8] A. A. Chen, V. Liu Tsang, D. R. Albrecht, S. N. Bhatia, *BioMEMS Biomed Nanotechnol.* **2007**, *7*, 23–38.
- [9] M. Lee, B. M. Wu, *Meth. Mol. Biol.* **2012**, *868*, 257–267.
- [10] T. S. Sampath Kumar, in *Characterization of Biomaterials*, 1st ed. (Eds: A. Bandyopadhyay, S. Bose 2) Elsevier Science, Amsterdam, **2013**, ch. 2, pp. 11–47.
- [11] S. Tully-Dartez, H. E. Cardenas, P. Sidney Sit, *Tissue Eng. Part C Meth.* **2010**, *16*, 339–345.
- [12] C. Canali, A. Heiskanen, H. B. Muhammad, P. Høyum, F. Pettersen, M. Hemmingsen, A. Wolff, M. Dufva, Ø. G. Martinsen, J. Emnéus, *Biosens. Bioelectron.* **2015**, *63*, 72–79.
- [13] Y. S. Cho, M. W. Hong, Y. Y. Kim, Y. Cho, *J. Appl. Polym. Sci.* **2014**, *31*, 1–8.
- [14] G. E. Archie, *AIME Trans.* **1942**, *146*, 54–62.
- [15] H. S. Salem, G. V. Chilingarian, *J. Petroleum Sci. Eng.* **1999**, *23*, 83–93.
- [16] F. S. Kadhim, A. Samsuri, A. Kamal, *Life Sci. J.* **2013**, *10*, 2451–2458.
- [17] P. Glover, *Geophysics* **2009**, *28*, 82–85.
- [18] P. N. Sen, C. Scala, M. H. Cohen, *Geophysics* **1981**, *46*, 781–795.
- [19] K. S. Mendelson, M. H. Cohen, *Geophysics* **1982**, *47*, 257–263.
- [20] S. Choi, T. Kwon, H. Im, D. Moon, D. J. Baek, M. Seol, J. P. Duarte, Y. Choi, *ACS Appl. Mater. Interf.* **2011**, *3*, 4552–4556.
- [21] A. R. Heiskanen, C. F. Spiegel, N. Kostesha, T. Ruzgas, J. Emnéus, *Langmuir* **2008**, *24*, 9066–9073.
- [22] W. Dai, N. Kawazoe, X. Lin, J. Dong, G. Chen, *Biomaterials* **2010**, *31*, 2141–2152.
- [23] H. Lu, H. H. Oh, N. Kawazoe, K. Yamagishi, G. Chen *Sci. Technol. Adv. Mater.* **2012**, *13*, 064210 (7p).

Received: August 8, 2014

Accepted: October 11, 2014

Published online: ■ ■ ■ ■, 2014

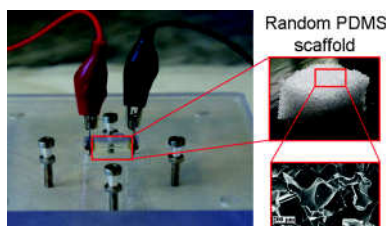
FULL PAPERS

*C. Canali, S. Mohanty, A. Heiskanen,
H. B. Muhammad, Ø. G. Martinsen,
M. Dufva, A. Wolff, J. Emnéus**

■■ – ■■



**Impedance Spectroscopic
Characterisation of Porosity in 3D
Cell Culture Scaffolds with Different
Channel Networks**



Supporting Information:

Impedance spectroscopic characterisation of porosity in 3D cell culture scaffolds with different channel networks

Chiara Canali et al.

Electrical impedance spectroscopy (EIS) based results are strongly dependent on the degree of contact between the scaffolds and plate electrodes. The corrugated surface of random scaffolds (Fig. S1 A) forms voids between the electrodes and scaffolds resulting in leakage current, i.e. the electric field can bypass the scaffolds through the surrounding electrolyte (Fig. S1 B b-c). This phenomenon was already pointed out by Tully-Dartez *et al.* in measurements using cylindrical electrodes embedded inside chitosan scaffolds [1]. To eliminate the effect of leakage current they used sealing with wax. In our approach targeting to a more universal technique using plate electrodes at the ends of the scaffolds, introduction of a sealing material would impede the future possibility for combined cell culture investigations.

To explore in more detail the effect of the electric field bypassing the scaffold, finite element (FE) simulations were carried out using Comsol Multiphysics v4.3b. 2D models of the measurement setup containing two electrodes and the PDMS scaffold were created in the AC-DC module for studying the electric potential (Fig. S1 B a) and the current density distribution (Fig. S1 B b-c) across the PDMS random scaffold. Only the gold surface (200 nm) of the electrodes was modelled. The conductivity of PBS filling the measurement setup and the scaffold pores was set as 1.35 S/m based on calibration with a standard solution having a known conductivity (Hanna Instruments, cat. 663-5047). The mesh consisted of 40908 tetrahedral elements with an average element quality of 0.91. The presented 2D model as a simplification of the random scaffold is sufficient to illustrate the electric field bypassing the scaffold in the X-Y plane, although it does not focus on the current path through the pore network filled with PBS. This is due to the limited connectivity in the presented X-Y plane. In a 3D model the overall contribution of the electric field would comprise also connectivity along the Z plane.

[1] S. Tully-Dartez, H.E Cardenas, P. Sidney Sit, *Tissue Eng Part C Methods* **2010**, *16*, 339-345

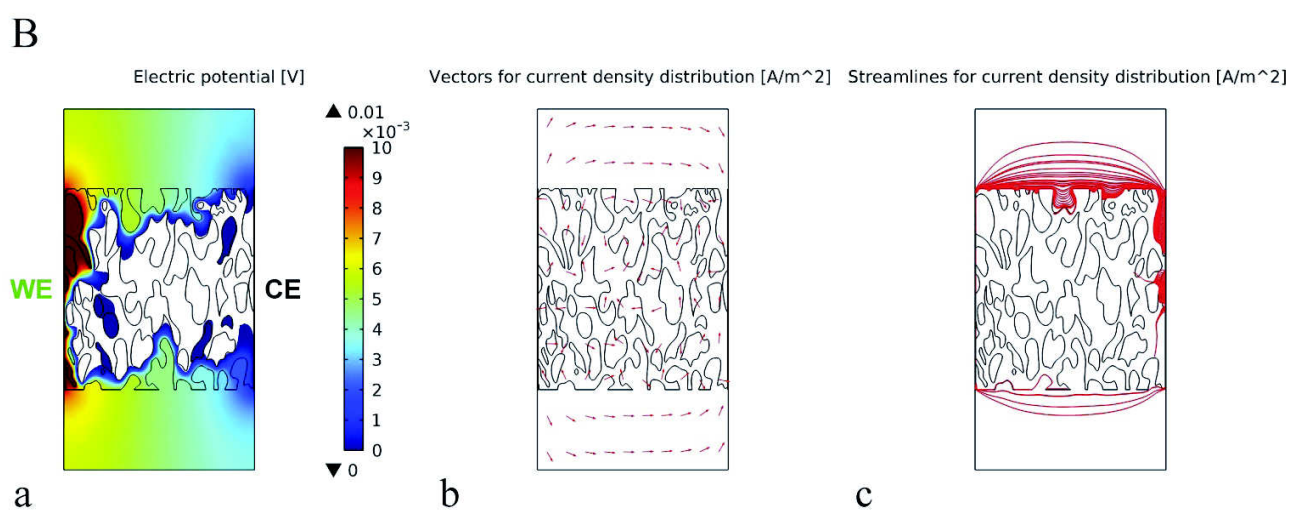
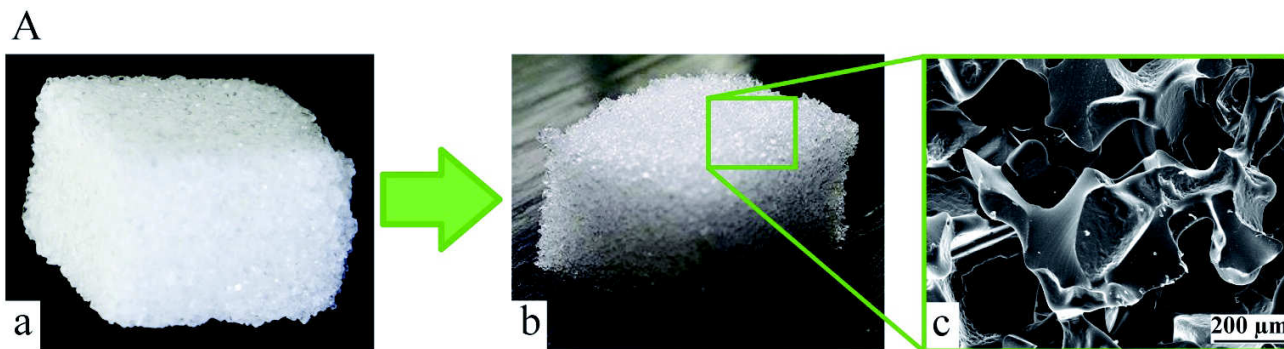
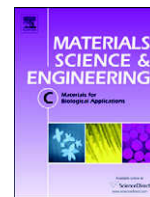


Fig. S1. (A) Schematics of the random scaffold topology. (a) Sugar cube as negative template; (b) the correspondent PDMS random scaffold and (c) SEM image of the random pore network distribution. - (B) FE analysis of the measurement setup containing the random scaffold: (a) electric potential [V]; (b) vectors for current density distribution [A/m^2]; (c) streamlines for current density distribution [A/m^2]. Only the gold surface of the electrodes is modelled. (WE = working electrode, CE = counter electrode)

Paper IV

Fabrication of scalable and structured tissue engineering scaffolds using water dissolvable sacrificial 3D printed moulds

S. Mohanty; L. B. Larsen, J. Trifol Guzman, P. Szabo, H. V. R. Burry, C. Canali, M. Dufva, J. Emnéus and A. Wolff
Mater. Sci. Eng. C, 55, 2015, 569–578



Fabrication of scalable and structured tissue engineering scaffolds using water dissolvable sacrificial 3D printed moulds



Soumyaranjan Mohanty^a, Layla Bashir Larsen^a, Jon Trifol^b, Peter Szabo^b, Harsha Vardhan Reddy Burri^a, Chiara Canali^a, Marin Dufva^a, Jenny Emnéus^a, Anders Wolff^{a,*}

^a DTU Nanotech, Department of Micro- and Nanotechnology, Technical University of Denmark, Ørstedsgade, DK-2800 Kgs. Lyngby, Denmark

^b Danish Polymer Centre, Department of Chemical and Biochemical Engineering, Søtofts Plads, Building 229, DK-2800 Kgs. Lyngby, Denmark

ARTICLE INFO

Article history:

Received 23 February 2015

Received in revised form 7 May 2015

Accepted 4 June 2015

Available online 9 June 2015

Keywords:

Tissue engineering

3D printing

Scalable

PVA

ABSTRACT

One of the major challenges in producing large scale engineered tissue is the lack of ability to create large highly perfused scaffolds in which cells can grow at a high cell density and viability. Here, we explore 3D printed polyvinyl alcohol (PVA) as a sacrificial mould in a polymer casting process. The PVA mould network defines the channels and is dissolved after curing the polymer casted around it. The printing parameters determined the PVA filament density in the sacrificial structure and this density resulted in different stiffness of the corresponding elastomer replica. It was possible to achieve 80% porosity corresponding to about 150 cm²/cm³ surface to volume ratio. The process is easily scalable as demonstrated by fabricating a 75 cm³ scaffold with about 16,000 interconnected channels (about 1 m² surface area) and with a channel to channel distance of only 78 μm. To our knowledge this is the largest scaffold ever to be produced with such small feature sizes and with so many structured channels. The fabricated scaffolds were applied for in-vitro culturing of hepatocytes over a 12-day culture period. Smaller scaffolds (6 × 4 mm) were tested for cell culturing and could support homogeneous cell growth throughout the scaffold. Presumably, the diffusion of oxygen and nutrient throughout the channel network is rapid enough to support cell growth. In conclusion, the described process is scalable, compatible with cell culture, rapid, and inexpensive.

© 2015 The Authors. Published by Elsevier B.V. This is an open access article under the CC BY-NC-ND license (<http://creativecommons.org/licenses/by-nc-nd/4.0/>).

1. Introduction

In recent years, there has been a great demand for the development of bioartificial organs/tissues in the field of organ transplantation and in vitro toxicological drug screening [1]. One of the primary challenges in translation of tissue engineering to clinical application is the difficulty in scaling up complex, biological effective tissues and organs to the size relevant for human [2]. Although small scale three-dimensional (3D) scaffold constructs have been achieved to mimic organs for e.g., in vitro drug testing [3], the applied fabrication approaches are not easily translated to constructs of human organ size. When engineering tissues in vitro, there is a requirement for structures or scaffolds that are able to support cell growth and at the same time mimicking the physiological environment including the geometrical, topographical and physical features of the targeted tissue. Specifically for the generation of thick 3D tissues, the development of highly dense vascular networks that can meet the nutrient and oxygen requirements of large masses of living cells remains a tissue engineering challenge. This often limits the size of engineered tissues to a few hundred micrometres [4]. The ideal

tissue engineering scaffold supports the spatial distribution of cells in a three dimensional structure, provides mechanical stability to the cells and enables optimum nutrient transport and metabolic waste removal [5,6]. Numerous approaches exist to create 3D highly vascularized engineered tissue scaffolds to accommodate a high density of cells in high surface to volume ratio structures [6,7]. One strategy has been to use highly porous structures with interconnected pores/microchannels that provide space for penetration and growth of cells and enable favourable mass transport characteristics [8,9]. The structural, mechanical and mass transport properties of such scaffolds are determined by parameters such as pore size, pore shape, porosity, pore interconnectivity, permeability, scaffold surface area, scaffold effective stiffness and scaffold material [10].

Scaffolds consisting of stochastic, disordered or random micropores are one of the oldest and most widely used templates for tissue engineering [11,12]. Manufacturing techniques such as solvent casting-particulate leaching [13], phase separation [14], gas foaming [15], emulsion freeze drying [16] and fibre meshes [17] have been used to generate engineered scaffolds of foam-like internal structure with a random architecture and a limited control of scale [18]. Although such processing techniques are quick, scalable and economical, they do not enable accurate control of the microarchitectural details such as the

* Corresponding author.

E-mail address: anders.wolff@nanotech.dtu.dk (A. Wolff).

pore size, geometry, their interconnections and distribution within the scaffold [19]. The possibility to control the inner architecture of scaffolds is desirable as it enables the control over its mechanical strength, the effective surface area for cell growth, and nutrient flow profiles within the scaffold [18]. To produce scaffolds with fine control over scaffold architecture in three dimensions, layer-by-layer assembly techniques, where layers of polymers, patterned by moulding or embossing processes, are stacked, have been investigated by many researchers [20,21]. These techniques enable the formation of channels with precisely defined dimensions. However, the requirement for microfabricated master moulds and manual alignment of layers implies a slow and tedious process for achieving a multi-layered 3D construct [22].

Recently there has been a move towards employing 3D printing [10, 23,24] as a rapid prototyping technique to fabricate micro-scale porous structures of desired complexities, allowing a true engineering of the scaffold [18]. These methods involve the creation of 3D objects using layer by layer deposition approach. Such techniques have successfully been employed in tissue engineering to develop scaffolds based on hard polymeric materials [25,26] and hydrogels [27,28]. The application of scaffolds made from soft polymers or elastomeric materials is desirable when engineering soft tissues [12,29,30]. For the fabrication of elastomeric scaffolds with microfluidic networks, micromoulding and individual layer-by-layer assembly techniques have commonly been used [20,31]. However such techniques require the use of complex fabrication technologies and manual assembly for producing large scale structures. Thus the fabrication of 3D elastomeric scaffolds with defined microarchitectural details in cost-effective, scalable manner remains a challenge.

Recently, processes combining 3D printing and moulding have been used for making structured 3D scaffolds. For example, 3D microvascular networks within polymer matrices have been fabricated by 3D printing of sacrificial wax moulds, casting of low viscosity epoxy around the moulds and subsequent removal of the moulds [23,32]. However the use of wax (which has a melting temperature of about 60 °C) limits the materials that can be cast around the mould to form the scaffold since polymers requiring higher temperatures for cross-linking cannot be employed. Furthermore, the complete removal of the sacrificial

wax components (which may not be biocompatible) can be challenging, in particular if you have a large 3D structure with complex geometry. Perfusable 3D scaffolds have also been demonstrated in a similar manner by casting extracellular matrix (ECM) containing cells around a 3D printed sacrificial sugar glass lattice and subsequently dissolving the lattice to form vascular networks [24]. However, it is probably difficult to print large 3D structures in the very brittle sugar glass, and the interfilament distance (defined by the printing process) is limited to a minimum of 1 mm. It may therefore not be feasible to use this technique for creating dense vascular channels in large scale structures.

This paper presents a new scalable and general approach for manufacturing structured pores/channels in 3D polymer based scaffolds. The method involves 3D printing (using a commercially available filament based 3D printer) of a sacrificial polyvinyl alcohol (PVA) mould whose geometrical features are designed according to the required vascular channel network. In addition to its biocompatibility, PVA is an ideal material because its water solubility in combination with its high melting temperature (190 °C) makes it robust for subsequent polymer casting and curing steps. A desired polymer is cast around the PVA mould, cross-linked and then the mould is dissolved, leaving behind a structured porous scaffold in the desired polymer material. The fabrication method was here demonstrated for two different polymers, the silicone elastomer polydimethylsiloxane (PDMS), and the synthetic hydrogel poly(2-hydroxyethyl methacrylate) (pHEMA). The scalability of the method was demonstrated by fabricating a 75 cm³ large PDMS scaffold structure with 16,000 channels. Moreover, it was also shown that the PDMS scaffolds when properly pre-treated could support hepatocyte growth and proliferation for up to 12 days with high viability and proper function.

2. Materials and methods

2.1. Fabrication of structured porous elastomeric scaffolds

The method used to fabricate elastomeric polymer scaffolds with structured channels is schematically presented in Fig. 1. First, a commercial, low-cost 3D filament printer (MakerBot 2X) was used to print

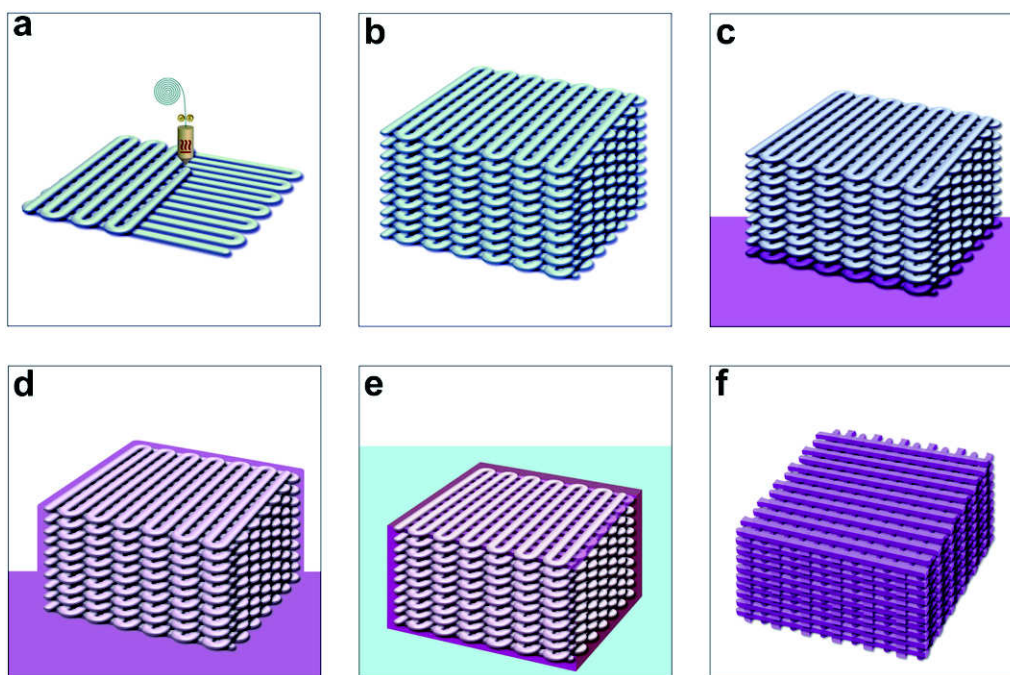


Fig. 1. Schematic illustration of the steps involved in the fabrication of structured porous elastomeric scaffolds. A sacrificial 3D mould was printed in PVA (a, b). The printed PVA mould was transferred into a container containing pre-cured PDMS (c). Vacuum was applied to ensure complete filling of pre-cured PDMS into the pores of the mould (d). Following crosslinking of the PDMS, the sacrificial PVA mould was dissolved in water (e) leaving behind the structured PDMS scaffold (f).

a sacrificial mould. A solid 3D cube of the specified length, width and height was designed using a computer aided design (CAD) software package (SolidWorks 2013). The 3D CAD design was exported as .STL mesh file format for processing using the 3D printer software (Makerware 2.4.1, MakerBot). Commercially available water dissolvable polymer, polyvinyl alcohol (PVA) (MakerBot, USA) filaments were used to print the sacrificial mould. In the printing process a moving nozzle (x- and y-axis control) extrudes a heated polymer filament which then solidifies as it is deposited (Fig. 1(a)). Following deposition of each layer, the mould is lowered (z-axis control) and the extrusion procedure is repeated such that successive layers are built on top of each other to form a 3D object (Fig. 1(b)). The printer settings used for printing PVA moulds are given in Table 1. The extrusion temperature and feed-rates were optimised for printing PVA.

The printing infill density was varied to generate structures with varying porosity. The infill density is the parameter that defines the amount of material filled into the object and subsequently relates to the porosity of the 3D printed structure. The infill density can range from 0% to 100%, where 0% results in a completely hollow object and 100% infill results in a completely solid object. In order to generate structures with different porosities, moulds were printed with infill densities ranging from 20% to 80%. An illustration of the infill patterns and densities that were employed is shown in Supplementary Fig. 1.

The 3D printed microvascular network of the PVA mould was replicated into elastomeric structures of polydimethylsiloxane (PDMS): PDMS pre-polymer solution (Sylgard 184, Dow Corning) was mixed with the curing agent in a 10:1 ratio (as per the manufacturer's guidelines). The mixture was degassed in vacuum and poured into a petri dish containing the printed mould (Fig. 1(c)). PDMS fills the pores of the mould through capillary action and, in addition, vacuum was applied for 2–3 h to ensure complete filling of the micro-channels of the mould with PDMS (Fig. 1(d)). PDMS was cured at a temperature of 60 °C in an oven for 4 h. Once cured, excess PDMS around the mould was removed to expose the PVA layer. This was done to assist the subsequent dissolution of PVA in water: The whole structure was immersed into a water bath (Fig. 1(e)) until the PVA mould was completely dissolved (6 h), and the elastomeric PDMS with microvascular network architecture was obtained (Fig. 1(f)).

Cuboidal PVA moulds of $25 \times 25 \times 10 \text{ mm}^3$ and $25 \times 25 \times 4 \text{ mm}^3$ (length \times width \times height) were printed and used for casting PDMS scaffolds and these scaffolds were used for mechanical testing and cell culturing studies respectively.

2.2. Characterizations of scaffolds

2.2.1. Scanning electron microscopy (SEM) imaging

The structural morphology and microstructure of the printed PVA mould as well as the resulting PDMS porous scaffolds were analysed using scanning electron microscopy (JEOL, Tokyo, Japan). Prior to SEM analysis, moulds and scaffolds were dried in an oven at 50 °C overnight and sputter coated with gold. Samples were then analysed using 12 kV of accelerating voltage. Pore sizes of the moulds and scaffolds were measured from SEM micrographs using ImageJ software. For each sample, ten measurements of pore dimensions were acquired.

For cell-seeded scaffolds, samples were washed with PBS and fixed with 2.5% glutaraldehyde in PBS overnight. Next the samples were

dehydrated in a series of ethanol solutions (50%, 70%, 90% and 100%), the samples were further air-dried and then the samples were ready for SEM observation.

2.2.2. Porosity measurement

The porosity of the PDMS scaffold was measured using Eq. (1) as described in the literature [33].

$$\text{Porosity}(\%) = \frac{V - \left(\frac{M}{\rho}\right)}{V} \times 100\% \quad (1)$$

where V is the volume of the scaffold, which is calculated using its outer dimension, M is the mass of the porous PDMS scaffold, and ρ is the density of PDMS (0.965 g/cm^3).

Four scaffolds from each type of scaffold (with dimensions $23 \times 23 \times 6 \text{ mm}^3$) were dried overnight at 80 °C, and weighed to obtain the mass of the samples. The porosity was then calculated from the weight and the dimensions using Eq. (1).

2.2.3. Mechanical testing

The mechanical properties of dry PDMS scaffolds (with dimensions of $25 \times 25 \times 10 \text{ mm}^3$) of varying porosity (20–80%) were tested by conducting uniaxial compression tests. A constant compression speed of 0.5 mm/min was applied to each sample using a tensile test machine with a 5 kN load cell (INSTRON Model 4301, Instron Engineering Corporation, Canton, MA, USA). The compressive modulus was estimated from the slope of the stress–strain curve in the elastic region, which was in the range of 12%–20% strain. The stress at 20% strain was obtained. The values reported were an average from four tested samples.

2.2.4. Surface roughness

The surface topography of the PVA mould and PDMS scaffold was visualised using SEM. PDMS scaffold surface roughness was measured using an optical measuring device (Alicona infinite focus). The parameters R_a and R_z were obtained from a standard spectrum of roughness.

2.2.5. Wettability

To assess wettability of the scaffolds, contact angle measurements were carried out on scaffolds before and after treatment with oxygen plasma. The contact angle was measured using the sessile drop method by depositing 3 μl of an ultrapure water drop on the scaffold. Three individual measurements were carried out on three independent scaffolds.

2.2.6. Surface area calculation

To estimate the surface area of the scaffolds, the dimensions of the filaments constituting the mould were acquired from SEM images of the mould. As previously described, the scaffold is formed by printing layers of filaments (with a height of 0.2 mm) organised in the x–y axis. The surface area was calculated from the SEM images of a single layer and then multiplied by the number of layers.

2.3. Culturing cells in scaffolds

2.3.1. Cells

Human hepatoblastoma (HepG2) cells were obtained from the German Collection of Microorganisms and Cell Cultures (DSMZ, Braunschweig, Germany). The cells were maintained in Roswell Park Memorial Institute (RPMI) 1640 growth medium supplemented with 10% foetal bovine serum (FBS, Sigma-Aldrich Chemie GmbH, Switzerland) and 100 $\mu\text{g/ml}$ penicillin and 10 $\mu\text{g/ml}$ streptomycin in a humidified incubator at 37 °C and 5% CO_2 . Cells were cultured to confluence in standard polystyrene cell culture flasks, and then released using 0.025% trypsin/EDTA solution. The cell suspension was centrifuged and the cell pellet was washed twice with phosphate buffered saline (PBS) and then re-suspended in fresh growth medium. The cell density was

Table 1
3D printing parameters used for fabricating sacrificial PVA mould.

3D printing parameters	Settings
Layer height	0.2 mm
Infill pattern	Woodpile or hexagonal
Nozzle temperature	200 °C
Build platform temperature	40 °C
Feed-rate	20 mm/s

measured using a haemocytometer and adjusted as required for the seeding on the 3D scaffolds.

2.3.2. Scaffold preparation for cell culture

PDMS scaffolds (fabricated with 80% infill moulds) were frozen in liquid nitrogen and punched into cylindrical scaffolds (having a diameter of 6 mm and height 4 mm) using a tissue puncher (Harris Uni-Core, USA). To render them hydrophilic, the scaffolds were modified with oxygen plasma using a 13.56 MHz RF generator equipped Atto Plasma System (Diener Electronic GmbH, Ebhausen, Germany). Initially the plasma chamber was evacuated to a pressure below 15 Pa, after which oxygen was introduced (pressure stabilization at 30 Pa) and the plasma was ignited (power 50 W) for a duration of 2 min for each side of the scaffold. The treated scaffolds were transferred into an autoclavable glass vial containing sterile water and autoclaved at 120 °C for 20 min for sterilisation. To promote cell attachment to the scaffolds, the scaffolds were coated with 40 µg/ml of Collagen I (Collagen I rat protein, Life Technologies, A1048301) at 4 °C overnight. The scaffolds were washed twice with phosphate buffered saline (PBS) and excess collagen was removed by centrifugation of the samples at 1000 rpm. Finally, the scaffolds were placed in a petri dish containing RPMI medium and incubated inside a humidified incubator at 37 °C and 5% CO₂ for 2 h prior to cell seeding.

2.3.3. Cultivation of HepG2 cells inside the scaffolds

HepG2 cells were cultured in the fabricated scaffolds to evaluate the ability of PDMS 3D constructs to support cell adhesion, proliferation and spreading. For cell seeding a customised cell loading platform was developed as shown schematically in Supplementary Fig. 2. A cell seeding plate with 16 cylindrical holes (having a diameter of 6 mm) and a rectangular support frame was fabricated in 6 mm thick Poly(methyl methacrylate) (PMMA) using a CO₂ laser cutter machine (Epilog Mini 18 Laser, CO 80403, USA). The seeding plate and frame were sterilised by immersion in 0.5 M sodium hydroxide solution for 2 h followed by rinsing in sterile water. The frame and seeding plate were placed inside a sterile petri dish such that the seeding plate was raised and had no direct contact with the petri dish. The collagen coated scaffolds from the incubator were inserted into the holes in the seeding plate. A suspension containing 250,000 cells in 20 µl of media was prepared and loaded into each scaffold. After seeding, the petri plate was incubated at 37 °C for 3 h to allow the cells to attach to the scaffold. Every hour the loading plate was inverted upside down to enable better cell infiltration into the scaffold. Finally the scaffolds were removed from the seeding plate and transferred into a 24 well plate. 1 ml of cell culture medium was added to each well. The medium was refreshed every 2 days and old medium was collected for cellular functionality assays. On days 4, 8 and 12 of the culture period, two scaffolds from each time point were sacrificed and used for live/dead staining.

2.3.4. Biochemical assays

Cell proliferation was estimated using the colorimetric indicator alamarBlue® assay (Life Technologies). The cell-scaffold constructs were transferred into a 24 well plate each containing 1 ml of RPMI and alamarBlue® solution (in a 10:1 ratio) and incubated for 2 h in a humidified incubator at 37 °C. The absorbance of the extracted dye, which is proportional to the number of cells attached to the scaffold, was measured spectrophotometrically using a microplate reader (PerkinElmer, USA) at wavelengths of 570 nm. Three independent scaffolds were measured in triplicates, and the background (i.e., alamarBlue® absorbance measured at day 0) was subtracted.

For the HepG2 functionality test, extracellular concentration of albumin secretion from the HepG2 cells was determined by using an enzyme-linked immunosorbent assay (ELISA) (Bethyl Laboratories, USA) according to the manufacturer's instructions. All samples were measured in triplicates and the standard deviation (SD) of mean was

determined from 3 independent scaffolds. The absorbance was measured at 450 nm using a spectrophotometer (PerkinElmer, USA).

2.3.5. Cell imaging

To visualise cell viability in the scaffolds, a live/dead-assay was performed using a live/dead cell imaging kit (Life Technologies LIVE/DEAD® Cell Imaging Kit), which is based on a cell-permeable dye for staining of live cells (excitation/emission 488 nm/515 nm) and a cell-impermeable dye for staining of dead and dying cells (excitation/emission 570 nm/602 nm). Briefly, the cell-laden scaffolds were removed from the culture medium and gently washed with PBS. They were then incubated in the dye solution for 30 min at 37 °C (as per manufacturer's instructions). The scaffolds were imaged using a fluorescence microscope (Zeiss Axio Observer, ZI). 3D reconstructions were compiled from 20 imaged sections (each of 30 µm thickness).

To visualise the cell proliferation and distribution through the cross section of the scaffolds, cell-laden scaffolds were stained with cell-permeable nuclear stain Hoechst 33342 (NucBlue® Live Ready Probes® Reagent, life technologies) for live cell nuclei and ethidium homodimer-1 (life technologies) for dead cell nucleus for 10 min. The scaffolds were then dissected longitudinally using a sterile scalpel and each section was observed under a fluorescence microscope. 3D reconstructions were compiled from 20 imaged sections (each of 30 µm thickness).

An immunofluorescence study was performed to visualise the morphology of cells attached to the scaffold surface: After 12 days of cell growth, the cell-laden scaffolds were immunostained with beta-tubulin as cell cytoskeleton and nucleus. The construct was fixed (4% paraformaldehyde), permeabilized (30 min, 0.1% Triton X-100 in phosphate buffered saline (PBS)), and blocked (30 min, 0.1% Tween 20 and 1% bovine serum albumin in PBS) for unspecific binding of the antibodies. The construct was stained with primary antibody as monoclonal anti- α -tubulin IgG1 (2 h, 1:200, Life Technologies) followed by TO-PRO-3 nuclear stain (1:1000, Life Technologies). The scaffold was then cut through the centre using a sterile scalpel and visualised under a Zeiss ApoTome fluorescence microscope. 3D reconstructions were compiled from 20 imaged sections (each having a thickness of 5 µm).

3. Results

3.1. Scaffold fabrication

Scaffolds were fabricated by casting PDMS around sacrificial moulds printed using two different infill patterns (woodpile and hexagonal) and four different infill densities. Photographs and SEM images of the printed moulds and resulting PDMS scaffolds of the two different infill patterns are shown in Fig. 2. The scaffolds possessed well-defined, porous structures. The square and hexagonal pore structure of both PVA moulds and PDMS scaffolds were observed to be uniform and consistent (Fig. 2(a, b, e, f)). The structural features of the PVA mould are faithfully replicated in the PDMS scaffold (Fig. 2(c, d, g, h)).

The woodpile infill pattern results in structures comprising orthogonal arrays of filaments with the centre-to-centre spacing between adjacent filaments differing based on the chosen infill density (Fig. 3). Infill densities of 20, 40, 60 and 80% produces structures where filaments in a layer had a distances of 1482, 593, 253 and 78 µm respectively. As the infill density increases, the centre-to-centre spacing of the filaments in the PVA mould decreases (Fig. 3a–d). SEM images of the mould showed that the printed PVA filaments have an elliptical cross-section with a width of 400 µm and a height of 200 µm (Supplementary figure). The channels in the resulting PDMS scaffold have an elliptical profile from a cross section view (width 344 µm, height 190 µm) (shown in Supplementary Fig. 5) and a square profile (average side length 344 µm) from the top view. The channel dimensions in the PDMS scaffold are slightly smaller than the dimension of the PVA filaments of the mould due to shrinkage of PDMS during the curing process. The channel to channel distance varied from 1.4 mm at 20% infill density down to

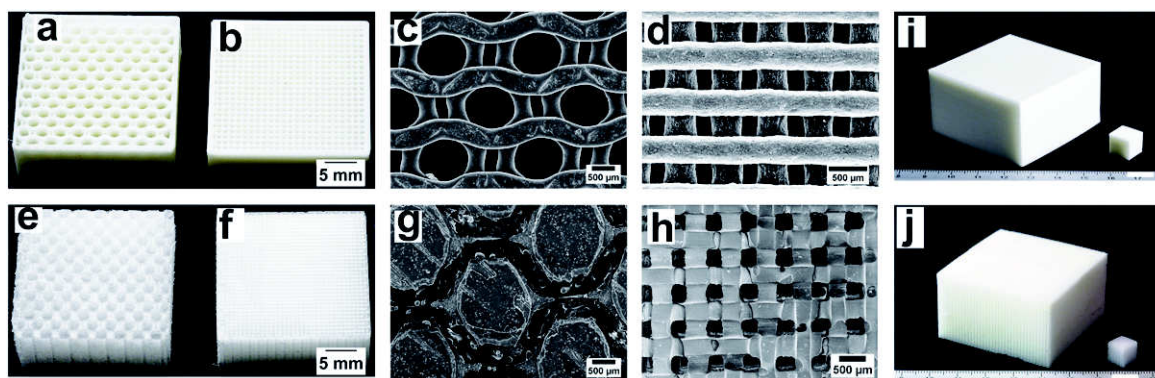


Fig. 2. Photographs of moulds and scaffolds with hexagonal (a, e) and woodpile (b, f) infill patterns. SEM images of moulds and scaffolds with hexagonal (c, g) and woodpile (d, h) infill patterns. (i) Optical image of a 50 layered (1 cm³ cube) and 150 layered (75 cm³ cube) 3D printed PVA mould. (j) Optical image of 50 layered (1 cm³ cube) and 150 layered (75 cm³ cube) PDMS scaffolds replicated from the mould (i). Scale bar in (i) and (j): 1 cm.

78 μm at 80% infill density of the printed mould. Thus the employed 3D printing technique enables the layer by layer assembly of a different number of PVA filaments forming a porous 3D mould. To demonstrate the scalability of the fabrication process, a larger cubic mould (75 cm³) was fabricated and employed for generating a replica PDMS scaffold with the same dimensions. Fig. 2(i) shows an image of two cubic moulds of dimensions 1 cm³ and 75 cm³ printed using 80% infill settings and Fig. 2(j) shows the resulting PDMS scaffolds. Thus, as demonstrated in Fig. 2, the periodic micro- and macroscale structural patterns of the PVA mould were well replicated in the PDMS scaffolds.

3.2. Scaffold characterisation

3.2.1. Porosity

The experimentally determined porosity of fabricated scaffolds is presented in Fig. 4. The porosity of the scaffolds varied linearly as a function of the infill density of the printed mould from 19.9% porosity at 20% infill up to 81.2% porosity at 80% infill (Fig. 4(a)).

3.2.2. Surface area

The calculated surface areas of a 1 cm³ fabricated scaffolds of varying porosities are shown in Fig. 4(b). As the infill density of the mould increases from 20% to 80%, there is also a corresponding increase (from 52.5 cm²/cm³ to 150.9 cm²/cm³, respectively) in the surface area of the channels within the PDMS scaffold volume. As the infill density of the mould increases (Fig. 3(a–d)) the density of channels also increases

(Fig. 3(e–h)), which results in a linear increase in the total surface area of the channels (Fig. 4(b)).

3.2.3. Mechanical testing

The assessment of the compressive characteristics of scaffolds is known to play a significant role in many tissue-engineering applications [34]. Compression tests of the scaffolds varying in porosity were performed to assess the stress–strain relationship and evaluate their compressive moduli (Fig. 5). The compressive modulus was determined as the slope of the initial linear portion of the stress vs. strain curve (12–20%). The compressive modulus were determined to be 1.84 ± 0.023 , 0.84 ± 0.044 , 0.36 ± 0.046 and 0.075 ± 0.047 MPa for the 20, 40, 60, and 80% porosity scaffolds, respectively. Results showed that the energy absorption of the scaffolds is greatly reduced with increasing porosity. There is also a dramatic decrease in the compressive modulus and in the stress at 20% strain with increasing scaffold porosity.

3.2.4. Surface roughness

The roughness of the 3D printed PVA mould and corresponding PDMS scaffold was assessed using SEM. As shown in Fig. 6(a–d), the presence of features such as pillars and grooves visible on the PVA mould are faithfully replicated in the PDMS scaffolds. The roughness of the PDMS scaffold was measured using an optical profilometer. The relative height and surface roughness are shown in the surface profile image (Fig. 6(e)) and the roughness parameters R_a and R_z of the PDMS scaffold surface were measured to be approximately 1.036 μm and 1.32 μm, respectively.

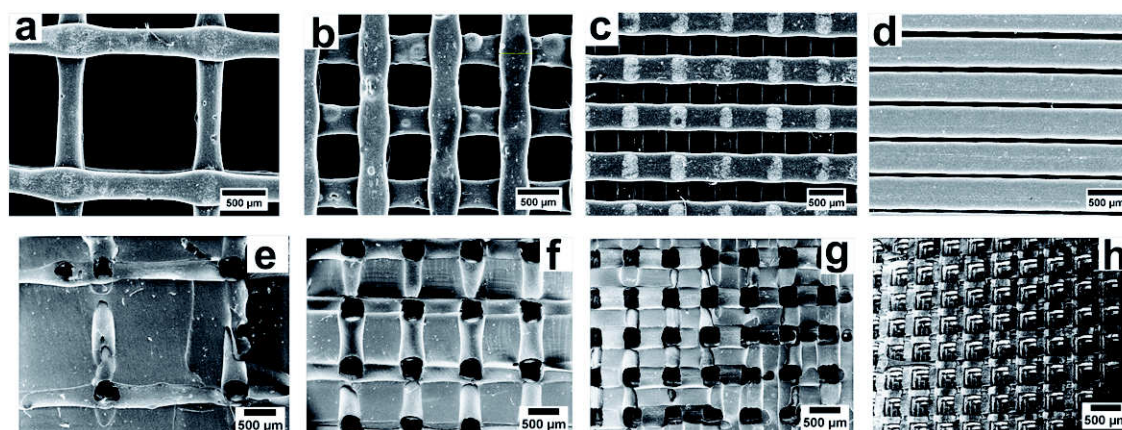


Fig. 3. SEM micrographs of 3D printed PVA moulds of 20, 40, 60 and 80% infill densities (a–d) and corresponding PDMS scaffolds (e–h).

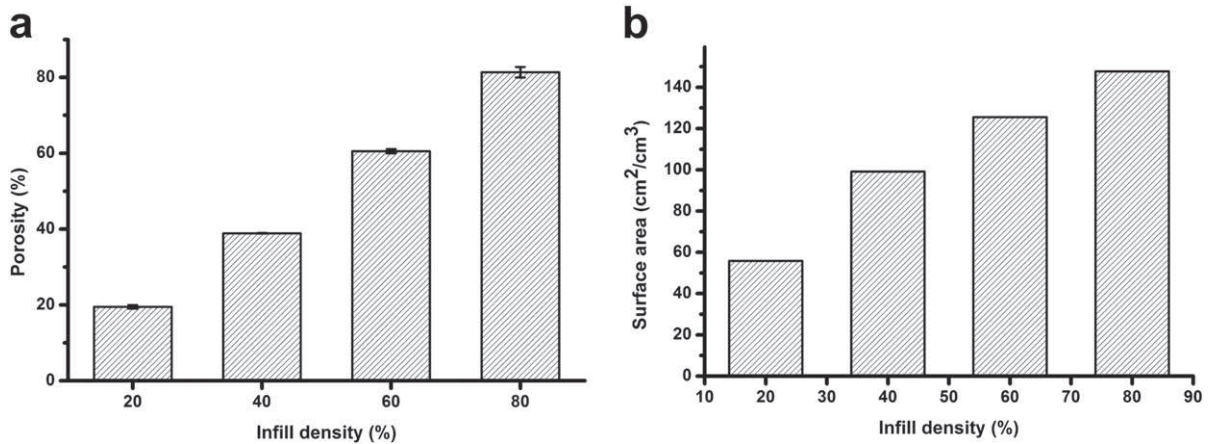


Fig. 4. Measured porosity (error bars = SD, n = 4) (a) and calculated surface to volume ratio (b) of scaffolds fabricated from mould with different infill densities.

3.3. Culturing cells in scaffold

3.3.1. Preparing scaffold for cell culturing (surface treatment)

To enable cell seeding and culturing within a porous scaffolds, it is important to render the scaffold surface hydrophilic [35]. This is required to ensure that the cell suspension and culture media can be absorbed within the scaffold pores. Oxygen plasma treatment was applied to the fabricated scaffolds to achieve this. Using this treatment, the contact angle of the scaffold surface decreased from $122^\circ \pm 3.5^\circ$ to 0° and media was able to infiltrate the pores of the scaffold (Supplementary Fig. 3).

3.3.2. Cell proliferation, viability and function

Following the surface treatment, the scaffolds were prepared for cell culturing, seeded with cells, and incubated as described in [Materials and methods](#). Cell viability and proliferation in the PDMS scaffolds with 80% porosity were investigated over a 12 day culture period using biochemical assays and imaging techniques. Cell proliferation in the scaffold was quantified using the alamarBlue® assay. As shown in [Fig. 7\(a\)](#), the fluorescence intensity increased linearly over the culture period, indicating an increase in the number of cells in the scaffolds with time. The functionality of HepG2 cells cultured on the scaffolds was established by measuring the extracellular albumin production ([Fig. 7\(b\)](#)). There was an increase in albumin production from day 1 to day 12 of the cultures which correlate with the increased cell density in the scaffolds.

Live/dead staining of the cell-scaffold construct was carried out to assess the viability of cells cultured on the scaffolds. [Fig. 8](#) shows the

confocal microscopy images of stained HepG2 cells on days 4, 8 and 12 of the culture period. Through the culture period, the density of living cells (stained green) increased. On day 12 of the culture, a confluent layer of live cells was visible on the scaffolds. In all cases, no dead cells were observed, so close to 100% cell viability was maintained throughout the 12 days of culture period.

3.3.3. Cell infiltration and distribution within the scaffolds

At different time points during the culture period, the infiltration and distribution of HepG2 cells within the PDMS scaffolds were investigated. This was done by staining the scaffolds with nuclear stain Hoechst 33342 (NucBlue® Live Ready Probes® Reagent, Life Technologies) for live cell nuclei and ethidium homodimer-1 (life technologies) for dead cell nucleus. To visualise cell distribution through the cross section of the scaffold, it was dissected along its central axis and imaged using fluorescence microscopy. [Fig. 9](#) shows live cell nuclei (stained blue) on the scaffold on days 4, 8 and 12 of the culture. Close to 100% cell viability was observed (no dead cells could be seen) with cells present throughout the cross section of the scaffold by the end of the culture period. Scaffolds acquired from day 4 of the culture showed a higher density of cells closer to the top and bottom face of the scaffold and a sparse density of cells in the central regions of the scaffold. But with longer culture time, cells appeared to proliferate and are seen to be homogeneously distributed throughout the channels of the scaffolds at days 8 and 12.

Immunostaining of the scaffold was carried out to visualise the morphology of cells cultured on the scaffolds. [Fig. 10](#) shows a homogeneous and confluent distribution of cells in the central region of the scaffold,

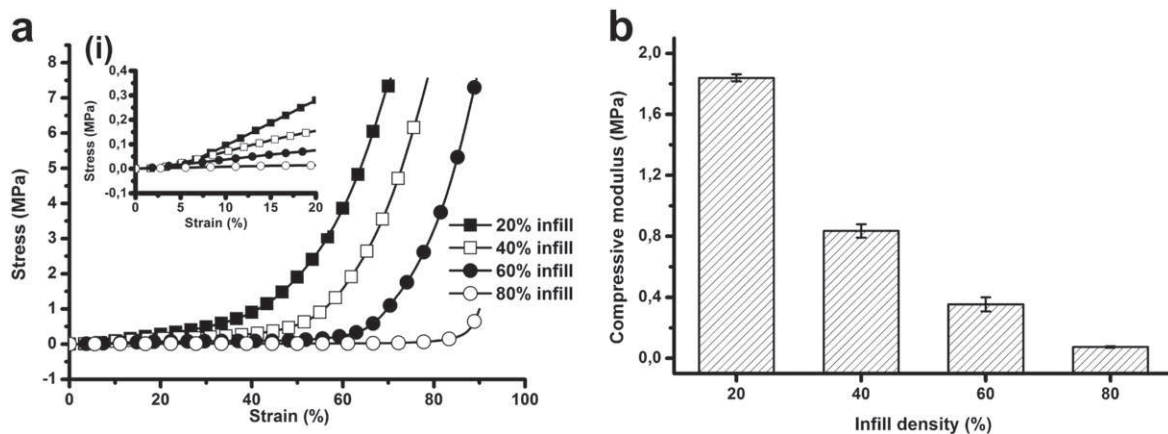


Fig. 5. (a) Stress–strain curves at 4 N load for different scaffolds, (b) compressive moduli of different PDMS scaffolds (error bars = standard deviation of 4 samples (n = 4)).

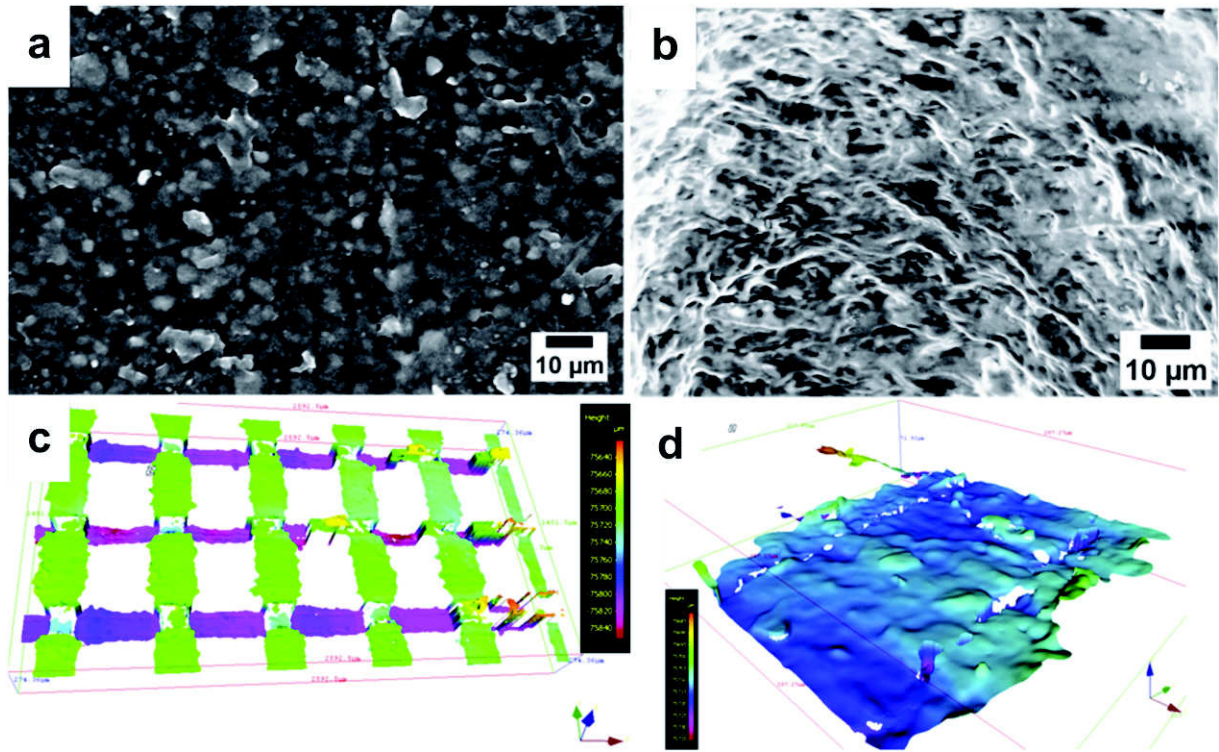


Fig. 6. Surface roughness analysis: SEM images showing microfeatures in the PVA mould surface (a) and PDMS scaffold (b, c & d). Surface profile image of PDMS scaffold surface generated from optical profilometer (c) and zoom in of image c (d).

highlighting the cytoskeleton beta-tubulin (green) and cell nucleus (red). After 12 days of cell culture the cells were uniformly distributed with high density of live cell in the centre of the scaffold. Immunofluorescence staining of the beta-tubulin demonstrated that the cells were well attached to the surface with a spread-out cell morphology.

HepG2 cell adhesion on scaffold was also investigated through SEM as shown in the Supplementary Fig. 5(a, b & c). After 4 days of culture, the interaction between cells and the scaffold surface was examined. Cells cultured on PDMS scaffold formed a well spread morphology and exhibited excellent cell adhesion.

4. Discussion

In this paper, a new scalable and reproducible technique for fabricating 3D polymer scaffolds with defined micro-architectures has been

presented. The technique is simple and involves casting of a desired polymer material within a 3D printed water-soluble PVA mould, which defines the microarchitecture/geometry of pores or channels within the scaffold (Figs. 1–3). 3D printing parameters were optimised to enable the production of reproducible moulds with high yield. The technique was applied to fabricate ‘woodpile’ like scaffolds with regularly spaced aligned polymer filaments in the x and y directions. Scaffolds of porosities ranging from 20 to 80% and channel to channel distances ranging from 78 μm to 1482 μm were fabricated by specifying the infill density of the moulds. Scaffolds with hexagonal micro-features were also obtained by using moulds with hexagonal infill patterns. The dimensions of the channels formed in the PDMS replica scaffolds were ellipsoidal shaped with dimensions (344 μm \times 190 μm) that were slightly smaller than that of the filaments in the printed mould (400 μm \times 200 μm), due to shrinkage during elastomer curing.

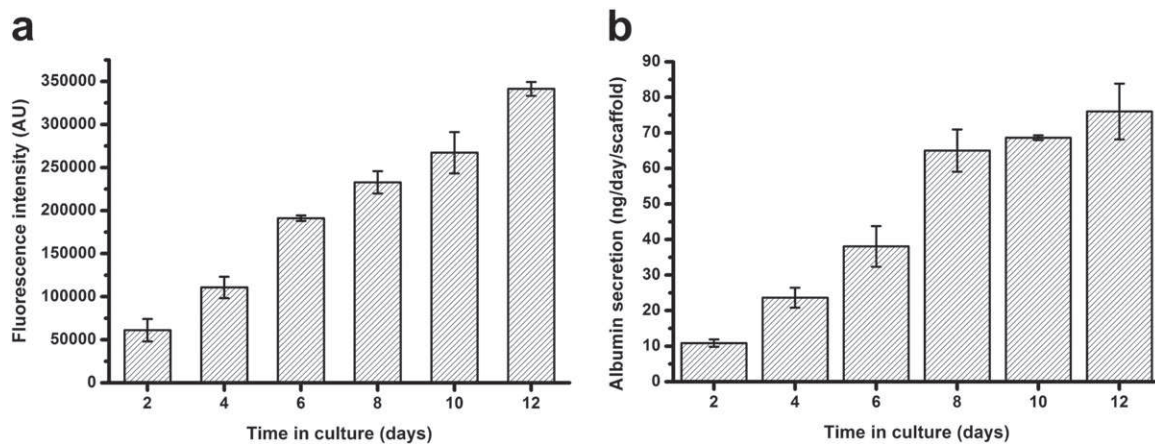


Fig. 7. (a) Change in alamarBlue® fluorescence intensity of scaffolds over culture time. The fluorescence intensity is proportional to the amount of cells. (b) Albumin production of HepG2 cells grown in PDMS scaffolds over 12 days of culture. Error bars indicate standard deviation of 3, independent scaffolds.

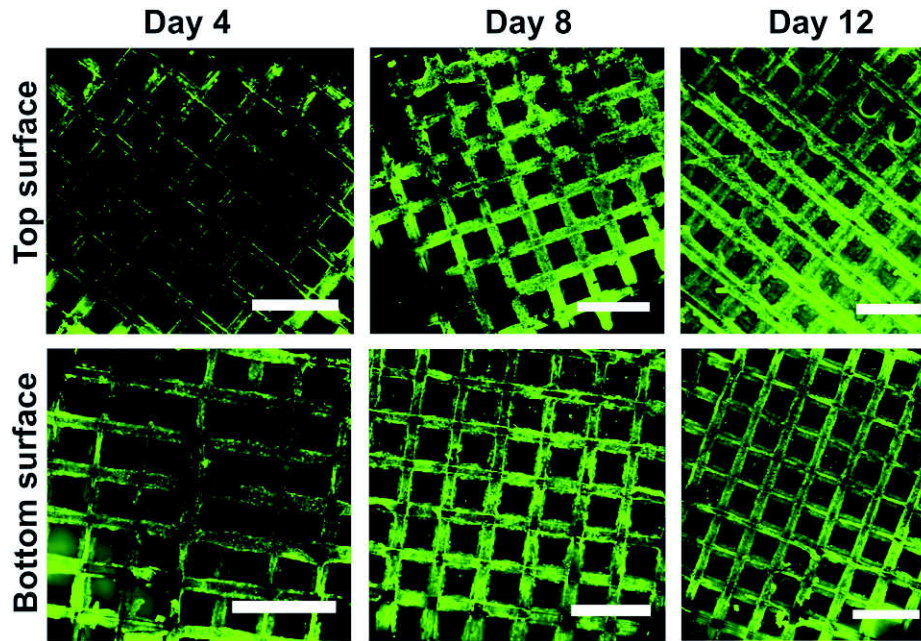


Fig. 8. Live/dead staining of HepG2 cells grown on the top and bottom parts of the PDMS scaffold for 4, 8 and 12 days. Scale bars represent 1 mm.

We used the biocompatible elastomeric polymer PDMS to demonstrate the ease of fabrication and scaling of scaffold structure, and furthermore showed that it has potential as a scaffold for growth of liver cells. However, the method has general applicability, meaning that other mouldable materials can be structured in a similar manner. To prove this point, poly-2-hydroxyethyl methacrylate (pHEMA) hydrogel scaffolds were produced by monomer/crosslinker casting around PVA mould, photocrosslinking (Supplementary Fig. 4, and Material and method in the Supplementary section) and subsequent dissolution of the PVA mould.

The silicone elastomer PDMS is optically clear, and, in general, inert, non-toxic, and non-flammable. Its applications range from contact lenses and medical devices to additives in cosmetics and food products. PDMS is also widely used as a material for microfluidic cell culturing and the high number of publications using it indicates that it is a biocompatible material [36]. In general the effects of PDMS or silicones on cells need to be evaluated on a case by case situation, as PDMS in some situations has subtle effect on gene expression [37], but we clearly show here that the fabricated PDMS elastomer scaffold supports HepG2 growth and function (Figs. 7–10). This type of elastomer scaffold could be used as a part of a life support system (LSS), e.g., an extracorporeal liver [38] to temporarily relieve liver disease patients. In such application PDMS offers several advantages: 1) It is easy to fabricate PDMS scaffold structures using the PVA sacrificial moulding method presented here. 2) PDMS is a structurally strong material for building large meshes

(Fig. 2j). 3) PDMS is easy to sterilise by autoclavation (in contrast to some hydrogels). 4) In contrast to hydrogels and many biodegradable materials PDMS does not shrink, swell or warp significantly with time meaning that rational fluidics optimisation can be done as well as robust fluidic connections for perfusions. 5) There are FDA approved medical grade silicone elastomers which should be compatible with the here described fabrication method.

It is well recognised that in order to be of clinical relevance, tissue constructs must be scaled up to the macroscale, not only in length and width, but also in thickness [20]. The presented fabrication method overcomes existing challenges in creating thicker constructs in a simple and reproducible manner by using precision assembly technology to control the micro-architectural details. The scalability of the process was demonstrated by producing a 75 cm³ large scaffold structure with 16,000 channels with a channel to channel distance of only 78 μ m (Fig. 2(j)). To our knowledge this is the largest scaffold ever to be produced with such small features sizes and with so many structured channels. Thus the process enables a more efficient scale up of scaffolds both in size and in throughput, while also allowing versatility in the implementation of 3D microarchitectural designs.

It is well established that the micro-roughness of a scaffold surface plays an important role in cell attachment and proliferation [39–42]. For this reason, the topological features of the scaffold were analysed using SEM to measure the surface roughness. Geometrical and topological features of the 3D printed PVA mould (Fig. 6a and b) were well

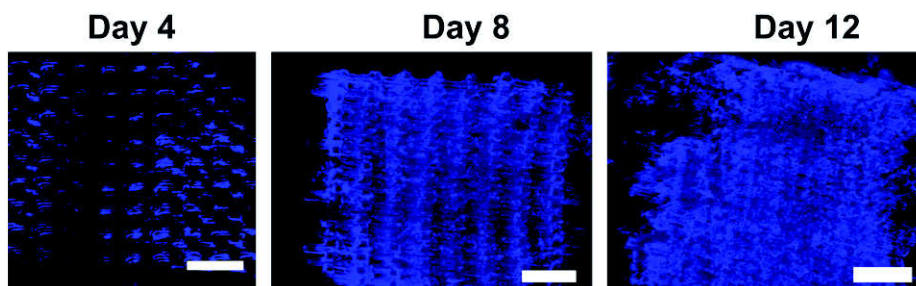


Fig. 9. Visualisation of cell distribution through the central section of the scaffold stained with NucBlue® (live cells: blue) and ethidium Homodimer-1 (EthD-1) (dead stain: red) on days 4, 8, and 12 of HepG2 cell culturing. Scale bars: 1 mm.

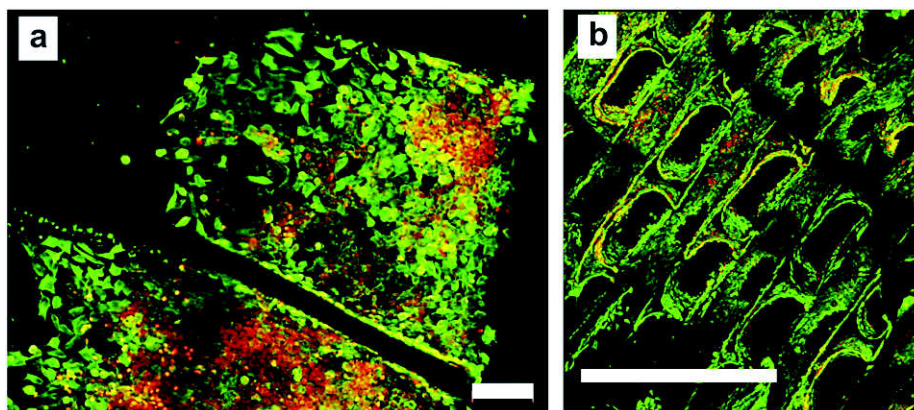


Fig. 10. HepG2 cell morphology and attachment to PDMS scaffold using immunostaining (a & b). Cell cytoskeleton beta tubulin (green) and nucleus (red). (a) Top surface of the scaffold. (b) Longitudinal cross section of the scaffold. Scale bar of image: a) with 100 μ m and b) with 1 mm.

replicated in the PDMS scaffold (Fig. 6c and d), giving the scaffold micro- and nano-scale roughness. Such micro- and nano-scale roughness can be an advantage for cell attachment and proliferation [43]. Our results are in agreement with this: We observed confluent layer of well-attached cells with spread-out cell morphology (Fig. 10).

It is well known that cells respond to the material on which they grow, both in terms of cytoskeleton, cell morphology, cell differentiation and function [45,46]. The mechanical properties of the fabricated scaffolds of varying porosities were therefore characterised. The compressive modulus of the scaffolds were estimated to be 1.84, 0.84, 0.34, 0.075 MPa for 20, 40, 60 and 80% porous scaffolds, respectively. The inverse relationship between scaffold porosity and compressive modulus is expected because scaffold with a higher porosity has less material/mass to resist applied load and therefore has a lower compressive modulus. If the stiffness of the PDMS scaffold should be a problem it can be adjusted by changing the ratio of pre-polymer to curing agent [46] or by selecting hydrogel materials such as pHEMA (Supplementary Fig. 4) could be used for casting the scaffold.

A highly available surface area in a scaffold can provide high ligand density for initial cell attachment and proliferation [47]. We chose to use the scaffold with the highest porosity (80%) for culturing cells since it has the lowest compressive modulus, enables better mass transport, and has the highest specific surface area (Fig. 4b) for cell attachment.

Until now it has been a challenge to maintain viable cells within the inner cores of thick engineered tissue constructs due to insufficient oxygen and nutrient levels [33]. To regenerate artificial tissues a homogeneous cell distribution should be maintained inside the porous scaffold structure [48,49]. The scaffolds presented in this work were able to sustain cells with 100% viability throughout the 12 day culture period. Metabolic assays and total cell DNA quantification assays do not give information on cell infiltration and distribution inside the scaffold. In order to visualise this aspect, the cell nucleus stained scaffolds were imaged at the top, bottom and cross sectional surfaces (Fig. 9). Cells were seen to be uniformly distributed throughout the channels of the scaffolds and along the cross sectional length of the scaffold. The achieved homogeneity can be attributed to the following: Firstly, the cell loading procedure employed ensures an even distribution of cells throughout the scaffolds. Secondly, the parallel and perpendicular structured channels in the scaffold allow sufficient oxygen and nutrient mass transport into the scaffold which promotes cell survival and proliferation. Thus at the end of the culture period, cells were seen to be uniformly distributed throughout the scaffolds and along the cross sectional length of the scaffold. Results from immunostaining clearly showed good HepG2 cell morphology and attachment to the scaffold surface (Fig. 10). Cell functionality was assessed by measuring albumin secretion of cells in scaffolds over time (Fig. 7b). The increase in albumin secretion through

the culture period indicates that the cells were able to maintain their functionality while cultured in the presented 3D scaffold.

5. Conclusions

In this study, we have demonstrated a new technique for fabricating scaffolds by 3D printing a sacrificial water dissolvable PVA mould, casting polymer around it and subsequently dissolving the sacrificial mould, leading to structured scaffolds. Different designs of PDMS scaffolds were successfully prepared, and the fabrication technique allowed the tuning of physical and mechanical properties by controlling the 3D printing parameter. By observing the biological activity of the hepatocytes in the scaffold we confirm that along with maintaining very high cellular viability the scaffold could also support high level of cellular albumin secretion throughout the cultivation period. After 12 days of cell culturing we observed a very high density of cells, homogeneously distributed across the scaffold due to good mass and oxygen transport into the scaffold. The fabrication method can also be applied to other synthetic or natural polymers as demonstrated by fabricating scaffolds in the hydrogel pHEMA. Furthermore, as we have demonstrated, the fabricated scaffold can be scaled up to sizes relevant for bioartificial organs. In conclusion, the described process is scalable, compatible with cell culture, rapid, and inexpensive.

Supplementary data to this article can be found online at <http://dx.doi.org/10.1016/j.msec.2015.06.002>.

Acknowledgments

This work has been financially supported by EU project NanoBio4Trans (“A new nanotechnology-based paradigm for engineering vascularised liver tissue for transplantation”, grant no: 304842). We thank K. Kuldeep and Aradhya Mallikarjunaiah Chetan for their great support in carrying out with the fabrication of 3D scaffolds and Jesper Scheel for taking photographs of the large scaffold.

References

- [1] L.G. Griffith, M.A. Swartz, Capturing complex 3D tissue physiology in vitro, *Nat. Rev. Mol. Cell Biol.* 7 (3) (Mar 2006) 211–224.
- [2] K.C. Rustad, M. Sorkin, B. Levi, M.T. Longaker, G.C. Gurtner, Strategies for organ level tissue engineering, *Organogenesis* 6 (3) (2010) 151–157.
- [3] A. Khademhosseini, R. Langer, J. Borenstein, J.P. Vacanti, Microscale technologies for tissue engineering and biology, *Proc. Natl. Acad. Sci. U. S. A.* 103 (8) (Feb 2006) 2480–2487.
- [4] A. Khademhosseini, J.P. Vacanti, R. Langer, Progress in tissue engineering, *Sci. Am.* 300 (2009) 64–71.
- [5] D.M. Hoganson, H.I. Pryor, J.P. Vacanti, Tissue engineering and organ structure: a vascularized approach to liver and lung, *Pediatr. Res.* 63 (5) (May 2008) 520–526.

- [6] T. Lu, Y. Li, T. Chen, Techniques for fabrication and construction of three-dimensional scaffolds for tissue engineering, *Int. J. Nanomedicine* 8 (Jan 2013) 337–350.
- [7] H.A. Almeida, P.J. Bártolo, Design of tissue engineering scaffolds based on hyperbolic surfaces: structural numerical evaluation, *Med. Eng. Phys.* 36 (8) (Aug 2014) 1033–1040.
- [8] R. Langer, Perspectives and challenges in tissue engineering and regenerative medicine, *Adv. Mater.* 21 (32–33) (Sep 2009) 3235–3236.
- [9] M.D. Guillemette, H. Park, J.C. Hsiao, S.R. Jain, B.L. Larson, R. Langer, L.E. Freed, Combined technologies for microfabricating elastomeric cardiac tissue engineering scaffolds, *Macromol. Biosci.* 10 (11) (Nov 2010) 1330–1337.
- [10] C.G. Jeong, S.J. Hollister, Mechanical and biochemical assessments of three-dimensional poly(1,8-octanediol-co-citrate) scaffold pore shape and permeability effects on in vitro chondrogenesis using primary chondrocytes, *Tissue Eng. A* 16 (12) (2010) 3759–3768.
- [11] M.E. Kolewe, H. Park, C. Gray, X. Ye, R. Langer, L.E. Freed, 3D structural patterns in scalable, elastomeric scaffolds guide engineered tissue architecture, *Adv. Mater.* 25 (32) (Aug 2013) 4459–4465.
- [12] S.J. Hollister, Scaffold design and manufacturing: from concept to clinic, *Adv. Mater.* 21 (32–33) (Sep 2009) 3330–3342.
- [13] A. G. Mikos, G. Sarakinos, J. P. Vacanti, R. S. Langer, and L. G. Cima, "Biocompatible polymer membranes and methods of preparation of three dimensional membrane structures." Google Patents, 1996.
- [14] H. Lo, M.S. Ponticciello, K.W. Leong, Fabrication of controlled release biodegradable foams by phase separation, *Tissue Eng.* 1 (1) (Jan 1995) 15–28.
- [15] D.J. Mooney, D.F. Baldwin, N.P. Suh, J.P. Vacanti, R. Langer, Novel approach to fabricate porous sponges of poly(D,L-lactic-co-glycolic acid) without the use of organic solvents, *Biomaterials* 17 (14) (Jul 1996) 1417–1422.
- [16] K. Whang, K.E. Healy, A novel method scaffolds to fabricate bioabsorbable, 36 (4) (1995) 837–842.
- [17] A. Saraf, G. Lozier, A. Haesslein, F.K. Kasper, R.M. Raphael, L.S. Baggett, A.G. Mikos, Fabrication of nonwoven coaxial fiber meshes by electrospinning, *Tissue Eng. C Methods* 15 (3) (Sep 2009) 333–344.
- [18] B. Derby, Printing and prototyping of tissues and scaffolds, *Science* 338 (6109) (Nov 2012) 921–926.
- [19] W.-Y. Yeong, C.-K. Chua, K.-F. Leong, M. Chandrasekaran, Rapid prototyping in tissue engineering: challenges and potential, *Trends Biotechnol.* 22 (12) (Dec 2004) 643–652.
- [20] X. Ye, L. Lu, M.E. Kolewe, K. Heaton, K.M. Fishcher, J. Coppeta, L.E. Freed, Scalable Units for Building Cardiac Tissue, *Advanced Materials* (Deerfield Beach, Fla.) 26 (42) (2014) 7202–7208.
- [21] A.P. Golden, J. Tien, Fabrication of microfluidic hydrogels using molded gelatin as a sacrificial element, *Lab Chip* 7 (6) (Jun 2007) 720–725.
- [22] J. He, Y. Wang, Y. Liu, D. Li, Z. Jin, Layer-by-layer micromolding of natural biopolymer scaffolds with intrinsic microfluidic networks, *Biofabrication* 5 (2) (Jun 2013) 025002.
- [23] D. Theriault, S.R. White, J.A. Lewis, Chaotic mixing in three-dimensional microvascular networks fabricated by direct-write assembly, *Nat. Mater.* 2 (4) (Apr 2003) 265–271.
- [24] J.S. Miller, K.R. Stevens, M.T. Yang, B.M. Baker, D.T. Nguyen, D.M. Cohen, E. Toro, A.A. Chen, P.A. Galie, X. Yu, R. Chaturvedi, S.N. Bhatia, C.S. Chen, Rapid casting of patterned vascular networks for perfusable engineered three-dimensional tissues, *Nat. Mater.* 11 (9) (Sep 2012) 768–774.
- [25] J.M. Sobral, S.G. Caridade, R.A. Sousa, J.F. Mano, R.L. Reis, Three-dimensional plotted scaffolds with controlled pore size gradients: effect of scaffold geometry on mechanical performance and cell seeding efficiency, *Acta Biomater.* 7 (3) (Mar 2011) 1009–1018.
- [26] H.A. Declercq, T. Desmet, P. Dubruel, M.J. Cornelissen, The Role of Scaffold Architecture and Composition on the Bone Formation by Adipose-derived Stem Cells, vol. 202014, 434–445.
- [27] L.E. Bertassoni, J.C. Cardoso, V. Manoharan, A.L. Cristino, N.S. Bhise, W.A. Araujo, P. Zorlutuna, N.E. Vrana, A.M. Ghaemmaghami, M.R. Dokmeci, A. Khademhosseini, Direct-write bioprinting of cell-laden methacrylated gelatin hydrogels, *Biofabrication* 6 (2) (Apr 2014) 024105.
- [28] R. Gauvin, Y.-C. Chen, J.W. Lee, P. Soman, P. Zorlutuna, J.W. Nichol, H. Bae, S. Chen, A. Khademhosseini, Microfabrication of complex porous tissue engineering scaffolds using 3D projection stereolithography, *Biomaterials* 33 (15) (May 2012) 3824–3834.
- [29] L.E. Freed, G.C. Engelmayr, J.T. Borenstein, F.T. Moutos, F. Guilak, Advanced material strategies for tissue engineering scaffolds, *Adv. Mater.* 21 (32–33) (Sep 2009) 3410–3418.
- [30] J. Gao, P.M. Crapo, Y. Wang, Macroporous elastomeric scaffolds with extensive micropores for soft tissue engineering, *Tissue Eng.* 12 (4) (Apr 2006) 917–925.
- [31] H. Park, B.L. Larson, M.D. Guillemette, S.R. Jain, C. Hua, G.C. Engelmayr, L.E. Freed, The significance of pore microarchitecture in a multi-layered elastomeric scaffold for contractile cardiac muscle constructs, *Biomaterials* 32 (7) (Mar 2011) 1856–1864.
- [32] D. Theriault, R.F. Shepherd, S.R. White, J.A. Lewis, Fugitive inks for direct-write assembly of three-dimensional microvascular networks, *Adv. Mater.* 17 (4) (Feb 2005) 395–399.
- [33] Q. Zhang, H. Luo, Y. Zhang, Y. Zhou, Z. Ye, W. Tan, M. Lang, Fabrication of three-dimensional poly(ϵ -caprolactone) scaffolds with hierarchical pore structures for tissue engineering, *Mater. Sci. Eng. C* 33 (4) (May 2013) 2094–2103.
- [34] S.J. Hollister, Porous scaffold design for tissue engineering, *Nat. Mater.* 4 (July 2005) 518–524.
- [35] S. Oh, Fabrication and characterization of hydrophilic poly(lactic-co-glycolic acid)/poly(vinyl alcohol) blend cell scaffolds by melt-molding particulate-leaching method, *Biomaterials* 24 (22) (Oct 2003) 4011–4021.
- [36] E. Berthier, E.W.K. Young, D. Beebe, Engineers are from PDMS-land, biologists are from Polystyrenia, *Lab Chip* 12 (7) (Apr 2012) 1224–1237.
- [37] J.M. Łopacińska, J. Emnéus, M. Dufva, Poly(dimethylsiloxane) (PDMS) affects gene expression in PC12 cells differentiating into neuronal-like cells, *PLoS One* 8 (1) (Jan 2013) e53107.
- [38] A.J. Strain, J.M. Neuberger, A bioartificial liver—state of the art, *Science* 295 (5557) (Feb 2002) 1005–1009.
- [39] R.G. Flemming, C.J. Murphy, G.A. Abrams, S.L. Goodman, P.F. Nealey, Effects of synthetic micro- and nano-structured surfaces on cell behavior, *Biomaterials* 20 (6) (Mar 1999) 573–588.
- [40] L. Marcotte, M. Tabrizian, Sensing surfaces: challenges in studying the cell adhesion process and the cell adhesion forces on biomaterials, *IRBM* 29 (2–3) (Apr 2008) 77–88.
- [41] X. Liu, J.Y. Lim, H.J. Donahue, R. Dhurjati, A.M. Mastro, E.A. Vogler, Influence of substratum surface chemistry/energy and topography on the human fetal osteoblastic cell line hFOB 1.19: Phenotypic and genotypic responses observed in vitro, *Biomaterials* 28 (31) (Nov 2007) 4535–4550.
- [42] S. Sant, A. Khademhosseini, Fabrication and characterization of tough elastomeric fibrous scaffolds for tissue engineering applications, *Conf. Proc. IEEE Eng. Med. Biol. Soc.* 2010 (Jan 2010) 3546–3548.
- [43] A. Dolatshahi-Pirouz, M. Nikkhal, K. Kolind, M.R. Dokmeci, A. Khademhosseini, Micro- and nanoengineering approaches to control stem cell-biomaterial interactions, *J. Funct. Biomater.* 2 (4) (Jun 2011) 88–106.
- [44] T. Yeung, P.C. Georges, L.A. Flanagan, B. Marg, M. Ortiz, M. Funaki, N. Zahir, W. Ming, V. Weaver, P.A. Janmey, Effects of substrate stiffness on cell morphology, cytoskeletal structure, and adhesion, *Cell Motil. Cytoskeleton* 60 (1) (Jan 2005) 24–34.
- [45] B. Trappmann, J.E. Gautrot, J.T. Connelly, D.G.T. Strange, Y. Li, M.L. Oyen, M.A. Cohen Stuart, H. Boehm, B. Li, V. Vogel, J.P. Spatz, F.M. Watt, W.T.S. Huck, Extracellular-matrix tethering regulates stem-cell fate, *Nat. Mater.* 11 (7) (Jul 2012) 642–649.
- [46] F.J. O'Brien, B.A. Harley, I.V. Yannas, L.J. Gibson, The effect of pore size on cell adhesion in collagen-GAG scaffolds, *Biomaterials* 26 (4) (Feb 2005) 433–441.
- [47] P. Thevenot, A. Nair, J. Dey, J. Yang, L. Tang, Method to analyze three-dimensional cell distribution and infiltration in degradable scaffolds, *Tissue Eng. C Methods* 14 (4) (Dec 2008) 319–331.
- [48] H. Lee, S. Ahn, L.J. Bonassar, W. Chun, G. Kim, Cell-laden poly(ϵ -caprolactone)/alginate hybrid scaffolds fabricated by an aerosol cross-linking process for obtaining homogeneous cell distribution: fabrication, seeding efficiency, and cell proliferation and distribution, *Tissue Eng. C Methods* 19 (10) (Oct. 2013) 784–793.

Paper V

Bioimpedance monitoring of 3D cell culturing - Complementary electrode configurations for enhanced spatial sensitivity

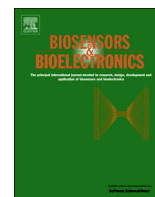
C. Canali, A. Heiskanen, H. B. Muhammad, P. Høyum, F. Pettersen, M. Hemmingsen, A. Wolff, M. Dufva, Ø. G. Martinsen and J. Emnéus
Biosens. Bioelectron., 2015, 63, 72–79



ELSEVIER

Contents lists available at ScienceDirect

Biosensors and Bioelectronics

journal homepage: www.elsevier.com/locate/bios

Bioimpedance monitoring of 3D cell culturing—Complementary electrode configurations for enhanced spatial sensitivity

Chiara Canali^a, Arto Heiskanen^a, Haseena Bashir Muhammad^a, Per Høyum^{b,c}, Fred-Johan Pettersen^c, Mette Hemmingsen^a, Anders Wolff^a, Martin Dufva^a, Ørjan Grøttem Martinsen^{b,c}, Jenny Emnéus^{a,*}^a Department of Micro- and Nanotechnology, Technical University of Denmark, Produktionstorvet Building 423, Kgs. Lyngby 2800, Denmark^b Department of Physics, University of Oslo, Oslo, Norway^c Department of Biomedical and Clinical Engineering, Oslo University Hospital, Oslo, Norway

ARTICLE INFO

Article history:

Received 21 May 2014

Received in revised form

4 July 2014

Accepted 8 July 2014

Available online 14 July 2014

Keywords:

Bioimpedance

3D cell culture

Gelatin scaffold

Multiplexed measurements

Three-terminal impedance

Sensitivity field distribution

ABSTRACT

A bioimpedance platform is presented as a promising tool for non-invasive real-time monitoring of the entire process of three-dimensional (3D) cell culturing in a hydrogel scaffold. In this study, the dynamics involved in the whole process of 3D cell culturing, starting from polymerisation of a bare 3D gelatin scaffold, to human mesenchymal stem cell (MSC) encapsulation and proliferation, was monitored over time. The platform consists of a large rectangular culture chamber with four embedded vertical gold plate electrodes that were exploited in two- and three terminal (2T and 3T) measurement configurations. By switching between the different combinations of electrode couples, it was possible to generate a multiplexing-like approach, which allowed for collecting spatially distributed information within the 3D space. Computational finite element (FE) analysis and electrochemical impedance spectroscopic (EIS) characterisation were used to determine the configurations' sensitivity field localisation. The 2T setup gives insight into the interfacial phenomena at both electrode surfaces and covers the central part of the 3D cell culture volume, while the four 3T modes provide focus on the dynamics at the corners of the 3D culture chamber. By combining a number of electrode configurations, complementary spatially distributed information on a large 3D cell culture can be obtained with maximised sensitivity in the entire 3D space. The experimental results show that cell proliferation can be monitored within the tested biomimetic environment, paving the way to further developments in bioimpedance tracking of 3D cell cultures and tissue engineering.

© 2014 Elsevier B.V. All rights reserved.

1. Introduction

The current challenge in systems biology is to explore the intricate dynamics that orchestrate the cellular microenvironment where complex signalling pathways spatially and temporally direct cellular phenotype towards tissues formation, function and pathophysiology (Huh et al., 2011). The physico-chemical phenomena that take place in the extracellular three dimensional (3D) environment significantly contribute to tissue organisation, but may be hidden by compensating mechanisms when operated in two dimensional (2D) cell culture models (Tibbitt and Anseth, 2009). Therefore, 3D cell cultures are believed to enable, in a more physiologically true manner, the formation of dynamic spatial gradients of soluble factors that influence cell migration, cell–cell communication and differentiation (Watt and Huck, 2013). To

reach this goal new scientific advances in the fields of biomimetic materials (Lu et al., 2013), molecular biochemistry (Baker and Chen, 2012) and microfluidic perfusion techniques (Buchanan and Rylander, 2013) are being explored to mimic biomechanical stability and more complex cell functionality.

Any sensing technique for real-time monitoring of 3D cell cultures must be able to collect real-time information of the time course of the biological processes at strictly controlled physiological-like conditions without damaging the cells. However, the advances so far are still some way off from providing fully robust, quick and user-friendly on-line detection solutions to follow biological dynamics throughout the 3D organisational complexity. Confocal imaging microscopy is widely used for monitoring cell culture evolution in terms of cell viability and differentiation with high subcellular resolution. Nevertheless, this approach still needs to be optimised for tissue engineering purposes. At this point it can be implemented only as an endpoint analysis since a large 3D scaffold has to be sectioned in thin slices (200–300 μm) to allow

* Corresponding author. Tel.: +45 25473548.

E-mail address: jenny.emneus@nanotech.dtu.dk (J. Emnéus).

light penetration (Smith et al., 2010). Furthermore, the scaffold should be optically transparent and composed of materials with low autofluorescence.

Electrical impedance measurements, including electrochemical impedance spectroscopy (EIS), are used to describe material properties as resistance to electrical current flow and ability to store electrical charge. Impedance measurements have been demonstrated as a powerful tool for the real-time study of complex biological systems both in vivo (Weijenborg et al., 2013) and in vitro (Giaever and Keese, 1984; Daza et al., 2013; Lei et al., 2012, 2014) by establishing a correlation between the electrical measurements and the biological phenomena in a non-destructive way. Physiological impedance measurements on tissues and organs have been extensively described by Grimnes and Martinsen (2008) and defined as bioimpedance. These measurements give an

insight of biological 3D systems, reflecting cell dimensions, density and integrity as well as the extracellular matrix composition. In vitro applications of impedance measurements may encompass 2D and 3D cell cultures. However, the methodology originally proposed by Giaever and Keese (1993) for monitoring 2D cultures (electric cell-substrate impedance sensing, ECIS) is still the main focus of such applications. The measurements reflect the electrode interface impedance (polarisation impedance, Z_p) modulated by adhering cells. Lei et al. (2012) and (2014) have applied 2-electrode impedance measurements on 3D cell cultures using thin agarose layers. However, the emergence of 3D culturing and tissue engineering warrant significant development of bioimpedance monitoring strategies to map spatial distribution of cells in larger scaffolds.

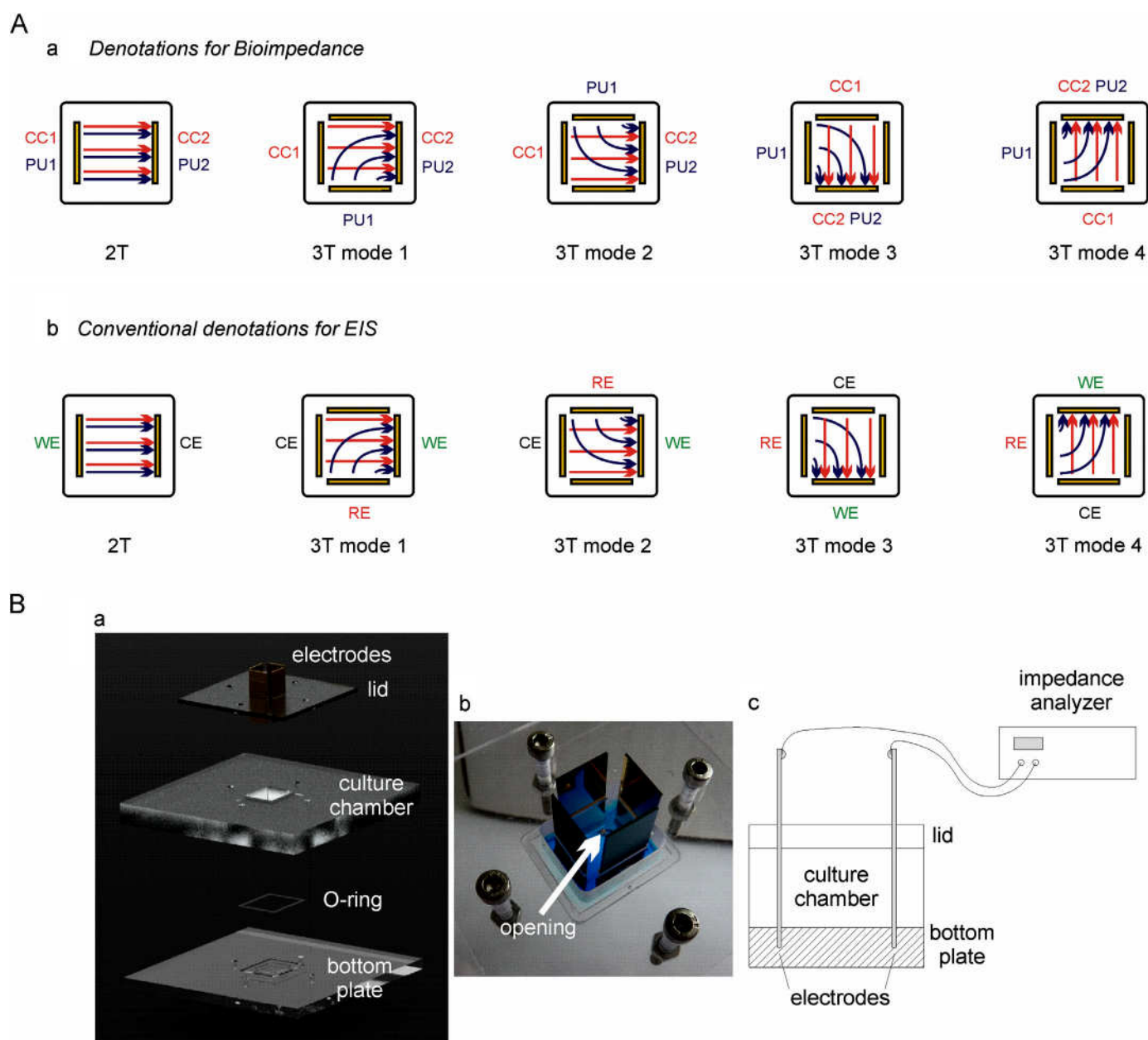


Fig. 1. (A) Schematics of the 2T and 3T (modes 1–4) configurations tested. In bioimpedance measurements (a) CC1 and CC2 form the current-carrying couple, PU1 and PU2 form the pick-up couple. Red (CC) and blue (PU) arrows represent a top view of the equipotential surface directions. In EIS analysis (b): WE= working electrode, CE= counter-electrode, RE= reference electrode. (B) Design of the overall bioimpedance platform. (a) The system consists of 3 layers: bottom plate accommodating the electrodes, culture chamber and lid. (b) Photograph of the system embedding four electrodes for 3T measurements. (c) Experimental setup for the 2T configuration. (For interpretation of the references to colour in this figure legend, the reader is referred to the web version of this article.)

To maximise the biophysical information obtained through *in vitro* bioimpedance measurements on tissue engineering scaffolds and 3D cell cultures, it is crucial to tailor parameters like electrode number, geometry, orientation and spacing. Furthermore, the sensitivity field in such bioimpedance measurements largely depends on the used configurations between electrode couples (current carrying, CC, and picking up, PU). The same electrode pair can have a dualistic role serving both as CC and PU, as in the case of a more conventional two-terminal (2T) configuration (Fig. 1Aa, 2T), which typically includes Z_p and the entire sample volume between the two electrodes. The measurement sensitivity is proportional to the square of the current density (Grimnes and Martinsen, 2008). Alternatively, three- and four-terminal (3T or 4T) configurations, as conventionally used in physiological bioimpedance, are also possible. 4T measurements are commonly used when there is a need to reduce the sensitivity close to both PU electrodes, either to avoid contribution from Z_p or to focus the measurements on a specific volume inside the sample. In this case, separate electrodes are used as CC and PU, none of them with a dualistic role. In 3T configurations, one electrode is common for the CC and PU couple with a dualistic role (Fig. 1Aa, 3T modes). The impedance of that electrode is the only one having a contribution from Z_p and reflecting the sample volume in its close proximity (Grimnes and Martinsen, 2007).

To our knowledge, bioimpedance monitoring has not been previously established for large 3D cultures applicable in tissue engineering. To fill this gap, we present here bioimpedance monitoring of 3D cultures, including the different stages from gelatin scaffold polymerisation and cell encapsulation to cell proliferation in the 3D environment. A number of alternative and complementary 2T and 3T electrode configurations (Fig. 1A) were applied between vertical gold plate electrodes (Fig. 1B) in a multiplexing-like approach to maximise the sensitivity in a 2-mL gelatin matrix with embedded human mesenchymal stem cells (MSCs). The difference and complementarity between 2T and 3T configurations were described by finite element (FE) analysis and EIS characterisation.

2. Material and methods

2.1. Design and fabrication of bioimpedance platform

The bioimpedance platform (Fig. 1B) was designed for static cell cultures and consists of a bottom plate with rectangular slits for mounting up to four electrodes adjacent to each sidewall of the culture chamber ($19 \times 16 \times 10 \text{ mm}^3$). The two parts were sealed together using a PDMS O-ring. The chamber is closed with an optically transparent lid having an opening (2-mm diameter) to enable culture medium removal and replenishment. The system components were fabricated of polycarbonate using micromilling. Vertical electrodes ($10 \times 25 \times 0.525 \text{ mm}^3$) were fabricated by thermally evaporating a 200-nm thick layer of gold onto an oxidised (650 nm) silicon wafer coated with a 20-nm titanium adhesion layer.

2.2. FE analysis

FE simulations were carried out using Comsol Multiphysics v4.3b to study the sensitivity field distribution within the bioimpedance platform with the different electrode configurations. The method for calculating the sensitivity field has been previously described by Pettersen and Høgetveit (2011). 3D models of the chamber containing four electrodes and a gelatin scaffold (5% w/v, 2 mL) were created in the AC-DC module. Gelatin parameters were set as 0.3 S/m for conductivity (σ) (Marchal et al., 1989) and

60 for relative permittivity (ϵ_r) (Ferguson et al., 1934). The electrode parameters were set as $45.6 \times 10^6 \text{ S/m}$ for σ and 1.5 for ϵ_r . The mesh consisted of 33,772 tetrahedral elements with an average element quality of 0.77.

For simulating the 2T configuration, 10 mV were applied to one electrode while the other was grounded. Electrical insulation was applied to the chamber chassis. The sensitivity field (S) was computed as $S=J^2 \text{ [m}^{-4}\text{]}$ (Høyum et al., 2010) where J is the relative surface density of the injected current. For the 3T configurations, 10 mV were applied between two opposing electrodes, and S was evaluated in relation to the adjacent PU couple at the corner of the chamber (Fig. 1Aa). In this case, S was calculated as $S=J_{PU} \cdot J_{CC} \text{ [m}^{-4}\text{]}$ where J_{PU} is the current density vector for the PU couple and J_{CC} is the current density for the CC couple.

2.3. EIS analysis of Z_p distribution in 2T and 3T configurations

Prior to any measurements, gold electrodes were cleaned by a 10-min treatment using a mixture of H_2O_2 (25% v/v) and KOH (50 mM) followed by a potential sweep from -200 mV to -1200 mV in 50 mM KOH (Heiskanen et al., 2008). EIS analysis was performed using an equimolar solution of $\text{K}_3[\text{Fe}(\text{CN})_6]$ and $\text{K}_4[\text{Fe}(\text{CN})_6]$ (10 mM) dissolved in 1 M KNO_3 . Electrode modification with sodium 3-mercapto-1-propanesulfonate (MPS, 63765 Fluka) was performed for EIS analysis of Z_p distribution. A sinusoidal perturbation of 10 mV (rms) with respect to the open circuit potential was applied in the frequency range between 10 MHz and 1 MHz using a Reference 600 potentiostat/galvanostat/ZRA (Gamry Instruments). 2T and 3T measurements were performed on conductivity standard solutions (Hanna Instruments) with σ values (25 °C): 84×10^{-4} (cat. 663-5054), 0.14 (cat. 663-5048), 1.29 (cat. 663-5047) and 11.18 S/m (cat. 663-5008) using an SI1260 impedance analyser and a 1294 impedance interface (Solartron Instruments) based on the protocol described above. Due to the platform symmetry and solution homogeneity, only mode 1 is reported for the 3T configuration. Fig. 1Ab shows the assignment of electrodes for EIS (see also Section S1 in Supplementary material).

2.4. Bioimpedance experiments

Experiments were carried out using 5% w/v gelatin (Fluka 48723). The hydrogel was covalently cross-linked using the microbial enzyme transglutaminase (Activa[®] RM, Ajinomoto) dissolved in $1 \times \text{PBS}$ (Sigma D8537). Bioimpedance was used to monitor: (1) polymerisation of the bare gelatin matrix, (2) encapsulation of MSCs (Gibco A15652) within the scaffold, and (3) MSCs growth over time. The used measurement volume was in all cases 2 mL. Bioimpedance measurements using Solartron SI1260/SI1294 were performed by applying a 10 mV AC in the frequency range between 100 Hz and 1 MHz. Two densities of MSCs (1.5×10^5 and 1.5×10^6 cells/mL) were encapsulated within the hydrogel by directly mixing the cell suspension with gelatin. Prior to measurements, the mixture was allowed to polymerise in the chamber for 2 h at room temperature. Separate measurements were conducted on the bare gelatin scaffold (also 10% w/v for comparison) during the process of polymerisation without any cells present.

To investigate the capability of the system to monitor cell growth, 5×10^5 cells/mL MSCs were loaded into the gelatin scaffold and measurements were performed over time. In this case, cross-linking of 5% gelatin was carried out in cell culture medium (RPMI 1640 with 10% fetal bovine serum and 1% penicillin/streptomycin). Scaffold polymerisation was allowed for 45 min (37 °C, 5% CO_2 in a humidified incubator) and then the culture chamber was filled with cell culture medium. Cells were grown for 48 h in the incubator. At the end of each growth experiment, cells

were recovered from gelatin to estimate the cell number and viability. Gelatin scaffolds were digested at 37 °C with a 250 µg/mL thermolysin (Sigma T7902) solution in 50 mM Tris and 10 mM CaCl₂. Cells were counted with a MOXI Z automated cell counter (Orflo Technologies) and viability was estimated using Trypan blue (Sigma T8158).

3. Results and discussion

3.1. FE analysis

Fig. 2 shows the solutions of the mathematical models for the spatial distribution of the sensitivity field of 2T (a) and 3T (b) configuration. The 3T setup allows several combinations of CC and PU electrode couples and four of them were chosen with the aim to focus on the dynamics occurring at the corners of the 3D culture chamber. Due to the platform symmetry and bulk homogeneity, only the FE model for 3T mode 1 (Fig. 1Aa) is shown here, while the complete FE analysis for all the 3T setups (modes 1–4) is reported in Fig. S1.

As expected, the 2T configuration senses the dynamics occurring in the whole volume between the two electrodes with significant contribution from Z_p at both interfaces (Fig. 2a). The 3T configuration mainly focuses on the volume between the PU couple at the corner of the respective culture chamber (Fig. 2b). Hence, by switching between modes 1–4 it is possible to build a multiplexing-like approach that provides an insight of the 3D space at the corners. A minor influence of the electrode edge on conduction was emphasised in these models. This localised charge density is related to the used electrode structure with conductive edges. This could be eliminated by insulating the edges using a passivation layer.

3.2. EIS analysis of Z_p distribution in 2T and 3T configurations

As discussed in the introduction and theoretically illustrated in the FE simulations (Fig. 2), Z_p has a different influence on 2T and 3T configuration. To experimentally validate this, we used EIS characterisation with the redoxactive probe $[\text{Fe}(\text{CN})_6]^{3-/4-}$ combined with a self-assembled monolayer (SAM) of MPS, modifying each electrode one-by-one (see the defined roles of the different electrodes in Fig. 1Ab). MPS renders a modified electrode with a negative net charge, which repels $[\text{Fe}(\text{CN})_6]^{3-/4-}$. When using a redoxactive probe, the Z_p in acquired impedance spectra shows

both a Faradaic (electron transfer: charge transfer resistance, R_{ct} , and mass transfer: Warburg impedance, Z_w) and non-Faradaic (double layer capacitance, C_{dl}) contribution. Due to repulsion by the negatively charged MPS SAM, especially the R_{ct} should increase on electrodes, whose Z_p is a part of the sensitivity field of the electrode configuration. Since the electrodes in the system are equal in size, in 2T configuration the contribution of Z_p at both electrodes should be equal, whereas in 3T configuration the contribution of Z_p should be eliminated at one of the PU electrodes. Fig. 3a shows two Nyquist plots, one for an unmodified WE and another for the same WE after MPS modification, the latter indicating a significant increase in R_{ct} . If the electrode assignment is reversed, i.e. the MPS-modified electrode is used as the CE, the acquired Nyquist plot is superimposable with the one in Fig. 3a. A corresponding set of Nyquist plots for mode 1 of 3T configuration (Fig. 1Ab) is shown in Fig. 3b. In this case, the MPS-modified electrode is the RE, the PU at which the Z_p is expected to be eliminated. This is verified by the fact that the Nyquist plots before and after MPS modification are superimposable. When a corresponding test is performed modifying the other PU, i.e. the WE in Fig. 1Ab, an increase in R_{ct} is observed (result not shown).

All together, these results demonstrate that the 2T configuration allows gathering of information about the interfacial phenomena at both electrode surfaces in addition to those occurring at the centre of the 3D sample. By combining the 2T information with the one acquired using the 3T configuration when switching between the four modes (Fig. 1A), it is possible to collect spatially distributed information that focuses on the culture chamber corners in a multiplexing-like approach. Additional EIS-based verification regarding the differences between the 2T and 3T configuration are shown in Fig. S4 and further discussed in Section S3 in Supplementary material.

3.3. EIS conductivity measurements

The system needs to account for changes in the cell-scaffold conductivity during cellular growth. For instance, a decrease in pH within the cell culture leads to an increase in conductivity, thus influencing the sensed impedance. Such changes may be correlated to different biochemical phenomena, e.g. hypoxia and cell death, bacterial contamination, aging of the culture. To ensure system reproducibility, the intra- and inter assay reproducibility were first determined and found to be excellent for the 2T and 3T measurement modes (Figs. S2 and S3). Impedance spectra were then acquired for different conductivity standard solutions using

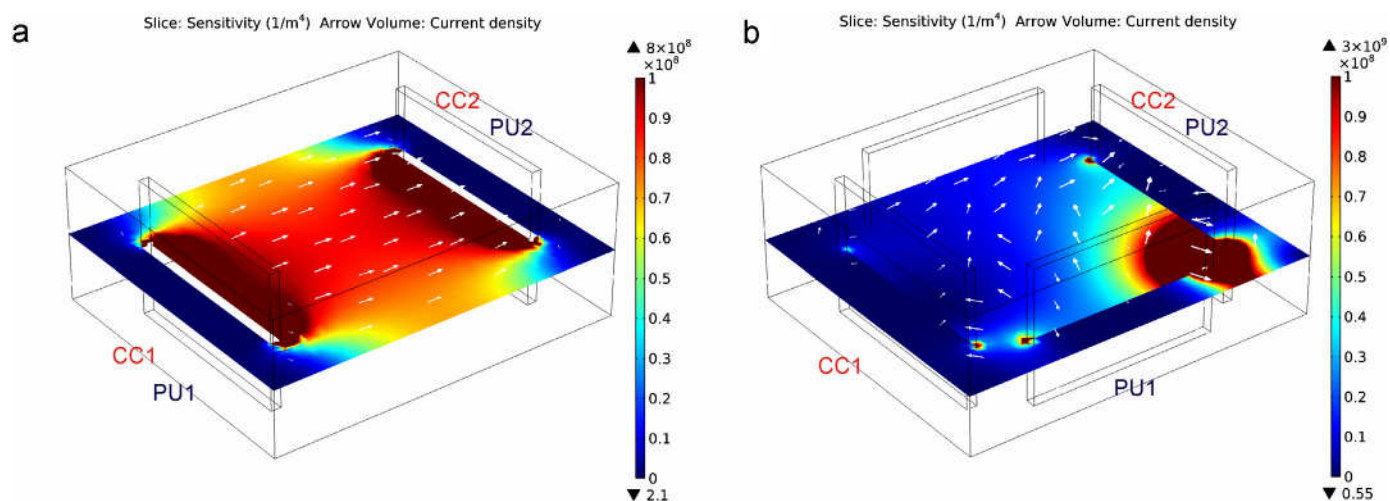


Fig. 2. FE analysis: Sensitivity field [m⁻⁴] distribution (slice view) and current density vectors for (a) 2T configuration and (b) 3T configuration (mode 1).

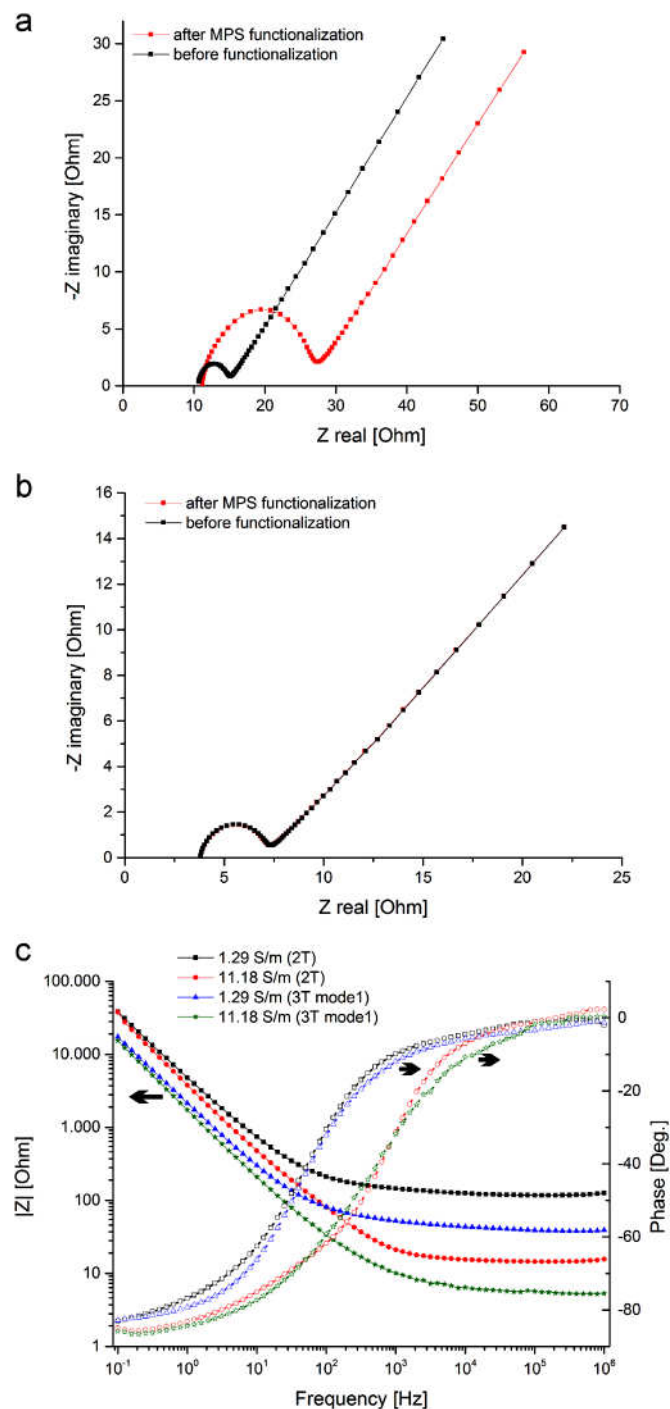


Fig. 3. Nyquist plots showing the effect of MPS functionalisation of (a) one electrode in the 2T configuration and (b) the PU1 in the 3T configuration (mode 1). (c) Discrimination between different conductivity standards using 2T and 3T configurations (mode 1).

the 2T and 3T (mode 1) configurations. As shown in Fig. 3c, the spectra (presented as Bode plots) provide a clear discrimination between standards of medium low (1.29 S/m) and high (11.18 S/m) conductivity. Due to the system isotropy, the acquired Bode plots for all the four modes of the 3T configuration showed good superimposability (Fig. S5).

The impedance spectra acquired using conductivity standard solutions are characterised by bulk resistance at high frequencies and Z_p (contribution of C_{dl}) at lower frequencies. For both 2T and 3T configuration, the cut-off frequency indicating the transition

between resistive and capacitive behaviour is roughly the same although a sharper transition is observed for the 2T configuration. Low-conductivity solutions (84×10^{-4} and 0.14 S/m) were also tested to evaluate the functionality of the setup under conditions, which often lead to artefacts especially at high frequencies due to the formation of parasitic conduction paths (Scully and Silverman, 1993; Stewart et al., 1993). Even under these conditions, the platform facilitated stable measurements, which were negligibly affected by noise (Fig. S6). A characteristic difference between the 2T and 3T configuration, related to the differential mapping of the 3D space as also illustrated in Fig. 2, can be seen in the high-frequency behaviour of $|Z|$, being systematically higher in comparison with the average of the four 3T modes (further details shown in S4).

3.4. Bioimpedance of gelatin scaffold polymerisation and cell encapsulation

Gelatin is a well-known biodegradable and biocompatible material often exploited as scaffold for tissue engineering, either alone or in combination with other molecules, such as chitosan (Kang et al., 1999; Huang et al., 2005). Engler et al. (2006) showed that MSCs were able to specify lineage and commit to phenotypes with extreme sensitivity to scaffold stiffness. This opened up a new perspective for the use of hydrogels as 3D cell culturing scaffolds due to their tuneable physico-chemical properties and ease of preparation.

Fig. 4a presents the ability of the 3T configuration (mode 1) to discriminate between 5% and 10% gelatin polymerisation. Gelatin contains mobile ions and readily reactive groups (amino, hydroxyl and thiol groups, hydrogen ions and small chain fragments up to several kDa), which partly lose their mobility during the polymerisation process. Under the influence of a small applied electric field, the ions migrate through the hydrogel, depending on the degree of cross-linking (Winter and Shifler, 1975). During the polymerisation process, new chemical bonds are formed with a decrease in the number of reactive groups and hydrogen ions until the system reaches a new thermodynamic stability. This leads to a decrease in gelatin conductivity, and therefore an increase in impedance, and as expected is more pronounced for 10% cross-linked gel (Fig. 4a). In our further study, 5% scaffold was employed since it displays a Young's modulus of approximately 3.6 kPa (data not shown), which is the stiffness common to many soft tissues (e.g. liver, kidney and some blood vessels) (Janmey and Miller, 2011).

Fig. 4 shows Bode plots for the 2T (b) and 3T (c) configuration acquired during polymerisation of 5% gelatin scaffold during 2-h period. At the beginning of the polymerisation (0 h), the standard deviation among acquired triplicate spectra was higher, especially for the 2T configuration (Fig. 4b). This may be explained by the higher ionic mobility at the beginning in comparison with the fully cross-linked polymer. Since each spectrum acquisition took 7 min, it is plausible to correlate the higher impedance variation with the higher ionic mobility. Moreover, the 2T configuration reflects a more significant contribution from both the gelatin bulk resistance (cf. conductivity standards, Fig. 3c) and Z_p at both electrodes, which may also explain the higher standard deviation in comparison with the 3T configuration, where the contribution of Z_p on one PU electrode is negligible. After the first hour of polymerisation, a 1.05 (± 0.02)-fold increase in $|Z|$ was detected with both configurations. Throughout the 2-h period, the 3T configuration provided lower impedance values in the whole frequency range. As an example, after 1 h, the $|Z|$ at 1 kHz was calculated to be 38.60% (standard deviation < 0.01) lower. This value should thus correspond to the impedance polarisation of one PU electrode at those specific conditions. This absolute variation of $|Z|$ agrees well

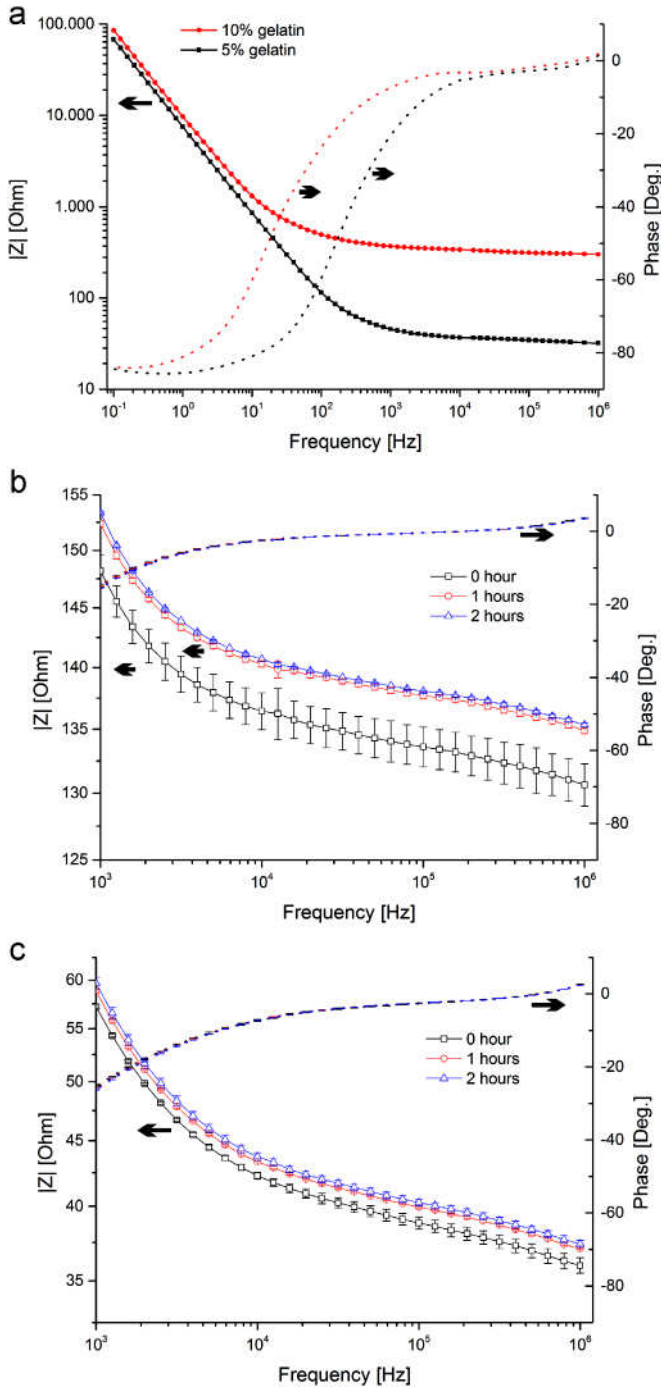


Fig. 4. (a) Bode plots showing the discrimination between two different degrees of crosslinking for thick gelatin scaffolds (5% and 10% w/v) for the 3T configuration (mode 1). Bode plots for the polymerisation of 5% gelatin over time at room temperature and the frequency range between 1 kHz and 1 MHz: (a) 2T and (b) 3T (mode 1) configuration. Data are presented as mean \pm standard deviation ($n=3$).

with the one found for the conductivity standard of 1.29 S/m (Fig. 3c) since gelatin was prepared in PBS at physiological concentration.

The two configurations were further characterised in terms of their ability to discriminate between different cell loadings within the 5% gelatin scaffold. This was achieved by directly mixing different MSCs densities (1.5×10^5 and 1.5×10^6 cells/mL) with a gelatin solution in PBS, which was poured into the culture chamber and let polymerise for 2 h at room temperature. Fig. 5 shows clearly that the 2T configuration (solid lines, solid symbols)

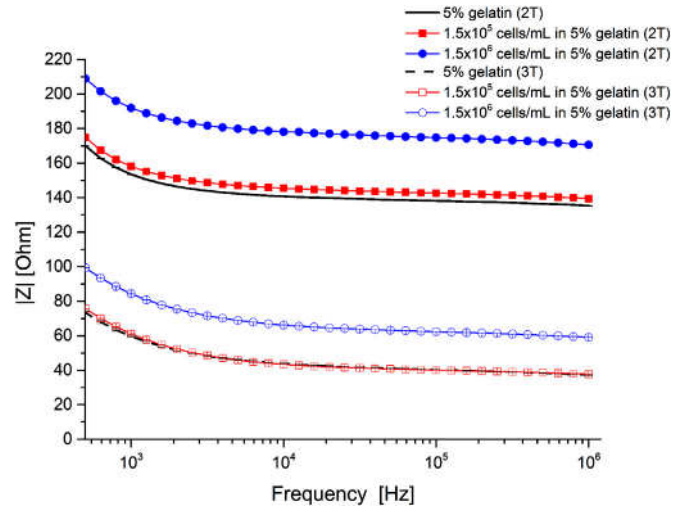


Fig. 5. Bode plots of the impedance modulus $|Z|$ between 500 Hz and 500 kHz: bare gelatin scaffold and different MSC densities encapsulated in the gelatin scaffold for the 2T (solid line for gelatin scaffold and solid lines/filled symbols for encapsulated cells) and 3T (mode 1) configuration (dashed line for gelatin scaffold and solid lines/open symbols for encapsulated cells). Data are presented as mean \pm standard deviation ($n=3$).

can discriminate between the bare gelatin scaffold (solid line) and the scaffold loaded with both cell densities, whereas the 3T configuration could only discriminate the higher cell density (solid lines, open symbols) from the bare gelatin scaffold (dashed line). This difference in sensitivity may be partially explained by the larger number of cells in the central volume of the culture chamber in comparison with the restricted zones at the corners where the 3T configuration modes are focused. Analogously to this, the lower detection limit of the 2T configuration is also related to the findings of Kalvøy et al. (2009) as well as the FE simulations and EIS characterisation presented above, i.e., in 2T configuration the highest sensitivity field is located around the entire width of the two electrodes (pronounced Z_p contribution for the 2T configuration).

3.5. Bioimpedance of 3D cell growth

As a proof of concept on the capability of the system to monitor cell proliferation and distribution over time, based on the above results, 5×10^5 cells/mL was chosen as a starting cell density. MSCs were encapsulated in a 5% gelatin scaffold and cultured in the chamber for 48 h. In this experiment, the gelatin scaffold was polymerised in cell culture medium to provide a proper environment for cell growth. The cell culture was performed under static conditions (37 °C, 5% CO₂ in a humidified incubator) while bioimpedance monitoring was performed in triplicate every 24 h. Fig. 6 shows the increase in $|Z|$ (at 4 kHz) for the 2T (a) and 3T (modes 1–4, b) configuration. This frequency was chosen based on spectral analysis (see Section S5 in Supplementary material), which indicates that the discrimination between time points was the highest for both configurations.

The two different configurations showed consistent results in terms of the increase in $|Z|$, albeit with different trends over time. For the 3T measurements, which respond to the dynamics occurring at the corners of the 3D culture chamber, the growth curve is still rising after 48 h (Fig. 6b), whereas the growth curve for the 2T measurements is approaching a saturation limit after 48 h (Fig. 6a), which may correspond to differences in cell distribution inside the gelatin matrix during the culture period. Corresponding results were obtained in bioimpedance monitoring of the growth of HeLa and HepG2 cells as well as neural stem cells (results not

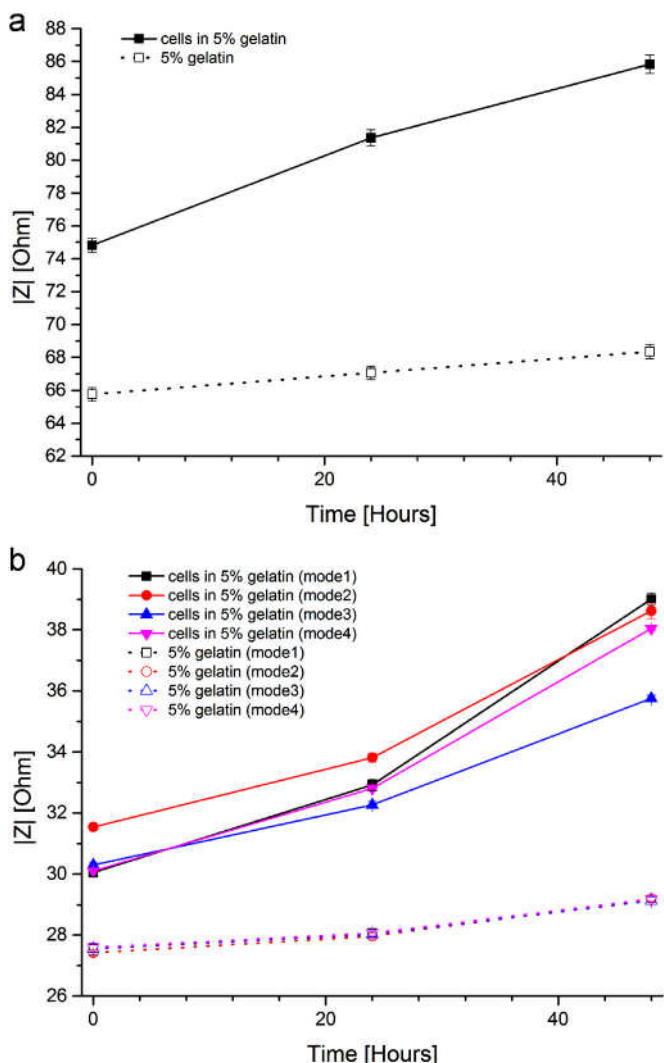


Fig. 6. Bioimpedance monitoring of MSC growth during 48-h culture period: $|Z|$ at 4 kHz is reported for (a) 2T and (b) 3T (modes 1–4) configurations. Data are presented for triplicate measurements as mean \pm standard deviation.

shown). In separate tests, the initial cell distribution in gelatin has been found to be homogeneous (results not shown). Based on this, the bioimpedance results support the hypothesis that the cells tend to proliferate more in the centre of the culture chamber than in the corners close to the chamber walls. Indirectly, this is also supported by the findings of Rao et al. (2012) showing differential behaviour glioblastoma cells (morphology and motility) in the bulk of 3D Matrigel in comparison with regions in the proximity of a solid substrate.

Due to the hydrogel scaffold thickness, the visualisation of the 3D culture over time with optical microscopy was not possible. Furthermore, the softness of 5% gelatin hampered the possibility of slicing the scaffold. At the end the experiment, the MSCs were therefore recovered from gelatin by incubating the scaffolds with a thermolysin solution at 37 °C to estimate the cell number and viability using the Trypan blue endpoint assay. Based on this assay, the average cell number was almost doubled from the initial value and all the cells were viable. This verifies that the increase in $|Z|$ is related to an increase in cell number over time and that cell viability is not affected by bioimpedance monitoring. The presented bioimpedance monitoring of 3D cell culture with spatial distribution of the sensitivity field and capability to discriminate between gelatin scaffolds with different degree of crosslinking (Fig. 4a) underline the suitability of the system for assessing, e.g.,

cell proliferation dependence of different type of cells on hydrogel stiffness, which was pointed out by Wang et al. (2010) as a factor influencing MSC proliferation rate in gelatin-based 3D matrix.

4. Conclusions

A bioimpedance based platform has been developed for real-time monitoring of the dynamics involved in the whole process of 3D cell culturing in large gelatin scaffolds, comprising enzymatic polymerisation, mesenchymal stem cell (MSC) encapsulation and proliferation. Using finite element (FE) simulations and electrochemical impedance spectroscopic characterisation, we demonstrate the distribution of the sensitivity fields and behaviour of impedance measurements when employing 2 terminal (2T) and 3 terminal (3T) electrode configurations. The 2T configuration maps the central part of the scaffold space, whereas the 3T configurations focus on the corners. The differential spatial distribution of the sensitivity fields were exploited in multiplexed bioimpedance monitoring of MSC proliferation inside the gelatin scaffolds maximising the obtained spatial information. This approach constitutes a first attempt of generating a flexible bioimpedance based method for monitoring large 3D cell cultures with spatial resolution, hence, bridging the gap between conventional impedance monitoring of 2D cultures and future electrical impedance tomography of 3D cultures.

Acknowledgements

This study and the Ph.D. fellowship of C. Canali were financially supported by the EU-funded project NanoBio4Trans (Grant no. 304842). We thank Lundbeckfonden, Denmark for financing scientific mobility (R148-2013-14502).

Appendix A. Supplementary information

Supplementary data associated with this article can be found in the online version at <http://dx.doi.org/10.1016/j.bios.2014.07.020>.

References

- Baker, B.M., Chen, C.S., 2012. *J. Cell Sci.* 125, 3015–3024.
- Buchanan, C., Rylander, M.N., 2013. *Biotechnol. Bioeng.* 110, 2063–2072.
- Daza, P., Olmo, A., Cañete, D., Yúfera, A., 2013. *Sens. Actuators B* 176, 605–610.
- Engler, A.J., Sen, S., Sweeney, H.L., Discher, D.E., 2006. *Cell* 126, 677–689.
- Ferguson, A.L., Malone, J.G., Case, L.O., 1934. *J. Chem. Phys.* 2, 94–98.
- Giaever, I., Keese, C.R., 1993. *Nature* 366, 591–592.
- Giaever, I., Keese, C.R., 1984. *Proc. Natl. Acad. Sci. USA* 81, 3761–3764.
- Grimnes, S., Martinsen, Ø.G., 2007. *J. Phys. D* 40, 9–14.
- Grimnes, S., Martinsen, Ø.G., 2008. *Bioimpedance and Bioelectricity Basics*, second ed. Academic Press, Oxford.
- Heiskanen, A.R., Spiegel, C.F., Kostesha, N., Ruzgas, T., Emnéus, J., 2008. *Langmuir* 24, 9066–9073.
- Høyum, P., Kalvøy, H., Martinsen, Ø.G., Grimnes, S., 2010. *Physiol. Meas.* 31, 1369–1379.
- Huang, Y., Onyeri, S., Siewe, M., Moshfeghian, A., Madhally, S.V., 2005. *Biomaterials* 26, 7616–7627.
- Huh, D., Hamilton, G.A., Ingber, D.E., 2011. *Trends Cell Biol.* 21, 745–754.
- Janmey, P.A., Miller, R.T., 2011. *J. Cell Sci.* 124, 9–18.
- Kalvøy, H., Frich, L., Grimnes, S., Martinsen, Ø.G., Hol, P.K., Stubhaug, A., 2009. *Physiol. Meas.* 30, 129–140.
- Kang, H.W., Tabata, Y., Ikada, Y., 1999. *Biomaterials* 20, 1339–1344.
- Lei, K.F., Wu, M., Liao, P., Chen, Y., Pan, T., 2012. *Microfluid. Nanofluid.* 12, 117–125.
- Lei, K.F., Wu, M.H., Hsu, C.W., Chen, Y.D., 2014. *Biosens. Bioelectron.* 51, 16–21.
- Lu, T., Li, Y., Chen, T., 2013. *Int. J. Nomed.* 8, 337–350.
- Marchal, C., Nadi, M., Tosser, A.J., Roussey, C., Gaulard, M.L., 1989. *Int. J. Hyperth.* 5, 725–732.
- Pettersen, F.J., Høgetveit, J.O., 2011. *J. Electr. Bioimp.* 2, 13–32.

- Rao, S.S., Bentil, S., DeJesus, J., Larison, J., Hissong, A., Dupaix, R., Sarkar, A., Winter, J.O., 2012. PLoS One 7, e35852.
- Scully, J.R., Silverman, D.C., 1993. *Electrochemical Impedance: Analysis and Interpretation*. ASTM International, Philadelphia, PA.
- Smith, L.E., Smallwood, R., Macneil, S., 2010. *Microsc. Res. Tech.* 73, 1123–1133.
- Stewart, K.C., Kolman, D.G., Taylor, S.R., 1993. *ASTM Spec. Tech. Publ.* 1188, 73–79.
- Tibbitt, M.W., Anseth, K.S., 2009. *Biotechnol. Bioeng.* 103, 655–663.
- Wang, L., Chung, J.E., Chan, P.P., Kurisawa, M., 2010. *Biomaterials* 31, 1148–1157.
- Watt, F.M., Huck, W.T.S., 2013. *Nat. Rev. Mol. Cell Biol.* 14, 467–473.
- Weijnenborg, P.W., Rohof, W.O.A., Akkermans, L.M.A., Verheij, J., Smout, A.J.P.M., Bredenoord, A.J., 2013. *Neurogastroenterol. Motil.* 25. (574–e458).
- Winter, J., Shifler, D., 1975. *Material Properties of Gelatin Gels*. Marvalaud Incorporated, Westminster, MD (Scientific Report)(AD-A008 396).

Supplementary material:

Bioimpedance monitoring of 3D cell culturing - complementary electrode configurations for enhanced spatial sensitivity

Chiara Canali et al.

S1. Bioimpedance and EIS measurement interfaces

In the manuscript we show how connections to the electrodes are generally denoted for bioimpedance applications and conventional electrochemical impedance spectroscopy (EIS) (Fig. 1A). Solartron SI1260 impedance analyzer and SI1294 impedance interface were originally designed for measuring impedance on materials (e.g. biomaterials) with high polarization impedance (Z_p). The SI1294 impedance interface has four terminals named GenHi, GenLo (i.e., the current-carrying electrode couple, CC) and VHi, VLo (i.e., the pick-up electrode couple, PU). The AC voltage is applied to GenHi while GenLo is grounded. Both the current through the sample and the voltage drop across the sample are measured between VHi and VLo in order to compute the impedance of the sample.

On the other hand, a general EIS interface typically refers to:

- a working electrode (WE) where the reaction/phenomenon of interest is occurring;
- a reference electrode (RE) with a stable and well-known electrode potential, against which the WE potential is measured;
- a counter electrode (CE) which merely closes the electric circuit.

In the manuscript, Fig. 1A schematically shows that, despite the different electrode denotations, it is possible to achieve the same configurations with both bioimpedance- and EIS-dedicated instruments. In a 2T configuration, CC1 and PU1 are connected to one electrode (i.e., WE), while CC2 and PU2 are connected to the other (i.e., CE, which is short-circuited with RE). In a 3T configuration, WE serves as both CC2 (for applying the sinusoidal potential together with CE, i.e. CC1) and PU2 (for picking up the signal together with RE). Only the Z_p at the WE contributes to the overall impedance, whereas the Z_p at the RE is eliminated.

S2. FE analysis

FE analysis showed that the four chosen modes of the 3T configuration mainly focus on the corners of the 3D culture chamber in the proximity of one of the PU electrodes (i.e., the WE). Hence, by switching among the four different combinations of electrode couples (mode 1-4) it is possible to build a multiplexing-like approach, which collects spatially distributed information at the corners of the 3D environment.

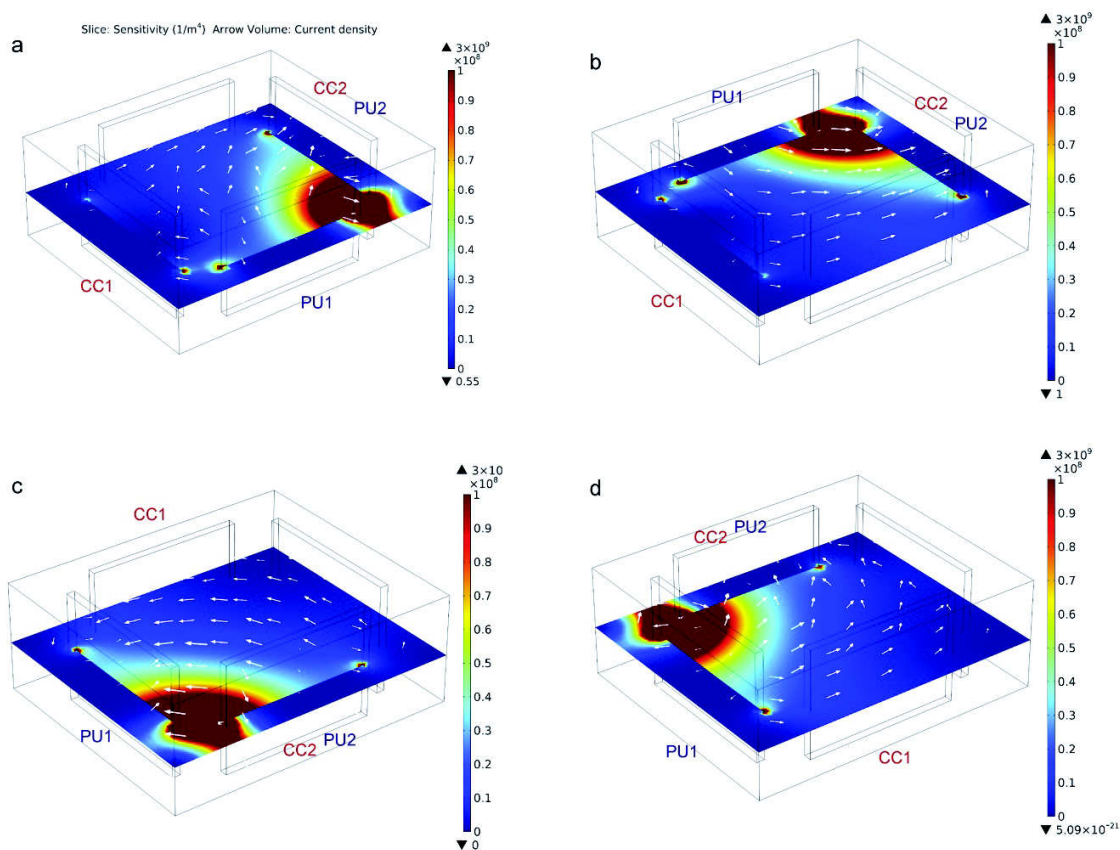


Fig. S1. Sensitivity field [m^{-4}] distribution (slice view) and current density vectors for the PU couple in the chosen modes of 3T configuration: mode 1 (a), mode 2 (b), mode 3 (c) and mode 4 (d). CC1 and CC2 form the current-carrying electrode couple, while PU1 and PU2 form the pick-up electrode couple.

S3. EIS characterization

Measurements performed for the EIS characterization of the platform displayed a very high intra- (Fig. S2) and inter-assay (Fig. S3) reproducibility with both 2T and 3T configuration.

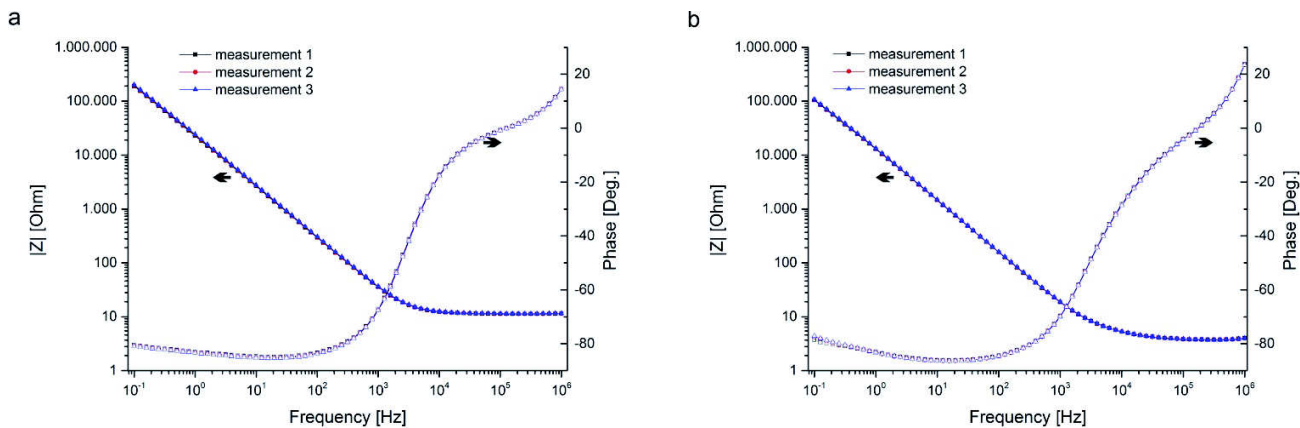


Fig. S2. Intra-assay reproducibility: EIS analysis with 2T (a) and 3T (mode 1, b) configuration in 1M KNO_3 solution.

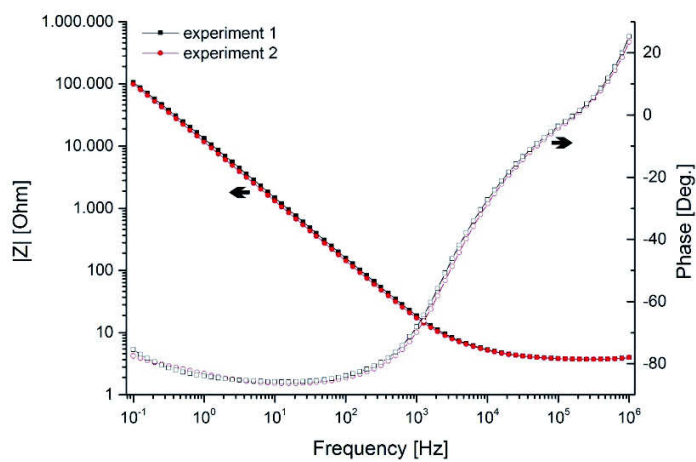


Fig. S3. Inter-assay reproducibility: EIS analysis with 3T configuration (mode 1) in 1M KNO_3 solution (two different experiments with two different electrode batches).

When using the 2T configuration, both electrodes contribute to the measured total impedance in a 3D sample. In conventional EIS, this generally refers to the solution resistance. This was demonstrated by connecting an extra 550 ohm resistor in series to each electrode one at a time. Independent on whether the resistor was connected to the WE or CE, the recorded Nyquist plot was shifted by 550 ohm (Fig. S4a).

Using the 3T configuration, the Nyquist plot was shifted by 550 ohm only when the resistor was added to the WE (Fig. S4b). This verifies that by switching among a number of 3T modes one can sense the dynamics occurring within the volume between the PU couple focusing on the processes at the periphery of the culture chamber. In particular the chosen four 3T modes address the sensing at the 3D sample's corners.

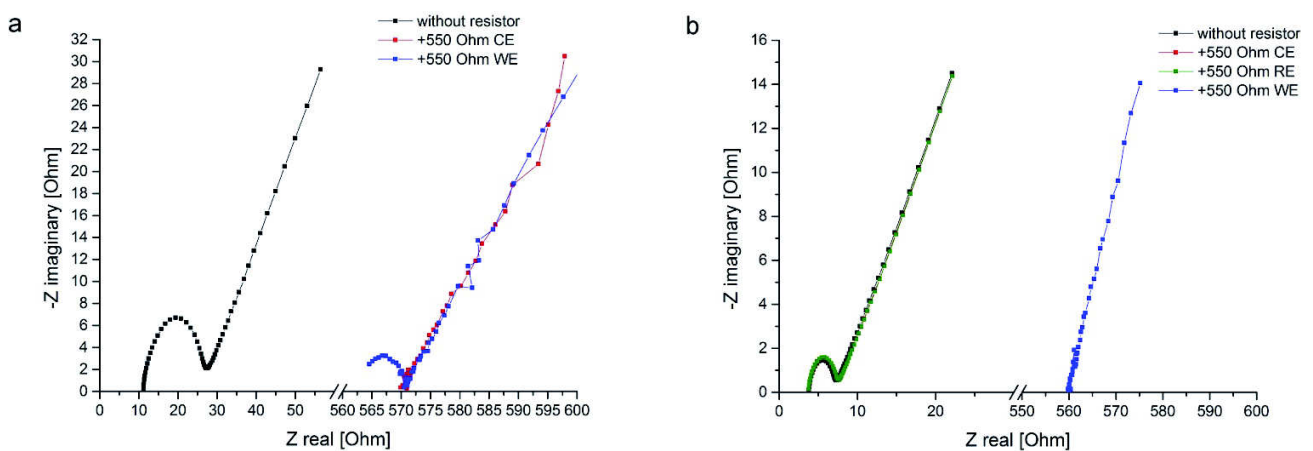


Fig. S4. Nyquist plots showing the effect of an extra 550 ohm resistor in series with each electrode of (a) the 2T configuration and (b) the 3T configuration.

This demonstrates that depending on the electrode configuration (2T or 3T), the setup can provide different spatial information of a 3D sample (e.g., 3D cell culture) in addition to the interfacial phenomena (e.g., polarization impedance, Z_p) at the electrode surfaces. These findings and FE simulations proved that the alternative configurations carry complementary spatially distributed information, which maps the physico-chemical properties of the 3D sample located in the culture chamber.

S4. Measurements on conductivity standard solutions

Fig. S5 shows Bode plots for the four 3T modes with the physiologically relevant standard having a conductivity of 1.29 S/m. Due to the system isotropy, the 3T modes gave almost superimposed spectra.

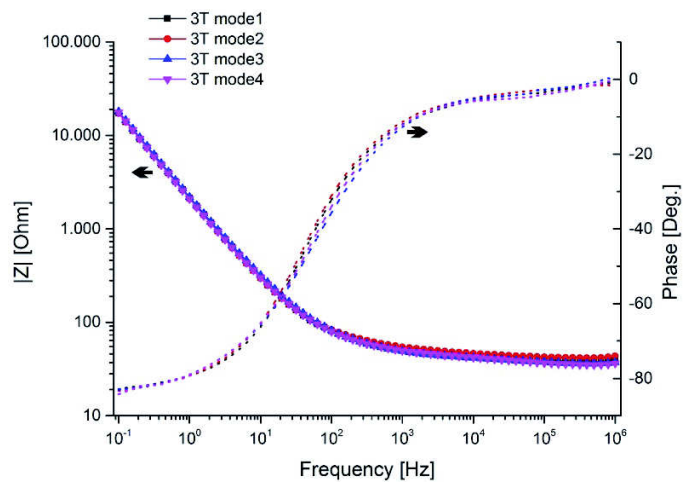


Fig. S5. Superimposable impedance spectra of the four chosen 3T multiplexing modes acquired in a homogeneous medium of physiological conductivity 1.29 S/m.

The system was also characterized in the presence of low-conductivity standards (84×10^{-4} and 0.14 S/m). EIS measurements in low-conductivity solutions are considered problematic due to high-frequency artefacts often arising from parasitic conduction paths. These may depend on the measurement electronics, the physical properties of the sensor (e.g. geometry, electrode porosity, wiring and connections) and the solution resistance. Since parasitic conduction occurs in a frequency range where interfacial phenomena (including electrode polarization) are expected, it may lead to a low signal-to-noise ratio (Scully et al., 1993; Stewart et al., 1993). Our system facilitates stable measurements in the low-conductivity standards, which were negligibly affected by noise even at higher frequencies (Fig. S6).

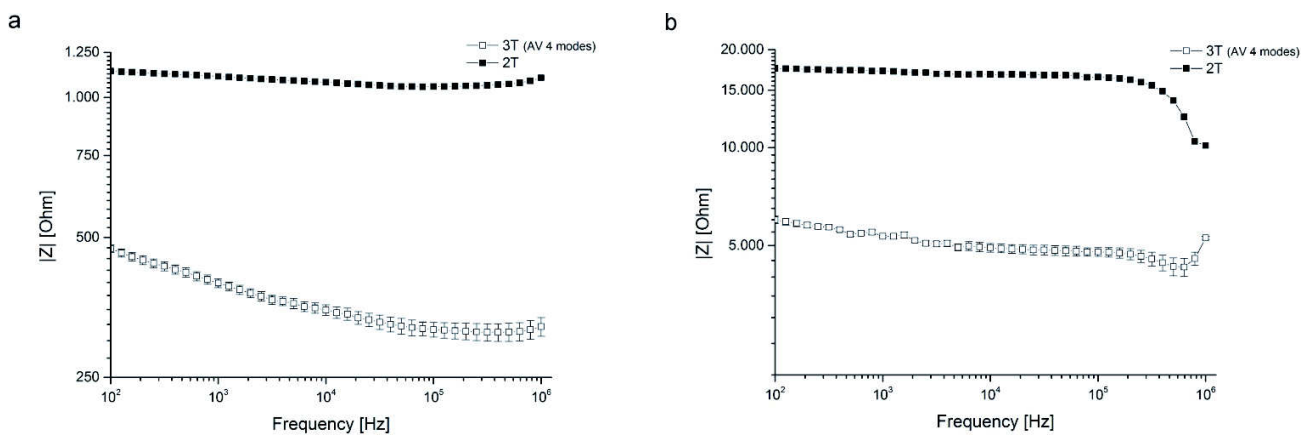


Fig. S6. EIS measurements on low-conductivity standard solutions: 84×10^{-4} (a) and 0.14 S/m (b) for 2T and 3T configurations. Due to bulk isotropy the spectrum for 3T configuration is presented as average of modes 1-4 \pm standard error of the mean ($n=8$). For the 2T configuration, data are reported as average \pm standard deviation ($n=2$). Measurements were negligibly affected by noise even at higher frequencies.

The 2T configuration always gave higher values of $|Z|$ as compared to the average of the exploited four 3T modes. At 1 kHz, $|Z|$ was 31.1 % higher for the 84×10^{-4} S/m solution, and 35.9 % and 43.4 % higher for the 0.14 and 1.29 S/m standard, respectively. At 1 kHz, $|Z|$ for the highest conductivity standard (11.18 S/m) was 65.7 % higher with the 2T configuration when compared to the average of the 3T configurations.

S5. Cell growth

The suitability of the platform for monitoring cell growth in a 3D environment was verified. MSCs at a density of 5×10^5 cells/mL were encapsulated in a 5% gelatin scaffold and cultured in the platform for 48 hours. The culture was performed under static conditions at 37°C in a humidified incubator (5% CO_2) and EIS measurements were carried out every 24 hours in triplicate.

Fig. S7 shows Bode plots for increase in cell number during the 48-h culture period for both 2T and 3T configuration. With time, the $|Z|$ Bode plots shifted upwards for both configurations (Fig. S7a). In the graph, multiplexing mode 1 was chosen as an example to represent the behaviour of the curve shift common to all the four proposed 3T modes. Bode plots for the phase angle showed a good separation between the 2T and 3T configuration in the frequency range between 500 Hz and 10 kHz (Fig. S7b). Based on this spectral analysis, the frequency of 4 kHz was chosen for presenting MSC growth over time.

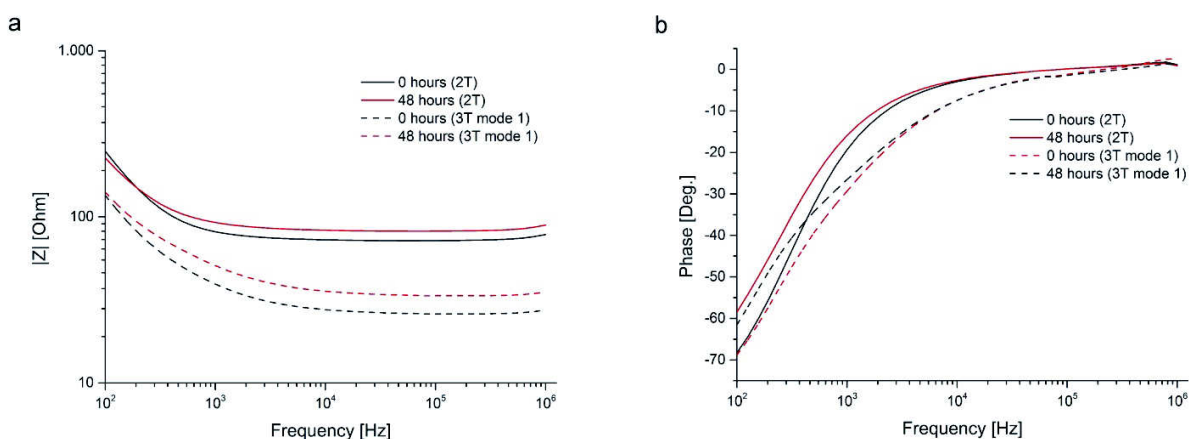


Fig. S7. Bode plots showing increase in MSC number during 48-h cell culture: (a) $|Z|$ and (b) phase angle.

Paper VI

An impedance method for spatial sensing of 3D cell constructs - Towards applications in tissue engineering

C. Canali, C. Mazzoni, L. B. Larsen, A. Heiskanen, Ø. G. Martinsen, A. Wolff, M. Dufva and J. Emnéus
Analyst, 2015, 140, 6079–6088



Cite this: DOI: 10.1039/c5an00987a

An impedance method for spatial sensing of 3D cell constructs – towards applications in tissue engineering†

C. Canali,^a C. Mazzoni,^a L. B. Larsen,^a A. Heiskanen,^a Ø. G. Martinsen,^{b,c} A. Wolff,^a M. Dufva^a and J. Emnéus^{*a}

We present the characterisation and validation of multiplexed 4-terminal (4T) impedance measurements as a method for sensing the spatial location of cell aggregates within large three-dimensional (3D) gelatin scaffolds. The measurements were performed using an array of four rectangular chambers, each having eight platinum needle electrodes for parallel analysis. The electrode positions for current injection and voltage measurements were optimised by means of finite element simulations to maximise the sensitivity field distribution and spatial resolution. Eight different 4T combinations were experimentally tested in terms of the spatial sensitivity. The simulated sensitivity fields were validated using objects (phantoms) with different conductivity and size placed in different positions inside the chamber. This provided the detection limit (volume sensitivity) of 16.5%, *i.e.* the smallest detectable volume with respect to the size of the measurement chamber. Furthermore, the possibility for quick single frequency analysis was demonstrated by finding a common frequency of 250 kHz for all the presented electrode combinations. As final proof of concept, a high density of human hepatoblastoma (HepG2) cells were encapsulated in gelatin to form artificial 3D cell constructs and detected when placed in different positions inside large gelatin scaffolds. Taken together, these results open new perspectives for impedance-based sensing technologies for non-invasive monitoring in tissue engineering applications providing spatial information of constructs within biologically relevant 3D environments.

Received 15th May 2015.

Accepted 9th July 2015

DOI: 10.1039/c5an00987a

www.rsc.org/analyst

1. Introduction

The membranes of biological cells are primarily composed of phospholipid bilayers embedding cholesterol and proteins. Hence, they are dielectrics with bound charges, displaying high resistivity (tens of $\text{k}\Omega \text{ cm}^2$) and capacitance ($1 \mu\text{F cm}^{-2}$). Cell membranes surround a conductive aqueous environment (cytosol) consisting of a mixture of small molecules and biological macromolecules. In biological tissues, cells are surrounded by proteinaceous hydrogel-like extra cellular matrix (ECM), which combines the cellular passive electrical properties with free charges of varying mobility. Hence, under the influence of an alternating electric field, cells and tissues

exhibit complex behaviour, which varies depending on the frequency range.^{1–3} Accordingly, electrical impedance spectroscopy (EIS) has been successfully applied as a non-invasive and cost-effective method for studying the physico-chemical properties of different biological materials in research spanning from cell biology^{4,5} and tissue engineering^{6,7} to physiology and medical technology.⁸

Although biophysical studies of cells in suspension have provided information on their electrical properties,⁹ presently the most widely used application of EIS is related to studies on 2D cultures of adherent cells as originally proposed by Giæver and Keese.¹⁰ 2-terminal (2T) impedance measurements, where the dielectric properties of cells modulate the interface impedance of electrodes, have been demonstrated to provide information on cell size, morphology, adhesion, spreading, proliferation and death.

In the last decade, there has been an increasing demand for cell culture models to bridge the gap between conventional 2D cultures and tissue engineering to better mimic the *in vivo* environment in terms of physiological and biomechanical behaviour.^{11,12} Cells cultured in a three-dimensional (3D) environment significantly differ in terms of cell–cell and cell–

^aDepartment of Micro- and Nanotechnology, Technical University of Denmark, 2800, Kgs. Lyngby, Denmark. E-mail: jenny.emneus@nanotech.dtu.dk

^bDepartment of Physics, University of Oslo, Sem Sælands vei 24, Fysikkbygningen, 0371 Oslo, Norway

^cDepartment of Biomedical and Clinical Engineering, Oslo University Hospital, 0372 Oslo, Norway

†Electronic supplementary information (ESI) available. See DOI: 10.1039/c5an00987a

matrix interactions from those grown in conventional 2D cultures. They acquire an *in vivo*-like morphology that better reflects the mechanisms of proliferation, survival, differentiation and migration.¹³ Such dynamics may be difficult to monitor using conventional microscopy techniques due to difficulties with light penetration and scattering effects in thick scaffolds. A promising tool in this regards is EIS detection, which has been demonstrated for monitoring thin 3D cultures.¹⁴ However, when increasing the dimensions of the 3D matrix towards the requirements of tissue engineering, the developed sensing method has to provide sufficient spatial resolution for mapping cell distribution. We have recently demonstrated EIS detection in large 3D cell cultures using complementary 2T- and 3T measurements to collect spatially distributed information within the 3D space.⁶

Further development of EIS monitoring in large scaffolds relevant for tissue engineering is, however, necessary to improve the achieved spatial resolution. Inspiration can be found in physiological impedance measurements on tissues and organs, usually defined as bioimpedance.¹⁵ These measurements give an insight into the composition, *i.e.* density and integrity, of tissues and organs, correlating the results to pathophysiological processes. More recently, electrical impedance tomography (EIT) has emerged as a suitable technique for imaging organs, *e.g.*, brain and breast, as well as their activity, *e.g.*, lung ventilation and gastric emptying.¹⁶ In EIT, four-terminal (4T) impedance measurements are commonly employed to minimise errors due to electrode interface impedance (*e.g.* polarisation impedance, Z_p)^{17,18} and to maximise the reciprocity of the measurement method.^{19,20} Two separate electrode couples are used as current carrying (CC) and voltage pick-up (PU) electrodes. The measured impedance is the transfer impedance,²¹ *i.e.* a part of the excitation signal carried by the CC couple is transferred to the PU couple depending on the material properties and composition. Modern instrumentation, having high input impedance, allows measurements in which the PU electrodes are not current carrying, eliminating the contribution of the PU electrode interfaces to the measured impedance.^{6,22,23} Moreover, the application of an independent CC couple facilitates measurements without the sensitivity field (S) being influenced by the interface impedance of the CC couple.

In this work, we present the characterisation and validation of an impedance-based method using multiplexed 4T impedance measurements for sensing the distribution of cell aggregates within large 3D gelatin scaffolds. An array of four rectangular measurement chambers, each chamber comprising eight platinum (Pt) needle electrodes positioned along the perimeter, was used for parallel analysis. Using different combinations of electrodes (modes) as the CC and PU couple, we demonstrate the potential of using multiplexed 4T measurements to gather information on the spatial distribution of cell aggregates within a 3D environment. Finite element (FE) simulations were used to study the influence of electrode positioning within the measurement chamber and the resulting sensitivity field (S).^{22,24} The approach was first validated using

cylindrical metal and plastic test objects (phantoms) of varying dimensions placed in different positions to find the detection limit (volume sensitivity), *i.e.* the smallest detectable volume with respect to the measurement chamber size, and a common frequency for the eight sensing modes to facilitate quick single frequency analysis. Artificial cylindrical 3D cell constructs, composed of a high density of human hepatoblastoma (HepG2) cells encapsulated in gelatin, were then introduced in different positions inside a larger gelatin scaffold in each measurement chamber. The presented 4T impedance sensing provides information on the spatial position of the constructs within biologically relevant 3D environments, opening new possibilities for non-invasive 3D monitoring in tissue engineering applications.

2. Experimental

2.1. FE simulation of sensitivity field (S) distribution

FE simulations were carried out using Comsol Multiphysics v.4.4 to map the sensitivity field (S) distribution for different combinations of current carrying (CC) and voltage pick-up (PU) electrodes placed within the measurement chamber. ESI S1,† provides details of different electrode configurations used in EIS (2T, 3T, 4T) and the technique for calculating S .²⁵ Regions of positive/(negative) sensitivity are defined where the measured impedance increases/(decreases) with an increase in the actual impedance of the sample.²⁶ It is relevant to point out that S does not quantitatively reflect what is experimentally measured, but it expresses how much weight the local impedance in a specific 3D sub-volume has on the total measured impedance.²⁵ Computational models were built to maximise regions of positive sensitivity, assuming the chamber was filled with a commercial conductivity standard solution with a conductivity close to that of physiological solutions ($\sigma = 1.3 \text{ S m}^{-1}$ and $\epsilon_r = 80$). The mesh consisted of 153 891 tetrahedral elements with an average element quality of 0.672. Eight different combinations of electrode pairs were optimised (Fig. 1Aa–h) to focus on the sensitivity field distribution in specific sub-volumes within the whole measurement chamber volume (Fig. 1Ba–h). A potential of 10 mV was applied. Electrical insulation was applied to the chamber walls. S was computed as $S = J_{\text{PU}}/J_{\text{CC}} [\text{m}^{-4}]$, where J_{PU} is the current density vector for the PU couple and J_{CC} is the current density for the CC couple.²⁵ ESI S2 and S3† show simulations of different (i) chamber geometries, (ii) electrode distances and (iii) phantoms (made of stainless steel and acrylic plastic) to assess the suitability of the method for sensing samples with a wide range of electric properties.

2.2. Design and fabrication of the measurement chamber array

An array of four chambers (dimensions: $16 \times 19 \times 10 \text{ mm}^3$) for parallel analysis was micromilled from a polycarbonate substrate having a thickness of 15 mm (Fig. 2). Within each chamber, eight cylindrical holes ($\varnothing 1.1 \text{ mm}$, 2 mm deep) were

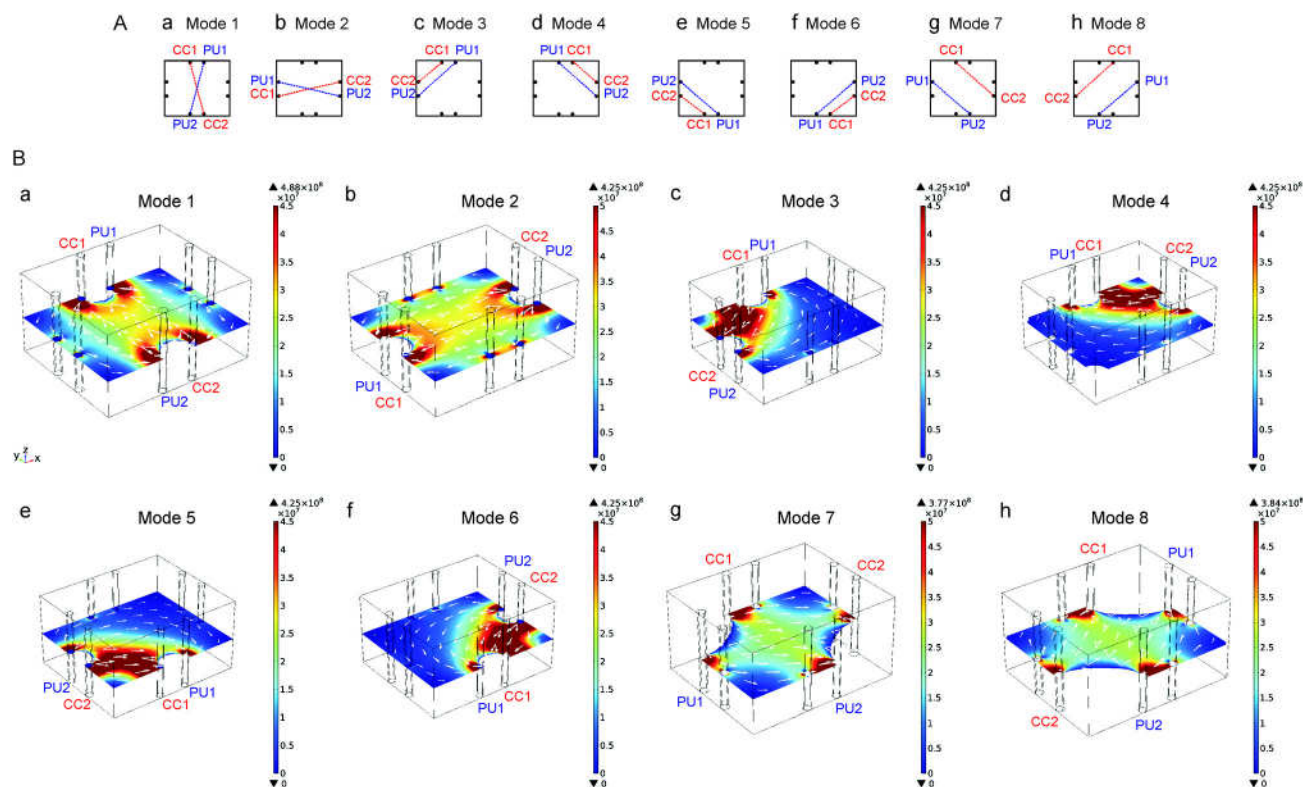


Fig. 1 (A) Schematics of the eight optimised 4T configurations (modes 1–8). CC1 and CC2 form the current-carrying electrode couple and PU1 and PU2 form the voltage pick-up couple. Red and blue dashed lines represent the directions of CC and PU electric fields, respectively. (B) FE simulations for S [m^{-4}] distribution (slice view): mode 1 (a), mode 2 (b), mode 3 (c), mode 4 (d), mode 5 (e), mode 6 (f), mode 8 (h). White areas in the horizontal cross-sections are associated with negative sensitivity.

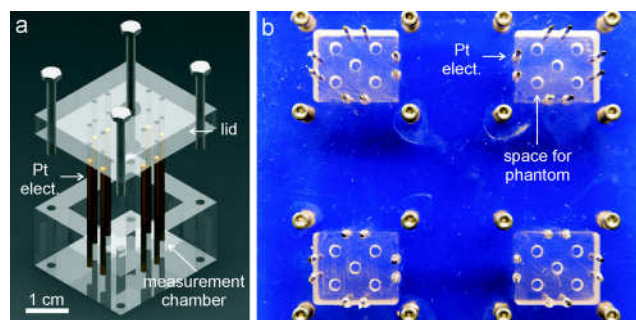


Fig. 2 (a) The measurement chamber design. (b) Photo of the measurement chamber, showing electrode position and openings for phantoms.

drilled along the periphery of the measurement chamber for holding the Pt electrodes (\varnothing 1 mm) in place. The electrode positioning was determined based on the results of the FE simulation. Pt was chosen as it has been demonstrated to be a suitable biocompatible material for AC applications.²⁷ Electrodes were located in couples, 4 mm apart from each other on each perpendicular side of the chamber (Fig. 2a). A lid for the measurement chamber was fabricated using 5 mm thick polycarbonate with holes in different positions (Fig. 2b) for place-

ment of (i) electrodes and (ii) cylindrical phantoms having different diameters (2, 3, 4, 5, 6, 8 mm). Crocodile clips were used for contacting the electrodes to the impedance analyser. Prior to each experiment, the Pt electrodes were cleaned for 10 min in acetone followed by rinsing with Milli-Q water (Millipore Corporation, Billerica, MA, USA) and potential cycling in 0.1 M H_2SO_4 (-0.4 to 1.7 V vs. Ag/AgCl (3 M KCl); approximately 40 cycles at a scan rate of 200 mV s^{-1}).

2.3. Phantom experiments

The eight simulated modes of 4T configuration were validated with phantom experiments using stainless steel and plastic cylinders of increasing dimensions (\varnothing 2–8 mm) placed in different positions (centre and four corners, Fig. 2b) inside the measurement chambers filled with conductivity standard solution (1.3 S m^{-1} Hanna Instruments, cat. 663-5047). A 10 mVAC potential was applied in the frequency range between 1 kHz and 1 MHz using an impedance analyser SI1260 and a SI1294 impedance interface (Solartron Instruments, Hampshire, UK). For all phantom experiments, characterisation data are presented as an average of three individual experiments in each chamber using fresh solution and rinsing the phantom with Milli-Q water prior to each experiment (average \pm s.e.m., $n = 12$).

2.4. Spatial sensing of artificial 3D cell constructs

Prior to impedance measurements, the chambers were sterilised with 70% ethanol for 20 min and allowed to dry in a laminar flow bench. Artificial 3D cell constructs (\varnothing 4.6 mm and height 10 mm) were prepared by encapsulating 10^7 HepG2 cells (American Type Culture Collection, Rockville, MD, USA) in 5% w/v gelatin (48723 Fluka). 12.5% (w/v) gelatin stocks were dissolved in serum-free cell culture medium (Roswell Park Memorial Institute RPMI 1640). The gel was covalently cross-linked using microbial transglutaminase (Activa® RM, Ajinomoto) dissolved in RPMI 1640 containing 10% fetal bovine serum and 1% penicillin/streptomycin. Cells were directly mixed with liquid gelatin and cast in a cylindrical mould with a piston for cylinder extrusion after curing (4 hours at 37 °C in a humidified 5% CO₂ incubator). Measurements were performed placing a cylindrical artificial 3D cell construct in two different positions inside the chamber (centre or top left corner), and 2 mL of 5% (w/v) gelatin was cast around and let polymerise for 2 hours. After gelatin polymerisation, the chamber was filled with cell culture medium. EIS spectra were acquired before and after medium addition, as described in Section 2.3. Data for artificial 3D cell constructs were compared with plain 5% (w/v) gelatin cylinders surrounded by 2 mL of 5% w/v gelatin. Measurements were performed in three independent experiments using a different cylinder and filling gelatin (each position tested in duplicate). Data are presented as average \pm s.e.m., $n = 6$. Control experiments comprised measurements on 5% (w/v) bulk gelatin scaffolds without any added gelatin cylinder. 21 individual experiments were performed (average \pm s.e.m., $n = 21$) using 5% (w/v) bulk gelatin scaffold (three different stock solutions) filling the same volume as in the presence of a gelatin cylinder ($16 \times 19 \times 6.6$ mm³).

3. Results and discussion

3.1. FE simulation of S distribution

Martinsen and Grimnes previously illustrated the significance of electrode configuration for impedance measurements focusing on a sub-volume in a physiological 3D sample.²¹ In this study, we optimised eight different modes of 4T configuration (Fig. 1A) for spatial sensing in a 3D environment. The electrode distance was evaluated with respect to the measurement chamber size (ESI S2†). To design configurations that individually focus on specific sub-volumes inside the chamber and cover the entire chamber volume (Fig. 1), sites for current injection and voltage measurement were established by minimising negative sensitivity zones. Based on FE simulations, modes 1 and 2 (Fig. 1Ba,b) are expected to have a sensitivity covering the entire chamber volume, however, mainly focusing on the centre. Mode 2, associated with longer current path, results in a higher simulated impedance. Modes 3, 4, 5 and 6 (Fig. 1Bc–f) focus on the corners in a symmetrical fashion, therefore, yielding the same impedance for a homogeneous 3D volume. They show very low sensitivity in the centre. Mode 3,

focusing on the top left corner, has $S = 0$ at the bottom right corner. Due to symmetry, all the other modes (4–6) have the maximum S in one corner, whereas $S = 0$ in the opposite corner (diagonally). Modes 7 and 8 (Fig. 1Bg,h) show symmetrical diagonal current paths through the centre of the chamber, with lower S with respect to modes 1 and 2. They also slightly sense two diagonally located corners and have large zones of negative sensitivity in the two other corners. The eight configurations were further evaluated based on FE simulation of a metal and plastic object (phantom) inside the chamber (ESI S3†). Results indicate that each mode individually provides S focusing on a specific sub-volume and that they provide information regarding the position of an object in the chamber through the distribution of relative impedance changes in the whole 3D volume.

3.2. Phantom experiments

Phantom experiments were used to verify FE simulations and determine the limit of detection for the sensing method. In impedance measurements, a metal phantom, having a higher conductivity than the surrounding electrolyte medium, decreases the measured impedance in comparison with measurements on the same solution without a phantom. In the case of a nonconductive phantom (plastic object), the effect is the opposite.²⁸ This applies to measurements when the phantom is placed in a zone of positive S (Fig. 1B). Fig. 3 and 4 show the impedance spectra obtained when using metal and plastic phantoms of increasing diameter, respectively, placed in the centre of the measurement chamber. The same analysis was performed for 4 mm diameter phantoms placed in the corners of the chamber. All the experimental results are summarised in ESI S4.†

Fig. 3a,b and 4a,b show acquired spectra for modes 1 and 2, respectively, in the presence of a metal or plastic phantom with increasing diameter placed in the centre of the chamber. Corresponding spectra for modes 3 and 7 are shown in Fig. 3c, d and 4c,d. A phantom placed in the centre of the chamber is primarily sensed with modes 1, 2 and 7, which focus on the entire volume, whereas mode 3 only slightly senses the presence of the phantom. On virtue of symmetry, modes 4–6 (Table S4†) show exactly the same behaviour as mode 3. Since mode 3 has weak sensitivity for the centre, the spectrum for the 2 mm metal phantom (Fig. 3c) fully overlaps with that of the blank. In the case of plastic phantoms, the spectrum for 2 mm phantom is below the impedance level of the blank, while that for the 3 mm phantom overlaps with the spectrum of the blank. From Fig. 3 and 4, it can be concluded that our method has the limit of detection of 4 mm in terms of object dimension regardless of material properties. This corresponds to 16.5% of the total volume in the centre of the chamber. This applies also to phantoms placed in the measurement chamber corners (Table S4†).

For all modes, the spectra acquired for the different metal phantoms show good discrimination in terms of phantom diameter in the frequency range 100–300 kHz, with mode 2 giving the highest impedance. For plastic phantoms, the impedance

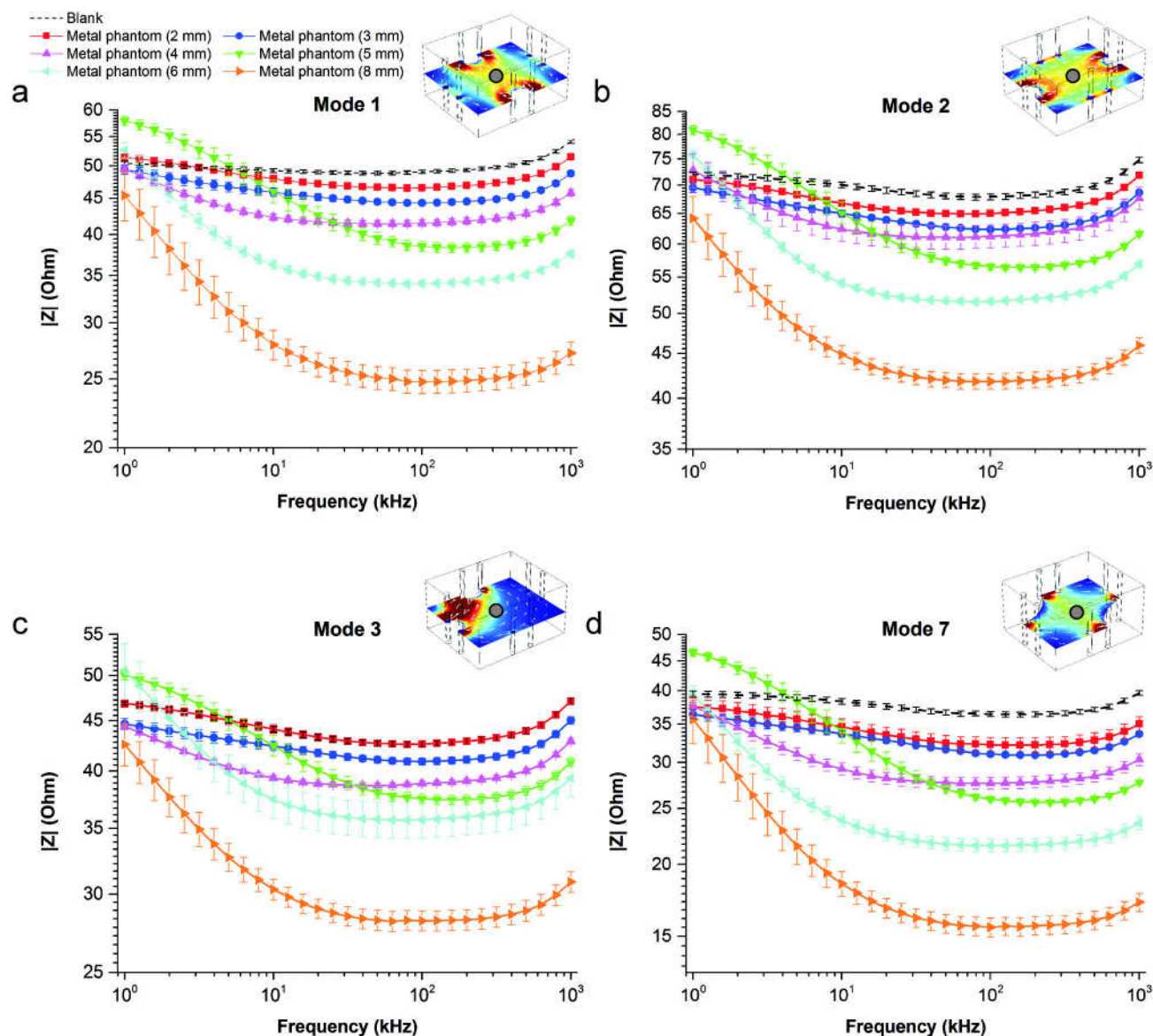


Fig. 3 Characterisation using a metal phantom of increasing diameter (2–8 mm) placed in the centre of the measurement chamber (indicated by a grey dot) filled with conductivity standard solution: (a) mode 1, (b) mode 2, (c) mode 3, (d) mode 7. Data are compared with spectra for the same solution (blank) and reported as average \pm s.e.m., $n = 12$.

magnitude of the spectra acquired for the different modes remains more constant through a wider frequency range. For general analysis of the spectra, 250 kHz is a suitable frequency when comparing the behaviour of different objects in the chambers. This choice of frequency has also the advantage that it is low enough not to be significantly affected by parasitics that appear at higher frequencies (above 300 kHz).

For a phantom placed in one of the chamber corners, all the modes show good discrimination at this frequency and summarised in Table S4, ESI S4.† Modes 3–6 show the highest S for a phantom placed in the corner where the mode has specific focus according to the FE simulation (Fig. 1Bc–f), with the S being lowest in the

opposite corner (diagonally). Modes 1 and 2 do not show any discrimination of phantoms placed in the corners due to their specific focus on the centre of the measurement chamber. Modes 7 and 8 have two diagonal corners where the presence of the phantom can be weakly sensed. However, the spectra acquired for a phantom in either of those corners are overlapping and cannot be discriminated, as expected from the FE analysis (Fig. 1Bg,h). In the two other corners, the presence of the phantom cannot be sensed due to the large zones of negative sensitivity. This represents a situation where the phantom is partially located in the zone of negative and positive sensitivity (depending on its size) which makes it difficult to distinguish the spectra for the phantoms from that of the blank.

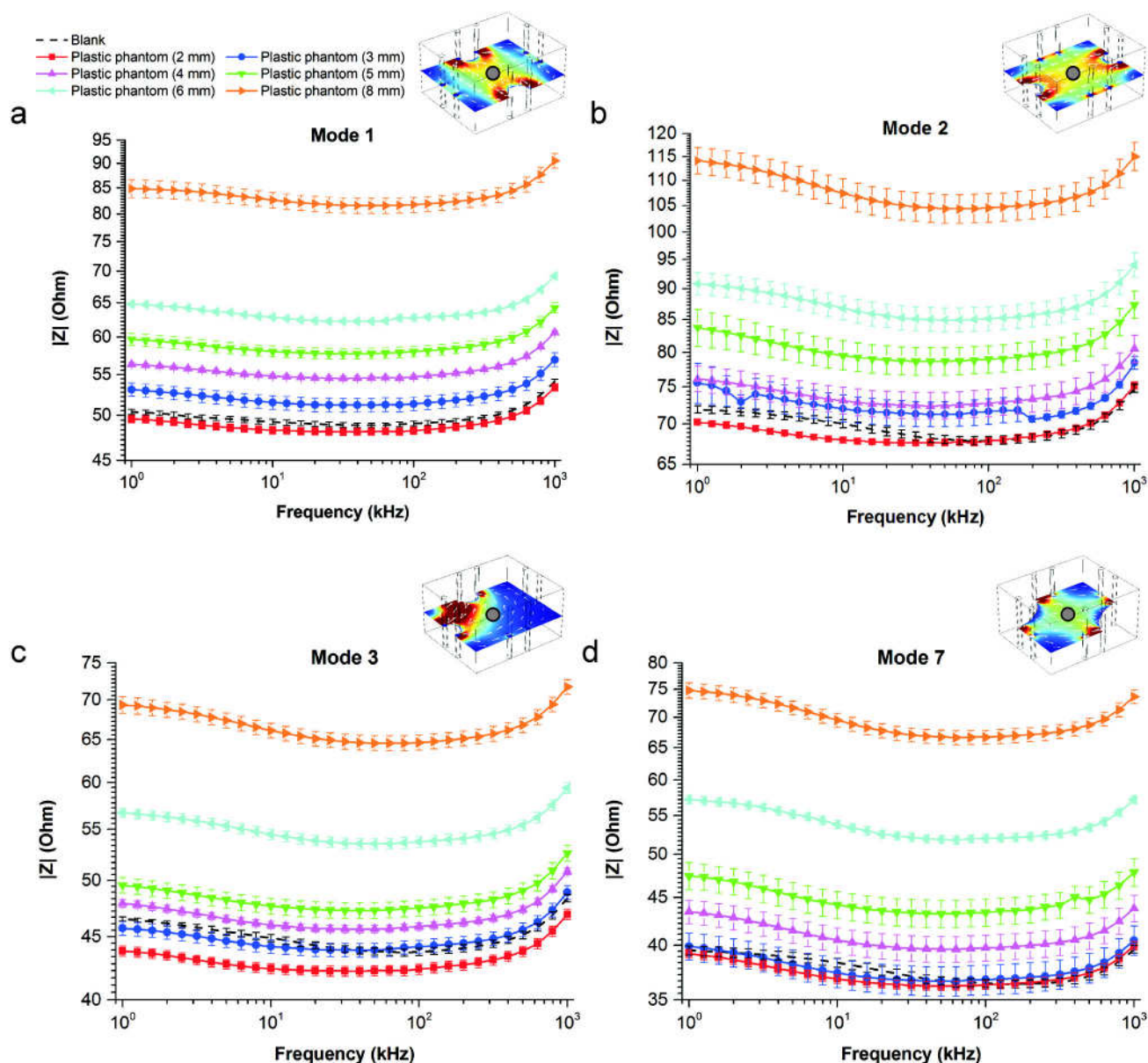


Fig. 4 Characterisation using a plastic phantom of increasing diameter (2–8 mm) placed in the centre of the measurement chamber (indicated by a grey dot) filled with conductivity standard solution: (a) mode 1, (b) mode 2, (c) mode 3, (d) mode 7. Data are compared with spectra for the same solution (blank) and reported as average \pm s.e.m., $n = 12$.

As expected, by increasing the phantom diameter, the absolute variation in measured impedance increased for all eight modes.

3.3. Spatial sensing of artificial 3D cell constructs

The sensing method was further validated with artificial 3D cell constructs using 5% (w/v) gelatin cylinders, embedding high density of HepG2 cells to mimic a biological tissue placed in the centre and at the top left corner of a large 5% (w/v) bulk gelatin scaffold. The Young's modulus of these enzymatically cross-linked gelatin constructs is approximately 3.6 kPa (data

not shown), which is within the stiffness range for soft tissues, such as liver.^{6,29,30}

The variability between different bulk gelatin scaffolds was assessed for impedance measurements with the eight different modes after medium addition on top (ESI S5†). The s.e.m. were in all cases one order of magnitude lower than the averaged impedance values at 250 kHz (Table S5†), indicating the good reproducibility of our method. This also demonstrates that there is low variability between different gelatin stocks and different 5% (w/v) bulk gelatin scaffolds. Since modes that focus on the chamber corners show current paths having the same length, they are expected to give the same impedance

value if the bulk gelatin scaffold is homogeneously distributed in the 3D space, with a smooth top surface. However, we found that the measured impedances were similar for corners on the same side, *i.e.* the impedance associated to the top left corner (mode 3, $43 \pm 3 \Omega$) was similar to the one measured for the bottom left corner (mode 5, $44 \pm 3 \Omega$) and the impedance for the top right corner (mode 4, $58 \pm 5 \Omega$) was similar to the one for the bottom right corner (mode 6, $56 \pm 5 \Omega$). This is probably due to the fact that the measurement chambers were always slightly tilted in the incubator, with slightly more medium

covering the left side of each scaffold. Hence, the higher conductivity of cell culture medium^{31,32} above the gelatin provides an additional current path bypassing the gelatin, which decreases the measured overall impedance. Modes 7 and 8, focusing primarily on the chamber centre and slightly on diagonal corners, showed similar values of impedance (37 ± 3 and $40 \pm 3 \Omega$, respectively).

Fig. 5 shows spatial characterisation using a plain gelatin cylinder placed at the top left corner and in the centre of the bulk gelatin scaffold (Fig. S6.1†). Based on the results reported

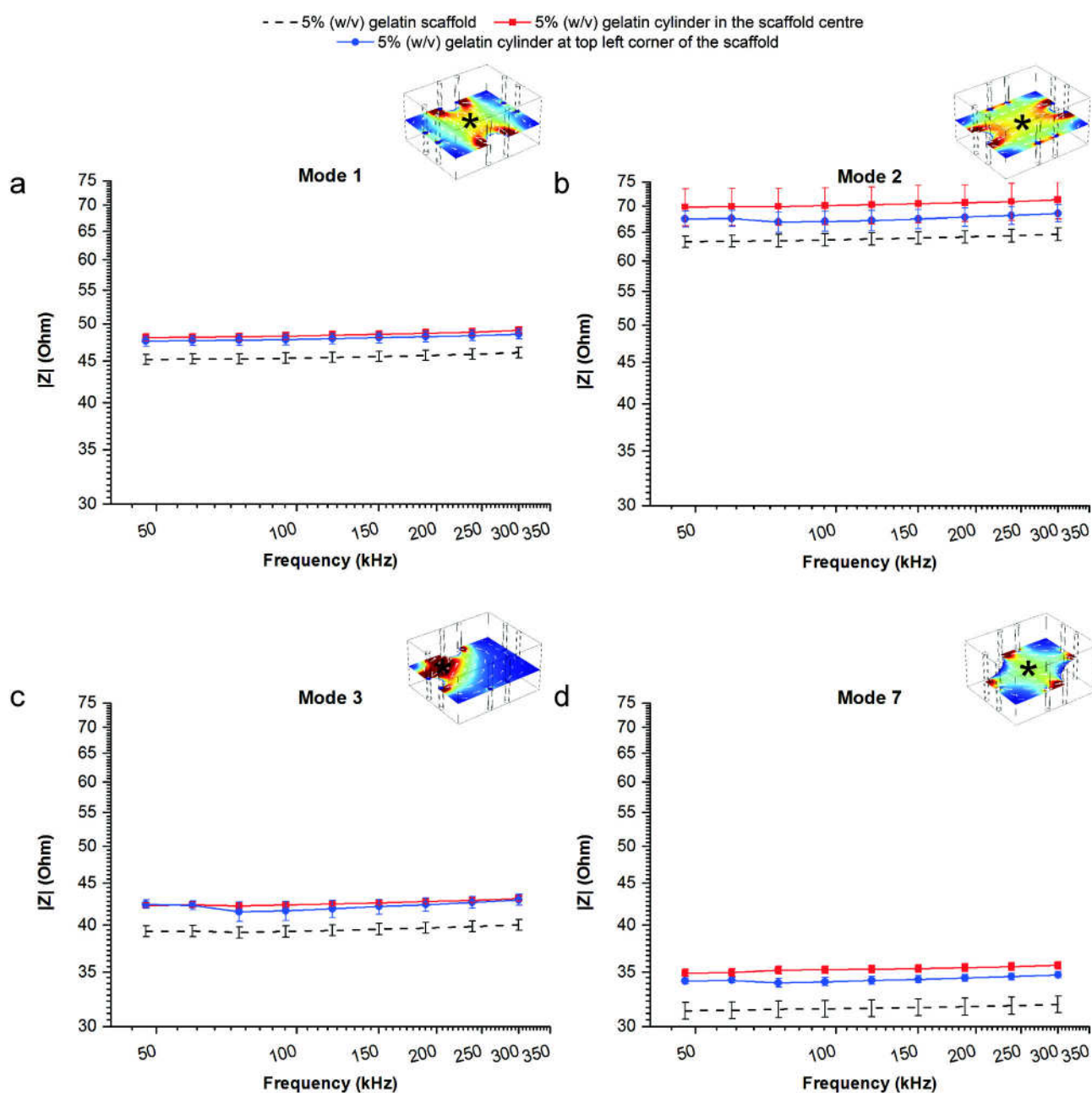


Fig. 5 Sensing of a 5% (w/v) gelatin cylinder embedded in bulk gelatin scaffold and placed either at the top left corner or in the centre: (a) mode 1, (b) mode 2, (c) mode 3, (d) mode 7. Data are compared with 5% (w/v) bulk gelatin scaffold (average \pm s.e.m., $n = 21$) and reported as average \pm s.e.m., $n = 6$. Other modes are shown in Fig. S6.2.† The position of the main focus of each mode is indicated by an asterisk.

above, measurements were taken after addition of medium on top of the scaffold and the most significant frequency range up to 300 kHz is shown. As expected, the sensing method cannot discriminate between cylinder positions since both cylinder and scaffold are made of the same biomaterial. However, disregarding the measurement mode, the impedance for scaffolds with embedded cylinders is always higher than for bulk gelatin scaffolds. This may be related to surface inhomogeneities originating when casting gelatin around the

cylinder or to the possibility that the cylinder becomes slightly more solidified than the bulk gelatin scaffold when this latter is solidifying in the chamber. None of the sensing modes shows any significant difference between the two tested positions (centre and top left corner). However, what was illustrated in the previous paragraphs for metal and plastic phantoms also applies for gelatin cylinders. Mode 1 (Fig. 5a) resulted in lower impedance than mode 2 (Fig. 5b) due to its shorter current path, while modes 7 (Fig. 5d) and 8

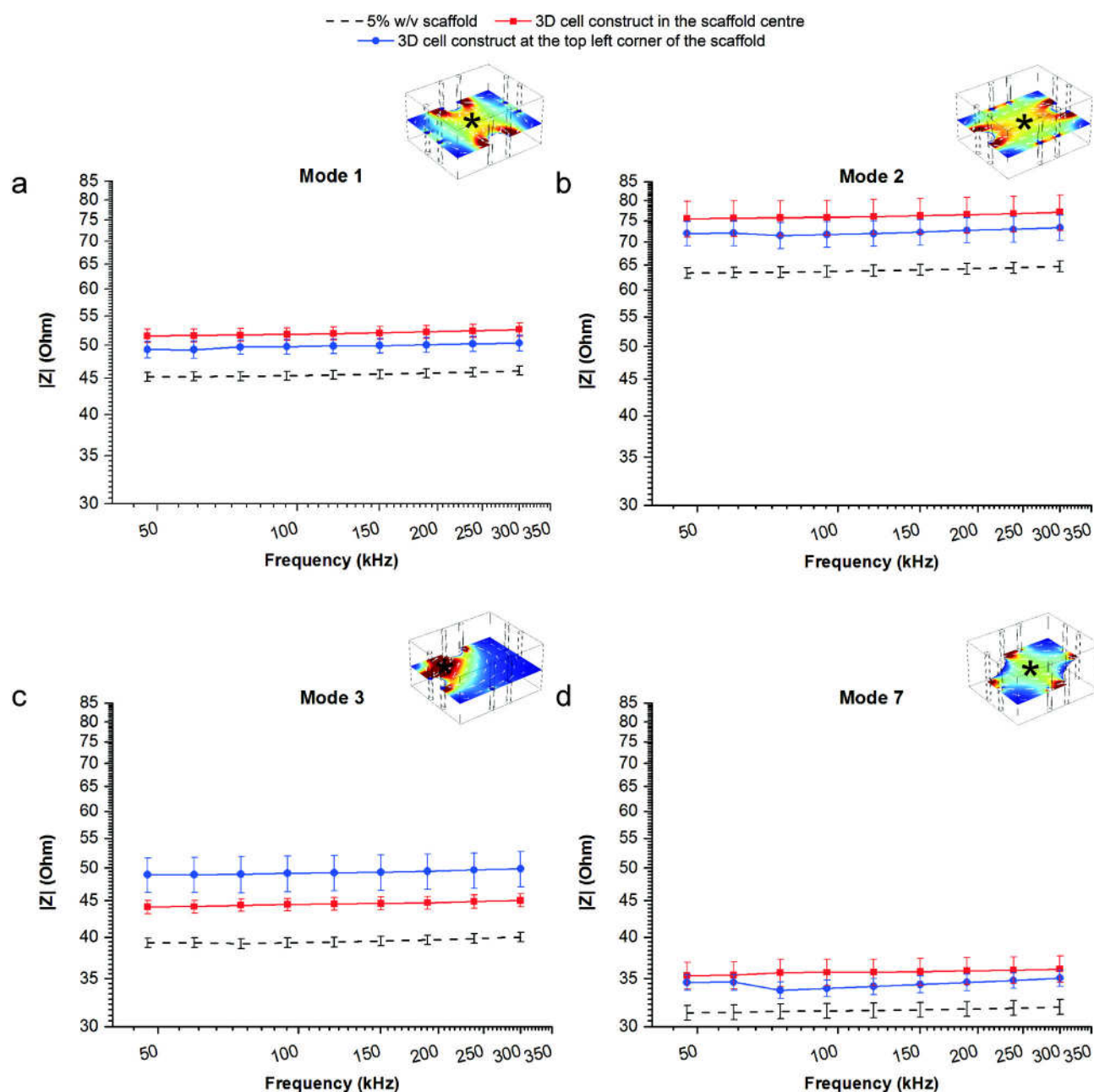


Fig. 6 Sensing of a 5% (w/v) gelatin cylinder containing 10^7 HepG2 cells as artificial 3D cell construct embedded in bulk gelatin scaffold and placed either at the top left corner or in the centre. Mode 1 (a), mode 2 (b), mode 3 (c), mode 7 (d). Data are compared with 5% (w/v) bulk gelatin scaffold (average \pm s.e.m., $n = 21$) and reported as average \pm s.e.m., $n = 6$. Other modes are shown in Fig. S6.3.† The position of the main focus of each mode is indicated by an asterisk.

(Fig. S6.2d†) resulted in similar impedance values as they have equal and symmetrical current paths. Due to the symmetrical current paths, the sensing modes focusing on the corners (mode 3: Fig. 5c; modes 4–6: Fig. S6.2a–c†) gave similar impedance values for a gelatin cylinder in the centre of the measurement chamber. Moreover, since the used gelatin cylinders and the surrounding scaffold had the same material composition, mode 3 did not show any difference in comparison with modes 4–6 when a gelatin cylinder was placed in the top left corner.

Fig. 6 and S6.3† show corresponding data for the artificial cylindrical 3D cell constructs placed at the top left corner and in the centre. For each sensing mode, the 3D cell constructs showed higher impedance in comparison with the plain gelatin cylinders (control, Fig. 5 and S6.2†). As expected, modes 1 and 2 (Fig. 6a and b) showed higher impedance when the cylinder was placed in the centre and lower impedance when it was placed in the top left corner. The same applies to modes 7 (Fig. 6d) and 8 (Fig. S6.3d†). The key validation of the sensing method was given by mode 3 (Fig. 6c), resulting in higher impedance when the 3D cell construct was placed at the top left corner (*i.e.* the position where it was shown to have the highest S). The spectrum for the top left corner is clearly separated from the one representing the centre, where mode 3 has a very low S . Mode 6 (Fig. S6.3c†), which has $S = 0$ at the top left corner, gives a further validation. In this case, the impedance magnitude of the spectra is considerably higher when the 3D cell construct was placed in the centre compared to the top left corner. Modes 4 and 5 (Fig. S6.3a,b†) showed a similar behaviour disregarding the position of the 3D cell construct.

The s.e.m. for all the acquired spectra in relation to the different modes and positions of the gelatin cylinders (with and without cells) were of the same order of magnitude and slightly below 10%. However, the s.e.m. for the plain gelatin cylinders is slightly lower, which can be explained by the fact that the presence of cells increases the inhomogeneity of the cylinders. The appearing differences in s.e.m. between the different modes may be derived from minor variations in electrode positioning which causes deviation from perfect symmetry. Additionally, repeated experiments using the same recleaned and reassembled electrodes in the measurement chambers may affect the electrode shape, therefore also contributing to differences between experiments.

The presented method allows addressing the detection of different sample sub-volumes in a biologically relevant 3D environment. Such method responds to the spatial distribution of cell aggregates in a biocompatible scaffold for tissue engineering. The simulation of the sensitivity field distribution related to each sensing mode provides qualitative information that describes its focus on a specific 3D sub-volume and its weight on the total measured impedance. Hence, the measured impedance using the different sensing modes can be applied in tissue engineering applications to obtain insight about proliferation and accumulation of cells in specific sub-volumes of a large 3D scaffold. This may be also applied for

scaffold characterisation in terms of structural features (*e.g.* channels mimicking vascularisation) and potentially used for co-cultures of different cell types.

4. Conclusions

Several electrode combinations (sensing modes) can be used for multiplexed 4-terminal (4T) impedance sensing to provide spatial information of objects placed in a biologically relevant 3D environment, which is compatible with tissue engineering applications. The results presented here demonstrate the potential and suitability of our impedance-based sensing method for future monitoring of tissue engineering processes, such as the formation of bioartificial organs. Our method is a first step towards miniaturisation of impedance detection to enable on-line monitoring with 3D spatial resolution and, provides the fundamental basis for reconstruction of images related to cell distribution in a 3D environment using several multiplexed measurements.

Acknowledgements

This study and the Ph.D. fellowship of C. Canali were financially supported by the EU-funded project NanoBio4Trans (grant no. 304842).

References

- 1 Y. Huang, X. Wang, F. F. Becker and P. R. C. Gascoyne, *Biophys. J.*, 1997, **73**, 1118–1129.
- 2 R. Pethig and D. B. Kell, *Phys. Med. Biol.*, 1987, **32**, 933–970.
- 3 H. P. Schwan and S. Takashima, *Bull. Inst. Chem. Res. Kyoto Univ.*, 1991, **69**, 459–475.
- 4 J. P. Frampton, M. R. Hynd, J. C. Williams, M. L. Shuler and W. Shain, *J. Neural Eng.*, 2007, **4**, 399–409.
- 5 C. Hildebrandt, H. Büth, S. Cho, Impidjati and H. Thielecke, *J. Biotechnol.*, 2010, **148**, 83–90.
- 6 C. Canali, A. Heiskanen, H. B. Muhammad, P. Høyum, F.-J. Pettersen, M. Hemmingsen, A. Wolff, M. Dufva, Ø. G. Martinsen and J. Emnéus, *Biosens. Bioelectron.*, 2015, **63**, 72–79.
- 7 C. Canali, S. Mohanty, A. Heiskanen, H. B. Muhammad, Ø. G. Martinsen, M. Dufva, A. Wolff and J. Emnéus, *Electroanalysis*, 2015, **27**, 193–199.
- 8 H.-G. Jahnke, A. Heimann, R. Azendorf, K. Mpoukouvalas, O. Kempfski, A. a Robitzki and P. Charalampaki, *Biosens. Bioelectron.*, 2013, **46**, 8–14.
- 9 H. P. Schwan, *Adv. Biol. Med. Phys.*, 1957, **5**, 147–209.
- 10 I. Giaever and C. R. Keese, *Proc. Natl. Acad. Sci. U. S. A.*, 1984, **81**, 3761–3764.
- 11 A. M. Greiner, B. Richter and M. Bastmeyer, *Macromol. Biosci.*, 2012, **12**, 1301–1314.
- 12 C. Moll, J. Reboredo, T. Schwarz, A. Appelt, S. Schürlein, H. Walles and S. Nietzer, *J. Vis. Exp. JoVE*, 2013, 2–7.

- 13 B. M. Baker and C. S. Chen, *J. Cell Sci.*, 2012, **125**, 3015–3024.
- 14 K. F. Lei, M.-H. Wu, C.-W. Hsu and Y.-D. Chen, *Biosens. Bioelectron.*, 2014, **51**, 16–21.
- 15 D. Holder, in *Electrical impedance tomography*, IOP Publishing, London, UK, 1st edn, 2005, pp. 411–422.
- 16 D. Holder, in *Electrical impedance tomography*, IOP Publishing, London, UK, 1st edn, 2005, pp. 423–449.
- 17 P. Kauppinen, J. Hyttinen and J. Malmivuo, *Int. J. Bioelectromagn.*, 2006, **7**, 344–347.
- 18 A. McEwan, G. Cusick and D. S. Holder, *Physiol. Meas.*, 2007, **28**, S197–S215.
- 19 D. B. Geselowitz, *IEEE Trans. Biomed. Eng.*, 1971, **BME-18**, 38–41.
- 20 J. Malmivuo, *J. Phys. Conf. Ser.*, 2010, **224**, 012001.
- 21 Ø. G. Martinsen and S. Grimnes, in *Bioimpedance and Bioelectricity Basics*, ed. Ø. G. Martinsen and S. Grimnes, Academic Press, 2nd edn, 2008, pp. 127–152.
- 22 S. Grimnes and Ø. G. Martinsen, *J. Phys. D: Appl. Phys.*, 2007, **40**, 9–14.
- 23 H. P. Schwan, *Ann. N. Y. Acad. Sci.*, 1968, **148**, 191–209.
- 24 B. H. Brown, A. J. Wilson and P. Bertemes-Filho, *Electron. Lett.*, 2000, **36**, 5–6.
- 25 F.-J. Pettersen and J. O. Høgetveit, *J. Electr. Bioimpedance*, 2011, **2**, 13–32.
- 26 Ø. G. Martinsen and S. Grimnes, in *International Federation for Medical and Biological Engineering*, 2009, pp. 1078–1079.
- 27 H. P. Schwan, *Biophysik*, 1966, **3**, 181–201.
- 28 S. Grimnes and Ø. G. Martinsen, *Encycl. Biomed. Eng.*, 2006, 1–9.
- 29 P. a Janmey and R. T. Miller, *J. Cell Sci.*, 2011, **124**, 9–18.
- 30 G. C. Reilly and A. J. Engler, *J. Biomech.*, 2010, **43**, 55–62.
- 31 H. Hsu, A. T. Ohta, P.-Y. Chiou, A. Jamshidi, S. L. Neale and M. C. Wu, *Lab Chip*, 2010, **10**, 165–172.
- 32 C. Canali, H. B. Muhammad, Ø. G. Martinsen and A. Heiskanen, *Sens. Actuators, B*, 2015, 544–550.

Supporting Information:

An impedance method for spatial sensing of 3D cell constructs – towards applications in tissue engineering

Chiara Canali et al.

Content:

- S1:** Theory – Electrode configurations in bioimpedance measurements
- S2:** FE simulation of alternative measurement chamber size and electrode distance
- S3:** FE simulation of metal and plastic phantoms
- S4:** Summary of phantom experiments
- S5:** Bioimpedance sensing of 5% (w/v) bulk gelatin scaffolds
- S6:** Bioimpedance sensing of 5% (w/v) gelatin cylinders and artificial 3D cell constructs
 - S6A)** Gelatin cylinders without cells
 - S6B)** Artificial 3D cell constructs

Section S1. Theory – Electrode configurations in bioimpedance measurements

The sensitivity field in bioimpedance measurements depends on several parameters, such as electrode number, geometry, orientation and spacing. Moreover, one crucial element to carefully consider is the used configuration between electrode couples (current carrying, CC, and voltage pick-up, PU). Two, three, four terminal (T) configurations may be used and they are illustrated in Fig. S1.1.

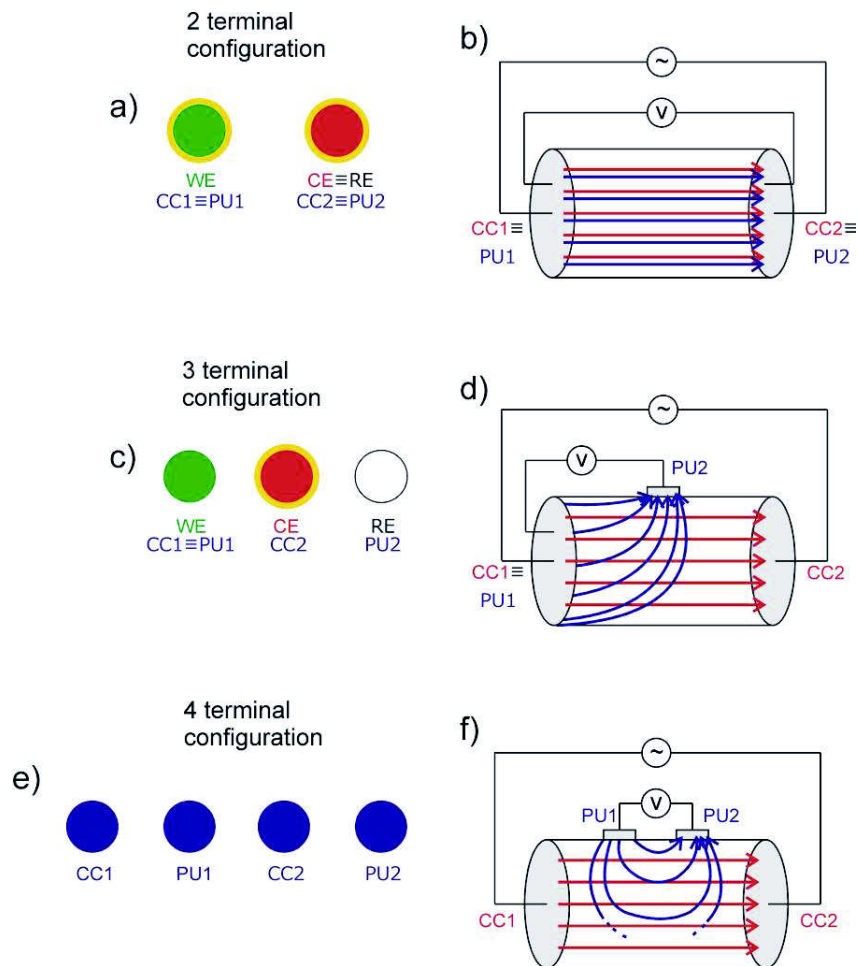


Fig. S1.1. Schematics of 2T (a), 3T (c) and 4T (e) configurations and their respective sensitivity fields (b, d, f) for a generic cylindrical conductor. In electrochemical analysis WE (green) is the working electrode, CE (red) is the counter electrode, RE (white) is the reference electrode. In bioimpedance measurements CC1 and CC2 form the current-carrying couple; PU1 and PU2 form the voltage pick-up couple. Polarisation impedance (Z_p) at the electrode surface is reported in yellow, if present (a, c, e). For the representation of the sensitivity fields (b, d, f), red and blue arrows refer to the direction of CC and PU electric fields, respectively.

In 2T configuration (Fig. S1.1a, b), the same electrode pair serves both as CC and PU and the measured impedance typically includes the polarisation impedance (Z_p) at both electrodes surface (Fig. S1a). Both CC electrodes are into the sensitivity zone for the measurement (Fig. S1b) and, therefore, the measured impedance is affected by their Z_p s (which can be very much greater than the sample impedance itself). The sensitivity field is always positive.

In 3T configuration (Fig. S1.1c, d), one electrode is common between the CC and PU couple (i.e. the counter electrode, CE). In other words, the CE is the only CC electrode which is still into the sensitivity zone for the measurement (Fig. S1.1d) and hence, the measured impedance is affected by its Z_p (which also reflects the sample volume in its close proximity, Fig. S1.1c).

In 4T configuration (Fig. S1.1e, f), two separate couples of CC and PU electrodes are used. This configuration eliminates all Z_p contributions; hence it is typically used for physiological measurements, where a specific focus on the mere properties of the biological sample is needed. In 4T measurements, the CC couple is placed outside the sensitivity zone for the measurement (Fig. S1.1f) and, hence, the measured impedance is not affected by Z_{pCC} . Moreover, with ideal voltage amplifiers (amp), PU electrodes are not current carrying (Fig. S1.2) so that Z_{pPU} does not contribute to the measured impedance as well (Fig. S1.1e). Modern amps have input impedance (Z_{amp}) in the GigaOhm range, meaning that they allow measuring impedance values up to the MegaOhm level without the sensitivity field being influenced by Z_{pCC} . This further explains why, in 4T configuration, the sensing is not influenced by Z_{pCC} even when CC and PU electrodes are close to each other.

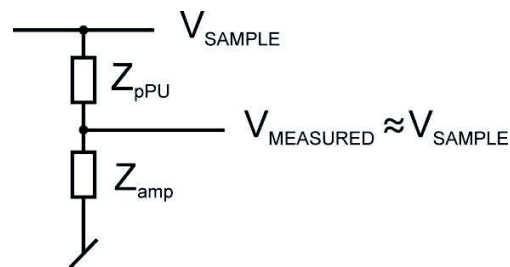


Fig. S1.2. Schematics of a 4T measurement. Using a 4T configuration, the sensing is focused only on the biological sample as the CC couple is placed outside the sensitivity zone for the measurement and the PU couple is not current-carrying. This means that the measured voltage ($V_{MEASURED}$) is approximately the voltage across the sample (V_{SAMPLE}). Z_{pPU} is the polarisation impedance of the PU electrodes and Z_{amp} the input impedance of the voltage amplifier.

In the beginning of impedance spectroscopy analysis it was mistakenly understood that the measured impedance reflects the impedivity (i.e., the property of “actual” impedance) of the sample bounded by the equipotential lines generated by current (or voltage) injection between the CC couple and passing through the PU couple. According to the *reciprocity theorem*, the measured impedance should be the same if the CC and PU couples are swapped. Therefore:

- the measurement sensitivity must be affected with some amount by all small sub-volumes in the sample (each of them displaying its own resistivity);
- small sub-volumes in the sample do not all equally contribute to the measured impedance;
- the measured impedance should be similar close to both electrode pairs;

- sub-volumes between CC and PU couples and close to the electrodes contribute more than sub-volumes far away from the electrodes.

The reciprocity theorem holds for all linear systems, i.e. those systems where the response to a sinusoidal perturbation is sinusoidal as well, with the same frequency of the input, but different amplitude and phase. Given the injected current between the CC couple as input (I) and the measured voltage (E) between the PU couple as output, the impedance (Z) is the *transfer impedance* (or *transimpedance*) which can be approximated as the ratio between E and I :

$$Z \equiv \frac{E}{I} \quad [\Omega]$$

Since Z is a transfer function, it cannot be used for calculating sample properties as conductivity (σ), resistivity (ρ) and relative permittivity (ϵ_r), with the exception of homogeneous and uniform materials.

Resistivity (ρ) is defined as the ratio between the voltage (E) and the current density lines (J), as described by the Ohm's law:

$$\rho = \frac{E}{J} \quad [\Omega \cdot \text{m}]$$

Hence, Z can be written as following:

$$Z = \iiint \rho \cdot \frac{J_{CC} \cdot J_{PU}}{I_{CC} \cdot I_{PU}} dv \quad [\Omega]$$

meaning that the total measured impedance is the sum of all local ρ values from each small sub-volume in the sample.

The sensitivity (S) of an impedance measurement is the scalar value representing the CC current density lines (J_{CC}) projection on the PU current density lines (J_{PU}). S is affected with some amount by all sample sub-volumes and, as previously explained, it does not depend on ρ value:

$$S = \frac{J_{CC} \cdot J_{PU}}{I_{CC} \cdot I_{PU}} \quad [\text{m}^{-4}]$$

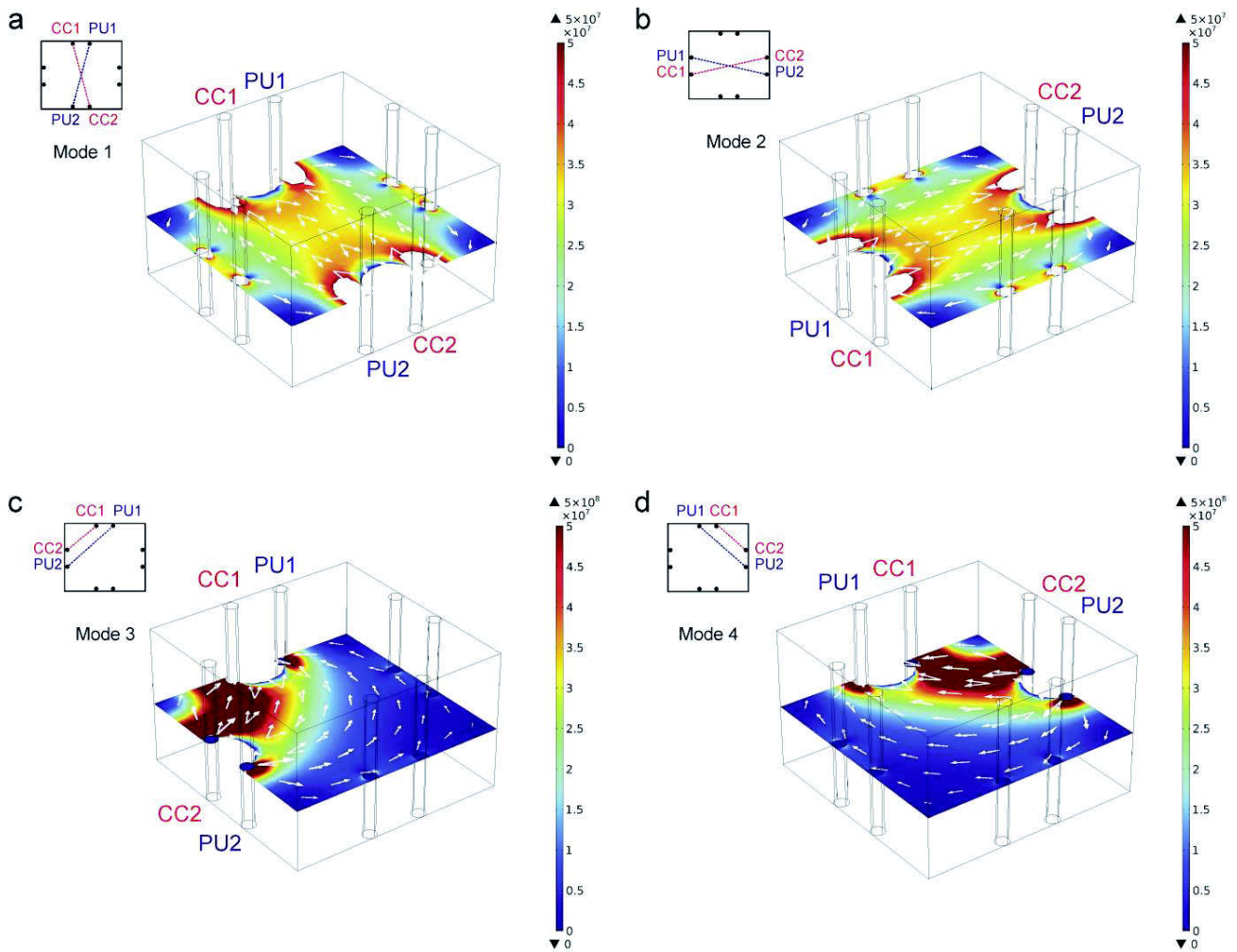
S is a positive (or negative) value if measured impedance increases (or decreases) when the impedivity of that region increases. This may be clearly seen by drawing the current density vectors between the CC and PU couples. If they are:

- in the same direction, S will be positive,
- superimposed, S will be maximum (since $\cos 0 = 1$, as for 2T measurements),
- in the opposite direction, S will be negative,
- in perpendicular direction, S will be 0 (since $\cos 90 = 0$).

By means of finite element (FE) analysis, it is possible to estimate the S value weighted for the resistivity (ρ) contribution of all sub-volumes in the sample, therefore estimating the local contribution of each sub-volume to the measured impedance. This latter is often called "volume impedance density" (VID). VID is the integration of S over the entire sample volume and, accordingly, it corresponds to the expression defining the transimpedance, Z .

Section S2. FE simulation of alternative measurement chamber size and electrode distance

Using the rectangular geometry showed in the manuscript, the sensitivity volume is “stretched” inside the measurement chamber, with symmetry between modes focusing on corners (3, 4, 5 and 6) and between modes 7 and 8. Using a square chamber with 16 mm side (Fig. S2.1), the simulated impedance values are one order of magnitude lower ($10^7 \Omega$) than those obtained with the chosen rectangular geometry ($10^8 \Omega$) because the current path is shorter. Moreover, the distribution of the sensitivity field (S) has the same global behavior as for the chosen rectangular geometry, with no advantage in using a square geometry.



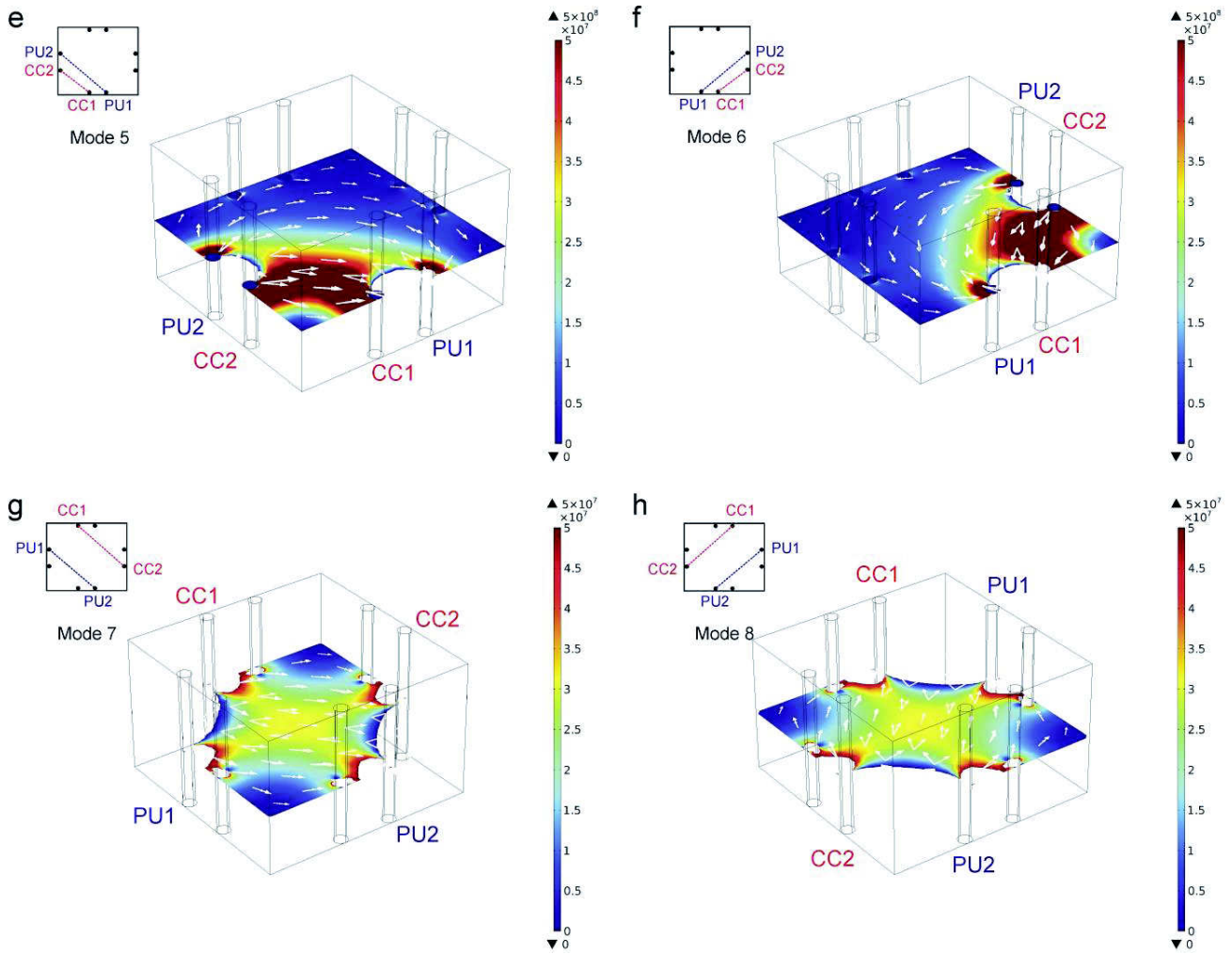
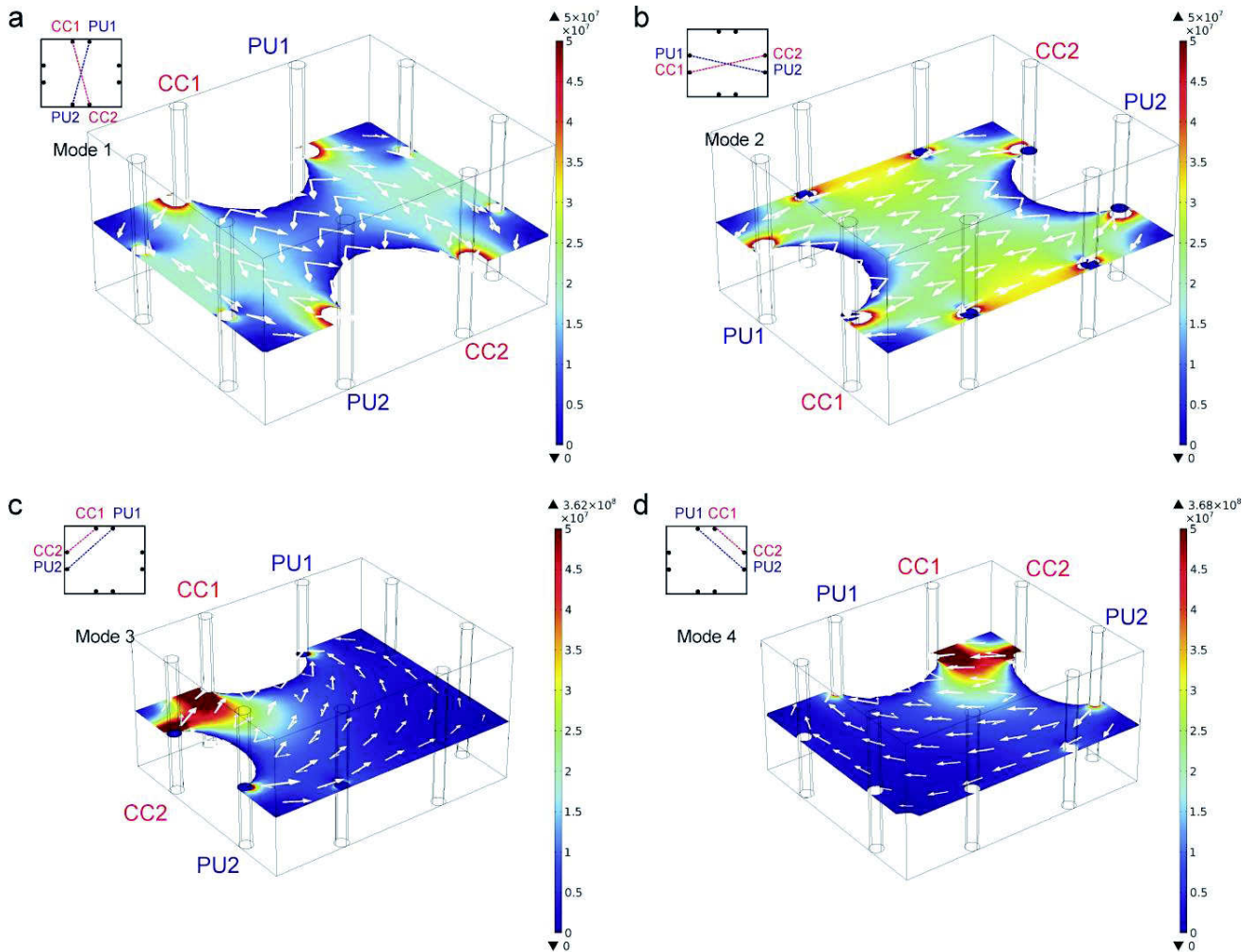


Fig. S2.1. FE analysis for S [m^{-4}] distribution using a square measurement chamber of 16 mm side, where the electrodes are placed 4 mm apart from each other on each side of the chamber. (a) Mode 1, (b) mode 2, (c) mode 3, (d) mode 4, (e) mode 5, (f) mode 6, (g) mode 7 and (h) mode 8.

Using the eight different modes for electrodes placed at a centre-to-centre distance of 8 mm (Fig. S2.2) and 12 mm (data not shown) on each measurement chamber side, the following conclusions were drawn.

- Modes 1 and 2: When increasing the electrode distance, the contribution from volumes associated with negative sensitivity becomes larger.
- Modes 3, 4, 5 and 6: Doubling the electrode distance, the focus on corners becomes extremely narrow and the sensitivity volume is extremely reduced.
- Modes 7 and 8: When increasing the electrode distance, mode 7 and 8 give a good sensitivity profile. However it is crucial to find a good compromise in terms of positive sensitivity field among all the different modes in order to place the electrodes in a common position to all of them. Therefore, the solution presented in the manuscript (chamber size $16 \times 19 \times 10 \text{ mm}^3$ with electrode couples where electrodes are placed 4 mm apart from each other on each side of the chamber) is definitely the best achievable one.



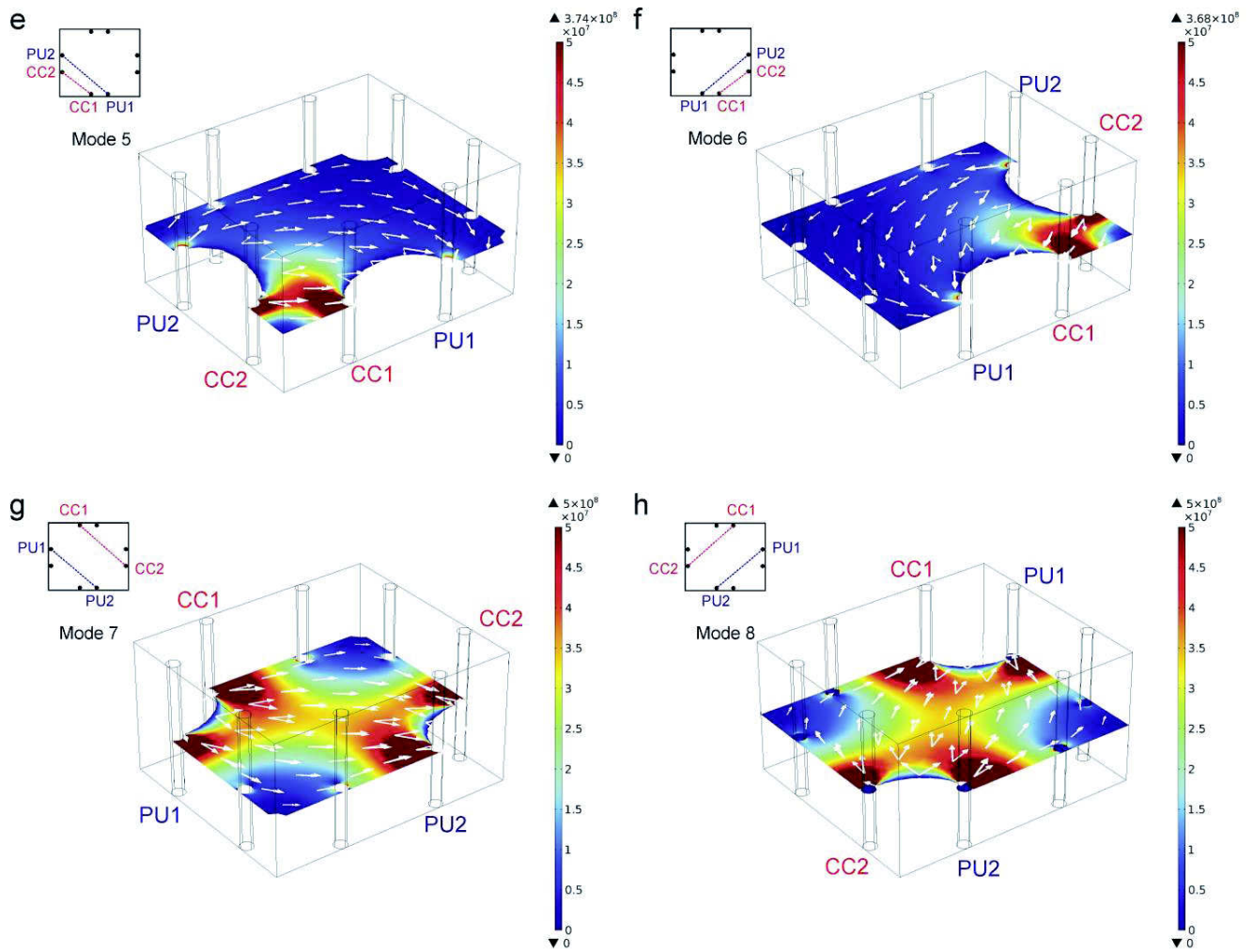
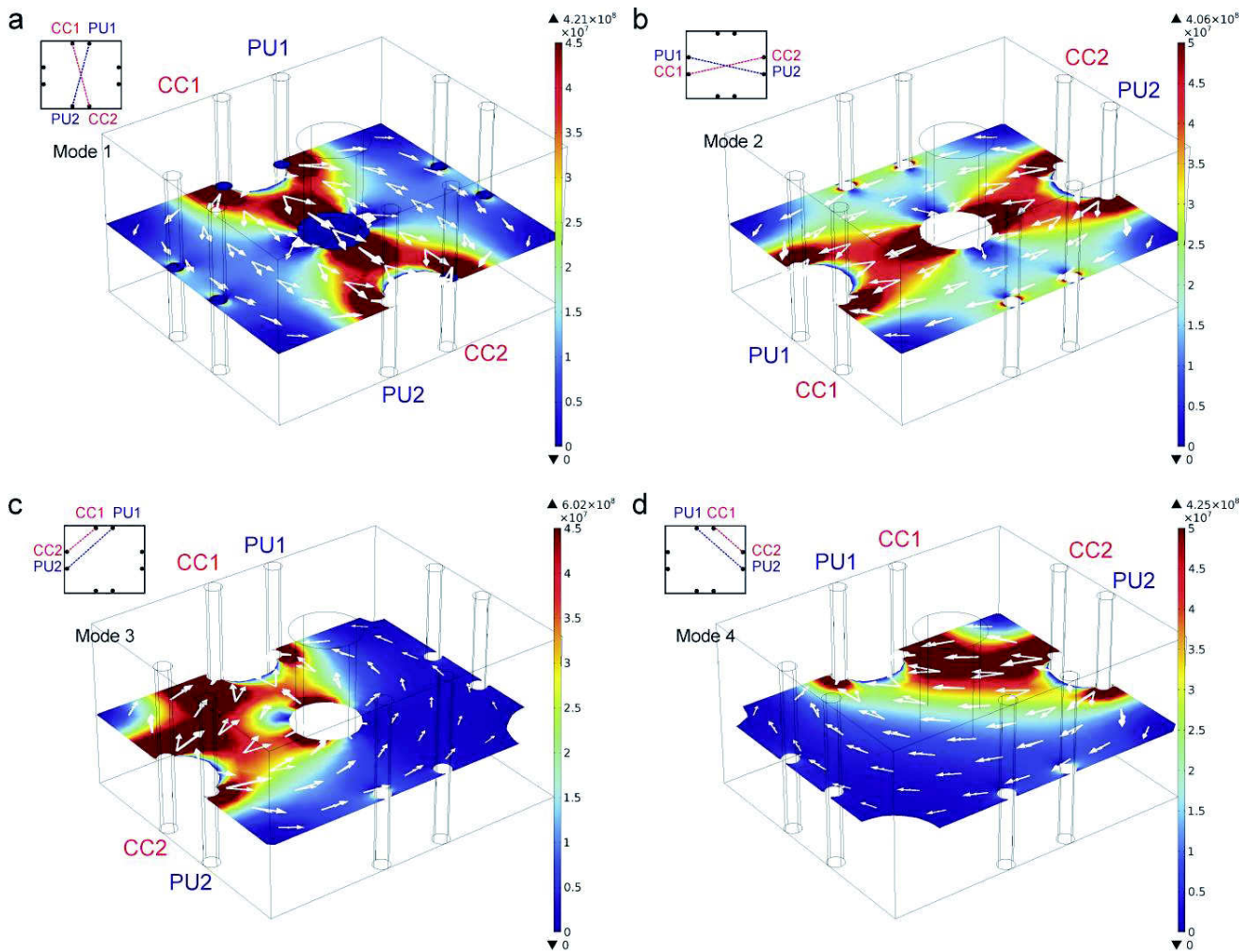


Fig. S2.2. FE analysis for S [m⁻⁴] distribution using a rectangular measurement chamber of $16 \times 19 \times 10$ mm³, where the electrodes are placed 8 mm apart from each other on each side of the chamber. (a) Mode 1, (b) mode 2, (c) mode 3, (d) mode 4, (e) mode 5, (f) mode 6, (g) mode 7 and (h) mode 8.

Section S3. FE simulation of metal and plastic phantoms

FE simulations were performed in presence of a vertical metal phantom (diameter of 4 mm and length of 10 mm, $\sigma = 4.032 \times 10^6$ S/m and $\epsilon_r = 1$) placed in the centre of the measurement chamber filled with saline solution ($\sigma = 1.3$ S/m and $\epsilon_r = 1$), Fig. S3.1. As expected from the theory described in Section S1, when the metal phantom is placed in volumes associated with positive S, the measured impedance decreases. Accordingly, as consequence of the Ohm's law for a volume conductor, a certain amount of current will be preferably absorbed by the phantom with a decrease in the measured impedance. FE simulations of a metal phantom placed in one corner of the measurement chamber (not reported) were consistent with the ones for the centre, here reported.



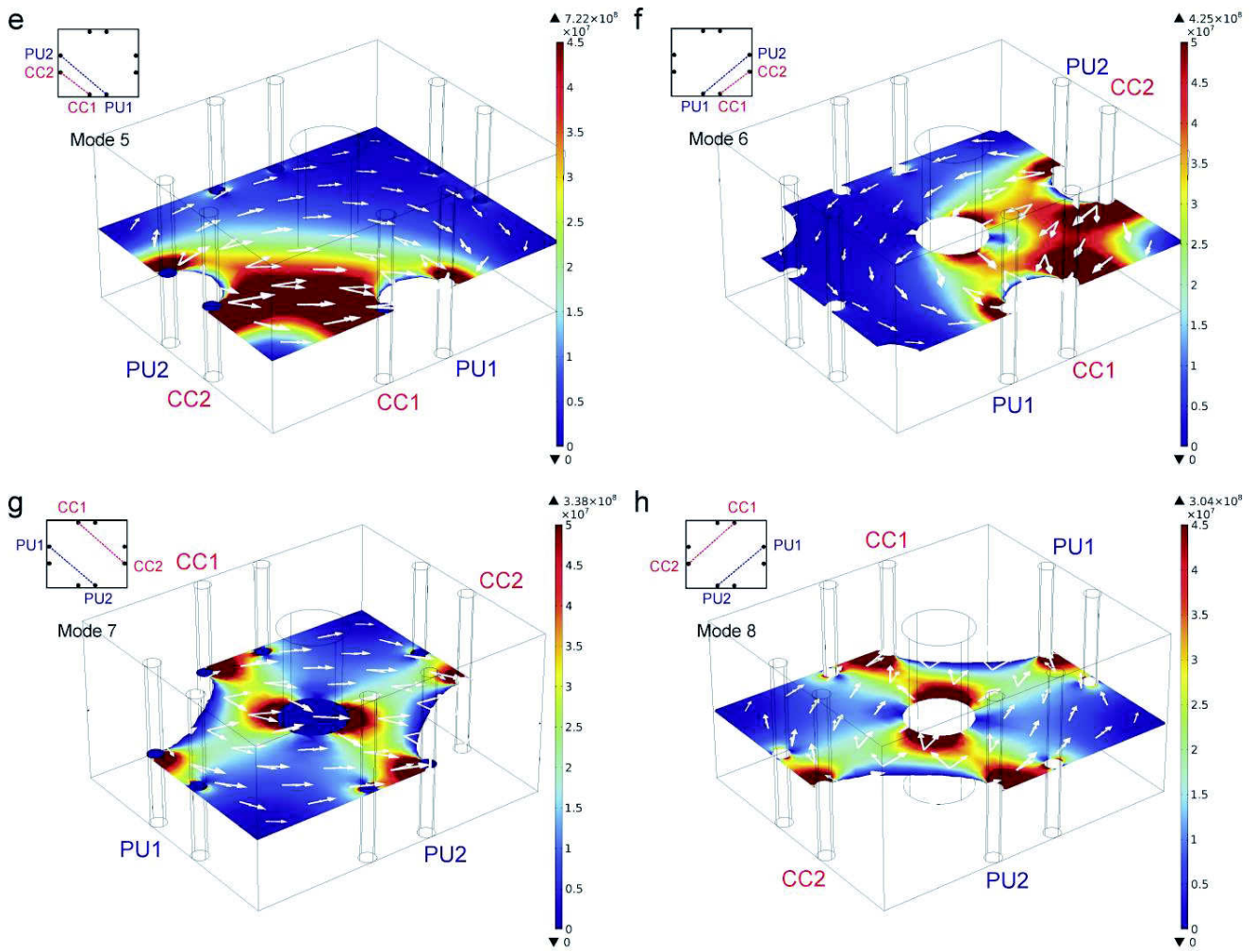
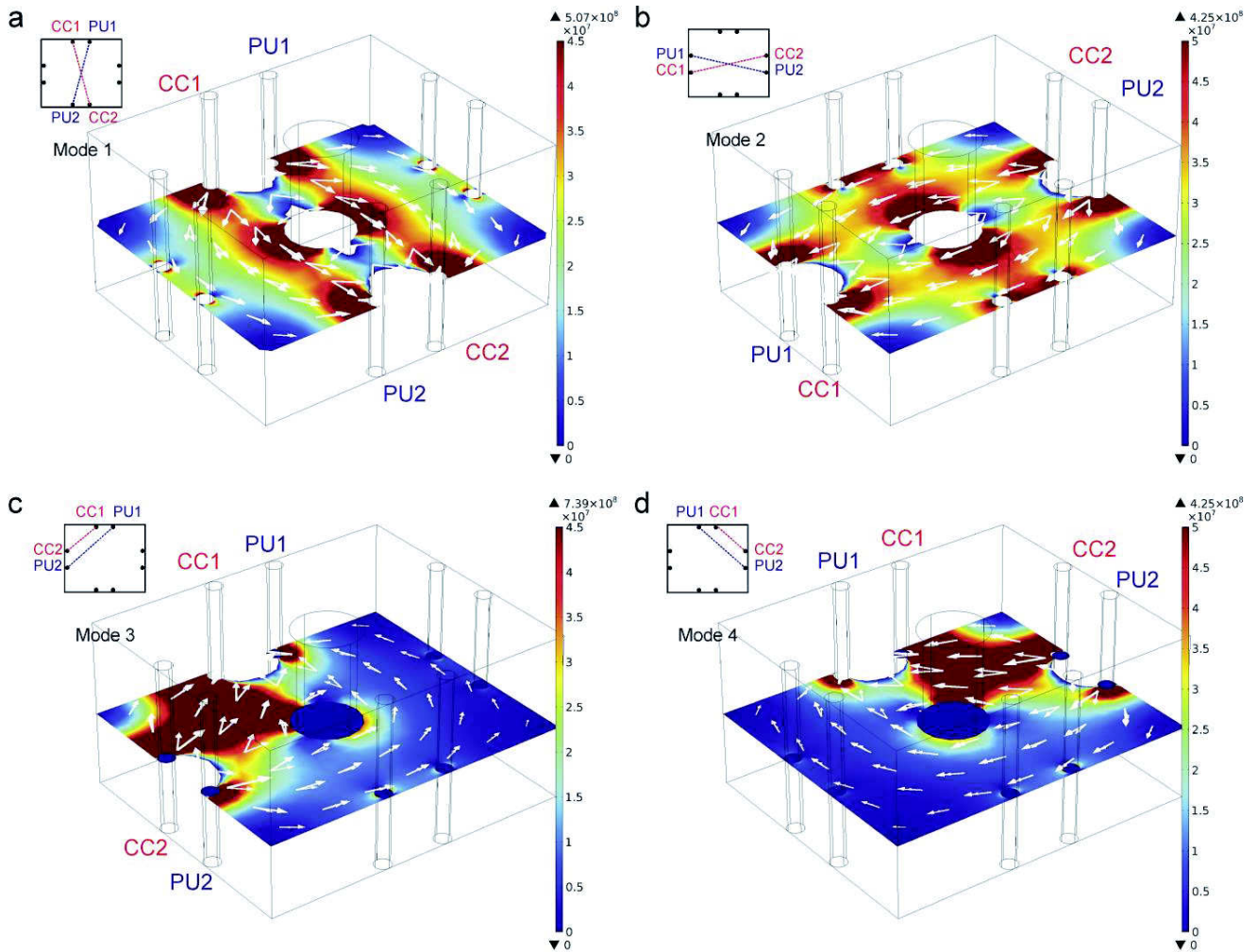


Fig. S3.1. FE simulations for S [m^{-4}] distribution in presence of a vertical metal phantom placed in the centre of the measurement chamber filled with saline solution: (a) mode 1, (b) mode 2, (c) mode 3, (d) mode 4, (e) mode 5, (f) mode 6, (g) mode 7 and (h) mode 8.

FE simulations were performed in presence of a vertical plastic phantom (diameter of 4 mm and length of 10 mm, $\sigma = 1 \times 10^{-19}$ S/m and $\epsilon_r = 1$) placed in the centre of the measurement chamber filled with saline solution ($\sigma = 1.3$ S/m and $\epsilon_r = 1$), Fig. S3.2. As expected from the theory described in Section S1, when the plastic phantom is placed in volumes associated with positive S, the measured impedance increases. Accordingly, as consequence of the Ohm's law for a volume conductor, the current path will tend to "avoid" the insulating phantom and will preferably go through the more conductive saline solution around. FE simulations for a plastic phantom placed in one corner of the measurement chamber (not shown) were consistent with the ones for the centre, here reported.



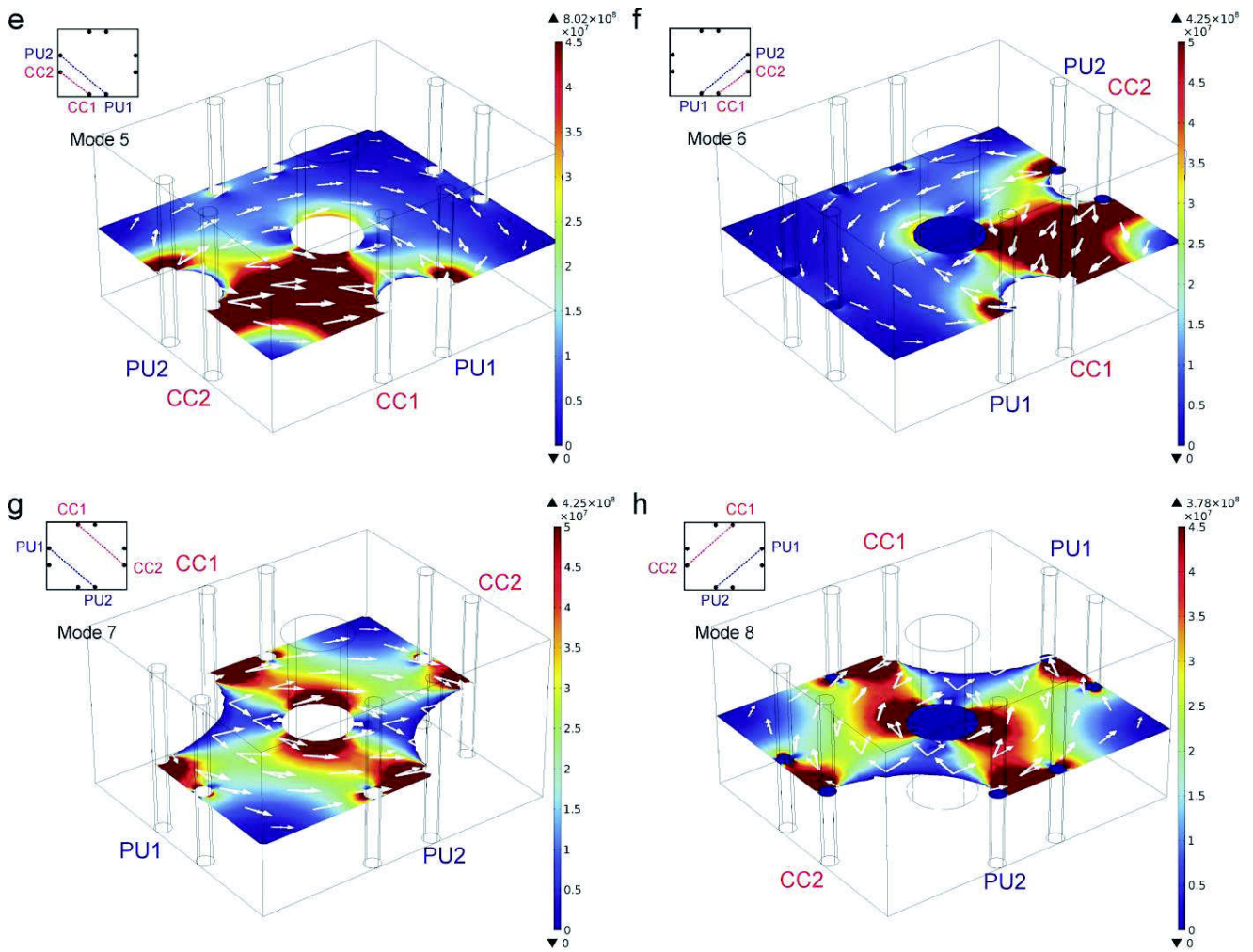


Fig. S3.2. FE simulations for S [m^{-4}] distribution in presence of a vertical plastic phantom placed in the centre of the measurement chamber filled with saline solution: (a) mode 1, (b) mode 2, (c) mode 3, (d) mode 4, (e) mode 5, (f) mode 6, (g) mode 7 and (h) mode 8.

Section S4. Summary of phantom experiments

Phantom experiments are typically used to evaluate the sensitivity and accuracy of the response of an imaging device to an object which mimics the properties of biological tissues and organs. Fields of application are, e.g., electrical impedance tomography (EIT), magnetic resonance imaging (MRI), computed tomography (CT) and ultrasounds. A phantom may consist of real animal or vegetal tissues (e.g. carrot, potato, ...), or any other kind of material (e.g. hydrogel) able to reproduce the physical properties of the final biological sample to be measured. Since phantom experiments allow characterising the spatial sensitivity of an imaging device, this approach was successfully applied to determine the spatial sensitivity of our 3D bioimpedance-based method. The simulated sensitivity fields (S) for the eight 4T modes were validated with phantom experiments using metal and plastic cylinders. Table S4 shows the relative impedance variation for 4 mm metal and plastic phantoms placed in different positions (centre and corners) inside the measurement chamber filled with saline solution of standard conductivity 1.3 S/m. The relative impedance variation was calculated as difference between the measured impedance in presence of the cylinder and the measured impedance for the saline solution only. For all phantom experiments, characterisation data are presented as an average of three individual experiments in each chamber using fresh solution and rinsing the phantom with Milli-Q water (average \pm s.e.m., n = 12).

Table S4. Impedance variation at 250 kHz for a 4 mm metal and plastic phantoms placed in different positions inside the measurement chamber filled with saline solution of conductivity 1.3 S/m (average \pm s.e.m., n = 12).

MODE 1		
Position	Metal (Ohm)	Plastic (Ohm)
<i>Centre</i>	-6.4 \pm 0.5	6.3 \pm 0.4
<i>Top Left</i>	-5.7 \pm 0.5	5.1 \pm 1.3
<i>Top Right</i>	-6.8 \pm 0.4	2.8 \pm 0.6
<i>Bottom Left</i>	-6.4 \pm 0.5	1.5 \pm 0.6
<i>Bottom Right</i>	-6.7 \pm 0.4	1.4 \pm 0.6

MODE 2		
Position	Metal (Ohm)	Plastic (Ohm)
<i>Centre</i>	-7.4 \pm 2.0	5.7 \pm 2.0
<i>Top Left</i>	-6.5 \pm 0.7	8.9 \pm 0.8
<i>Top Right</i>	-7.4 \pm 0.8	5.1 \pm 1.6
<i>Bottom Left</i>	-7.0 \pm 0.8	3.5 \pm 1.4
<i>Bottom Right</i>	-8.5 \pm 0.6	7.8 \pm 2.0

MODE 3

Position	Metal (Ohm)	Plastic (Ohm)
<i>Centre</i>	-3.9 ± 0.4	1.0 ± 0.4
<i>Top Left</i>	-12.5 ± 0.5	15.9 ± 0.7
<i>Top Right</i>	-2.9 ± 0.4	0.5 ± 0.4
<i>Bottom Left</i>	-3.6 ± 0.5	0.3 ± 0.5
<i>Bottom Right</i>	-2.2 ± 0.4	-4.7 ± 1.4

MODE 4

Position	Metal (Ohm)	Plastic (Ohm)
<i>Centre</i>	-4.4 ± 0.5	2.8 ± 0.5
<i>Top Left</i>	1.8 ± 0.7	4.3 ± 0.4
<i>Top Right</i>	-11.9 ± 0.5	16.0 ± 0.6
<i>Bottom Left</i>	0.0 ± 0.6	-0.8 ± 0.4
<i>Bottom Right</i>	-3.4 ± 0.6	1.4 ± 0.4

MODE 5

Position	Metal (Ohm)	Plastic (Ohm)
<i>Centre</i>	-3.9 ± 0.9	1.6 ± 0.8
<i>Top Left</i>	-4.1 ± 0.6	2.2 ± 0.4
<i>Top Right</i>	-2.8 ± 0.5	-3.3 ± 0.6
<i>Bottom Left</i>	-13.9 ± 0.4	11.3 ± 0.7
<i>Bottom Right</i>	-3.6 ± 0.3	3.7 ± 0.5

MODE 6

Position	Metal (Ohm)	Plastic (Ohm)
<i>Centre</i>	-4.1 ± 0.4	2.3 ± 1.3
<i>Top Left</i>	-1.6 ± 0.6	0.6 ± 0.4
<i>Top Right</i>	-4.0 ± 0.7	2.9 ± 0.5
<i>Bottom Left</i>	-4.1 ± 0.4	0.8 ± 0.4
<i>Bottom Right</i>	-13.4 ± 0.3	12.5 ± 0.7

MODE 7

Position	Metal (Ohm)	Plastic (Ohm)
<i>Centre</i>	-7.2 ± 0.8	5.7 ± 1.4
<i>Top Left</i>	-3.6 ± 1.0	-6.5 ± 0.7
<i>Top Right</i>	-5.6 ± 0.6	2.0 ± 0.5
<i>Bottom Left</i>	-5.8 ± 0.4	0.3 ± 2.2
<i>Bottom Right</i>	-2.0 ± 0.4	-6.8 ± 0.6

MODE 8

Position	Metal (Ohm)	Plastic (Ohm)
<i>Centre</i>	-7.7 ± 0.6	4.6 ± 0.9
<i>Top Left</i>	-7.4 ± 0.6	3.3 ± 0.5
<i>Top Right</i>	-3.0 ± 0.4	-3.4 ± 0.4
<i>Bottom Left</i>	-4.4 ± 0.5	-5.7 ± 0.7
<i>Bottom Right</i>	-7.0 ± 0.4	1.6 ± 0.4

Section S5. Biimpedance sensing of 5% (w/v) bulk gelatin scaffolds

Table S5 shows impedance ($|Z|$, real Z and imaginary Z) and phase angle (φ) values at 250 kHz for 5% (w/v) bulk gelatin scaffolds of $16 \times 19 \times 6.6 \text{ mm}^3$ size.

$|Z|$ was always equal to real Z , showing a decrease over time. This behaviour is opposite to what was expected, but can be explained when considering the cell culture medium diffusion through the scaffold over time. In fact, since polymerisation is associated with lower ionic mobility within the gelatin matrix, this would have been expected to decrease the scaffold conductivity, with an increase in the measured impedance. However, cell culture medium was added on top of the scaffolds at t_0 and a diffusion rate of $0.41 \mu\text{m}/\text{sec}$ was measured through the scaffold. This means that after 2 hours, the cell culture medium went through almost a half of the scaffold height and, after 4 hours, it went almost completely through it. Cell culture medium has high conductivity (1.6 - 1.8 S/m; C. Canali et al. 2015, H. Hsu et al. 2010, McIntosh et al. 2003), hence lowering the measured impedance over time.

Imaginary Z was almost constant over time and this may entail that the gelatin scaffolds made with our protocol have mainly a resistive behavior. Accordingly, the phase angle was almost zero and constant over time.

Table S5. Impedance ($|Z|$, real Z and imaginary Z) and phase angle values at 250 kHz for 5% (w/v) bulk gelatin scaffolds of $16 \times 19 \times 6.6 \text{ mm}^3$ size. Data are presented as average \pm s.e.m., $n = 21$.

MODE 1			
	t_0 (0 hours)	t_1 (2 hours)	t_2 (4 hours)
$ Z $ (Ohm)	48.2 ± 3	45.4 ± 5.5	40.8 ± 7.2
Z_{Re} (Ohm)	48.2 ± 3	45.4 ± 5.5	40.8 ± 7.2
Z_{Im} (Ohm)	0.7 ± 0.2	0.7 ± 0.2	1.0 ± 0.1
φ (Deg.)	0.0 ± 0.0	0.0 ± 0.0	0.0 ± 0.0

MODE 2			
	t_0 (0 hours)	t_1 (2 hours)	t_2 (4 hours)
$ Z $ (Ohm)	69.8 ± 5.3	64.8 ± 6.0	61.2 ± 8.2
Z_{Re} (Ohm)	69.8 ± 5.3	64.8 ± 6.0	61.2 ± 8.2
Z_{Im} (Ohm)	1.2 ± 0.16	1.2 ± 0.1	1.2 ± 0.1
φ (Deg.)	0.0 ± 0.0	0.0 ± 0.0	0.0 ± 0.0

MODE 3			
	t_0 (0 hours)	t_1 (2 hours)	t_2 (4 hours)
$ Z $ (Ohm)	43.2 ± 2.8	42.6 ± 4.4	37.0 ± 5.7
Z_{Re} (Ohm)	43.2 ± 2.8	42.6 ± 4.4	37.0 ± 5.7
Z_{Im} (Ohm)	0.9 ± 0.1	0.9 ± 0.1	0.8 ± 0.1
φ (Deg.)	0.0 ± 0.0	0.0 ± 0.0	0.0 ± 0.0

MODE 4

	t₀ (0 hours)	t₁ (2 hours)	t₂ (4 hours)
$ Z $ (Ohm)	57.8 ± 5.4	38.0 ± 3.8	40.7 ± 5.4
Z_{Re} (Ohm)	57.8 ± 5.4	38.0 ± 3.8	40.7 ± 5.4
Z_{Im} (Ohm)	1.0 ± 0.1	0.8 ± 0.1	0.7 ± 0.1
φ (Deg.)	0.0 ± 0.0	0.0 ± 0.0	0.0 ± 0.0

MODE 5

	t₀ (0 hours)	t₁ (2 hours)	t₂ (4 hours)
$ Z $ (Ohm)	44 ± 3.2	47.4 ± 5.8	36.7 ± 6.2
Z_{Re} (Ohm)	44 ± 3.2	47.4 ± 5.8	36.7 ± 6.2
Z_{Im} (Ohm)	0.9 ± 0.2	0.8 ± 0.1	0.7 ± 0.1
φ (Deg.)	0.0 ± 0.0	0.0 ± 0.0	0.0 ± 0.0

MODE 6

	t₀ (0 hours)	t₁ (2 hours)	t₂ (4 hours)
$ Z $ (Ohm)	55.8 ± 6.5	38.1 ± 4.1	38.7 ± 6.0
Z_{Re} (Ohm)	55.8 ± 6.5	38.1 ± 4.1	38.71 ± 6.0
Z_{Im} (Ohm)	0.9 ± 0.1	0.7 ± 0.1	0.7 ± 0.1
φ (Deg.)	0.0 ± 0.0	0.0 ± 0.0	0.0 ± 0.0

MODE 7

	t₀ (0 hours)	t₁ (2 hours)	t₂ (4 hours)
$ Z $ (Ohm)	37.2 ± 3.5	35.3 ± 4.2	32.4 ± 4.5
Z_{Re} (Ohm)	37.2 ± 3.5	35.3 ± 4.2	32.4 ± 4.5
Z_{Im} (Ohm)	0.8 ± 0.2	0.6 ± 0.1	0.7 ± 0.1
φ (Deg.)	0.0 ± 0.0	0.0 ± 0.0	0.0 ± 0.0

MODE 8

	t₀ (0 hours)	t₁ (2 hours)	t₂ (4 hours)
$ Z $ (Ohm)	40.1 ± 3.6	33.2 ± 3.8	31.3 ± 4.5
Z_{Re} (Ohm)	40.1 ± 3.6	33.2 ± 3.8	31.3 ± 4.5
Z_{Im} (Ohm)	0.9 ± 0.2	0.6 ± 0.1	0.7 ± 0.1
φ (Deg.)	0.0 ± 0.0	0.0 ± 0.0	0.0 ± 0.0

Section S6. Biopedance sensing of 5% (w/v) gelatin cylinders and artificial 3D cell constructs

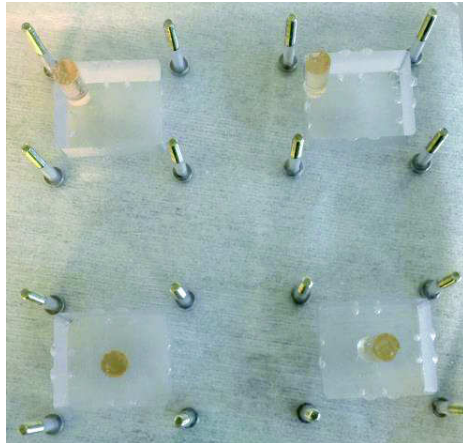


Fig. S6.1. Gelatin cylinders(with and without cells) were placed in two different positions inside the measurement chamber (centre or top left corner). Then, 2 mL of 5% (w/v) gelatin was casted around and let to polymerise for 2 hours at 37 °C in a humidified 5% CO₂ incubator. After gelatin polymerisation, the measurement chamber was filled with cell culture medium.

S6A) Gelatin cylinders without cells

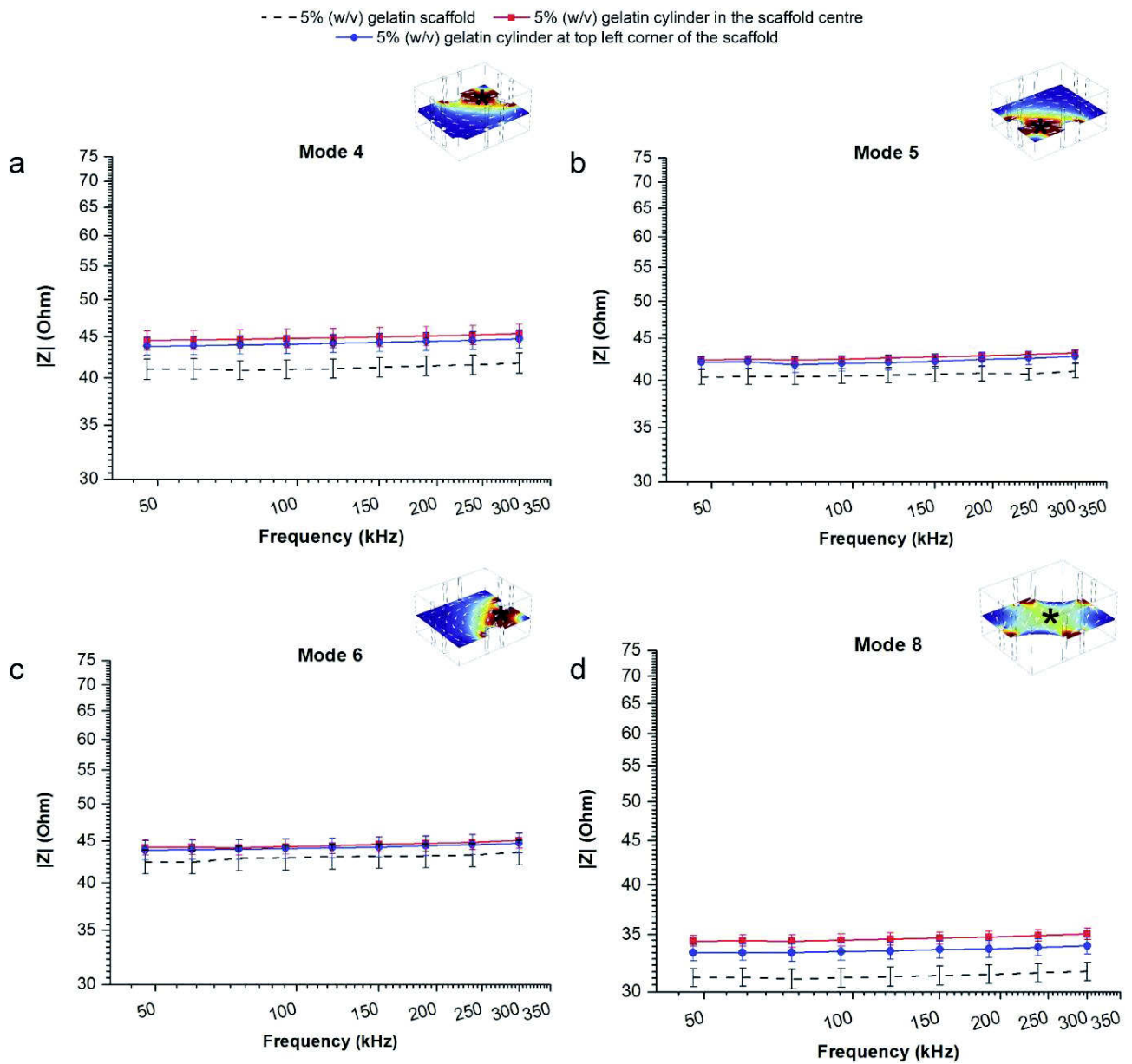


Fig. S6.2. Sensing of a 5% (w/v) gelatin cylinder embedded in bulk gelatin scaffold and placed either at the top left corner or in the centre: mode 4 (a), mode 5 (b), mode 6 (c), mode 8 (d). Data are compared with 5% (w/v) bulk gelatin scaffold (average \pm s.e.m., $n = 21$) and reported as average \pm s.e.m., $n = 6$. The position of the main focus of each mode is indicated by an asterisk.

S6B) Artificial 3D cell constructs

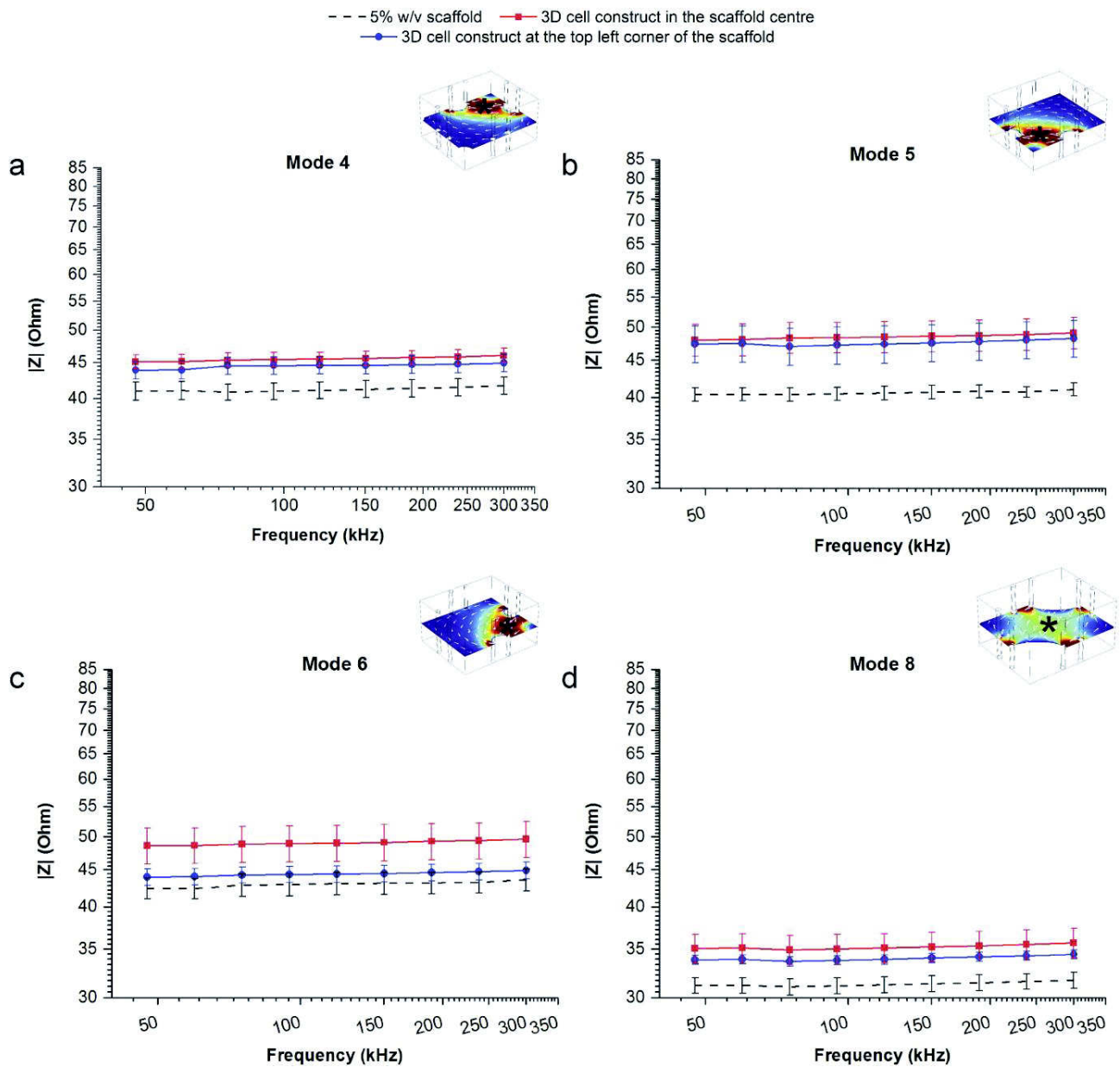


Fig. S6.3. Sensing of a 5% (w/v) gelatin cylinder containing 10^7 HepG2 cells as artificial 3D cell construct embedded in bulk gelatin scaffold and placed either at the top left corner or in the centre. Mode 4 (a), mode 5 (b), mode 6 (c), mode 8 (d). Data are compared with 5% (w/v) bulk gelatin scaffold (average \pm s.e.m., $n = 21$) and reported as average \pm s.e.m., $n = 6$. The position of the main focus of each mode is indicated by an asterisk.

Paper VII

Perfusion bioreactor array with integrated impedance sensors for tissue engineering applications

L. B. Larsen[†], C. Canali[†], M. Hemmingsen, K. Kuldeep, S. Mohanty, R. Pimentel, L. H. Jensen, M. Skolimowski, A. Wolff, F. Okkels, A. Heiskanen, M. Dufva and J. Emnéus

Manuscript to be submitted to *Biotechnology and Bioengineering*

[†] These two authors contributed equally to this work.

Paper VIII

Electrical impedance tomography for miniaturised 3D systems

C. Canali[†], K. Aristovicht[†], L. Ceccarelli, L. B. Larsen, A. Heiskanen, Ø. G. Martinsen, A. Wolff, M. Dufva and J. Emnéus

Manuscript submitted to *Analyst*

[†] These two authors contributed equally to this work.

APPENDIX II

Conference Contributions

Electrical impedance spectroscopy with optimised electrode configurations for 3D tissue engineering applications

Chiara Canali¹, Haseena Bashir Muhammad¹, Arto Heiskanen¹, Chiara Mazzoni¹, Lorenzo Ceccarelli¹, Ørjan Grøttem Martinsen², Anders Wolff¹, Martin Dufva¹, Jenny Emnéus¹

¹*Department of Micro- and Nanotechnology, Technical University of Denmark, 2800, Kgs Lyngby, Denmark*

²*Department of Physics, University of Oslo, 0316, Oslo, Norway*

chca@nanotech.dtu.dk

The current advances in biotechnological research have led to an increasing demand for solid analytical methods focusing on applications within the fields of tissue engineering, biomaterial science and 3D cell cultures. Furthermore, in vitro studies on cell functionality require a physiologically representative microenvironment in terms of extracellular matrix and controlled biochemical and biomechanical parameters. A major challenge in this regard is the monitoring of cellular proliferation within 3D scaffolds, which provide a platform for cell growth and cell-cell interaction in all three dimensions. Although traditional optical microscopic techniques are unsuitable for monitoring thick 3D constructs, electrical impedance spectroscopy (EIS) has been proven to be a sensitive, label-free and minimally invasive method for characterising passive electrical properties of biomaterials and biological systems both in vivo and in vitro.

We developed different EIS-based methods for real-time monitoring of 3D cell cultures embedding vertical plate and needle electrodes for static and perfusion-based cell culturing. Electrodes can be used in a multiplexing-like approach with different 2, 3 and 4 terminal configurations¹ to gain information about their spatial distribution in a 3D environment. The same setup can be used for characterising the scaffold architecture² and also estimating the influence of mammalian cell proliferation on medium conductivity. Optimised protocols for electrode functionalisation were developed using aqueous solvents to eliminate protein and cell adhesion to enhance detection reproducibility and electrode reusability. Validation with finite element simulations, phantom experiments mimicking cell clusters and cell-based experiments were performed aiming to incorporate spatial-enhanced 3D sensing into miniaturised perfusion bioreactors for real-time monitoring of cell proliferation in porous scaffolds.

References

1. Canali C. et al. 2015. Biosens. Bioelectron. 63, 72–79
2. Canali C. et al. 2015 Electroanalysis. 27, 193–199

On-line monitoring of 2D and 3D cell cultures: electrode configurations for impedance based sensors

Chiara Canali¹, Claudia Caviglia¹, Kinga Zór¹, Haseena Bashir Muhammad¹, Arto Heiskanen¹, Ørjan Grøttem Martinsen^{2,3}, Thomas L. Andresen¹, Anders Wolff¹, Martin Dufva¹, Jenny Emnéus¹

¹ Department of Micro- and Nano-technology, Technical University of Denmark, 2800, Kgs Lyngby, Denmark

² Department of Physics, University of Oslo, 0316, Oslo, Norway

³ Department of Biomedical and Clinical Engineering, Oslo University Hospital, 0424, Oslo, Norway

chca@nanotech.dtu.dk

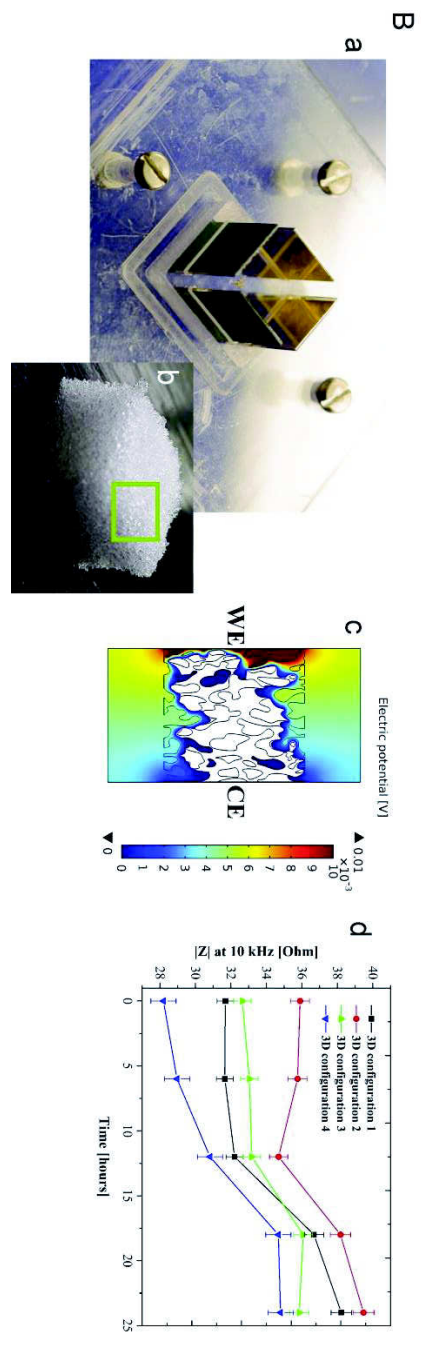
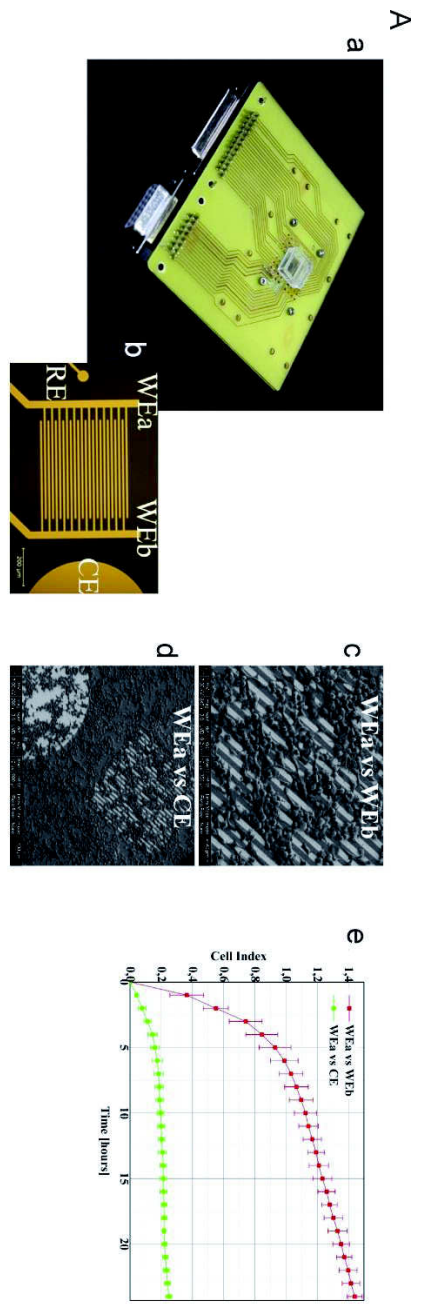
Key words: Electrical impedance spectroscopy; Interdigitated electrodes; Two-, three- and four-electrode measurements

Electrochemical impedance spectroscopy (EIS) has been proved to be a valuable technique for label-free, real-time and minimal invasive detection of cellular functions in fundamental and applied research.

During the last three decades, several two-dimensional (2D) impedance-based systems have been widely used for studying cell adhesion and spreading, proliferation and death. Nowadays, there is an increasing interest towards three-dimensional (3D) cell cultures, which are proposed to create and maintain a more in vivo-like environment. EIS can be applied at different stages when developing a 2D or 3D culture setup, starting from bare scaffold and electrode characterization to monitor cell proliferation and tissue functionality.

We present theoretical and experimental comparison of several electrode configurations (or modes) both in 2D (Fig. 1A) and 3D (Fig. 1B) used for following cell growth in real-time. Two different 2D modes were explored measuring between: i) the two combs (working electrode a vs b, WEa vs WEb), interdigitated configuration (Fig. 1Aa,b,c) and ii) WE versus a large counter electrode (CE), conventional “vertical” configuration, and found that the interdigitated configuration provides a higher sensitivity when monitoring HeLa cells adhesion, spreading and growth over 24-h (Fig. 1Ad).

In 3D environment there is a need for adding the third dimension to EIS sensing for spatial resolution to gain information about distribution of cells in the scaffold (Fig. 1Ba,b,c). Moreover, electrode number, geometry and orientation need to be optimized with respect to the deriving sensitivity field distribution. In order to gain information with a good resolution, we show that several two-, three- and four-electrode measurements can be combined to create complementary sensitivity fields which individually focus on specific volumes inside the 3D cell culture and, taken together, cover the whole measurement chamber volume. This approach was tested for growing hepatoblastoma (HepG2) cells embedded within a 5% w/v gelatin scaffold (Fig. 1Bd).



Enhanced multielectrode configurations in miniaturized 3D electrical impedance spectroscopy and tomography – Monitoring the overall process of tissue engineering with spatial sensing for future challenges in microfluidics

Chiara Canali¹, Haseena Bashir Muhammad¹, Arto Heiskanen¹, Chiara Mazzoni¹, Lorenzo Ceccarelli¹, Ørjan Grøttem Martinsen^{2,3}, David Holder⁴, Anders Wolff¹, Martin Dufva¹, Jenny Emnéus¹

¹ *Department of Micro- and Nano-technology, Technical University of Denmark, 2800, Kgs Lyngby, Denmark*

² *Department of Physics, University of Oslo, 0316, Oslo, Norway*

³ *Department of Biomedical and Clinical Engineering, Oslo University Hospital, 0424, Oslo, Norway*

⁴ *Department of Medical Physics and Bioengineering, University College London, WC1E 6BT, London, UK*

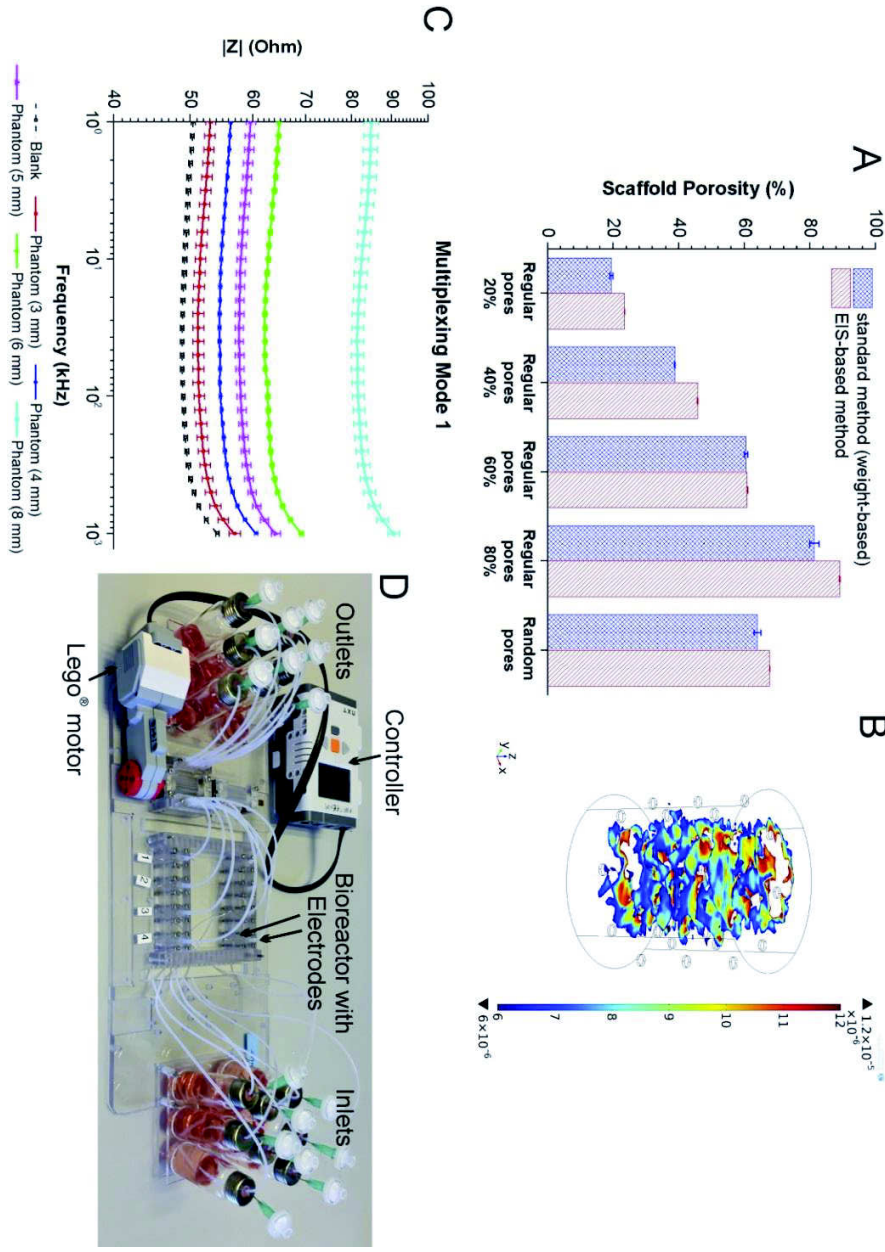
chca@nanotech.dtu.dk

Key words: Electrical impedance spectroscopy and tomography, 3D cell cultures, Culture medium and scaffold material characterization, Microfluidics

Over the past two decades, 3D cell culture models have attracted considerable attention to achieve in vivo-like structural organization, gene and protein expression, response to stimuli, drug metabolism, etc. A significant challenge in this regard is gaining spatial distributed information when monitoring cell proliferation on a biocompatible scaffold displaying well defined physico-chemical properties. Electrical impedance spectroscopy (EIS) have been shown to be a non-invasive method for biomaterial characterization and monitoring microfluidic cell cultures, gaining an insight on cell activity and proliferation over time.

We have developed and validated planar and needle-based multielectrode systems which offer the advantage of switching among different two-, three- and four-electrode configurations to focus impedance-based sensing on specific sub-volumes in a 3D cell culture. Information about scaffold architecture supporting cell organization (e.g. porosity, Fig. 1A), medium conductivity, and cell 3D spatial distribution can be obtained. Furthermore, four-electrode configurations can be also used for electrical impedance tomography (EIT)-based imaging to map the conductivity distribution within a miniaturized 3D cell culture system (Fig. 1B). Finite element simulations were used to optimize electrodes number, spacing and orientation with respect to the bioreactor geometry, by maximizing the deriving sensitivity field distribution for measurements. Validation with phantom experiments mimicking cell clusters (Fig. 1C) and cell-based experiments was performed aiming to incorporate

spatial-enhanced 3D sensing into a 8-channel bioreactor array with integrated microfluidics for real-time monitoring of cell proliferation in porous scaffolds (Fig. 1D). The integration of the non-invasive sensing methods developed enable monitoring of tissue development within otherwise inaccessible areas of a 3D tissue construct, overcoming limitations of more traditional optical techniques.





Perfusion-based three dimensional (3D) tissue engineering platform with integrated bioimpedance sensing

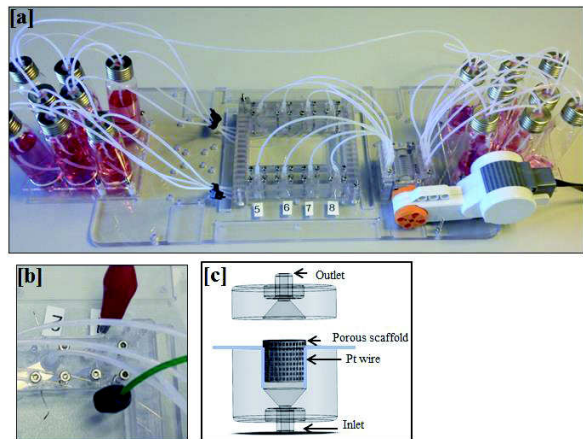
H. B. Muhammad, C. Canali, A. Heiskanen, M. Hemmingsen, A. Wolff, M. Dufva, J. Ennéus

Abstract — We present an 8-channel bioreactor array with integrated bioimpedance sensors, which enables perfusion culture of cells seeded onto porous 3D scaffolds. Results show the capability of the system for monitoring cell proliferation within the scaffolds through a culture period of 19 days.

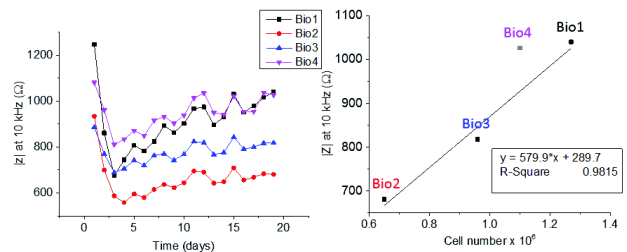
There is an increasing interest in the development of 3D tissue engineering systems for drug screening and organ development applications [1]. A significant challenge in this regard is the monitoring of cellular processes occurring within the scaffolds, particularly as traditional optical microscopic techniques are unsuitable for monitoring thick 3D constructs [2]. Impedance spectroscopy has been shown to be a powerful tool for non-invasively monitoring the electrical behavior of tissues and cell cultures [3]. Here we present the development of an 8-channel bioreactor array with embedded impedance sensors that enable real time monitoring of the proliferation of cells cultured on porous 3D scaffolds.

The cell culture platform consists of a polycarbonate based array of 4 x 2 bioreactors, cell culture media and waste storage vials, an 8-channel micropump and a motor (Fig. 1a). Each bioreactor unit comprises of a chamber for holding a porous scaffold, and two 400 μm diameter platinum (Pt) wires for impedance sensing (Fig. 1b, c). Human hepatoblastoma (HepG2) were seeded onto porous polymer scaffolds (6 mm diameter and 5 mm high) with a seeding density of 2 x 10⁶ cells/scaffold. The cell laden scaffolds were loaded into the bioreactors and culture media was perfused through them at a flow rate of 5 μL/min (corresponding to a media exchange in the bioreactor approximately every 18 minutes). Impedance measurements were carried out by applying a sinusoidal perturbation of 10 mV (rms) across the Pt electrodes in the frequency range spanning 10 Hz to 1 MHz. At the end of the cell culture period, the quantity of cells within the bioreactors was established by measuring the double stranded DNA content using the Quant-iT™ PicoGreen® dsDNA Reagent (P7581, Life Technologies). Fig. 2 [a] shows the measured impedance magnitude |Z| (at a frequency of 10 kHz) over the 19 day culture period for four bioreactors. There was an observed overall drop in impedance during the first three days of the experiment, which may correspond to the loss of cells that have not attached to the scaffold (following

seeding) due to perfusion of media. This was followed by a net increase in measured impedance over time in all cases.



[a] Cell culture platform with array of 4 x 2 perfusable bioreactors, [b] magnified view of bioreactor with integrated Pt based bioimpedance sensing electrodes, [c] Schematic of single bioreactor unit.



[a] |Z| at 10 kHz vs. time over a cell culture period of 19 days, [b] |Z| at 10 kHz vs. cell number in each bioreactor at the end of the 19 day culture period (data of Bio4 was masked from data fitting).

Fig. 2[b] shows the total cell count in each bioreactor at the end of the culture period, which demonstrates the correlation between cell density and measured impedance. Further investigations are currently underway to characterize the distribution of cells within the scaffold in order to assess its impact on the measured impedance.

REFERENCES

- [1] J. Rouwkema et al., "In vitro platforms for tissue engineering: implications for basic research and clinical translation," *J. Tissue Eng. Regen. Med.*, vol. 5, no. 8, pp. e164–7, Aug. 2011.
- [2] K. F. Lei et al., "Development of a micro-scale perfusion 3D cell culture biochip with an incorporated electrical impedance measurement scheme for the quantification of cell number in a 3D cell culture construct," *Microfluid. Nanofluidics*, vol. 12, no. 1–4, pp. 117–125, Jul. 2011.
- [3] C. Canali et al., "Bioimpedance monitoring of 3D cell culturing- Complementary electrode configurations for enhanced spatial sensitivity," *Biosens. Bioelectron.*, vol. 63, pp. 72–9, Jan. 2015.

*Research financially supported by the EU-funded project NanoBio4Trans (grant no. 304842)

All authors work at the Department of Micro and Nanotechnology, Technical University of Denmark, Ørstedes Plads, Kgs. Lyngby 2800, Denmark. Tel: +45 45 25 63 24; e-mail: hbm@nanotech.dtu.dk

IMPEDANCE-BASED DETECTION FOR FACING NEW CHALLENGES IN BIOTECHNOLOGY: ENHANCED 3D SENSING, CONDUCTOMETRY AND ELECTRODE FUNCTIONALIZATION

Chiara Canali¹, Arto R. Heiskanen¹, Haseena B. Muhammad¹, Martin Dufva¹, Anders Wolff¹, Jenny Ennéus¹

¹Department of Micro- and Nanotechnology, Technical University of Denmark, 2800 Kgs Lyngby, Denmark,
E-mail: chca@nanotech.dtu.dk

The outstanding advances of the biotechnological research have raised increasing demand for solid analytical methods with a special focus on application within medical and pharmaceutical sciences, tissue engineering and health care.

We developed different impedance-based methods for real-time monitoring of 3D cell cultures and their metabolic activity. Planar vertical electrodes can be applied in different 2, 3 and 4 terminal configurations in a multiplexing-like approach to provide spatially distributed information on cell proliferation for *in vitro* tissue cultures (Figure 1A). The same setup can be used for estimating the influence of mammalian cell proliferation on medium conductivity (Figure 1B) and therefore characterizing the culture in terms of its biochemical activity. Moreover, this approach allows evaluating the overall 3D environment, even in terms of the scaffold architecture supporting cell organisation, proliferation and differentiation (Figure 1C). We are currently developing protocols for electrode functionalization to eliminate protein and cell adhesion to enhance detection reproducibility and electrode reusability using the same setup described above. For this purpose, chemical modifications performed in aqueous solvents are explored making them suitable for on-line modification of electrodes in polymeric perfusion-based cell culture systems.

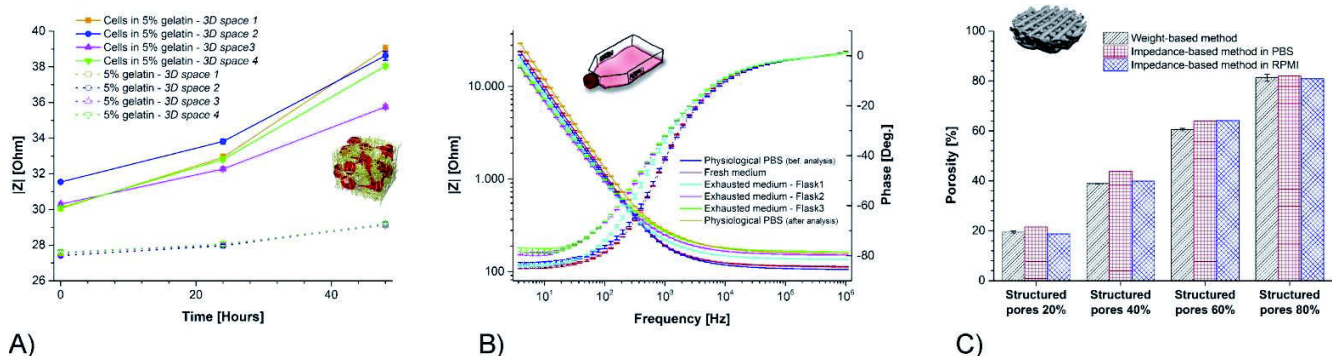


Figure 1. A) Spatial monitoring of cell growth for a 3D culture embedded in a 5% (w/v) gelatin scaffold ($|Z|$ at 4 kHz over time). B) Influence of mammalian cell proliferation on medium conductivity. C) Evaluation of porosity for different 3D cell culture scaffolds.



An innovative EIS based 3D printed conductometer

Chiara Canali, Arto Heiskanen, Haseena Bashir Muhammad, Martin Dufva and Jenny Emnéus*

chca@nanotech.dtu.dk

*Department of Micro- and Nanotechnology, Technical University of Denmark, Kongens Lyngby, Denmark

Electrical conductivity (σ) is a measure of the ability of a material to carry a current. Testing for σ is particularly significant when defining physico-chemical properties of electrolytes since it is related to ionic strength, mobility and valence, and is sensitive to shift in temperature, CO₂ content, and therefore pH. For this reason, σ and its variation over time convey a high degree of information, not only about inorganic and organic solutions, but more importantly about dynamics of biological processes.

The simplest approach to determine σ is by applying an alternating electric field between two electrodes and measuring the impedance value at the frequency for which phase angle value is equal to 0°. Modern instruments automatically adapt the frequency of analysis to the particular measuring conditions¹.

Here, an electrochemical impedance spectroscopy (EIS) based conductometer is presented as a sensitive, low cost instrument able to correlate the whole impedance spectrum to the σ value of solutions. The device can be easily 3D printed in acrylonitrile butadiene styrene (ABS) and incorporates two rectangular gold plate electrodes (Fig. 1).

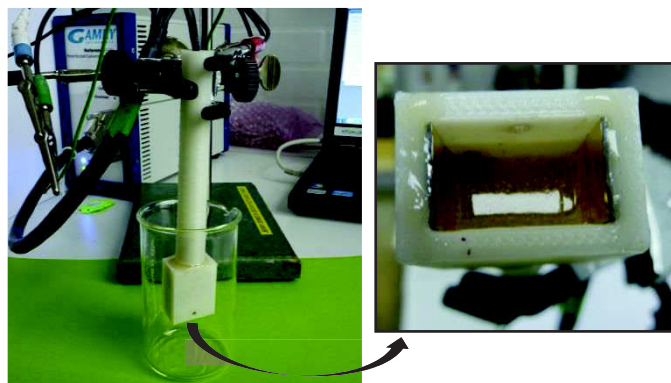


Figure 1: The EIS based conductometer interfaced with Reference 600 potentiostat (Gamry).

The cell constant of the measurement cell was determined to be $1.77 \pm 0.06 \text{ cm}^{-1}$ by EIS analysis on different σ standard solutions and then confirmed by geometrical measurements.

The device was tested by measuring σ of several dilutions of physiological phosphate buffered saline (PBS) solutions in the range 10^{-4} - 10^x exploiting both EIS and single frequency analysis. Reproducible results were obtained and validated against a commercial conductometer and literature search.

Taking together, all the results prove that the performance of the 3D printed conductometer described here is comparable to that of the commercial instrument and serves as an inexpensive and innovative alternative for quick evaluation of σ .

Reference:

1. "Conductivity. Theory and practice." Radiometer Analytical



Electrochemical impedance spectroscopy is a versatile technique for new challenges in 3D cell culture

Chiara Canali, Haseena Bashir Muhammad, Arto Heiskanen, Soumyaranjan Mohanty, Martin Dufva, Anders Wolff and Jenny Emnéus*

chca@nanotech.dtu.dk

*Department of Micro- and Nanotechnology, Technical University of Denmark, Kongens Lyngby, Denmark

Microtissue technology and 3D cell culture models have recently gathered attention by the scientific community since they more effectively promote physiological functions of cell differentiation and mimic tissue organization. In order to support cell adhesion and proliferation, and stimulate the biological cross talk between cells and scaffold, the physico-chemical properties and structural characteristics of the scaffold should be chosen carefully¹. Electrical impedance spectroscopy (EIS) has proven to be a powerful method to characterize passive electrical properties of inorganic and organic materials² but also of biological systems both *in vivo*³ and *in vitro*⁴.

Different generations of EIS based sensors are here presented which were designed and optimized in order to characterize new 3D polymeric scaffolds in terms of effective conductivity, porosity and compactness. The sensitivity field for EIS measurements on a volume conductor largely depends on the electrode geometry (size, shape and orientation) and configuration (2-, 3- and 4-probe measurements). Hence, different sensing configurations were designed, evaluated by finite element simulations (Comsol Multiphysics) and experimentally characterized. EIS characterization of scaffold materials and real-time monitoring of biological cell growth under static and perfusion culture conditions were carried out.

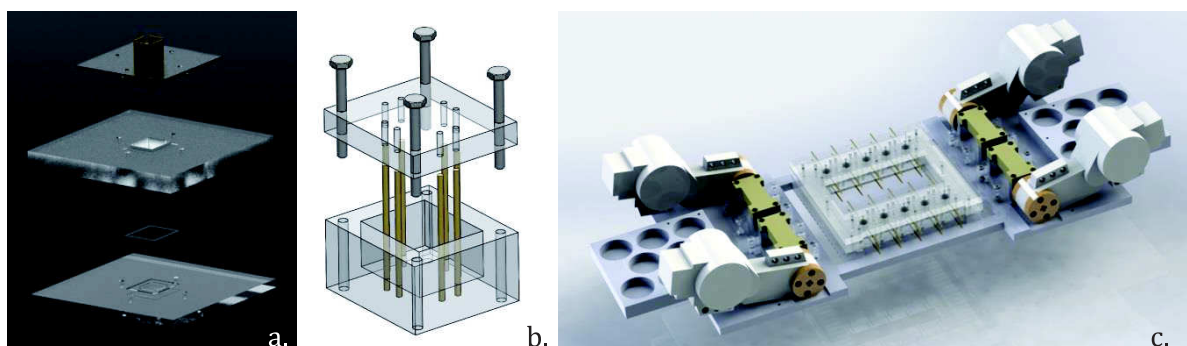


Figure 1: Three generations of sensors for 3D cell culture under static (a, b) and fluidic (c) conditions.

This method sets a next concrete perspective towards electrical impedance tomography applications for on-line imaging of dynamic 3D cell culture environments.

References:

1. Methods in Molecular Biology 695:17-39 (2011)
2. Journal of advanced research in physics 1(1), 011006 (2010)
3. Physiological Measurements 30(2):129-40 (2009)
4. Nature 366, 591-592 (1993)

A multiplexed electrical impedance-based device for bioengineering applications

Chiara Canali¹, Ørjan Grøttem Martinsen^{2,3}, Haseena Bashir Muhammad¹, Arto Heiskanen¹, Martin Dufva¹, Anders Wolff¹, Jenny Emnéus¹

¹ Department of Micro- and Nano-technology, Technical University of Denmark, 2800, Kgs Lyngby, Denmark

² Department of Physics, University of Oslo, 0316, Oslo, Norway

³ Department of Biomedical and Clinical Engineering, Oslo University Hospital, 0424, Oslo, Norway

chca@nanotech.dtu.dk

Electrical impedance is one of the most promising technologies used as an indicator for drug response and toxicity testing in cell-based assays, and for monitoring of cellular processes in tissue engineering applications. Bioimpedance-based medical devices have been applied for monitoring the state of tissues and the functioning of organs in vivo and in vitro.

In the present work the development of a novel, modular, impedance-based biomedical sensor is presented which is designed both for real-time monitoring of cellular dynamics within a 3D porous polymeric scaffold and for ex vivo analysis of biological tissues.

The system includes an array of four intelligent bioreactors (Fig. 1a) for parallel analysis where geometrical parameters such as electrode geometry and positioning were optimized by means of finite element (FE) simulations and mathematical analysis. An array of eight needle electrodes are positioned vertically around the periphery of the sample under study. Impedance measurements are carried out using a multiplexed approach where switching between different configurations of current-carrying (CC) and pick-up (PU) electrodes provides a greater positive sensitivity field to the volume of the sample under test (Fig. 1b).

Preliminary results obtained for assessing a 3D culture of cells (HepG2) encapsulated in a gelatin scaffold are shown in Fig. 1c. The growth of cells with time is represented by an increase in the impedance cell index. Variations between different configurations of CC and PU electrodes indicate the variation in spatial distribution of cells within the 3D scaffold. Thus, the bioimpedance-based device presented here has a high potential for real-time monitoring of the entire process of tissue engineering without affecting cell viability.

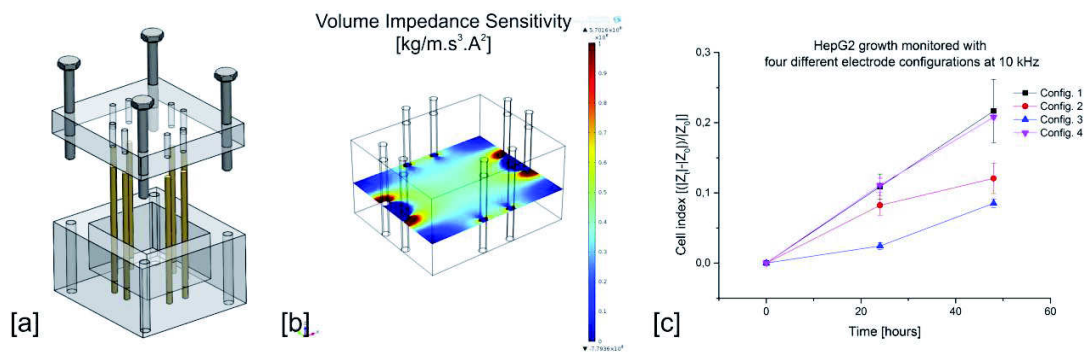


Fig 1: (a) Schematic of a single bioreactor with 8 needle electrodes, (b) FE simulation of sensitivity field using a single electrode configuration, (c) Results showing impedance CI with time for a 3D culture of cells.



Development of a lab-on-a-chip system with integrated sensors for 3D tissue engineering applications

Haseena Bashir Muhammad¹, Chiara Canali¹, Soumyaranjan Mohanty¹, Mette Hemmingsen¹, Maciej Skolimowski¹, Martin Dufva¹, Anders Wolff¹, Jenny Emnéus¹

¹ *Department of Micro- and Nano-technology, Technical University of Denmark, 2800, Kgs Lyngby, Denmark*

hbmu@nanotech.dtu.dk

Organ transplantation is often the primary life-saving medical approach for treatment of several diseases. However limitations in this procedure such as shortage of donor organs and tissue rejection have motivated research into the development of bioartificial organs as an alternative approach. In this work, the development of a novel, modular, microfluidic lab-on-a-chip system is presented which is designed to engineer liver tissue in an in vivo mimicking environment. The system incorporates smart bioreactors, designed to support a 3D porous scaffold with embedded cells and integrated sensors for monitoring the development of the tissue. Each bioreactor is designed to accommodate a microporous scaffold having dimensions of $5 \times 5 \times 5$ mm³ and includes spatially distributed bioimpedance based sensors which penetrate the scaffold for real time monitoring of the distribution, proliferation and viability of cells under continuous perfusion conditions. To enable delivery of nutrients and removal of tissue culture waste products, the system also incorporates peristaltic pumps, motors and reservoirs. An array of eight bioreactors are included, to enable parallel tissue culture experiments for optimisation of parameters such as flow rate, and to allow screening of various stem cell differentiation factors. The system components are fabricated using a combination of 3D rapid prototyping and microfabrication techniques. Proof of principle is demonstrated by culturing liver cancer cell line (HepG2 cells) in porous scaffolds based on polymers such as gelatin and polylactic acid.

The robust and versatile microfluidic platform presented in this work has a huge potential for 3D tissue engineering applications. The novelty of the device is in the employment of combined micro sensing and polymer scaffold engineering approaches for 3D organ engineering. The use of integrated non-invasive sensing strategies, overcome limitations in traditionally adopted optical techniques, and enable monitoring of tissue development within otherwise inaccessible areas of a 3D tissue construct.



A bioimpedance-based sensing system for monitoring cellular dynamics in a 3D culture environment

Chiara Canali¹, Haseena Bashir Muhammad¹, Ørjan G. Martinsen², Arto Heiskanen¹, Martin Dufva¹, Anders Wolff¹, Jenny Emnéus¹

¹ *Department of Micro- and Nano-technology, Technical University of Denmark, 2800, Kgs Lyngby, Denmark*

chca@nanotech.dtu.dk

There is currently an increasing interest in developing sensitive analytical methods for real-time monitoring of the entire process of tissue engineering, starting from a bare 3D polymer porous scaffold, to cell attachment, growth and differentiation, to form vascularised organ-on-a-chip systems. Bioimpedance has been demonstrated as a powerful tool for the study and modelization of biological systems both in vivo and in vitro, establishing a physical correlation between bioelectrical measurement and tissue growth characterization.

In this work, a bioimpedance-based 3D tissue culture Lab-On-A-Chip (LOC) system was designed and optimized in order to follow cellular dynamics under in vitro growth conditions mimicking the in vivo environment. Since important electrical characteristic of an electrode/tissue system are determined solely by geometrical configuration, simplified finite element models were used to optimize electrodes number and orientation and the deriving sensitivity field distribution inside the LOC. The resulting chip with two opposite couples of vertical rectangular plate electrodes was tested as a three-terminal configuration in which current-carrying (CC) and pick-up (PU) electrodes can be switched among different positions to extend a positive sensitivity field to the whole bulk volume. As proof-of-concept, the system was tested for growing different concentrations of mesenchymal stem cells embedded within gelatin scaffold. Preliminary results indicate that the bioimpedance-based LOC device here presented has a high potential for real-time monitoring of the entire process of tissue engineering without affecting cell viability.

Since different combinations of CC and PU electrodes can be exploited, this system will pave the way towards electrical impedance tomography applications to image the changes in 3D cell culture environments.

Design and optimisation of a lab-on-a-chip system with integrated sensors for 3D tissue engineering applications

Haseena Bashir Muhammad, Chiara Canali, Soumyaranjan Mohanty, Mette Hemmingsen, Maciej Skolimowski, Martin Dufva, Anders Wolff, Jenny Emnéus

^a Department of Micro- and Nano-technology, Technical University of Denmark, Kgs Lyngby, 2800, Denmark

e-mail: hbmu@nanotech.dtu.dk

Keywords: lab-on-a-chip, organ-on-a-chip, tissue engineering, bioimpedance sensors, microfluidics

Organ transplantation is often the primary life-saving medical approach for the treatment of several diseases. However limitations in this procedure such as shortage of donor organs and tissue rejection, have motivated research into the development of bioartificial organs as an alternative approach. To this end, various engineering technologies have been exploited for implementing systems to support and sustain the cultured tissue [1,2]. The main purpose of this work is to develop an extracorporeal bioartificial liver (BAL) by combining stem cell, 3D scaffold and micro sensing technologies. The development of a novel, modular, microfluidic lab-on-a-chip system is presented, which is designed to engineer liver tissue in an in vivo mimicking 3D micro environment.

The system incorporates polylactic acid (PLA) based smart bioreactors, designed to support a 3D porous scaffold with embedded cells, and integrated sensors for monitoring the development of the tissue. Each bioreactor (Figure 1) is designed to accommodate a microporous scaffold having dimensions of $5 \times 5 \times 5 \text{ mm}^3$ and includes spatially distributed bioimpedance based sensors which penetrate the scaffold for real time monitoring of the distribution, proliferation and viability of cells under continuous perfusion conditions (Figure 2). To enable delivery of nutrients and removal of tissue culture waste products, the system also incorporates peristaltic pumps, motors and reservoirs (Figure 3). Computational modeling (Comsol Multiphysics™ A/S, Kgs. Lyngby, Denmark) is performed to evaluate the fluidic and mass transport characteristics within the bioreactor (Figure 4). An array of eight bioreactors are included, to enable parallel tissue culture experiments for optimisation of culture parameters such as flow rate, and to allow screening of various stem cell differentiation factors. The system components are fabricated using a combination of 3D rapid prototyping (fused filament deposition) and microfabrication techniques. To demonstrate proof-of-principle, the system is initially evaluated by culturing liver cancer cell line (HepG2) in porous polymer scaffolds. The system is also used to assess the functional outcomes of employing porous scaffolds made from different polymer materials (such as gelatin and polylactic acid).

The novelty of the device is in the employment of combined sensing and polymer scaffold engineering approaches for 3D organ engineering. The use of integrated non-invasive sensing strategies, overcome limitations in traditionally adopted optical techniques, and enable monitoring of tissue development within otherwise inaccessible areas of a 3D tissue construct [3]. The robust and versatile device presented here shows great promise as a powerful high throughput platform for overcoming challenges in 3D tissue engineering and for use in advanced biomedical applications.

[1] J.S. Miller, K.R. Stevens, M.T. Yang et al., Nature Materials (2012), vol. 11(9), 768-774.

[2] L.M. Bellan, T. Kniazeva, E.S.Kim et al., Advanced Healthcare Materials (2012), vol 1(2), 164-167.

[3] F. Lei, M. Wu, P. Liao, Y.Chen, T. Pan, Microfluid Nanofluid (2012), vol. 12, 117-125.

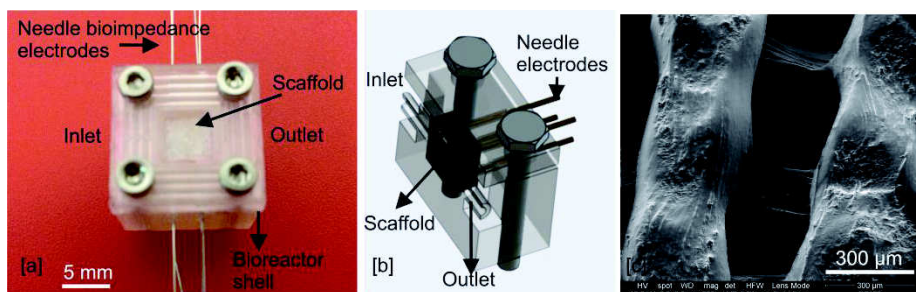


Figure 1. [a] 3D biochip containing scaffold and embedded electrode array, [b] Cross sectional schematic of biochip, [c] SEM image of Porous PLA scaffold.

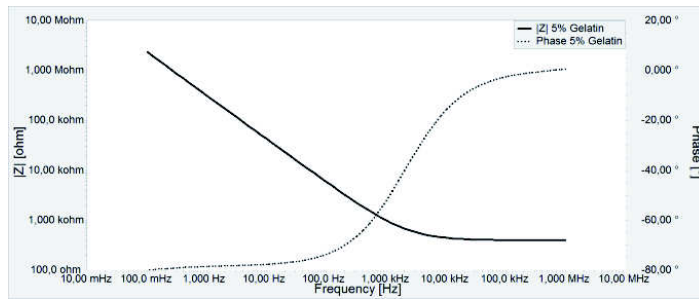


Figure 2. Bode plot obtained from preliminary experiments conducted using bioimpedance needle electrodes embedded within a gelatin scaffold showing impedance spectra under application of a 10 mV peak to peak sinusoidal voltage over a frequency spectra of 10 mHz to 1 MHz.

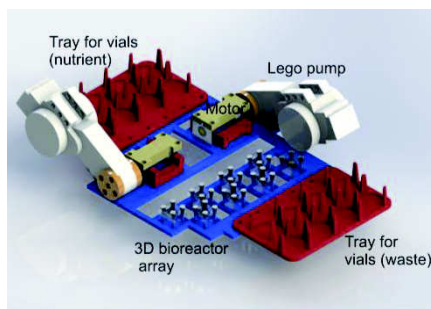


Figure 3. Design of the lab-on-a-chip system with 8 bioreactors, 2 micromotors and pumps and trays for holding vials for fluid storage.

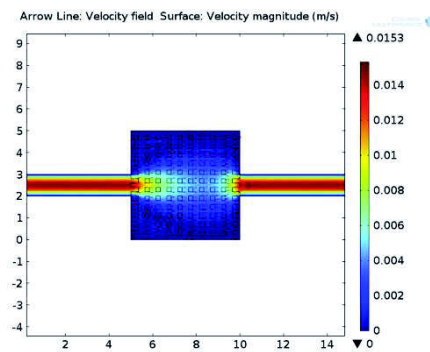
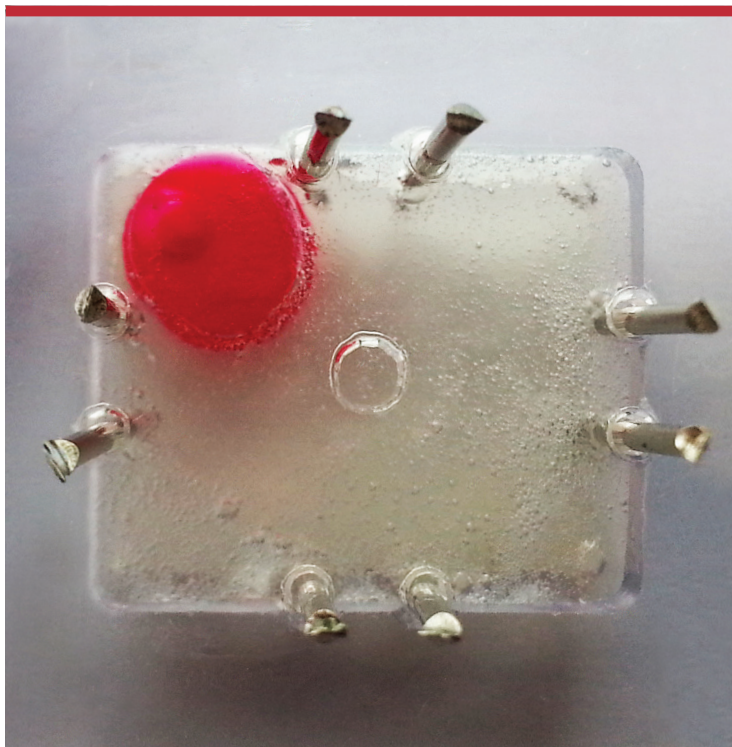


Figure 4. Simulation of fluid flow through microporous scaffold.



Copyright: Chiara Canali
All rights reserved

Published by:
DTU Nanotech
Department of Micro- and Nanotechnology
Technical University of Denmark
Ørsteds Plads, building 345B
DK-2800 Kgs. Lyngby